



# Trajectory-based analyses of ultrafast strong field phenomena

## Dissertation

zur Erlangung des akademischen Grades  
Doctor rerum naturalium  
(Dr. rer. nat.)

vorgelegt  
der Fakultät Mathematik und Naturwissenschaften  
der Technischen Universität Dresden

von  
**Lisa Ortmann**  
(geb. Keller)  
geboren am 15.11.1990 in Freiburg i. Br.

Max-Planck-Institut für Physik komplexer Systeme

Dresden 2019



1. Gutacher: Prof. Dr. Manfred Lein
2. Gutacher: Prof. Dr. Jan-Michael Rost
3. Gutacher: Prof. Dr. Walter Strunz

Eingereicht am 21.05.2019

Verteidigt am 09.09.2019







---

# Contents

## Chapter Preamble PAGE 1

Abstract . . . . .	1
Publication list . . . . .	5
Recurring acronyms and abbreviations . . . . .	7

## Chapter 1 Introduction and thesis outline PAGE 9

## Chapter 2 Fundamental concepts PAGE 15

2.1 Introduction to strong field ionization . . . . .	15
2.1.1 From single to multiphoton ionization . . . . .	15
2.1.2 Multiphoton versus tunneling ionization . . . . .	17
2.1.3 Atomic units . . . . .	18
2.1.4 Basic equations . . . . .	19
2.2 Approximations . . . . .	20
2.3 Classical and Quantum Trajectory Monte Carlo simulations . . . . .	21
2.3.1 The trajectory picture . . . . .	21
2.3.2 The initial conditions . . . . .	22
2.3.2.1 The adiabatic ionization rate . . . . .	22
2.3.2.2 The tunnel exit . . . . .	25
2.3.2.3 Implementation of the sampling process . . . . .	27
2.3.3 Propagation . . . . .	29
2.3.3.1 Propagation in CTMC simulations . . . . .	29
2.3.3.2 Propagation in QTMC simulations . . . . .	30

## Chapter 3 Revisiting nonadiabatic effects on initial conditions PAGE 35

3.1 Introduction to nonadiabatic theories . . . . .	35
3.2 Description of the problem addressed in this chapter . . . . .	39

3.3	Relation between the nonadiabatic theories of Yudin/Ivanov and Li . . . . .	41
3.4	Distinguishing between nonadiabatic theories at the detector . . . . .	45
3.5	Conclusion and Outlook . . . . .	49

**Chapter 4 Intensity and pulse duration dependence of Rydberg states** **PAGE 53**

4.1	Introduction to Rydberg states . . . . .	54
4.2	Intensity dependence . . . . .	55
4.2.1	Prior analytical estimates . . . . .	55
4.2.2	Including the ionization time width . . . . .	57
4.2.3	Nonadiabatic effects . . . . .	58
4.2.4	Wavelength correction . . . . .	62
4.2.5	Conclusion and Discussion . . . . .	65
4.3	Pulse duration dependence . . . . .	66
4.3.1	A primer on principal quantum numbers of Rydberg states . . . . .	67
4.3.2	Simulation results for the principal quantum number distribution . . . . .	67
4.3.3	Physical interpretation of the pulse duration effect . . . . .	68
4.3.4	Testing the effect of the envelope shape . . . . .	69
4.3.5	Analysis of trajectories . . . . .	70
4.3.6	Dependence of the Rydberg yield on pulse duration . . . . .	72
4.3.7	Comparison to other models . . . . .	74
4.3.8	Dependence of the principal quantum number distribution on pulse duration . . . . .	75
4.3.9	Conclusion and Discussion . . . . .	77

**Chapter 5 Emergence of a Higher Energy Structure in inhomogeneous fields** **PAGE 79**

5.1	Introduction to inhomogeneous fields . . . . .	80
5.1.1	Introduction to nano-attophysics . . . . .	80
5.1.2	Mathematical description of inhomogeneous fields . . . . .	82
5.1.3	Three different inhomogeneity regimes . . . . .	86
5.2	Emergence of a higher energy structure . . . . .	87
5.2.1	Choosing the parameters . . . . .	87
5.2.2	Simulations . . . . .	88
5.3	Analysis and optimization of the higher energy structure . . . . .	93
5.3.1	Analytical approximation via Mathieu equations . . . . .	94
5.3.1.1	Analytical approximation for the acceleration and thus the inhomogeneous field . . . . .	95
5.3.1.2	Analytical approximation for the velocity . . . . .	96
5.3.2	Analytical approximation using a perturbative approach . . . . .	98
5.3.3	Spectral position of the HES . . . . .	100
5.3.4	Spectral width of the HES . . . . .	103
5.3.5	Summary of the analysis of the HES . . . . .	106
5.4	Unifying effects in strong inhomogeneous fields . . . . .	107
5.4.1	An intuitive model for the energy upshift observed in the HES . . . . .	108
5.4.2	Unified model for HES and LEP . . . . .	109
5.4.3	A new analytical description of the energy upshift . . . . .	115
5.4.3.1	An analytical description including subcycle effects . . . . .	117

5.4.4	Explaining the experimentally observed linear intensity scaling . . .	120
5.4.5	Conclusion and Outlook . . . . .	121

**Chapter 6 Tracking the ionization site in a neutral diatomic molecule** **PAGE 123**

6.1	Goals and challenges in describing molecular effects . . . . .	123
6.2	The problem of tracking the ionization site in a molecule . . . . .	125
6.3	A new method for tracking the ionization site in a molecule . . . . .	127
6.3.1	Experimental results . . . . .	127
6.3.2	Performing molecular QTMC simulations . . . . .	129
6.3.3	Explanation for the asymmetry via trajectory analysis . . . . .	131
6.3.4	Comparison of theoretical and experimental results to identify the ionization site . . . . .	134
6.4	Conclusion and Outlook . . . . .	136

**Chapter 7 Conclusions and Outlook** **PAGE 139**

**Chapter A Appendix** **PAGE 145**

A.1	Tunnel exits and transverse momentum spreads in nonadiabatic theories .	145
A.2	Ionization time spreads of Yudin/Ivanov and Li as special cases of Bondar .	146
A.3	Interpretation of the intensity dependence of the Rydberg yield . . . . .	148
A.4	Equations of motion in the Coulomb-free electric field . . . . .	149
A.5	Term $\nu_1$ in the perturbative approach . . . . .	150
A.6	Graphically estimating $\beta$ for minimal HES width . . . . .	153

**Chapter Bibliography** **PAGE 155**

**Chapter Addendum** **PAGE 185**

	Acknowledgments . . . . .	185
	Declaration . . . . .	189



## Abstract

Semiclassical theories have proven to be a versatile tool in ultrafast strong field science. In this thesis, the power of classical trajectory Monte Carlo (CTMC) and quantum trajectory Monte Carlo (QTMC) simulations is celebrated by applying them in various strong field ionization settings.

One question to be addressed concerns the way nonadiabaticity in the ionization process manifests itself. It will be shown how the assumption of a vanishing initial longitudinal momentum is the reason for the strong broadening of the initial time spread claimed in a popular nonadiabatic theory. Moreover, it will become clear how the broader time spread of this theory and the non-zero initial longitudinal momenta of another widely applied nonadiabatic theory approximately compensate each other during propagation for typically studied nonadiabatic parameters. However, parameters in the nonadiabatic but still experimentally relevant regime will be found where this approximation breaks down and the two different theories lead to distinguishably different momentum distributions at the detector after all, thus allowing to test which theory describes the situation at the tunnel exit more accurately.

After having tunneled through the barrier formed by the laser and Coulomb potential, the electron does not necessarily leave the atom for good but can be captured in a Rydberg state. A study of the intensity-dependence of the Rydberg yield will reveal, among other things, nonadiabatic effects that can be used as an independent test of nonadiabaticity in strong field ionization. Moreover, it will be shown that the duration of the laser pulse can be used to control both the yield and principal quantum number distribution of Rydberg atoms.

The highly enhanced and spatially inhomogeneous fields close to a nanostructure are another setting in which atoms can be ionized. Here, the emergence of a prominent higher energy structure (HES) in the spectrum of photoelectrons will be reported. The narrow time-window in which the corresponding electrons are released suggests a promising method for creating a localized source of electron pulses of attosecond duration using tabletop laser technology. Having such potential applications in mind, analytical expressions are derived to describe the electrons' motion in the inhomogeneous field, thus being able to control the spectral position and width of the HES. Moreover, a unifying theory will be developed in which the recently reported experimental finding of a low-energy peak (LEP) can be understood to arise due to the same mechanism as the theoretically predicted HES, despite those two effects having been found in different energy regimes so far. This unifying theory will show how the well-established experimental technique in which the LEP was reported, i.e. ionization directly from the nanotip rather than from atoms in its vicinity, should allow the realization of a prominent and narrow peak at higher energies as it was theoretically described in the framework of the HES.

Despite being much weaker, the spatial inhomogeneity of the Coulomb potential can influence the photoelectron spectrum as well. It will be shown how the asymmetric Coulomb potential of a tilted diatomic molecule introduces an asymmetry in the photoelectron momentum distribution at the detector. The degree of asymmetry depends on whether the electron is born at the up- or downfield atom. This information is then used to quantify the ratio of ionization from the up- and downfield site from experimental photoelectron momentum distributions.



## Kurzfassung

Semiklassische Theorien haben sich als vielfältiges Werkzeug in dem Forschungsbereich der ultrakurzen und starken Laserfelder herausgestellt. In der vorliegenden Arbeit wird die Leistungsfähigkeit von Monte Carlo Simulationen mit klassischen und quantenmechanischen Trajektorien gefeiert, indem diese auf verschiedene Systeme der Starkfeldionisation angewendet werden.

Eine der Fragen, die behandelt werden wird, betrifft die Art und Weise, in der sich nichtadiabatische Effekte im Ionisationsprozess manifestieren. Es wird gezeigt werden, wie die Annahme eines verschwindenden Anfangsimpulses der Grund für die starke Verbreiterung der Startzeitenverteilung ist, welche in einer weitverbreiteten nichtadiabatischen Theorie angegeben wird. Zudem wird klar werden, wie die breitere Startzeitenverteilung dieser Theorie und der nichtverschwindende Anfangsimpuls einer anderen häufig angewandten nichtadiabatischen Theorie sich näherungsweise während der Propagation kompensieren, wenn typische nichtadiabatische Parameter verwendet werden. Es werden jedoch Parameter im nichtadiabatischen und dennoch experimentell relevanten Bereich gefunden werden, wo diese Näherung versagt und die zwei verschiedenen Theorien doch noch zu erkennbar verschiedenen Impulsverteilungen am Detektor führen. Dies erlaubt zu testen, welche Theorie die Situation am Tunnelausgang genauer beschreibt.

Nachdem das Elektron durch die Barriere getunnelt ist, die Coulomb- und Laserpotential formen, verlässt das Elektron das Atom nicht unbedingt endgültig, sondern kann in einem Rydbergzustand gefangen werden. Die Untersuchung der Intensitätsabhängigkeit des Rydbergertrags wird unter anderem nichtadiabatische Effekte hervorbringen, die als unabhängiger Test von Nichtadiabatizität in der Starkfeldionisation genutzt werden können. Zudem wird gezeigt, dass die Dauer des Laserpulses verwendet werden kann, um sowohl den Ertrag als auch die Verteilung der Hauptquantenzahl der Rydbergatome zu kontrollieren.

Ein anderes System, in welchem Atome ionisiert werden können, sind die hochgradig verstärkten und räumlich inhomogenen Felder nahe einer Nanostruktur. Hier wird von dem Auftreten einer markanten Hochenergiestruktur (HES) berichtet werden. Das schmale Zeitfenster, in welchem die zugehörigen Elektronen abgegeben werden, weist auf eine vielversprechende Methode zur Erschaffung einer lokalisierten Quelle hin, von der Elektronenpulse mit Pulsdauern im Attosekundenbereich ausgehen und in welcher ausschließlich Technologie verwendet wird, die auf einen optischen Experimentiertisch passt. Mit solchen Anwendungen im Hinterkopf werden analytische Ausdrücke hergeleitet, um die Bewegung der Elektronen im inhomogenen Feld zu beschreiben und auf diese Weise die spektrale Position und Breite der HES zu kontrollieren. Darüber hinaus wird eine verallgemeinernde Theorie entwickelt, in der der kürzlich berichtete experimentelle Fund eines Niederenergiepeaks aufgrund desselben Mechanismus erscheint wie die theoretische vorhergesagte HES, obwohl die beiden Effekte bislang in verschiedenen Energiebereichen gefunden wurden. Diese verallgemeinernde Theorie wird zeigen, wie die gut etablierte experimentelle Technik, mit welcher die Niederenergiestruktur erzeugt wurde, d.h. Ionisation direkt von der Nanospitze statt von Atomen in deren Nähe, die Realisierung eines markanten und schmalen Peaks bei hohen Energien ermöglicht, wie er zuvor nur theoretisch im Rahmen der HES beschrieben wurde.

Auch wenn die räumliche Inhomogenität des Coulombpotentials viel schwächer ist, kann auch sie das Photoelektronenspektrum beeinflussen. Es wird gezeigt werden,

wie das asymmetrische Coulombpotential eines verkippten zweiatomigen Moleküls eine Asymmetrie in der Elektronenimpulsverteilung am Detektor erzeugt. Der Grad der Asymmetrie hängt davon ab, ob das Elektron das Molekül am Atom, das oben oder unten im Laserpotential liegt, verlassen hat. Diese Information wird dann genutzt, um das Verhältnis der Ionisation von den beiden Atomen, die oben oder unten im Laserpotential liegen, aus experimentellen Photoelektronenimpulsverteilungen quantitativ zu ermitteln.



## Publication list

The work presented in this thesis has partially already been published as follows:

- **Emergence of a higher energy structure in strong field ionization with inhomogeneous electric fields**  
L. Ortmann, J. Pérez-Hernández, M. Ciappina, J. Schötz, A. Chacón, G. Zeraouli, M. F. Kling, L. Roso, M. Lewenstein, and A. S. Landsman.  
Physical Review Letters 119.5 (2017), p. 053204.  
(see Chapter 5 of this thesis)
- **Analysis of the higher-energy structure in strong-field ionization with inhomogeneous electric fields**  
L. Ortmann and A. S. Landsman.  
Physical Review A 97.2 (2018), p. 023420.  
(see Chapter 5 of this thesis)
- **Dependence of Rydberg-state creation by strong-field ionization on laser intensity**  
L. Ortmann, C. Hofmann, and A. S. Landsman.  
Physical Review A 98.3 (2018), p. 033415.  
(see Chapter 4 of this thesis)

Manuscripts in preparation that cover contents of this thesis:

- **Nonadiabatic effects on the initial longitudinal momentum and the ionization time distribution in strong field ionization**  
L. Ortmann, I. Ivanov, and A. S. Landsman.  
(see Chapter 3 of this thesis)
- **Controlling the quantum number distribution and yield of Rydberg states via the duration of the laser pulse**  
L. Ortmann, C. Hofmann, and A. S. Landsman.  
arXiv:1810.07164  
(see Chapter 4 of this thesis)
- **Unifying effects in strong inhomogeneous fields**  
L. Ortmann, L. Pi, and A. S. Landsman.  
(see Chapter 5 of this thesis)
- **Tracking the ionization site in neutral molecules**  
Author list not finalized yet.  
(see Chapter 6 of this thesis)

Work that I have been involved in during my PhD studies but that is not presented in this thesis resulted in the following publications:

- **Double-electron ionization driven by inhomogeneous fields**  
A. Chacón, L. Ortmann, F. Cucchietti, N. Suárez, J. A. Pérez-Hernández, M. F. Ciappina, A. S. Landsman, and M. Lewenstein.  
appeared in Applied Physics B 4.123 (2017), p. 1 as part of the topical collection ‘Enlightening the World with the Laser’, Springer, 2018, p. 491.

- 
- **Wannier-Bloch approach to localization in high-harmonics generation in solids**  
E. N. Osika, A. Chacón, L. Ortmann, N. Suárez, J. A. Pérez-Hernández, B. Szafran, M. F. Ciappina, F. Sols, A. S. Landsman, and M. Lewenstein.  
Physical Review X 7.2 (2017), p. 021017.
  - **Instantaneous ionization rate as a functional derivative**  
I. A. Ivanov, C. Hofmann, L. Ortmann, A. S. Landsman, C. H. Nam, and K. T. Kim.  
Communications Physics 1.1 (2018), p. 81.
  - **Above-threshold ionization in multicenter molecules: The role of the initial state**  
N. Suárez, A. Chacón, E. Pisanty, L. Ortmann, A. S. Landsman, A. Picón, J. Biegert, M. Lewenstein, and M. F. Ciappina.  
Physical Review A 97.3 (2018), p. 033415.
  - **Extraction of higher-order nonlinear electronic response in solids using high harmonic generation**  
S. Han, L. Ortmann, H. Kim, Y. W. Kim, T. Oka, A. Chacon, B. Doran, M. Ciappina, M. Lewenstein, S.-W. Kim, S. Kim, and A. S. Landsman.  
Nature Communications 10, 3272 (2019)
  - **Attosecond streaking delays in multi-electron systems**  
T. Zimmermann, L. Ortmann, C. Hofmann, J.-M. Rost, and A. S. Landsman.  
arXiv:1804.09583
  - **Symphony on Strong Field Approximation**  
K. Amini, J. Biegert, F. Calegari, A. Chacón, M. F. Ciappina, A. Dauphin, D. K. Efimov, C. F. de Morisson Faria, K. Giergiel, P. Gniewek, A. S. Landsman, M. Lesiuk, M. Mandrysz, A. S. Maxwell, R. Moszyński, L. Ortmann, J. A. Pérez-Hernández, A. Picón, E. Pisanty, J. Prauzner-Bechcicki, K. Sacha, N. Suárez, A. Zaïr, J. Zakrzewski, and M. Lewenstein.  
arXiv:1812.11447

## Recurring acronyms and abbreviations

ADK	referring to the adiabatic theory developed by Ammosov, Delone, and Krainov in [1]
ATI	above-threshold ionization
Bondar	referring to the nonadiabatic theory of Bondar published in [2]
CEP	carrier-envelope phase
CREI	charge resonance enhanced ionization
CTMC	classical trajectory Monte Carlo
CWP	classical Wigner propagation
FTI	frustrated tunneling ionization
HES	higher energy structure
HHG	high-harmonic generation
IR	infrared
KER	kinetic energy release
LEP	low-energy peak
Li	referring to the nonadiabatic theory of Li et al. published in [3]
LIED	laser-induced electron diffraction
PPT	referring to the nonadiabatic theory developed by Perelomov, Popov and Terent'ev in [4, 5]
QTMC	quantum trajectory Monte Carlo
SFA	strong field approximation
TDSE	time-dependent Schrödinger equation
TIPIS	tunnel ionization in parabolic coordinates with induced dipole and Stark shift, see [6] for details
XUV	extreme ultraviolet
YI	referring to the nonadiabatic theory of Yudin and Ivanov published in [7]



---

## Introduction and thesis outline

*“In science one tries to tell people, in such a way as to be understood by everyone, something that no one ever knew before. But in poetry, it’s the exact opposite.”*

— Paul Dirac

In 2018, half of the Nobel prize in physics was awarded to Gérard Mourou and Donna Strickland ‘for their method of generating high-intensity, ultra-short optical pulses’ [8, 9]. This reminded us not only of the ingenuity that was needed to create a laser that was both short-pulsed and of high intensity, but first and foremost it showed the relevance and impact of this invention. On the one hand, the intensity is so high that it can bend the Coulomb potential of an atom or molecule, making tunneling through the resulting barrier possible, or enables multiple photons to be absorbed by the atom or molecule [10]. On the other hand, the pulse duration of such lasers is at the time scale of electron motion in atoms and molecules, thus making it possible to time-resolve electron dynamics during and after ionization [11].

In the past decades, the methods to create short, intense laser pulses have been further refined: Ever shorter pulses have been generated and nowadays not only femtosecond but also attosecond pulses are routinely produced [11], high-harmonic generation (HHG) allows to create pulses over a wide range of wavelengths, and stabilization of the carrier-envelope phase (CEP) was achieved [12, 13].

These and many further advancements went hand in hand with the development of a wide variety of new applications. For example, control over the CEP allowed to observe electron localization during chemical reactions [14] and even steer such processes [15]. Another powerful technique is laser-induced electron diffraction (LIED), in which electrons that tunnel out and then diffract from their parent ion carry the fingerprint of the ionized orbital and the position of the nuclei [16–19]. Thus, the molecule can ‘take a picture of itself’ [20]. Similarly, also HHG uses the return of the tunnel-ionized electron to the parent ion for structural retrieval. Here, the electron recombines with its parent ion and the resulting radiation can not only be used as a light-source of smaller wavelengths but also contains information about the atomic or molecular structure [21–25] and the tunneling process itself [26]. Moreover, the recent finding that strong ultrashort laser pulses also lead to HHG radiation in solids [27] has opened a whole new subfield of attosecond science, which promises to help gain so far inaccessible information about electronic properties of a wide range of materials [28–32].

Many more techniques could be listed here which helped gain insights into the quantum mechanical process of strong field ionization and the properties of atoms, molecules, and solids. However, as with every physical technique, meaningful interpretation of all of those observations is not possible without a theoretical model. In the case of strong field attosecond physics, the highly nonlinear and typically non-perturbative nature of the underlying processes makes this a non-trivial task. The main problem originates from the fact that the Schrödinger equation cannot be solved exactly for the superposed laser and Coulombic field [33]. Of course, the Schrödinger equation can be solved numerically but even that usually only allows for a single-active electron approximation and, moreover, often it is not clear how to analyze and interpret such a ‘numerical experiment’.

Therefore, many models introducing various approximations have been developed which allow for less numerically expensive calculations and, in particular, provide results that can be interpreted more intuitively. The strong field approximation (SFA) has proven to be such a tool. In it, the time-dependent Schrödinger equation (TDSE) is solved in an approximate way by applying a systematic perturbation theory in which the Coulomb potential is typically completely neglected in the continuum [33, 34]. Despite such a crude approximation, this theoretical model has reproduced and helped understand many strong field phenomena, such as HHG [35], above-threshold ionization (ATI) [36, 37] or double-ionization [38]. One way to further simplify SFA calculations is to apply saddle point approximations when evaluating highly oscillatory integrals, which reduces computational costs appreciably and lets the resulting quantum paths be interpreted as the most likely trajectories [35].

This, however, is by far not the only model that allows for an intuitive interpretation of strong field phenomena by means of trajectories. In fact, one of the first methods to reveal that the return of the tunnel-ionized electron to the parent ion accounts for the intriguing strong field phenomenon of HHG was an unsophisticated and yet powerful trajectory model, the aptly named ‘simple-man model’, which is also referred to as the ‘three-step model’ [39]. In this one-dimensional model a classical trajectory describing the electron is started with zero initial velocity and the Coulomb potential of the residual ion is not included during propagation. In this framework, the highest kinetic energy a returning electron can have is 3.17 times the cycle-averaged kinetic energy  $U_p$ , which explains the cutoff of the HHG spectrum found at  $3.17U_p + I_p$  (with  $I_p$  the ionization potential). Thus, we have already made the acquaintance with all three steps of the ‘three-step model’: ionization, propagation, and recollision. Since its initial success, the simple-man model has been applied to many other strong field settings and has been developed further into ever more elaborate ways to describe the post-ionization electron dynamics [40–42].

Obviously, one can easily extend the model and include the Coulomb potential of the residual ion, even though one thus sacrifices analytical tractability. Another crucial improvement of this model is the use of not only a single trajectory released at the field maximum with zero velocity, which in the framework of quasistatic ionization theories can be interpreted as the most likely trajectory, but employing a swarm of trajectories with initial conditions that follow the probability distribution obtained from strong field ionization rates [43, 44]. The statistical nature of the selection of initial conditions along with the fact that the propagation is done classically by solving Newton’s equation of motion explains the name of these methods: classical trajectory Monte Carlo simulations, often abbreviated as CTMC simulations.

The strength of CTMC models lies in their full inclusion of the Coulomb potential, which e.g. the SFA does not have, and in the possibility to analyze trajectories, which the numerical solution of the TDSE does not allow. These advantages have made CTMC simulations a tool that has helped understand many effects in different areas of strong field ionization in the past decades, among which are double-ionization [45–47], Rydberg states [48–52] and Coulomb-related effects such as the low-energy structure [53–55] or Coulomb focusing [43, 46], to mention but a few.

The power of CTMC simulations has grown with ever more accurate probability distributions to describe the initial conditions of the electron at the tunnel exit. Especially going beyond using a quasistatic ionization theory and capturing nonadiabatic effects has been of interest in recent years and is still under discussion [2, 3, 7, 56–61].

One effect that cannot be captured in the framework of purely classical trajectories, though, is the interference pattern the photoelectron distribution at the detector exhibits. However, a method to include a semiclassical phase along the pathway of the classical trajectory was introduced to overcome this shortcoming. Indeed, the resulting model named ‘Quantum Trajectory Monte Carlo’ (QTMC) [62] and further refinements [60] successfully reproduce key features of the photoelectron interference pattern [60, 63–68], thus having opened a wide range of new phenomena that can be explained by trajectory-based Monte Carlo methods.

The work presented in this thesis celebrates the power of CTMC and QTMC by making copious use of it and, in particular, by applying it to cases that are difficult or impossible to describe in the framework of SFA. To highlight this point, let us briefly review the main prerequisites for the application of the SFA [33]:

1. The field of the laser is so strong that multiphoton and tunnel ionization are the dominant ionization processes.
2. The Coulomb potential of the residual ion has a negligibly small effect on the dynamics in the continuum.
3. The dipole approximation can be applied which, in particular, requires a spatially homogeneous description of the electric field.

Although there are adaptations of the SFA that introduce Coulomb corrections [69, 70], they are just that: corrections. In processes where the Coulomb potential plays a key role and needs to be included with high accuracy, this is often not sufficient and CTMC and QTMC reveal their power. In chapter 4, this will become clear in the study of frustrated tunneling ionization and the herein created Rydberg states, which is an effect that was first understood by that very method of CTMC [48]. Revisiting the research done on the intensity dependence [49], it will be shown how Rydberg states can be used to test nonadiabatic effects in a way that contrasts the commonly used methods in that it does not depend on the momentum distribution and therefore does not involve the issues of adiabatic or nonadiabatic calibration of the absolute intensity [71]. Moreover, section 4.3 will show how the pulse duration can be used to control the yield and quantum number distribution of Rydberg states. As it will become clear that the underlying effect depends sensitively on the Coulomb potential, this will be a case in point for showing the importance of including the Coulomb potential during the propagation process [72].

The versatility of CTMC will become even clearer in chapter 5, where it is applied to inhomogeneous fields as they are typically created in the vicinity of a nanostructure.



In this case, the electric field exhibits a strong spatial dependence and consequently the dipole approximation breaks down and thus also the applicability of the SFA (see point 3. in the above list). CTMC, in contrast, can fully include the inhomogeneity of the electric field and with its help we will, for the first time, observe and understand the emergence of a higher energy structure (HES) in the photoelectron spectrum [73, 74]. The fact that this accumulation of highly energetic electrons is observed in both TDSE and CTMC simulations shows that the underlying mechanism can be captured in the classical limit. This insight will lead us to a more general understanding of the formation of peak structures in inhomogeneous fields and in the last section of this chapter a theory will be developed to describe these features in a unified framework. In particular, a peak structure that was observed independently by experimentalists [75] in inhomogeneous fields and was named ‘low-energy peak’ due to its location in the low-energy regime is found to be explained by that unified theory in which also the appearance of the HES is understood.

Chapter 6 will then present a theory that allows to retrieve information about the ionization site in a diatomic molecule. So far, such studies were restricted to ionization from charged molecules with Coulomb explosion ensuing the ionization process. Here, in contrast, a method is developed for the ionization of neutral molecules that makes use of the deflection of the electron in the asymmetric Coulomb potential of the tilted molecule. Since the degree of deflection depends strongly on which atom that electron was ionized at, the resulting asymmetry in the photoelectron momentum distribution at the detector can be mapped onto the ionization rates of the up- and downfield atom in the molecule. Including the Coulomb potential as accurately as possible is of utmost importance in this case, which serves as another example of a system that can be described better by a CTMC or QTMC method than by SFA. In this chapter, experimental data will prove that the mentioned deflection effect is indeed visible. Comparing the resulting experimental asymmetry to the theoretically calculated one, the ionization rates at the different ionization sites can be determined from experimentally obtained photoelectron momentum distributions. This direct applicability to experimental data and the fact that the momentum distribution that is observed at the detector exhibits strong interference fringes calls for using a QTMC rather than a CTMC simulation in that case in order to model the experimental setting with highest accuracy.

Speaking of accuracy in the description of the physical system leads us to the content of chapter 3, which will set the stage for the above-described applications by discussing nonadiabatic effects on the initial conditions at the tunnel exit. If the laser field changes slowly when compared to the dynamics of the bound state, the bound state can adapt adiabatically to the changing laser field. In this limit, quasistatic assumptions work very well. However, it is less clear how to describe the ionization process theoretically when the laser field and thus also the potential barrier move faster and nonadiabatic effects set in. Different nonadiabatic theories developed in the past give seemingly contradictory answers to the question of how nonadiabaticity manifests itself at the tunnel exit. While one of the most popular theories claims a strong broadening of the ionization time spread and makes the case for zero longitudinal momentum at the tunnel exit [7], another prominent nonadiabatic theory [3] shows that the initial longitudinal momentum is by far not negligible and arrives at a considerably less broad time spread. Chapter 3 is devoted to resolving the confusion that has resulted from these discrepancies by showing how these two major nonadiabatic theories relate



---

to each other and by presenting a test that aims at finding out which theory describes the situation at the tunnel exit more accurately by means of comparison with TDSE simulations.

The thesis will be rounded off in chapter 7 by a short summary of the findings presented in this work along with some concluding remarks and an outlook on open questions and potential future work related to this thesis.



---

## Fundamental concepts

*“If I have seen further, it is by standing on the shoulders of giants.”*

— Isaac Newton

This chapter introduces various general concepts and the related nomenclature that will be used and referred to throughout the thesis. Introductions to the more specialized subfields for which new results are presented in chapters 3 to 6 are found at the beginning of the respective chapters.

### 2.1 Introduction to strong field ionization

#### 2.1.1 From single to multiphoton ionization

In 1905, Einstein’s work on the photoelectric effect and the light quantum hypothesis were published [76], thus revolutionizing the field of light-matter interaction. The photoelectric effect as described by Einstein is characterized by the following features [77]:

- (a) For a given material, meaning a specific work function, there is a minimum frequency of the incident radiation below which the photoelectrons will not be emitted.
- (b) At a fixed frequency of the incident light and for a given material, the photoelectron rate is proportional to the intensity of the incident light.
- (c) Above the minimum frequency described in (a), the maximal kinetic energy of the photoelectron does not depend on the intensity of the incident light and is described by  $E_{kin,max} = \hbar\omega - I_p$ , with  $I_p$  the ionization potential or work function.

Even though all experimental data available at that time could be explained in this framework, the advent of lasers, in particular those with higher intensities, produced results that contradicted these ‘laws’. The reason for this breakdown is that Einstein’s photoelectric effect is built on the assumption of a single photon being absorbed. However, as theoretically postulated by Maria Göppert-Mayer in 1931 [78] even before the first laser was built, and as verified experimentally in the early 1960s [79, 80], an electron can be ionized by the help of two photons. With the rise of ever more intense

lasers, this concept was found to be more general with multiple photons bridging the energy gap from the binding energy to the continuum. This process is depicted in the top left panel of Fig. 2.1 and is sometimes referred to as the ‘vertical channel’. Concerning the features listed above to describe photoionization, these have to be modified in the following way:

- (a') Even below the minimum frequency for the onset of single-photon ionization, multiple photons can provide the energy for the release if the intensity of the incident laser is sufficiently high.
- (b') In the perturbative regime, the ionization rate scales like  $I^{n_{ph}}$  with  $n_{ph}$  the number of photons absorbed [33]. Einstein's single-photon ionization can be considered a special case of that, with  $n_{ph} = 1$ .
- (c') The maximal kinetic energy of the photoelectrons needs to be modified.

As for the last point, it was formulated in such a vague way on purpose since the photoelectron spectrum in strong field ionization turned out to be more complicated than one would think [81, 82] and warrants some more words than fit into the above list. What one expected from the photoelectron spectrum was that it would follow  $E_{kin,max} = n'_{ph}\hbar\omega - I_p$ , with  $n'_{ph}$  the minimal number of photons required to overcome the ionization potential  $I_p$ . However, it was observed that far more photons can be absorbed in the ionization process than are needed to overcome the ionization potential, leading to higher maximal kinetic energies than had been predicted [81]. This effect is nowadays called above-threshold ionization, short ATI, and manifests itself in photoelectron spectra of several peaks that are separated by the photon energy  $\hbar\omega$ . One observation that did not quite fit into the picture, though, was that as intensity increases, the lowest order peaks are reduced and eventually suppressed [82, 83]. Later, the explanation for this peak suppression was found in the shift of the atomic states' energies in the presence of a laser field [84, 85]. The level-shift due to the dynamic stark effect is given by the ponderomotive energy

$$U_p = \frac{E_0^2}{4\omega^2}, \quad (2.1)$$

the cycle-averaged kinetic energy of the electron's quiver motion in the laser field [86, 87], where  $E_0$  is the maximum field strength and  $\omega$  the angular frequency of the laser field. Consequently, the kinetic energy of the photoelectrons is given by

$$E_{kin} = n_{ph}\hbar\omega - I_p - U_p, \quad (2.2)$$

with  $n_{ph}$  the number of actually absorbed photons. Seeing this equation one might be wondering why the effect of the Stark shift was not recognized faster since it should also shift all peaks from the expected position at  $n_{ph}\hbar\omega - I_p$  by  $U_p$ . This shift, though, was not observed in the early experiments due to the long pulses utilized in those days [82, 85, 88]. The long pulse duration entailed that the electron could leave the laser focus before the intensity had decreased significantly. Upon leaving the focus, the gradient force gave the electron energy of the amount of the ponderomotive potential. Thus, the energy loss from the shift of the ionization potential was compensated and the peaks appeared at  $n_{ph}\hbar\omega - I_p$  after all, leaving the suppression of the lowest order peaks the only conspicuous feature hinting at the Stark shift. Only when the pulses became shorter did the peaks in the ATI spectrum shift by  $U_p$ .

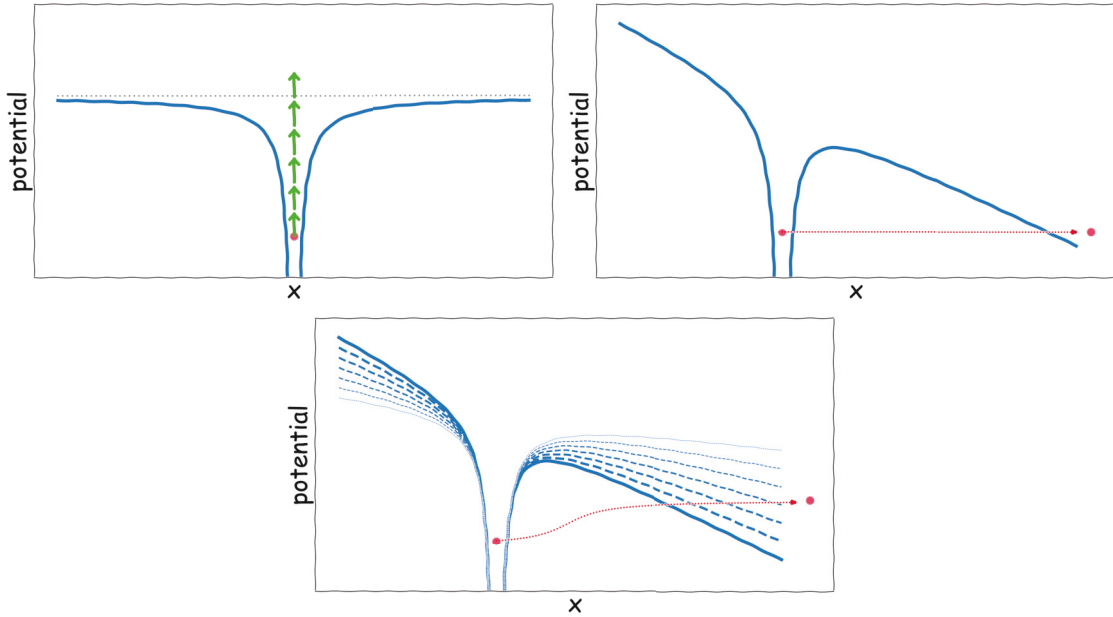


**Figure 2.1:** Illustration of the different ionization channels in the strong field regime. Top left panel: Multiphoton regime, Top right panel: Tunneling regime, Bottom panel: Intermediate nonadiabatic regime.

### 2.1.2 Multiphoton versus tunneling ionization

Multiphoton ionization, or the ‘vertical channel’, is not the only way an electron can leave an atom or molecule. If the ponderomotive energy  $U_p$  is much larger than the ionization potential, the electron can tunnel through the barrier that is formed by the superposed atomic or molecular potential and the laser electric field [83]. This so-called ‘horizontal channel’ is depicted in the top right panel of Fig. 2.1. Even though the tunneling process seems to be distinctly different from the multiphoton ionization channel, the seminal work by Keldysh [89] from 1965 showed that these mechanisms are closely related, being the two limiting cases of nonlinear photoionization [90]. To quantify which laser and atomic parameters lead to ionization in which of these regimes, Keldysh introduced the following parameter

$$\gamma = \frac{\omega \sqrt{2I_p}}{E_0} = \sqrt{\frac{I_p}{2U_p}}. \quad (2.3)$$

For  $\gamma \ll 1$ , we are in the adiabatic limit with tunneling as the dominant ionization process, whereas  $\gamma \gg 1$  marks the multiphoton regime, often referred to as the deep non-adiabatic regime. This also makes sense intuitively, as with a higher laser frequency  $\omega$ , hence a larger  $\gamma$ , fewer photons are required to overcome the ionization energy  $I_p$  and multiphoton ionization is more likely. Conversely, for more intense fields, corresponding to a smaller  $\gamma$ , the barrier width, which can be approximated by  $I_p/E_0$  when assuming a triangular barrier, is smaller and the tunneling probability increases exponentially [91]. From Fig. 2.1 it also becomes clear that in tunnel ionization the time and direction of the electron’s liberation strongly depends on the instantaneous electric field, whereas multiphoton ionization is commonly assumed to happen independently of the phase of the laser field since the electron is released over the top of the potential well [7, 91].

In the intermediate regime of  $\gamma \approx 1$  the two ionization processes co-exist, ‘ready to lend each other a helping hand’ [33], with the electron absorbing energy while moving under the barrier, thus experiencing a narrower barrier and escaping more easily [92]. A pictorial description of this process can be found in the bottom panel of Fig. 2.1. While this intermediate regime is of particular interest as many strong field experiments are conducted in it, it is less straight-forward to describe the ionization process theoretically here. In the past decades, this has resulted in a vivid discussion about the nature of nonadiabaticity, particularly about how it affects when and at which velocity the electron appears in the continuum. Although these questions were not only addressed by CTMC and QTMC simulations [93, 94], they are of particular relevance for these Monte Carlo calculations since this type of simulation relies on an accurate description of initial conditions. Chapter 3 of this thesis contributes to the nonadiabaticity discussion in the framework of CTMC by showing why two seemingly contradictory and yet widely-used nonadiabatic theories for initial conditions give equivalent momentum distributions at the detector over a wide range of parameters and how, after all, there are parameters at which one can distinguish which theory describes the situation at the tunnel exit more accurately. As this requires a more exhaustive description of the intermediate nonadiabatic regime, a more detailed introduction into this field is deferred to the beginning of chapter 3.

For the sake of completeness, I want to close this section with a brief word of caution concerning the applicability of the Keldysh parameter. Even though an extremely low frequency,  $\omega \rightarrow 0$ , or a significantly high intensity,  $I \rightarrow \infty$ , would technically result in a small  $\gamma$ , the above mentioned concepts break down in these limits, as expounded in [95].

### 2.1.3 Atomic units

As some equations in the previous section were already written in a unit system different from the canonical SI units, it is high time we introduced this system of ‘atomic units’, short ‘a.u.’. It is built on the introduction of four independent quantities in atomic units given in Table 2.1.

atomic unit of mass	$m_e$	$\approx 9.1 \times 10^{-31}$ kg	electron mass
atomic unit of electric charge	$e$	$\approx 1.6 \times 10^{-19}$ C	absolute value of electron charge
atomic unit of action	$\hbar$	$\approx 1.05 \times 10^{-34}$ Js	reduced Planck’s constant
atomic unit of permittivity	$4\pi\epsilon_0$	$\approx 1.1 \times 10^{-10}$ F/m	inverse of Coulomb’s constant

**Table 2.1:** *Fundamental atomic units.*

Using these units in the context of atomic and molecular systems has many advantages, not least because they render the electronic Schrödinger equation dimensionless [96]. Moreover, many key atomic properties have values of order unity in atomic units. For example, in the classical Bohr model of the hydrogen atom in its ground state (with infinite nuclear mass), the electron moves on a circle of a radius of 1 a.u. with an orbital velocity of 1 a.u., the electric field strength due to the nucleus is 1 a.u., and the ionization energy amounts to 1/2 a.u. [97]. The conversion of these derived

atomic units into SI units, along with further quantities that are frequently used in the context of strong field phenomena, are listed in Table 2.2.

Unless explicitly stated otherwise, atomic units will be used throughout this thesis, frequently omitting ‘a.u.’.

Length	$a_0 = 1$ a.u.	$\approx 0.529 \times 10^{-10}$ m
Velocity	1 a.u.	$\approx 2.1877 \times 10^6$ m/s
Energy	$E_h = 1$ a.u.	$\approx 4.359744 \times 10^{-18}$ J
Time	1 a.u.	$\approx 2.4188 \times 10^{-17}$ s
Electric field	$E_h/(ea_0) = 1$ a.u.	$\approx 0.51422 \times 10^{12}$ V/m
Intensity	for peak electric field at 1 a.u.	$\approx 3.51 \times 10^{16}$ W/cm <sup>2</sup>

**Table 2.2:** A selection of derived atomic units that are frequently used in strong field ionization physics.

### 2.1.4 Basic equations

Throughout this thesis, except for chapter 5 about spatially inhomogeneous fields, a laser pulse that is linearly polarized in the x-direction and that is defined as follows will be used:

$$\mathbf{E}(t) = E_0 \cos(\omega t + \phi_{CEP}) \cos^2\left(\frac{\omega t}{2N}\right) \hat{\mathbf{x}}. \quad (2.4)$$

As already mentioned,  $E_0$  and  $\omega$  are the maximal field strength and central angular frequency of the laser, respectively.  $\phi_{CEP}$  denotes the carrier-envelope phase (CEP), which determines the absolute phase shift of the primary oscillation (first cosine function in eq. (2.4)) under the envelope ( $\cos^2$  function in eq. (2.4)) and which is of particular importance in short pulses. Unless stated otherwise,  $\phi_{CEP} = 0$  is chosen. The length of the pulse is encoded in the number of optical cycles  $N$ . At various points, when the context is deemed sufficiently clear concerning the single dimension of the laser pulse, the vector notation of the electric field may be omitted.

Closely related to the electric field, there is the vector potential  $\mathbf{A}(t)$ , the negative time derivative of which is the electric field  $\mathbf{E}(t)$ :

$$-\frac{\partial \mathbf{A}}{\partial t} = \mathbf{E}(t). \quad (2.5)$$

The importance of the vector potential lies in the fact that if the Coulomb potential is neglected during the propagation step, the translation invariance leads, according to Nöther’s theorem, to the conservation of the canonical momentum  $\mathbf{p}$

$$\mathbf{p} = \frac{\partial L}{\partial \dot{\mathbf{r}}} = m\dot{\mathbf{r}} + q\mathbf{A} = \mathbf{v} - \mathbf{A} = \text{const}, \quad (2.6)$$

where  $L$  is the classical Lagrangian and it was used that, as the moving particle is an electron, the mass is 1 a.u. and the charge  $q = -1$  a.u.. Since the vector potential can be set to zero after the pulse has passed, we can use the following relation

$$\mathbf{v}(t_f) = \mathbf{v}(t_0) - \mathbf{A}(t_0), \quad (2.7)$$

where  $t_0$  and  $t_f$  are the times at which the electron is born in the continuum and arrives at the detector, respectively.

So far, only the laser field has been described. When propagating the electron after the ionization step, we also have to take into account the Coulomb potential of the residual ion, though:

$$V(\mathbf{r}) = -\frac{1}{\sqrt{r^2 + SC}}. \quad (2.8)$$

The softcore parameter  $SC$  is introduced for mere numerical reasons so as to smooth the singularity. It was chosen to be  $SC = 0.01$  in the calculations presented in this thesis, unless stated otherwise.

In addition, one can also take account of the dipole of the ion in the laser field [6, 98]:

$$V_D(\mathbf{r}, t) = -\alpha_I \frac{\mathbf{E}(t) \cdot \mathbf{r}}{r^3}. \quad (2.9)$$

This term describes the dipole that is induced due to the asymmetry in the charge distribution of the residual ion in the laser field and is characterized by the polarizability  $\alpha_I$ .

## 2.2 Approximations

In the following, the most common, if often tacit, assumptions of theoretical strong field physics [99] are presented, which are also applied throughout this thesis with only a few exceptions that will be noted explicitly when relevant.

### 1. Dipole Approximation:

The underlying assumptions of the dipole approximation are that the length scales of the atom and the electron excursion are small compared to the wavelength of the laser and that the velocity of the electron is considerably smaller than the speed of light [100, 101]. As a consequence, the vector potential can be approximated to be spatially homogeneous and it is merely left with a time-dependence,  $\mathbf{A}(t)$ , which was already applied in the definitions presented in the previous section. The lack of spatial dependence also implies that the magnetic field component of the laser field vanishes due to the relation  $\mathbf{B} = \nabla \times \mathbf{A}(t) = 0$  [101]. The dipole approximation will break down in chapter 5 when we will be dealing with inhomogeneous electric fields close to a nanostructure.

### 2. Depletion is neglected:

If the laser field is particularly strong or the pulse exceptionally long, ionization may become saturated with no atoms left to be ionized [102]. As the laser parameters used in this thesis should not lead to such depletion, this effect is completely neglected.

### 3. Electron does not leave the laser focus:

Even though this point can be considered a special case of the dipole approximation, for historical reasons it is mentioned separately here. In the early days of strong field ionization physics, pulse durations exceeded some hundreds of femtoseconds and as a consequence the electron could leave the laser focus and effects due to the gradient force at the focus margins had to be taken into account [99], as illustrated above by the example of ATI in section 2.1.1. However, nowadays pulses typically are much shorter and this effect can be neglected [103].



## 4. Non-relativistic approximation:

The onset of relativistic effects is expected to be observed when  $2U_p$  gets into the regime of the rest energy of the electron,  $2U_p/c^2 \simeq 1$ , and is actually one way to violate the dipole approximation [95, 101]. However, even for the smallest wavelength used in this thesis, which is 400 nm, one would have to exceed an intensity of  $I = 10^{19}$  W/cm<sup>2</sup> to get into this relativistic regime. As the largest intensities used in this thesis will be in the order of  $I = 10^{15}$  W/cm<sup>2</sup>, we can safely neglect relativistic effects.

## 5. Clamped-nuclei approximation:

The nucleus in atoms is assumed to be fixed, positioned at the origin of the coordinate system, since its mass is more than a thousand times larger than that of the electron. Analogously, also the nuclei in molecules are approximated to stay fixed at equilibrium internuclear distance during and after ionization.

In some special cases, which will be marked as such, the Coulomb potential will be neglected to attain analytical estimates, making use of the relations presented in section 2.1.4 that contain the velocity and vector potential.

## 2.3 Classical and Quantum Trajectory Monte Carlo (CTMC/QTMC) simulations

### 2.3.1 The trajectory picture

Considering that the release of the electron via strong field ionization is a process that flies in the face of classical mechanics, as we have seen at the beginning of this chapter, one may expect semiclassical models to be of little help. There are a large number and diversity of features that can be captured in a classical or semiclassical picture [43, 45–55], though, and in one way or another many of these theories draw on a concept that is commonly referred to as the three-step model [39]. Actually, as far as this thesis is concerned, we only need the first two steps of this model, namely ionization and propagation. An important feature of many semiclassical models is that the propagation step is performed in a classical framework. Even though one should have to deal with the dynamics of a complicated wavefunction in the propagation step, *‘the central object in time-dependent quantum mechanics – the wavepacket – behaves very much like a classical trajectory. Its center, both in position and momentum, is often well described by a guiding classical trajectory, while its spatial width is simply a manifestation of the Heisenberg uncertainty principle. In other words, the correspondence principle between classical and quantum mechanics is fully operative in time-dependent quantum mechanics, often even at low energies, in contrast with the correspondence principle in time-independent quantum mechanics which is valid only at high quantum numbers’* (David Tannor in his book on time-dependent quantum mechanics [104]). This quantum-classical correspondence, often expressed in Ehrenfest’s theorem [105], can be applied in typical strong field systems to approximate the electron’s motion in the continuum as long as the electron does not return too close to the parent ion and recombination becomes relevant [106–108].

The following two sections are devoted to introducing the classical and quantum trajectory methods employed in the framework of this thesis and basically follow the

above-mentioned concept of separation into an ionization and propagation step: The ionization step is described by a statistical ensemble of trajectories mimicking the quantum mechanical ionization rates (section 2.3.2), and the propagation step is implemented as a classical propagation of these trajectories solving Newton's equation of motion where quantum features can be added by dragging a phase along (section 2.3.3). Note that in this thesis the term 'semiclassical' will be used in reference to both the classical trajectory Monte Carlo (CTMC) and quantum trajectory Monte Carlo (QTMC) method as in both cases the initial conditions are to mimic the quantum mechanical nature of the ionization process. Other authors, however, prefer to reserve the term 'semiclassical' for methods that include a quantum-mechanically motivated phase during propagation, such as is the case in QTMC, and refer to methods that don't exhibit this feature, such as CTMC, as 'classical'.

## 2.3.2 The initial conditions

The term 'Monte Carlo' in the classical and quantum trajectory Monte Carlo methods stems from the statistical nature of the first step in these simulations: In the ionization step, an ensemble of trajectories is used to sample the probability distribution of ionization times and initial momenta, which then also determine the initial spatial coordinates. This part of setting the initial conditions is crucial and, as the subsequent propagation step is deterministic, defines the quality of the final momentum distribution. Here, we summarize the derivation of the most frequently used probability distribution, often referred to as ADK (short for Ammosov, Delone, and Krainov, the authors of [1]) or KFR (short for Keldysh [89], Faisal [109], and Reiss [110]), in the quasistatic limit, basically following Ref. [33]. At the end of this section also the tunnel exit, the initial condition in space, and the implementation of the sampling will be discussed.

### 2.3.2.1 The adiabatic ionization rate

As expounded in sections 2.1.1 and 2.1.2, the ionization step in the typical strong field regime cannot be captured in a classical theory but requires a (non-relativistic) quantum mechanical description. Therefore one obviously starts with the Schrödinger equation

$$i \frac{\partial}{\partial t} |\Psi(t)\rangle = \hat{H}(t) |\Psi(t)\rangle = \left( \underbrace{\frac{1}{2} \hat{\mathbf{p}}^2 + V(\mathbf{r})}_{\hat{H}_0} + \underbrace{\mathbf{r} \cdot \mathbf{E}(t)}_{\hat{V}_L} \right) |\Psi(t)\rangle, \quad (2.10)$$

where  $V(\mathbf{r})$  denotes the Coulomb potential,  $\hat{H}_0$  the field-free Hamiltonian and the term  $\hat{V}_L$  describes the interaction with the laser in the length gauge. Even though the choice of the gauge is not of physical relevance at this point, it will be so later on when the gauge invariance is broken due to approximations [111, 112]. Even though

$$|\Psi(t)\rangle = -i \int_0^t dt' \left( e^{-i \int_{t'}^t \hat{H}(t'') dt''} \right) \hat{V}_L(t') \left( e^{-i \int_0^{t'} \hat{H}_0(t'') dt''} \right) |\Psi_i\rangle + e^{-i \int_0^t \hat{H}_0(t'') dt''} |\Psi_i\rangle, \quad (2.11)$$

with the initial state  $|\Psi(t=0)\rangle = |\Psi_i\rangle$ , is an exact solution of eq. (2.10), evaluating the operators in the exponential function is not analytically tractable [33]. However, we can assign physical meaning to the individual terms which will set the stage for introducing some powerful approximations. From time 0 to  $t'$  the electron is bound in the atomic or molecular potential and is only affected by the field-free operator  $\hat{H}_0$ . Then,

at  $t'$  the laser field  $\hat{V}_L$  induces the electron to transition to the continuum, where the evolution then continues from time  $t'$  to the time  $t$  the system is evaluated at. Now, the key approximation of the strong field approximation (SFA) is made by neglecting the Coulomb potential after the electron's transition to the continuum. This entails that the continuum operator is the Volkov operator  $\hat{H}_e = \frac{1}{2}\hat{\mathbf{p}}^2 + \mathbf{r} \cdot \mathbf{E}(t)$ , which can be expressed analytically using the instantaneous energy  $e(t'') = (\mathbf{v}(t) - \mathbf{A}(t) + \mathbf{A}(t''))^2/2$ , thus obtaining

$$e^{-i \int_{t'}^t \hat{H}_e(t'') dt''} |\mathbf{v}'\rangle = e^{-i \int_{t'}^t e(t'') dt''} |\mathbf{v}\rangle \Leftrightarrow \langle \mathbf{v} | e^{-i \int_{t'}^t \hat{H}_e(t'') dt''} = e^{-i \int_{t'}^t e(t'') dt''} \langle \mathbf{v}' | \quad (2.12)$$

for the continuum states  $|\mathbf{v}\rangle$  and  $|\mathbf{v}'\rangle$ , which are plane waves of velocities  $\mathbf{v} = \mathbf{v}(t)$  and  $\mathbf{v}' = \mathbf{v}(t')$ . Using this result and  $\mathbf{v}' = \mathbf{v} - \mathbf{A}(t) + \mathbf{A}(t')$ , the transition amplitude to a Volkov state of velocity  $\mathbf{v}$  is given by

$$\langle \mathbf{v} | \Psi \rangle = \Psi(\mathbf{v}, t) = -i \int_0^t dt' e^{-i \frac{1}{2} \int_{t'}^t dt'' (\mathbf{v} - \mathbf{A}(t) + \mathbf{A}(t''))^2} \langle \mathbf{v} - \mathbf{A}(t) + \mathbf{A}(t') | \hat{V}_L(t') | \Psi_i \rangle e^{i I_p t'}. \quad (2.13)$$

The last term of eq. (2.11) does not appear here since we assume that there is no initial population in the continuum [33]. Moreover, we can see that the term  $\langle \mathbf{v} - \mathbf{A}(t) + \mathbf{A}(t') | \hat{V}_L(t') | \Psi_i \rangle$  only contributes as a non-exponential prefactor. For the sake of analytical tractability we content ourselves with exponential accuracy and therefore work with

$$\Psi(\mathbf{v}, t) \propto \int_0^t dt' e^{-i S(\mathbf{v}, t, t')}, \quad (2.14)$$

where

$$S(\mathbf{v}, t, t') = \int_{t'}^t dt'' \left( \frac{1}{2} (\mathbf{v}(t) - \mathbf{A}(t) + \mathbf{A}(t''))^2 \right) - I_p t'. \quad (2.15)$$

As the exponent in the integral of eq. (2.14) is highly oscillatory, cancellation effects appear when evaluating this integral and the saddle point approximation can be used to find those parts that contribute significantly to this integral. The saddle point  $t_s$  with respect to  $t'$  is found by solving the following equation:

$$\left. \frac{\partial S(\mathbf{v}, t, t')}{\partial t'} \right|_{t_s} = -\frac{1}{2} (\mathbf{v}(t) - \mathbf{A}(t) + \mathbf{A}(t_s))^2 - I_p = 0 \quad (2.16)$$

and  $\Psi(\mathbf{v}, t)$  is then calculated as  $e^{-i S(\mathbf{v}, t, t_s)}$ . In the following, eq. (2.16) is solved for a continuous wave that is linearly polarized in x-direction,  $E(t) = E_x(t) = E_0 \cos(\omega t)$ , with a vector potential  $A(t) = -E_0/\omega \sin(\omega t)$ :

$$\frac{1}{2} \left( v_x(t) + \frac{E_0}{\omega} \sin(\omega t) - \frac{E_0}{\omega} \sin(\omega t_s) \right)^2 + \frac{1}{2} (v_{\perp}^2(t) + 2I_p) = 0, \quad (2.17)$$

where  $v_{\perp} = \sqrt{v_y^2 + v_z^2}$ . Since the saddle point is complex, we write  $t_s = t_0 + i t_i$  and as we are interested in the time when the electron appears in the continuum, which we assume to coincide with the time becoming real-valued, we set  $t = t_0$ . Note that this assumption also forces the ionization process to be instantaneous (in real time), which is a controversial feature of the ionization process that has led to heated debates of what some call the 'tunneling time' [91, 92, 113–118]. Moreover, a common approximation in this step is to set  $\mathbf{v} = 0$ . Even though this is motivated by that velocity having the

largest transition amplitude, one has to be careful in particular about setting the velocity component along the polarization axis to zero, as - contrary to the belief of many [7, 33, 119] - any assumption about  $v_x$  is strongly intertwined with the ionization time spread one obtains. This insight is at the heart of the discussion of nonadiabatic effects in chapter 3 and will be explained in more detail there. For now, though, we are interested in slowly varying fields, in the adiabatic limit, where the mentioned effect is small and  $\mathbf{v} = 0$  is set also here. Thus being interested in the most probable trajectory, one then also sets  $t_0 = 0$ , meaning ionization is assumed to happen at the peak of the field where the field is strongest and the barrier is most suppressed. Applying various trigonometric relations, one can separate eq. (2.17) into a real and an imaginary part. The imaginary part can be solved by setting either  $t_i = 0$  or  $t_0 = 0$ , where the latter is chosen due to its physical meaningfulness, as has just been discussed. From the real part of the equation we then obtain

$$\sinh(\omega t_i) = \frac{\omega}{E_0} \sqrt{2I_p} = \gamma. \quad (2.18)$$

In the adiabatic limit, for small  $\omega$ , one can approximate this to be  $\omega t_i = \gamma$  [33] and  $t_i = \gamma/\omega = \sqrt{2I_p}/E_0$  coincides with the Keldysh tunneling time [91]. One possible interpretation of this is that for the electron to appear in the continuum with  $v_x = 0$  at  $t = 0$ , it has to start tunneling at  $t_s = i t_i = \sqrt{2I_p}/E_0$ . Using  $v_x(i t_i) = v_x(t_s) = v_x(t) - A_x(t) + A_x(t_s)$  in the saddle point equation (eq. (2.16)), one obtains

$$\frac{1}{2}(v_x(i t_i))^2 = -I_p \Rightarrow v_x(i t_i) = i\sqrt{2I_p}. \quad (2.19)$$

This imaginary momentum is decelerated to 0 at  $t = 0$  ( $v_x(0) = 0$ ) [91]. Assuming a constant deceleration  $a$  this leads to  $v_x(0) - v_x(i t_i) = -i\sqrt{2I_p} \approx -a t_s = -a \cdot i t_i$ . Using  $t_i = \sqrt{2I_p}/E_0$ ,  $a = E_0$  solves this equation and thus  $E_0$  can be interpreted as the driving force of the deceleration. Thus, we have  $v_x(t'') = E_0 t''$  and using  $v_x(t'') = v_x(t) - A_x(t) + A_x(t'')$  in the action integral of eq. (2.15) results in

$$\begin{aligned} S(\mathbf{v} = 0, t = 0, t' = t_s = i t_i) &= \int_{i t_i}^0 \left( \frac{1}{2} (E_0 t'')^2 \right) dt'' - i I_p t_i = -\frac{1}{2} E_0^2 \frac{1}{3} (i t_i)^3 - i I_p t_i \\ &= i \frac{1}{2} E_0^2 \frac{1}{3} \left( \sqrt{2I_p}/E_0 \right)^3 - i I_p \sqrt{2I_p}/E_0 = -\frac{i}{3} \frac{(2I_p)^{3/2}}{E_0}. \end{aligned} \quad (2.20)$$

Consequently, the probability of ionization at the peak of the laser field with velocity  $\mathbf{v} = 0$  is

$$P \propto |\Psi(\mathbf{v} = 0, t = 0)|^2 = \left| e^{-iS(\mathbf{v}=0, t=0, t'=t_s)} \right|^2 = \exp\left(-\frac{2(2I_p)^{3/2}}{3E_0}\right). \quad (2.21)$$

Strictly speaking, this equation does not include any time-dependence. After all, we not only assumed a slowly varying, quasistatic field but also set  $t_0 = 0$ . However, what is commonly done to sneak in a time-dependence is to assume that the field changes so slowly that the system adapts adiabatically to the new field strength and that therefore one can replace  $E_0$  by the absolute value of the instantaneous field,  $|E(t)|$ , in order to approximate the time-dependence of the ionization rate in the adiabatic limit  $\gamma \ll 1$ .

In a similar fashion, one can also obtain a transverse velocity distribution - despite the fact that  $v_\perp$  was set to zero above. The way this is done is motivated by eq. (2.17),

where the term  $I_p + v_\perp^2/2$  is found. Replacing  $I_p$  in eq. (2.21) by that term results in a velocity distribution

$$P \propto \exp\left(-\frac{2(2I_p + v_\perp^2)^{3/2}}{3E_0}\right). \quad (2.22)$$

This can be interpreted as  $v_\perp \neq 0$  decreasing the ionization probability due to an increase of the ionization potential to  $I_p + v_\perp^2/2$ . Being bound more deeply, the electron has to penetrate a broader tunneling barrier and tunneling is less likely. As the velocities  $v_\perp$  that contribute significantly to the ionization are therefore relatively small, a common simplification is

$$(2I_p + v_\perp^2)^{3/2} = (2I_p)^{3/2} \left(1 + \frac{v_\perp^2}{2I_p}\right)^{3/2} \approx (2I_p)^{3/2} \left(1 + \frac{3}{2} \frac{v_\perp^2}{2I_p}\right), \quad (2.23)$$

where in the last step the assumption  $v_\perp^2/(2I_p) \ll 1$  was used. The velocity dependence can therefore be written as a Gaussian function that is multiplied to eq. (2.21)

$$P \propto \exp\left(-\frac{2(2I_p)^{3/2}}{3E_0}\right) \cdot \exp\left(-\frac{\sqrt{2I_p}}{E_0} v_\perp^2\right). \quad (2.24)$$

### 2.3.2.2 The tunnel exit

Ionization rates, as the ones that were derived in the preceding section, can be used as probability distributions for the initial times and momenta. To actually launch those trajectories we also need to know *where* to start them, though. For one particular trajectory in the ensemble, the tunnel exit is determined by the fixed ionization time and initial momentum. However, despite being deterministic in the mentioned sense, there is a variety of theories that give different prescriptions for how to calculate the initial spatial coordinate for a trajectory with given ionization time and initial momentum. In the following, a brief overview of the most common of these tunnel exit theories is given.

- The triangular barrier:  
By far the most simple ansatz to calculate the tunnel exit is to assume that the barrier formed by the superposed laser and Coulomb field can be approximated by a triangle, as illustrated by the red lines in the left panel of Fig. 2.2. This corresponds to only taking account of the laser field, in terms of the shape of the potential, and reducing the effect of the Coulomb potential to putting the electron at the correct binding energy  $-I_p$ . More formally, this concept is described by a constant electric field and a short-range potential [33]. The width of this barrier is  $I_p/E(t_0)$ , with  $E(t_0)$  the electric field at the time the electron is born in the continuum and, taking into account the direction into which the potential is bent, the tunnel coordinate is given by  $x = -I_p/E(t_0)$ . Note that the concept of the triangular barrier is the same as the one underlying the Keldysh tunneling time and, as there the assumption is a static field, this description works best in the adiabatic limit.
- The TIPIS-exit:  
TIPIS is an acronym for ‘tunnel ionization in parabolic coordinates with induced

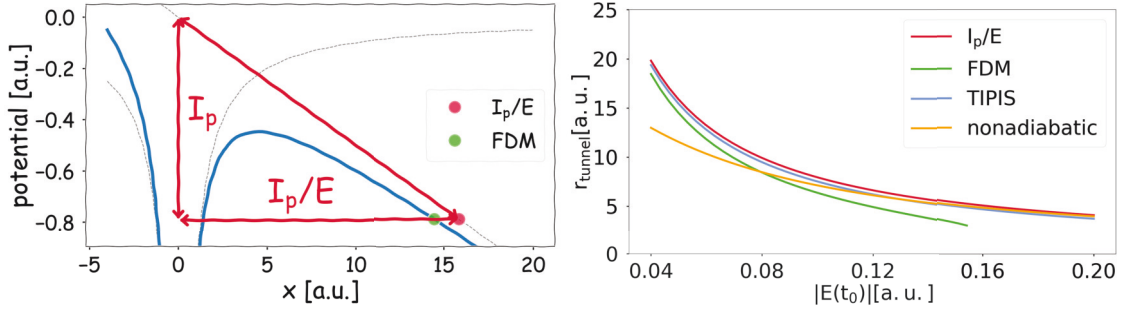


**Figure 2.2:** Left panel: Pictorial description of the tunnel exit in the triangular barrier and in the field-direction model (FDM). Right panel: Comparison of the different tunnel exit theories. A similar figure is found in [120], where also further details concerning the various tunnel exit theories are discussed. In both panels neon is ionized ( $I_p = 21.56$  eV,  $\alpha_N = 2.67$ ,  $\alpha_I = 1.33$ ). The field strength in the left panel is  $E_0 = 0.05$  and the wavelength in the right panel is  $\lambda = 800$  nm. The field strength at which the FDM curve ends corresponds to the apex of the barrier coinciding with the energy of the ionization potential so that beyond this field strength the FDM obviously does not give physically meaningful results.

dipole and Stark shift' [6]. As the name suggests, the dipole and Stark shift are included in the description of the potential and parabolic coordinates are used to separate the Schrödinger equation of the superposed laser and Coulombic field [121], using the approximation that the electron does not tunnel out too close to the ion ( $r_{\text{tunnel}} > 5$  a.u.). This reduces the problem to one dimension and allows for an analytical description of the tunnel exit, which is usually given in the following approximate form [122]:

$$r_{\text{tunnel}} = \frac{I_p(t_0) + \sqrt{I_p^2(t_0) + 4\beta_2 E(t_0)}}{2E(t_0)} \quad \text{with } \beta_2 = 1 - \frac{\sqrt{2I_p(t_0)}}{2} \quad (2.25)$$

with the Stark shifted ionization potential  $I_p(t_0) = I_{p,0} + \frac{1}{2}(\alpha_N - \alpha_I)E^2(t_0)$ , where  $\alpha_N$  and  $\alpha_I$  denote the polarizability of the atom and ion, respectively, and  $I_{p,0}$  is the ionization potential in the absence of any shifts [98, 122]. Note that the underlying assumption is still a quasistatic field and TIPIS should therefore be most valid in the adiabatic regime. Also, as eq. (2.25) only provides the tunnel radius, one has to calculate the coordinates from it by taking the instantaneous field direction into account.

- Nonadiabatic tunnel exits:

Even though different nonadiabatic theories arrive at different results concerning the ionization time spread and the initial longitudinal momentum (see chapter 3 for details), they usually agree on the tunnel exit

$$r_{\text{tunnel}} = \left| \frac{E_0}{\omega^2} \cos(\omega t_0) \left( 1 - \sqrt{1 + \frac{\omega^2(2I_p + v_{\perp}^2)}{E^2(t_0)}} \right) \right|. \quad (2.26)$$

Note that here linear polarization and a field of  $E_0 \cos(\omega t)$  were assumed. As this rendering of the equation following the notation in [3] may appear unusual to those familiar with what is usually referred to as the PPT (short for Perelomov,



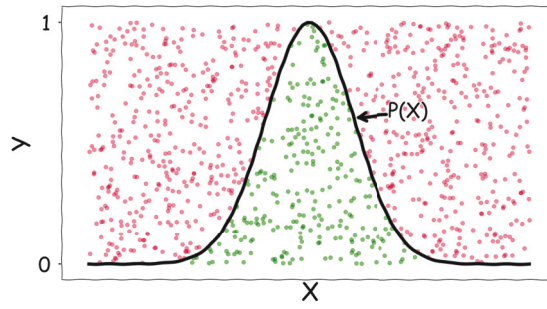


**Figure 2.3:** Illustration of the concept behind a reject-sampling algorithm for sampling initial conditions: Events are sampled uniformly in the  $X$ - $Y$ -space. All events with  $Y_i > P(X_i)$  (red dots) are rejected, all events with  $Y_i \leq P(X_i)$  (green dots) are accepted.

Popov and Terent'ev, the authors of [4, 5]) tunnel exit, the equivalence of these tunnel exits is shown in Appendix A.1.

- Some lesser-known tunnel exit equations:

In order to demonstrate that the above list is not exhaustive, the mention of two additional ways to calculate the tunnel radius seems appropriate. The first is the field-direction model [48], in which the equation  $-1/x - |E(t_0)|x = -I_p$  is solved, yielding

$$r_{\text{tunnel}} = \frac{I_p + \sqrt{-4|E(t_0)| + I_p^2}}{2|E(t_0)|}. \quad (2.27)$$

Per definition and as can be seen in the left panel of Fig. 2.2, this tunnel coordinate is found directly on the superposed laser and Coulomb potential, at the intersection with the horizontal line through the ionization potential,  $-I_p$ . A related approach can be taken for molecular potentials, where the situation gets far more complicated due to the mutual distortion of the Coulomb potentials at different atomic sites. Using the point where the  $I_p$ -line intersects the superposed laser and Coulombic potential as the tunnel exit, similar to the way it is done in the field direction model from above, can sometimes help take into account the special geometry of the molecular potential better [123].

A visual comparison of the different tunnel radii according to the above-mentioned theories is shown in Fig. 2.2. One can see how the nonadiabatic theory differs from the three other, adiabatic approaches at small field strengths (corresponding to a larger  $\gamma$ ) and converges to the triangular exit in the adiabatic limit of strong fields.

Even though the discrepancies seem minor, one has to bear in mind that directly at the tunnel exit the Coulomb potential is largest. Therefore, many strong field ionization features are highly sensitive to the choice of the tunnel exit [115, 120, 124, 125].

### 2.3.2.3 Implementation of the sampling process

The creation of initial conditions is done in two steps: First, the ionization time  $t_0$  and the initial momentum  $\mathbf{v}_0$ , which in the following are summarized in the variable  $\mathbf{X} = [t_0, v_{0,x}, v_{0,y}, v_{0,z}]$ , are sampled according to a chosen probability distribution  $P(\mathbf{X})$ , e.g. the adiabatic rate given in eq. (2.22). Then, in the second step, the tunnel exit is

calculated individually for each trajectory in the resulting ensemble  $\{\mathbf{X}_1, \mathbf{X}_2, \dots, \mathbf{X}_{\mathcal{N}}\}$ , i.e. for all  $\mathbf{X}_i$  with  $i \in \{1, \dots, \mathcal{N}\}$ .

In principle, there are two ways to deal with the fact that the trajectories are weighted according to the probability distribution  $P(\mathbf{X})$ : One can sample trajectories such that in each dimension of  $\mathbf{X}$  the values are sampled according to a uniform distribution and the corresponding weights  $P(\mathbf{X})$  are stored during the propagation process until the trajectories are evaluated at the detector, with their weights taken into account only then. Alternatively, one can create the initial conditions such that the ensemble of trajectories exhibits a distribution of initial conditions that fulfills  $P(\mathbf{X})$ .

The way of uniform sampling turns out to be problematic because the probability distribution we are dealing with usually peaks rather sharply around the field maxima due to the exponential dependence on the field strength. Therefore, most trajectories of the uniform distribution carry a small weight. As the computational cost of propagating such a trajectory with negligible weight is about the same as for any other trajectory, this approach is computationally expensive and becomes a real problem when we include the phase using the QTMC method and need more trajectories to resolve the interference pattern.

Conversely, sampling the trajectories such that the distribution of their initial conditions already follows  $P(\mathbf{X})$ , where then each trajectory has equal weight *after* the sampling, is computationally less demanding since then only a few trajectories whose initial conditions correspond to a negligibly small  $P(\mathbf{X})$  have to be propagated [60].

As built-in pseudo-random number generators of most programming languages only provide uniform or Gaussian distributions, some extra work has to be done to sample initial conditions according to  $P(\mathbf{X})$  in this second way, though. Here, two options to solve this problem are shown, where the first one was used only for the adiabatic results presented in chapter 4.2 and the second version was used in the remaining parts of this thesis:

1. Sampling with Gaussian functions and correcting the weight:

As can be seen from eq. (2.24), the momenta perpendicular to the instantaneous polarization approximately follow a Gaussian distribution in the adiabatic limit. Even though it is less obvious, also the time spread can be approximated by a Gaussian function. To see this feature analytically, one has to replace  $E_0$  by  $E_0 \cos(\omega t_0) := E_0 \cos(\phi)$  in the first exponential term of eq. (2.24) and expand the exponent into a Taylor series in  $\phi$  around 0 up to second order [71, 90]:

$$\begin{aligned} \frac{1}{E(\phi)} &= \frac{1}{E_0 \cdot \cos(\phi)} \approx \frac{1}{E_0} \left( 1 + \frac{1}{2} \phi^2 + \mathcal{O}(\phi^4) \right) \\ \Rightarrow P(\phi) &\approx \exp\left(-\frac{\phi^2}{2\sigma_\phi^2}\right) \quad \text{with } \sigma_\phi = \frac{\sqrt{3 \cdot E_0}}{2^{5/4} \cdot I_p^{3/4}}. \end{aligned} \tag{2.28}$$

Since implementations of Gaussian distributed random numbers are readily available, sampling this distribution can be realized in almost as simple a way as sampling a uniform distribution. This distribution can then either be used as an approximation, e.g. for quick calculations that aim at merely estimating effects, or the weight of each trajectory can be corrected in the final evaluation of the trajectories ‘at the detector’ according to the full eq. (2.22) or any other probability distribution [106].



## 2. Reject-sampling algorithm:

Another way to sample non-Gaussian probability distributions is a reject-sampling algorithm. To that end, the maximum of the probability distribution  $P(\mathbf{X})$  is normalized to 1 and  $\mathcal{N}$  uniformly distributed random numbers  $Y_i$  ( $i = \{1, \dots, \mathcal{N}\}$ ) are generated in the interval  $[0, 1]$ . Also, in each dimension of  $\mathbf{X}$ ,  $\mathcal{N}$  uniformly distributed random numbers are generated. Then, for each of the  $\mathcal{N}$  resulting tuples the condition

$$Y_i < P(\mathbf{X}_i) \quad (i = 1, \dots, \mathcal{N}) \quad (2.29)$$

is evaluated and if found ‘true’, the set of initial conditions  $\mathbf{X}_i$  is accepted as a trajectory, otherwise it is rejected and discarded. The concept of this reject-sampling process is illustrated in Fig. 2.3 for a hypothetical one-dimensional distribution. In the limit of large  $\mathcal{N}$ , the ensemble of trajectories that were accepted in that process will have initial conditions  $\mathbf{X}$  distributed according to  $P(\mathbf{X})$ . In practice, about  $10^5$ - $10^6$  trajectories suffice to converge a CTMC calculation and about  $10^8$  trajectories are required in QTMC simulations. Even though the above-mentioned problem of the ionization time distribution peaking sharply around the field extrema also affects the efficiency of the reject-sampling mechanism adversely as it results in most trajectories being rejected, the numerical advantage over sampling uniformly and doing book-counting of the weights after propagation lies in the fact that only the evaluation of eq. (2.29) and not a full numerical propagation has to be done on those ‘non-contributing’ trajectories.

## 2.3.3 Propagation

### 2.3.3.1 Propagation in CTMC simulations

After the trajectories are sampled, they are propagated solving Newton’s equation of motion in the superposed laser and atomic field,

$$\ddot{\mathbf{r}} = -\mathbf{E}(t) - \nabla(V(\mathbf{r}) + V_D(\mathbf{r})) = -\mathbf{E}(t) - \nabla\left(\frac{-1}{\sqrt{r^2(t) + SC}} - \alpha_I \frac{\mathbf{E}(t) \cdot \mathbf{r}(t)}{r^3(t)}\right), \quad (2.30)$$

where the last term in the gradient describes the induced dipole of the residual ion in the laser field, which is characterized by the polarizability  $\alpha_I$  [58, 124]. The softcore parameter  $SC$  is chosen to be 0.1 and its purpose lies in softening the Coulomb singularity so as to avoid numerical complications. Note that here, in contrast to the situation when solving the TDSE numerically [126, 127], the choice of the softcore parameter has nothing to do with the ionization potential. Moreover, it is found that variation of the softcore parameter does not significantly influence the CTMC result [106]. Therefore, the choice of the exact value of  $SC$  is not relevant here.

The time integration of eq. (2.30) is done numerically using matlab’s *ode45* function [128, 129]. This adaptive time-step explicit Runge-Kutta scheme is of fourth order in calculation and of 5th order in error estimate. Each electron is propagated being oblivious of the existence of the other trajectories. This single-active electron approach makes the propagation processes of the individual trajectories independent of each other, thus allowing for parallelized computation [60].

The numerical propagation is done till the end of the pulse. As the electron is exposed to the long-range Coulomb potential even after the pulse is over, the propagation needs to continue, though. However, with the Coulomb potential exerting the

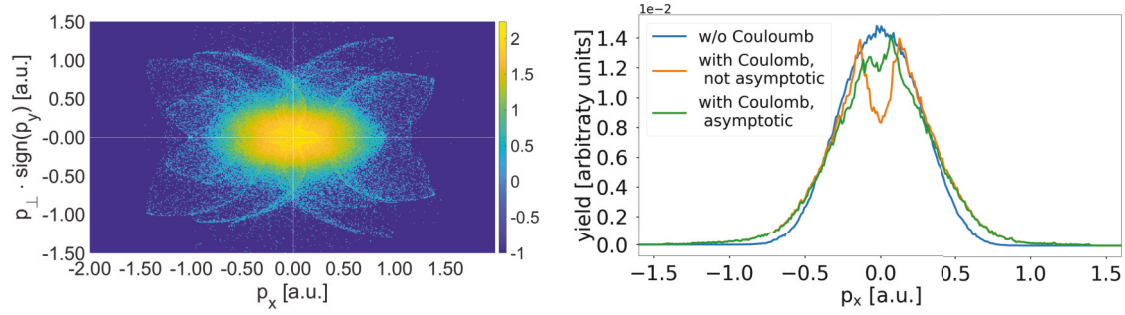


**Figure 2.4:** Results of CTMC simulations with helium ionized by an 8-cycle laser pulse with a central wavelength of  $\lambda = 800$  nm and an intensity of  $I = 2 \cdot 10^{14}$  W/cm<sup>2</sup>. Left panel: 2D momentum distribution with Rydberg states filtered out and asymptotic propagation performed as described in the text. The yield is given in arbitrary units on a logarithmic scale in the colorbar. Right panel: Longitudinal momentum distribution for various ways of propagating the electrons. In the case where no Coulomb potential was included, no Rydberg states were filtered out and no asymptotic propagation was performed as these steps are only physically meaningful with a Coulomb potential included in the calculation.

only remaining force this can be done analytically. The classical mechanics of the hyperbolic motion uniquely determines the asymptotic momentum to be

$$\mathbf{p}_a = p_a \frac{p_a(\mathbf{L} \times \mathbf{a}) - \mathbf{a}}{1 + p_a^2 L^2} \quad (2.31)$$

with  $\mathbf{L} = \mathbf{r} \times \mathbf{p}$  and  $\mathbf{a} = \mathbf{p} \times \mathbf{L} - \mathbf{r}/r$  the conserved angular momentum and Runge-Lenz vector, respectively [124]. The momentum  $\mathbf{p}$  and position  $\mathbf{r}$  at the end of the pulse determine the absolute value,  $p_a$ , of the asymptotic momentum

$$\frac{p_a^2}{2} = \frac{p^2}{2} - \frac{1}{r}. \quad (2.32)$$

Obviously, these equations for the asymptotic propagation only lead to physically meaningful results if the right-hand side of eq. (2.32) is positive, corresponding to a total energy that is positive at the end of the pulse. The fate of electrons with a negative total energy, in contrast, is not to end up at the detector but to stay bound. More details on these Rydberg states can be found in chapter 4. For now, suffice it to say that Rydberg electrons need to be filtered out when one is interested in the momentum distribution at the detector. As Rydberg electrons are naturally related to small momenta  $p$  at the end of the pulse, this filtering leaves a characteristic dip in the momentum distribution close to zero when looked at directly after the pulse has passed [49]. The Coulomb potential that is taken account of in the asymptotic propagation leads to a partial ‘mending’ of this ‘hole’, as can be seen by the exemplary calculation show in Fig. 2.4.

All of the above procedures for the ionization and propagation of trajectories is valid for atoms. The description of molecular processes requires modifications of the presented concepts and equations, which will be dealt with in chapter 6.

### 2.3.3.2 Propagation in QTMC simulations

So far, the propagation step was completely classical and only the sampling step included quantum mechanical information encoded in the ionization rates that are used

as probability distributions of the initial conditions. However, using the concept of Feynman's quantum paths one can assign a phase to each trajectory that then changes during propagation [62]. Taking this phase into account when evaluating the trajectories at the detector has shown to reproduce quantum mechanical interference features [60, 62, 63, 65, 130–135].

The way the phase is introduced is based on the Feynman path integral formalism under the assumption of the classical action being asymptotically large compared to the quantum action  $\hbar$ , which allows to evaluate the corresponding integrals in the saddle point approximation [60]. In that classical limit, the probability transition amplitude between two points in space-time,  $(\mathbf{r}_0, \mathbf{t}_0)$  and  $(\mathbf{r}_f, \mathbf{t}_f)$ , corresponding to the tunnel exit and the detector, respectively, can be written as [62]

$$\langle \mathbf{r}_f | U_{sc} | \mathbf{r}_0 \rangle = C e^{iS_{cl}(\mathbf{r}_0, \mathbf{r}_f)}, \quad (2.33)$$

where  $U_{sc}$  is the semiclassical propagator and  $C$  denotes a prefactor that is of secondary importance since our primary interest is in the phase [60]. This phase is determined by the classical action

$$S_{cl}(\mathbf{r}_0, \mathbf{r}_f) = \int_{t_0}^{t_f} L dt = \int_{t_0}^{t_f} (\mathbf{p}\dot{\mathbf{r}} - H(\mathbf{r}, \mathbf{p})) dt \quad (2.34)$$

with  $L$  denoting the Lagrangian and  $H$  being the classical Hamiltonian which, in length gauge, reads

$$H(\mathbf{r}, \mathbf{p}) = \frac{\mathbf{p}^2}{2} + \mathbf{E}(\mathbf{r}) \cdot \mathbf{r} - \frac{Z}{r}. \quad (2.35)$$

At the detector, we are interested in the final momentum rather than in the final position<sup>1</sup> and, therefore, we need  $\langle \mathbf{p}_f | U_{sc} | \mathbf{r}_0 \rangle$  rather than  $\langle \mathbf{r}_f | U_{sc} | \mathbf{r}_0 \rangle$ . Inserting a unity operator,  $\langle \mathbf{p}_f | U_{sc} | \mathbf{r}_0 \rangle = \int d\mathbf{r}_f \langle \mathbf{p}_f | \mathbf{r}_f \rangle \langle \mathbf{r}_f | U_{sc} | \mathbf{r}_0 \rangle$ , and using the momentum space representation of the position eigenstate<sup>2</sup>,  $\langle \mathbf{p} | \mathbf{r} \rangle \propto e^{-i\mathbf{p}\mathbf{r}}$ , we obtain

$$\langle \mathbf{p}_f | U_{sc} | \mathbf{r}_0 \rangle \propto e^{iS_{cl}(\mathbf{r}_0, \mathbf{r}_f)} e^{-i\mathbf{p}_f \mathbf{r}_f}. \quad (2.36)$$

Equivalently, the new phase reads

$$\begin{aligned} \phi' &= S_{cl}(\mathbf{r}_0, \mathbf{r}_f) - \mathbf{p}_f \mathbf{r}_f = \int_{t_0}^{t_f} (\mathbf{p}\dot{\mathbf{r}} - H(\mathbf{r}, \mathbf{p})) dt - \mathbf{p}_f \mathbf{r}_f \\ &= \int_{t_0}^{t_f} (-\dot{\mathbf{p}}\mathbf{r} - H(\mathbf{r}, \mathbf{p})) dt + \mathbf{p}\mathbf{r} \Big|_{t_0}^{t_f} - \mathbf{p}_f \mathbf{r}_f \\ &= \int_{t_0}^{t_f} (-\dot{\mathbf{p}}\mathbf{r} - H(\mathbf{r}, \mathbf{p})) dt - \mathbf{p}_0 \mathbf{r}_0, \end{aligned} \quad (2.37)$$

where in the last but one step integration by parts was employed:

$$\int_{t_0}^{t_f} \mathbf{p}\dot{\mathbf{r}} dt = \mathbf{p}\mathbf{r} \Big|_{t_0}^{t_f} - \int_{t_0}^{t_f} \dot{\mathbf{p}}\mathbf{r} dt. \quad (2.38)$$

<sup>1</sup>More formally, one may argue that a full scattering process is characterized by  $\mathbf{p}_0$  for  $t \rightarrow -\infty$  and  $\mathbf{p}_f$  for  $t \rightarrow \infty$ , which would be described by  $\langle \mathbf{p}_f | U_{sc} | \mathbf{p}_0 \rangle$ . Analogously, the 'half-scattering process' of ionization is described by  $\langle \mathbf{p}_f | U_{sc} | \mathbf{r}_0 \rangle$  [60].

<sup>2</sup>The equation to obtain the eigenstates of the position operator is  $\hat{x}|x\rangle = x|x\rangle$ . The equation for the corresponding eigenfunction in momentum space consequently reads  $i\hbar \frac{\partial}{\partial p} \langle p|x\rangle = x \langle p|x\rangle$ , where  $i\hbar \frac{\partial}{\partial p}$  is the representation of the position operator in momentum space. The solution of this equation is  $\langle p|x\rangle = a \cdot e^{-ipx/\hbar}$  with a constant  $a$ .

Now, one can use

$$\dot{\mathbf{p}}\mathbf{r} = -\mathbf{E}\mathbf{r} - \frac{Z}{r}, \quad (2.39)$$

which equals Newton's equations of motion when derived with respect to the spatial coordinates ( $\dot{\mathbf{p}} = -\mathbf{E} - \nabla Z/r$ ). Adding  $p^2/2 - Z/r$  to both sides of eq. (2.39) and applying eq. (2.35) yields

$$\dot{\mathbf{p}}\mathbf{r} + H(\mathbf{r}, \mathbf{p}) = \frac{\mathbf{p}^2}{2} - \frac{2Z}{r}. \quad (2.40)$$

Using this relation in eq. (2.37) gives

$$\phi' = - \int_{t_0}^{t_f} \left( \frac{\mathbf{p}^2}{2} - \frac{2Z}{r} \right) dt - \mathbf{p}_0 \mathbf{r}_0. \quad (2.41)$$

Including also the initial phase from the time evolution of the ground state,  $\exp(iI_p t_0)$ , we obtain the semiclassical phase [60]

$$\phi = - \int_{t_0}^{t_f} \left( \frac{\mathbf{p}^2}{2} - \frac{2Z}{r} \right) dt - \mathbf{p}_0 \mathbf{r}_0 + I_p t_0, \quad (2.42)$$

which, for a more general potential  $V(\mathbf{r})$ , reads

$$\phi = - \int_{t_0}^{t_f} \left( \frac{\mathbf{p}^2}{2} + V(\mathbf{r}) - \mathbf{r} \cdot \nabla V(\mathbf{r}) \right) dt - \mathbf{p}_0 \mathbf{r}_0 + I_p t_0. \quad (2.43)$$

Each trajectory is assigned such a semiclassical phase. The evaluation at the detector is then performed by binning the space of final momenta and summing up the trajectories coherently in each bin:

$$R_{QTM C}(\mathbf{p}) = \left| \sum_j \sqrt{w_j} \exp(i\phi(t_{0,j}, \mathbf{v}_{0,j})) \right|^2. \quad (2.44)$$

Note that the weight of each bin in CTMC, in contrast, is obtained by an incoherent sum

$$R_{CTMC}(\mathbf{p}) = \sum_j w_j. \quad (2.45)$$

In practice, the fact that  $w_j$  appears under a square root in eq. (2.44) is best accounted for by directly sampling  $\sqrt{w}$  rather than  $w$  [60]. With the trajectories distributed that way the weight of each bin is calculated as

$$R_{QTM C}(\mathbf{p}) = \left| \sum_j \exp(i\phi(t_{0,j}, \mathbf{v}_{0,j})) \right|^2. \quad (2.46)$$

Note, though, that sampling  $\sqrt{w}$  instead of  $w$  is just one option to implement the QTM C method. It seems also worth emphasizing that including the phase as it was derived above does not change the probability distribution  $w$ , but  $w$  is still the same probability distribution as the one used in CTMC simulations, in the most simple case given by the ADK rate presented in eq. (2.24).

After this lengthy derivation, let us step back and think about how CTMC and QTM C fit into the bigger picture. As we have seen, most clearly probably in the derivation

of the adiabatic ionization rate in section 2.3.2.1, CTMC and QTMC use the quantum mechanical information encoded in the transition amplitudes of the SFA to sample the initial conditions at the tunnel exit. At this point, the transition to trajectories comes at the expense of losing the quantum information of the propagation process, albeit advantageous in that it allows us to fully include the Coulomb force of the residual ion, as well as other effects such as forces due to the induced dipole or electron-electron correlation. However, including the semiclassical phase, thus making the CTMC a QTMC, some quantum information interference can be captured after all. Even though QTMC does not capture all features encoded in the full TDSE, the basic features in the interference pattern of the momentum distribution are reproduced in QTMC and have helped understand experimental results and TDSE outcomes better [60, 62, 63, 65, 130–135]. Of course, not all effects need the inclusion of the phase - e.g. the effects that will be presented in chapters 3, 4, and 5 can be explained in the framework of CTMC simulations. However, when comparing to experimental data in which interference effects play a prominent role, as will be the case in chapter 6, including the phase becomes important.



## Revisiting nonadiabatic effects on initial conditions

*"How wonderful that we have met with a paradox. Now we have some hope of making progress."*

— Niels Bohr

### Overview of this chapter

The long-standing question of how nonadiabaticity manifests itself in strong field ionization has brought up two seemingly contradictory effects. Firstly, that nonadiabaticity leads to a strong broadening in the spread of ionization times, which is obtained in a theory that assumes a vanishing initial longitudinal momentum [7]. And secondly, non-zero longitudinal momenta at the tunnel exit are predicted in a nonadiabatic theory which yields a narrower time spread [3].

In this chapter, it is shown that these findings about the ionization time spread and the initial longitudinal momentum are not independent of each other but that assumptions about the initial longitudinal momentum strongly influence the ionization time distribution. Moreover, it will be found that the broader time spread in one theory and the non-zero initial longitudinal momentum in the other theory compensate each other during propagation leading to about the same longitudinal momentum distribution at the detector to a good approximation for typically studied nonadiabatic parameters. Thus, it is explained why both theories were so successful so far in explaining nonadiabatic experiments despite their fundamentally different predictions of initial conditions.

However, parameters in the nonadiabatic but still experimentally relevant regime will be found where this approximation breaks down and the two different theories lead to distinguishably different momentum distributions at the detector after all. Comparison with numerical solutions of the time-dependent Schrödinger equation provides evidence for the theory with a non-zero initial longitudinal momentum and narrow time spread to be the more accurate one.

### 3.1 Introduction to nonadiabatic theories

Before we dive into the intricacies of the different nonadiabatic effects described in the overview above, we should acquaint ourselves with the basics of nonadiabatic theories. As we have seen in chapter 2, the initial conditions are vital for the success of CTMC



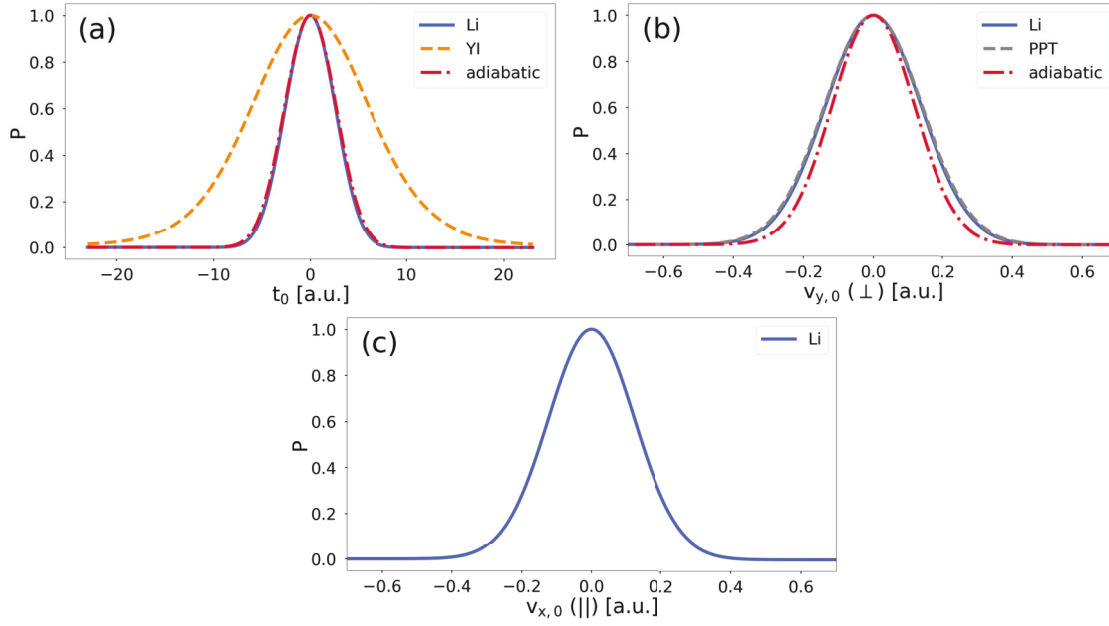


**Figure 3.1:** Normalized ionization probabilities  $P$  as a function of (a) the ionization times  $t_0$ , (b) the velocity along a direction transverse to the polarization axis, and (c) parallel to it. In all cases helium is ionized at an intensity of  $I = 5 \cdot 10^{13}$  W/cm<sup>2</sup> and a wavelength of  $\lambda = 800$  nm with the time dependence of the field being a plain cosine function ( $E_0 \cos(\omega t)$ ). The different theories used are specified in the legend, with YI referring to the work of Yudin and Ivanov [7], Li using [3], PPT being described in [4, 5, 136], and the label ‘adiabatic’ uses the theory introduced in section 2.3.2.1. In (a) and (c), the initial transverse momentum was set to zero and in (b) ionization at the peak of the field ( $t_0 = 0$ ) was assumed. Note that the distribution of the initial longitudinal momentum in (c) was obtained by calculating  $P_{Li}(t_0(v_{x,0}))$ , where eq. (3.6) determines the relation between  $t_0$  and  $v_{x,0}$ . Also, the reason for not including velocity spreads for the theory of YI in these plots is the fact that this theory does not give any such distribution since it focuses solely on the time dependence of the ionization rate.

and QTMC simulations and it was shown how the ionization rate can be used as the probability distribution describing these initial conditions. However, the derivation of the ionization rate in section 2.3.2.1 assumed a static field and the time-dependence was snuck into the equations by replacing the static field  $E_0$  by the time-dependent field  $E(t)$ , the underlying assumption being that the potential changes so slowly that the system adapts adiabatically to the changing field. This approximation is fully valid only in the adiabatic limit of  $\gamma \ll 1$ , though, and most strong field experiments are performed at a wavelength of  $\lambda = 800$  nm and an intensity of  $I = 10^{13} - 10^{15}$  W/cm<sup>2</sup>. When a typical target like helium ( $I_p = 0.9$ ) is ionized under these conditions, this corresponds to a Keldysh parameter of  $\gamma = 0.45 - 4.5$  and we are not in the adiabatic limit anymore but in the intermediate nonadiabatic regime.

Different theories have tried to take into account that the system does not adapt adiabatically because, loosely speaking, the barrier is moving while the electron is tunneling out. The first theory to tackle this nonadiabaticity problem was developed by Perelomov, Popov, and Terent’ev (PPT) [4, 5] in 1966. They solved the Schrödinger equation for an atomic potential described as  $V(x) = \sqrt{2I_p} \delta(x)$ , which allowed them to use a Green’s function ansatz. From the resulting wavefunction they calculated the



current density. The integrals therein were evaluated by applying the method of steepest descent (also known as saddle point approximation) and it was averaged over one laser cycle, thus obtaining an analytical expression for the corresponding ionization rate [106]. Applying the short-range potential has the added benefit of being able to apply the SFA and neglect the Coulomb potential during propagation. Therefore, this theory gives the ionization rate in terms of the photoelectron momenta  $\mathbf{p}$  after the laser pulse has passed, i.e. ‘at the detector’. In exponential accuracy, it reads<sup>1</sup>

$$P_{PPT}(\mathbf{p}, \gamma) = \exp \left( -\frac{2I_p}{\omega} h(\gamma) - \frac{1}{\omega} \left( p_x^2 \left( \operatorname{arcsinh}(\gamma) - \frac{\gamma}{\sqrt{1+\gamma^2}} \right) + (p_y^2 + p_z^2) \operatorname{arcsinh}(\gamma) \right) \right) \quad (3.1)$$

with

$$h(\gamma) = \left( 1 + \frac{1}{2\gamma^2} \right) \operatorname{arcsinh}(\gamma) - \frac{\sqrt{1+\gamma^2}}{2\gamma}. \quad (3.2)$$

After this theory had not been noticed much for about 30 years, the advent of stronger and shorter laser pulses, the subsequent discovery of HHG from atoms along with the explanation in the simple-man model and the establishment of CTMC simulations have sparked new interest in this work and nonadiabatic descriptions in general. In particular, improvements in the direction of a subcycle description have been attained, i.e. not averaging the ionization rate over the laser cycle, most notably by Yudin and Ivanov who derived a subcycle-resolved nonadiabatic ionization rate [7] that has been widely applied in the past two decades [67, 137–145]. Starting with eq. (2.14) and using the idea of evaluating the integrals via a saddle point approximation, i.e. by applying eq. (2.16), the basic concept of this theory is the same as the one presented in section 2.3.2.1 for deriving the adiabatic ionization rate. Setting both the transverse and longitudinal momentum to zero, justified by the fact that these are the most likely momenta in linearly polarized light, but not setting the ionization time to zero in contrast to the way the adiabatic theory was derived, Yudin and Ivanov arrive at the following time-dependent ionization rate with subcycle resolution

$$P_{YI}(t_0, \gamma) = \exp \left( -\frac{E_0^2 f^2(t_0)}{\omega^3} \Phi(\gamma(t_0), \theta(t_0)) \right) \quad (3.3)$$

with

$$\begin{aligned} \Phi(\gamma, \theta) &= \left( \gamma^2 + \sin^2(\theta) + \frac{1}{2} \right) \ln(c) - \frac{3\sqrt{b-a}}{2\sqrt{2}} \sin(|\theta|) - \frac{\sqrt{b+a}}{2\sqrt{2}} \gamma, \\ a &= 1 + \gamma^2 - \sin^2(\theta), \\ b &= \sqrt{a^2 + 4\gamma^2 \sin^2(\theta)}, \\ c &= \sqrt{\left( \sqrt{\frac{b+a}{2}} + \gamma \right)^2 + \left( \sqrt{\frac{b-a}{2}} + \sin(|\theta|) \right)^2}, \end{aligned} \quad (3.4)$$

where in  $\theta(t_0) = \omega t_0 + k\pi$  the integer  $k$  has to be chosen such that  $\theta(t_0) \in [-\pi/2, \pi, 2]$ , and  $\gamma(t_0) = \gamma/f(t_0)$  includes effects due to the envelope  $f$ . The most important feature of this time-dependent ionization rate is that it states that nonadiabaticity manifests itself in a strong broadening of the ionization time spread. This can be seen in

<sup>1</sup>Note that Mur et al. rewrote the original PPT results presenting them in a more accessible way in [136].

Fig. 3.1 (a), which shows that the time distribution according to eq. (3.3) (dotted orange line) is considerably broader than the distribution of the adiabatic ionization theory (dash-dotted red line).

More recently, a nonadiabatic theory was published by Li et al. [3] which gives a non-negligible longitudinal momentum at the tunnel exit. Just like in the derivation of the adiabatic ionization rate in section 2.3.2.1 and just like it was done by Yudin and Ivanov, this derivation builds again on eq. (2.14) and draws on the concept of evaluating the integrals via a saddle point approximation, i.e. applying eq. (2.16). Here, however, no assumption about the initial longitudinal or transverse velocity is made, which results in the following ionization rate

$$P_{Li}(t_0, v_{\perp,0}) = \frac{\omega^2 (2I_p)^{5/2}}{2E_0^4 \gamma^2(t_0, v_{\perp,0}) (\gamma^2(t_0, v_{\perp,0}) + \cos^2(\omega t_0)) \cos^2(\omega t_0)} \times \exp\left(-\frac{E_0^2}{\omega^3} \left\{ \left( \sin^2(\omega t_0) + \gamma^2(t_0, v_{\perp,0}) + \frac{1}{2} \right) \operatorname{arcsinh}(\gamma(t_0, v_{\perp,0})) - \frac{1}{2} \gamma(t_0, v_{\perp,0}) \sqrt{1 + \gamma^2(t_0, v_{\perp,0})(1 + 2\sin^2(\omega t_0))} \right\}\right), \quad (3.5)$$

where  $\gamma(t_0, v_{\perp,0}) = \omega \sqrt{2I_p + v_{\perp,0}^2} / |E(t_0)|$  with  $v_{\perp,0}$  denoting the initial transverse velocity and where the electric field is assumed to be  $E(t) = E_0 \cos(\omega t)$ . Thus, envelope effects are not inherently included and can only be accounted for in an approximate fashion replacing  $E_0$  by  $E_0 f(t)$ , analogously to the way it was done in the formulation of Yudin and Ivanov. Therefore, one has to bear in mind that this ionization rate is most accurate for long pulses and that deviations due to the approximate manner of accounting for envelope effects may appear for short pulses. Looking at the time spread of eq. (3.5) displayed in Fig. 3.1 (a) we can see that this ionization rate does not exhibit the strong nonadiabatic broadening predicted by Yudin and Ivanov but has about the same width as the adiabatic curve. Moreover, not having set the initial longitudinal momentum to zero, this theory arrives at the following expression for this quantity

$$v_{\parallel}(t_0, v_{\perp,0}) = \frac{E_0}{\omega} \sin(\omega t_0) \left( \sqrt{1 + \frac{\omega^2 (v_{\perp,0}^2 + 2I_p)}{E_0^2 \cos^2(\omega t_0)}} - 1 \right). \quad (3.6)$$

Comparing panels (b) and (c) of Fig. 3.1 makes clear that in the intermediate nonadiabatic regime the initial longitudinal momentum spread<sup>2</sup> of Li et al. has a width comparable to that of the initial transverse spread and is thus fundamentally different from the initial longitudinal ‘spread’ of Yudin and Ivanov, which is a  $\delta$  function at zero.

These findings of Yudin and Ivanov on the one hand and of Li et al. on the other hand, and the fact that these results seem to contradict each other will be at the core

<sup>2</sup>Note that even though an ensemble of trajectories sampled in the framework of this theory exhibits a distribution of initial longitudinal momenta, for fixed values of the ionization time and initial transverse velocity the longitudinal momentum is deterministic. Therefore, the way a spread of initial longitudinal momenta is obtained is not by sampling e.g. the distribution displayed in Fig. 3.1 (c). Rather, a distribution of ionization times and initial transverse velocities is obtained by sampling  $P_{Li}(t_0, v_{\perp,0})$  (eq. (3.5)) and then each trajectory with initial condition  $(t_0, v_{\perp,0})$  is assigned an initial longitudinal momentum according to eq. (3.6). Thus, the non-zero initial longitudinal momentum obtained here is conceptually different from the artificially assumed spreads of this quantity that were introduced to match experimental results in many a nonadiabatic theory [58, 59, 146–151].

of the rest of this chapter. First, though, let us try to gain a more complete picture of nonadiabatic theories by also looking at the transverse momentum at the tunnel exit. From Fig. 3.1 (b) it can be seen that the transverse distribution is broader in the nonadiabatic cases (PPT and Li) than in the adiabatic limit. Moreover, this figure reveals that even though the various nonadiabatic theories seem to disagree in terms of the initial longitudinal momentum and the ionization time spread, the situation is much clearer for the distribution of the transverse momenta, for which most common nonadiabatic theories give identical results. Consequently, there is not much need for discussions along these lines and therefore the initial transverse distribution will take a backseat in this chapter.

Another quantity that is modified when taking nonadiabatic effects into account is the tunnel exit, the initial spatial coordinate. As we have already seen in the right panel of Fig. 2.2, the electron is born closer to the nucleus in nonadiabatic theories. This effect can be understood by the pictorial description of the tunneling process in the bottom panel of Fig. 2.1, where the energy gain under the barrier effectively reduces the barrier width. Even though it may not be directly obvious due to different notations, the tunnel exit derived in PPT [4, 5] on the one hand, which is commonly used when the time-dependence of Yudin and Ivanov is applied, and by Li et. al on the other hand, are identical, as is shown in Appendix A.1. Therefore, the subject of nonadiabatic tunnel exits will not be addressed further here.

Note that all of the above-mentioned results are valid for linearly polarized light. In elliptically polarized light further nonadiabatic effects are observed, for a more detailed discussion of which the reader is referred to e.g. [58, 61, 136, 152, 153]. Here, only one of the most prominent effects shall be mentioned, which is the shift of the most likely initial transverse momentum. In the adiabatic limit, the initial transverse momentum is centered around zero. Taking into account nonadiabatic effects in elliptically polarized light, however, the most probable initial transverse momentum is shifted in the direction perpendicular to the electric field at the peak and inside the plane of polarization, in the rotation direction of the field [154].

## 3.2 Description of the problem addressed in this chapter

As already indicated above, the predictions for the initial longitudinal momentum and the ionization time spread as obtained by Yudin and Ivanov [7] and Li et al. [3], which we will from now on frequently abbreviate as ‘YI’ and ‘Li’, respectively, are fundamentally different. While YI sets the initial longitudinal momentum to zero due to its supposed negligibility and obtains a strong broadening in the spread of ionization times, Li derives a theory in which the initial longitudinal momentum is not negligible at all and the ionization time spread is considerably more narrow.

These theories, of course, are not the only ones aiming at describing nonadiabatic effects in strong field ionization. In this chapter, though, both YI and Li will serve as the respective poster child of the works that claim or make use of a vanishing initial longitudinal momentum and/or a broad time spread on the one hand, or make the case for a non-zero initial longitudinal momentum distribution on the other hand. To briefly illustrate that YI and Li are only the tip of the iceberg, let us briefly take stock of nonadiabatic results and their applications: Even though there are not many who claim to have found evidence for the longitudinal momentum to be zero at the tunnel exit [56], a lot of theories claim that despite a non-zero initial longitudinal momentum being

physically possible in principle, it can be set to zero if one is interested only in exponential accuracy even in the nonadiabatic regime [7, 33]. And many a theory [94, 116, 143] and theoretical explanation [67, 137–145] was built on this assumption. Others, in contrast, find evidence for and emphasize the non-negligible effect of not setting the initial longitudinal momentum to zero [3, 58–61, 93, 146–151, 155, 156], some of which [58, 59, 146–151] were criticized for introducing a longitudinal momentum spread at the tunnel exit in a way that made calculations match experimental results but without further physical justification [93, 119]. To add to the confusion, both YI and Li succeed in explaining many experiments in the nonadiabatic regime [61, 67, 130, 137–141] despite their strongly different initial conditions.

A vigilant reader may now ask if these issues might be resolved by the fact that the longitudinal momentum at the detector depends not only on the longitudinal momentum at the tunnel exit but also on the time-spread, as e.g. expressed in eq. (2.7). Thus, this apt remark may continue, could not the larger time spread in YI compensate for the lack of initial longitudinal momentum spread? The answer will be yes and no. Yes, in the sense that in this chapter it will be shown that indeed the theories of YI and Li are coupled in a way that predicts similar longitudinal momentum distributions at the detector to an approximation that is applicable to parameters under which many typical nonadiabatic strong field experiments are performed. And ‘No’ in that we will see that this approximation breaks down for parameters that are not even exotic but should be experimentally feasible and relevant.

Those who skipped the ‘No’ part of the preceding section or who are generally wary of theorists warning against approximations breaking down in some seemingly arcane regime may wonder why one should care to find out which theory is more accurate if both lead to the same final result to a good approximation anyway. Besides the obvious reason that answering this question sheds light on the nature of the tunneling process (an argument which may not convince the pragmatic type of reader just described), this question is also crucial for any experiment and theory where the highest accuracy to describe the initial conditions at the tunnel exit is required, as it is e.g. the case in attoclock experiments and their interpretation [92, 113–116, 118]. One theoretical method where the answer to the question about the initial conditions after tunnel ionization is of very obvious relevance is the recently proposed method of backpropagation [116], which interprets the attoclock. There, electrons are propagated forwards till the end of the pulse first by solving the TDSE numerically and are backpropagated to the tunneling event classically afterward. The crucial question, though, is when to stop the backpropagation [94], and using the condition of the trajectory having strictly zero longitudinal velocity to reconstruct the instance of the electron’s birth in the continuum was employed but is still under discussion [157]. Moreover, even though the final longitudinal momentum spread is found to be comparable for initial conditions from YI and Li for a wide range of typical nonadiabatic parameters, other strong field observables, such as HHG spectra or Rydberg state characteristics, may be more sensitive to the described difference in initial conditions.

After this motivation, we now tackle the problem of the exact form of the spread of the ionization time and of the longitudinal momentum at the tunnel exit.

### 3.3 Relation between the nonadiabatic theories of Yudin/Ivanov and Li

Both the theory presented in YI and Li invoke the saddle point equation

$$\frac{\partial S}{\partial t_s} = \frac{1}{2}(\mathbf{p} + \mathbf{A}(t_s))^2 = -I_p \quad (3.7)$$

with the complex-valued saddle point  $t_s$ , the vector potential  $\mathbf{A}$ , and the canonical momentum  $\mathbf{p}$ , where the latter is assumed to be conserved in the tunneling process and is evaluated at the time  $t_0 = \text{Re}\{t_s\}$  at which the electron appears in the continuum with initial velocity  $\mathbf{v}_0$ ,  $\mathbf{p} = \mathbf{v}_0 - \mathbf{A}(t_0)$ . We will restrict our study to linearly polarized light with the direction of polarization along the x-axis, as described in eq. (2.4). Up to here, things follow the derivation of the adiabatic ionization rates in section 2.3.2.1. The main difference in the nonadiabatic derivation is that the time-dependence of the carrier oscillation,  $E_0 \cos(\omega t)$ , is used throughout<sup>3</sup>, instead of resorting to the approximation of a static field  $E_0$ . Despite the basic approach being the same for YI and Li, the derivations diverge at the point where assumptions are made about the initial momenta.

In YI it is claimed that one can set both  $v_{\perp,0}$  and  $v_{\parallel,0}$ , the initial transverse and longitudinal momentum, to zero if one is interested only in exponential accuracy of the time-dependent ionization rate. The resulting ionization rate exhibits the typical nonadiabatic broadening that has already been shown in Fig. 3.1 (a) and seems to be widely accepted as one of the central nonadiabatic features [158, 159]. As already pointed out, the ionization distribution derived by Li et al. [3] also starts with eq. (3.7). Contrary to YI, though, the real and imaginary part of the resulting saddle point equations are then solved making no further assumptions regarding  $v_{\parallel,0}$  or  $v_{\perp,0}$ . Thus, an ionization rate  $P(v_{\perp,0}, t_0)$  (see eq. (3.5)) is obtained and, in particular, an expression for the initial longitudinal momentum (see eq. (3.6)), which is zero only for ionization directly at the field extrema.

Given the strongly different ionization time distributions obtained from YI and Li and given that the non-zero initial longitudinal momenta from Li are not negligible even in the intermediate nonadiabatic regime (see e.g. Fig. 2 in [3]), one is probably inclined to think that it should not be too difficult to find out which of the two theories describes experimental results more accurately. The fact that the discussion on the way nonadiabaticity manifests itself has been going on for over a decade now [57, 160–163] and that both theories were used successfully to explain experiments and TDSE results [60, 61, 67, 130, 137–141] already shows that it is probably not so easy after all. In the following, we show that the initial longitudinal velocity and the time spread are coupled in a way that, under approximations valid for the parameters that were typically chosen in nonadiabatic studies so far, leads to almost the same final momentum distribution.

First of all, we look for numerical evidence for this claim and perform CTMC simulations. Electrons with a total energy that is negative after the pulse has passed (Rydberg states) are filtered out and an asymptotic propagation is performed as described

<sup>3</sup>The envelope  $f(t)$  is not included explicitly in the *derivation* of either nonadiabatic theory, as already mentioned in section 3.1. However, for not too short pulses one can include the envelope to a good approximation by replacing  $E_0$  by  $E_0 \cdot f(t)$  in the *final* result. This procedure is also explicitly suggested in YI and is commonly used to account for the envelope [2, 60].



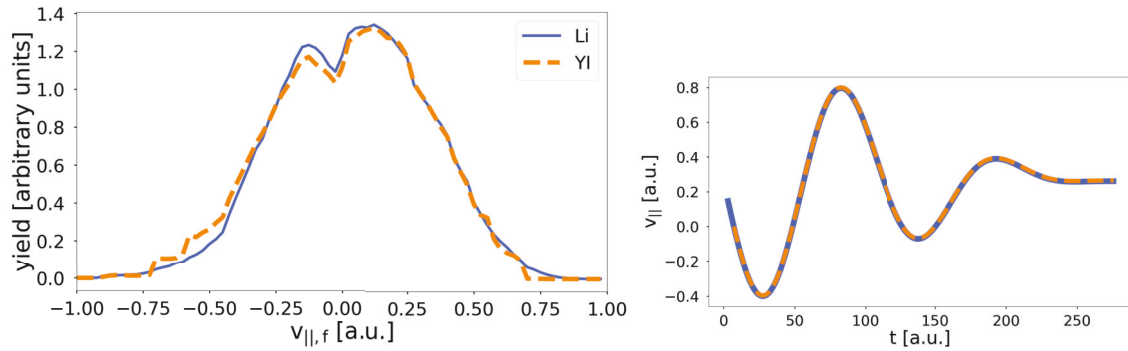


**Figure 3.2:** Left panel: Longitudinal momentum distribution at the detector obtained from a CTMC simulation with initial conditions according to [4, 7] (YI) and [3] (Li), where helium is ionized in a 5-cycle laser with  $I = 5 \cdot 10^{13}$  W/cm<sup>2</sup> and  $\lambda = 800$  nm. Right panel: Time-dependent longitudinal velocity for trajectories with  $P = 0.6$ , which are born at  $t_{0,YI} = 6.14$  a.u. and  $t_{0,Li} = 2.61$  a.u. according to Fig. 3.1 (a), and the initial longitudinal momentum set to zero or described by eq. (3.6), respectively.

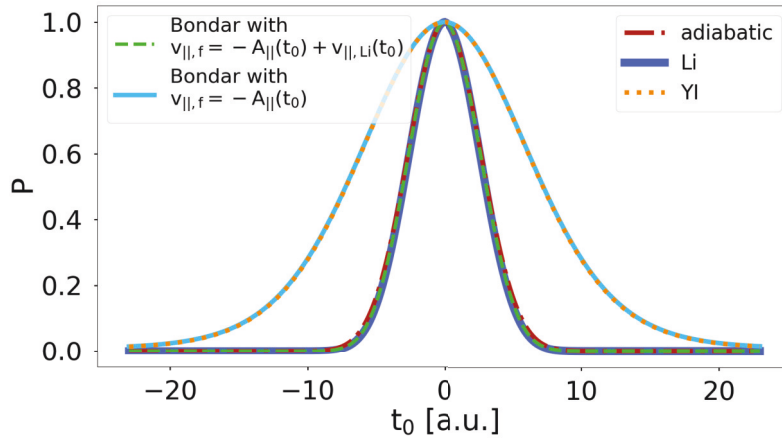


**Figure 3.3:** Normalized ionization probability  $P$  as a function of ionization times  $t_0$  for the same parameters as those used in Fig. 3.1 and, again, the transverse momenta were set to zero. The difference to Fig. 3.1 (a) is that the ionization time distributions as obtained by Bondar [2] are added. Using  $p_{||} = -A(t_0)$  (corresponding to  $v_{||}(t_0) = 0$ ) in doing so, we retrieve the time distribution given by YI and using  $p_{||} = v_{||}(t_0) - A(t_0)$  with  $v_{||}(t_0)$  according to eq. (3.6), we retrieve the time distribution of Li.

in section 2.3.3.1. The results are displayed in the left panel of Fig. 3.2. For the calculations with YI the nonadiabatic initial transverse momentum spread and tunnel exit given in [4, 5, 136] were used since YI only provides the time spread. Although the calculations presented in Fig. 3.2 are done in the obviously nonadiabatic regime, with the parameters being the same as in Fig. 3.1 and thus  $\gamma = 2.0$ , the two nonadiabatic theories under consideration indeed give about the same final momentum distribution with discrepancies too minor to be expected to be seen in an experiment. In the right panel of Fig. 3.2, the longitudinal velocity is plotted as a function of time for two trajectories with initial conditions according to YI and Li which - despite the different ionization time and initial velocity - both correspond to the same ionization probability according to Fig. 3.1. Here, we can see intuitively how the broader time spread in YI (corresponding to the dashed orange line of YI being born further away from  $t_0 = 0$  than the blue line of Li) compensates for the lack of initial longitudinal momentum and can therefore result in the same final longitudinal momentum as Li. From these trajectories it also becomes clear that compensation happens at the very beginning of propagation.

To understand that this compensation is not due to a particular choice of laser and atomic parameters but holds true over a wide range of parameters, it is instructive to look at the nonadiabatic theory presented by Bondar [2]. Designed to generalize the result of YI, this theory does not replace the canonical momentum  $\mathbf{p}$  at all, also not by  $\mathbf{p} = \mathbf{v}(t_0) - \mathbf{A}(t_0)$  as is the case in Li. Moreover, Bondar neglects the Coulomb potential during propagation and therefore the conserved canonical momentum  $\mathbf{p}$  equals the final velocity at the detector. Thus, Bondar obtains a probability distribution  $P(v_{\parallel,f}, v_{\perp,f})$ .

Why is Bondar's theory mentioned here when we are actually interested in understanding why YI and Li give about the same momentum distribution at the detector over a wide range of nonadiabatic parameters? The reason lies in the fact that the ionization time distributions of YI and Li can be obtained as special cases of the theory presented by Bondar by replacing the canonical momentum by  $-A(t_0)$  for YI or  $v_{\parallel}(t_0) - A(t_0)$  with  $v_{\parallel}(t_0)$  according to eq. (3.6) for Li, which is also seen in Fig. 3.3. As these relations between the ionization time spread of Bondar and those of YI and Li are not directly obvious, they are explained in Appendix A.2. The important conclusion from this finding is that YI and Li are two different ways of shifting the nonadiabatic velocity spread at the detector into time and velocity spreads at the tunnel exit. Or, more generally, that the different assumptions YI and Li make about the initial longitudinal velocity strongly influence the time distribution and that, therefore, these two quantities are strongly coupled. At this point it should also be emphasized that this statement goes beyond the long-known effect the ionization time has on the longitudinal momentum at the detector,  $v_{\parallel,f} = v_{\parallel}(t_0) - A(t_0)$ , when Coulomb effects are neglected during propagation. Here, in contrast, the different assumptions about the longitudinal momentum at the tunnel exit affect the ionization time distribution.

As for the distribution at the detector, the fact that the initial conditions of YI and Li both lead to the final distribution of Bondar is the key to understanding why YI and Li lead, to a good approximation, to the same final results. Since  $P(p_{\parallel})$  according to Bondar determines at which probability the final velocity  $v_{\parallel,f} = p_{\parallel}$  is found at the detector, independent of whether the replacement of that canonical momentum  $p_{\parallel}$  with initial conditions is done according to YI or Li, it is clear that for both theories we should find

the same longitudinal velocity distribution at the detector under the given approximations.

In order to get a more intuitive picture of how this fixed momentum distribution at the detector can be shifted into time and velocity spreads at the detector, some illustrative calculations are presented in the following. At the expense of introducing some further approximations, it will become clear that even though the longitudinal velocity and time spread in Li are motivated physically, there are – in principle – infinitely many ways to shift one particular momentum distribution at the detector to time and velocity spreads at the tunnel exit:

Even though the full probability distribution given by Bondar in Ref. [2] for the momentum distribution at the detector includes many terms for which it is not immediately clear how they can be approximated, for illustrative purposes we assume that we can approximate it by a Gaussian distribution of width  $\sigma_p$ :

$$P(p_{\parallel}) \approx \exp\left(-\frac{p_{\parallel}^2}{2\sigma_p^2}\right). \quad (3.8)$$

The main point this equation should convey is that there is a unique probability distribution for the longitudinal momentum at the detector, independent of how we introduce ionization times or initial longitudinal velocities. This statement is also true, if maybe less obvious, for the full expression given in [2].

Since the underlying assumption for the momentum distribution at the detector in [2] is that the Coulomb potential can be neglected during propagation, which leads to conservation of the canonical momentum  $\mathbf{p}$ , the longitudinal velocity at time  $t$  is given by  $v_{\parallel}(t_0) + A(t) - A(t_0)$  and since  $A(t) = 0$  at the end of the pulse, the final velocity is

$$v_{\parallel,f} = p_{\parallel} = v_{\parallel}(t_0) - A(t_0). \quad (3.9)$$

Setting  $v_{\parallel}(t_0) = 0$ , as it is done in YI [7], we obtain

$$v_{\parallel,f,YI} = -A(t_{0,YI}) = \frac{E_0}{\omega} \sin(\omega t_{0,YI}) \approx E_0 t_{0,YI} \quad (3.10)$$

for the longitudinal momentum at the detector, where in the last step the underlying assumption is that ionization happens close to the field maximum.

Conversely, using the non-zero velocity according to eq. (3.6), as obtained by Li, we get

$$\begin{aligned} v_{\parallel,f,Li} &= \frac{E_0 \sin(\omega t_{0,Li})}{\omega} \left( \sqrt{1 + \frac{\omega^2 2I_p}{E_0^2 \cos^2(\omega t_{0,Li})}} - 1 \right) + 1 \\ &= \frac{E_0 \sin(\omega t_{0,Li})}{\omega} \sqrt{1 + \frac{\omega^2 2I_p}{E_0^2 \cos^2(\omega t_{0,Li})}} \\ &\approx E_0 t_{0,Li} \sqrt{1 + \gamma^2} = E_0 t_{0,Li} \alpha \end{aligned} \quad (3.11)$$

with  $\alpha = \sqrt{1 + \gamma^2}$  and  $\gamma = \frac{\omega \sqrt{2I_p}}{E_0}$ , where – again – ionization close to the field maximum was assumed and hence  $\sin(\omega t_0) \approx \omega t_0$  and  $\cos(\omega t_0) \approx 1$ .



Plugging eqs. (3.10) and (3.11) into eq. (3.8) we obtain a probability distribution for the ionization times for YI and Li, respectively:

$$P_{YI}(t_0) \propto \exp\left(-\frac{E_0^2 t_0^2}{2\sigma_p^2}\right) = \exp\left(-\frac{t_0^2}{2\sigma_{t_0,YI}^2}\right), \text{ with } \sigma_{t_0,YI} = \frac{\sigma_p}{E_0} \quad (3.12)$$

and

$$P_{Li}(t_0) \propto \exp\left(-\frac{E_0^2 t_0^2 \alpha^2}{2\sigma_p^2}\right) = \exp\left(-\frac{t_0^2}{2\sigma_{t_0,Li}^2}\right), \text{ with } \sigma_{t_0,Li} = \frac{\sigma_p}{E_0 \alpha}. \quad (3.13)$$

From this we can conclude  $\sigma_{t_0,Li} \cdot \alpha = \sigma_{t_0,YI}$ . As  $\alpha > 1$  originates from the non-vanishing initial longitudinal momentum, we can thus see how the non-vanishing initial longitudinal momentum in Li leads to a smaller ionization time spread, with the effect becoming larger as we venture into the deeper nonadiabatic regime since a larger  $\gamma$  results in a larger  $\alpha$ . Or, put the other way around, it shows how the lack of initial longitudinal momentum in YI leads to a broadening of the ionization time spread. The above derivation is instructive also in that we see that even though  $\alpha$  is physically motivated to be  $\sqrt{1 + \gamma^2}$  in Li, in principle any real number greater or equal 1 could be inserted instead. This would modify the ionization time spread and the longitudinal momenta at the tunnel exit, but we would still obtain the probability distribution given by eq. (3.8). This illustrates how much freedom a probability distribution for only the longitudinal momenta at the detector gives in terms of the ionization time spread and the longitudinal momenta at the tunnel exit. One may even consider starting all trajectories directly at the field maximum (zero ionization time spread) and consequently use the momentum spread  $\sigma_p$  at the detector directly for the longitudinal momentum distribution at the tunnel exit. Extreme cases such as this make clear that not any arbitrary choice of how to convert the momentum distribution at the detector to the ionization time spread and longitudinal momenta at the tunnel exit is physically meaningful and that we should try to find out which replacement is the most physical. Further reasons for not replacing the canonical momentum arbitrarily will be seen in section 3.4, where we will observe that the freedom of shifting the momentum spread to the ionization time spread is restricted.

### 3.4 Distinguishing between the nonadiabatic theories at the detector

In the preceding section, we have seen that Bondar gives a probability distribution that prescribes the distribution of longitudinal momenta at the detector  $v_{||,f}$  and that the initial conditions of YI and Li can be derived as special cases of this theory, which helped us understand why Li and YI agree so well at the detector despite their different initial conditions. Moreover, the numerical example presented in Fig. 3.2, where the Coulomb potential was fully included, shows that the underlying approximation of Bondar, i.e. neglecting the Coulomb potential, works well. Under these circumstances, one may consider looking for parameters at which YI and Li give discernible results at the detector pointless.

In the following, however, we will see that it is possible after all and that the parameters that do the trick are experimentally feasible: Ionizing hydrogen with a laser pulse at an intensity of  $I = 1 \cdot 10^{14}$  W/cm<sup>2</sup> and a wavelength of  $\lambda = 400$  nm ( $\gamma = 2.1$ ), the

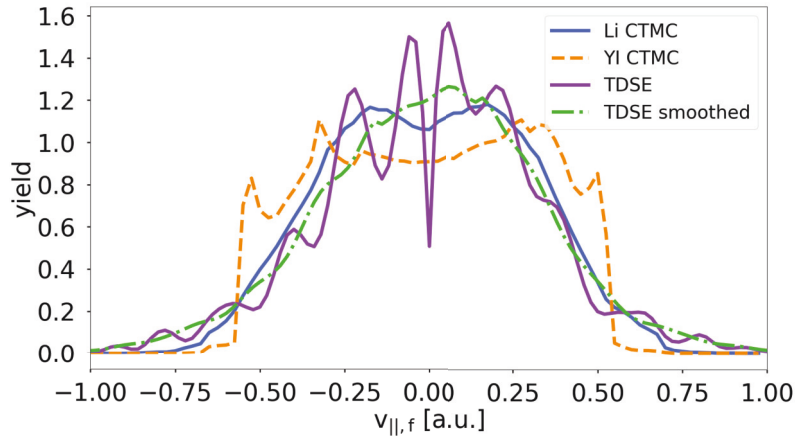


**Figure 3.4:** *Distribution of the final longitudinal momentum obtained from CTMC simulations using Li and YI as well as from TDSE simulations for hydrogen ionized in a 5-cycle pulse with an intensity of  $I = 1 \cdot 10^{14}$  W/cm<sup>2</sup> and a wavelength of  $\lambda = 400$  nm. The curves are normalized such that the areas under the TDSE and CTMC results are identical. The TDSE result gives much better agreement with the CTMC result using Li than with the CTMC result obtained with YI.*

two nonadiabatic theories produce two distinguishable final longitudinal momentum distributions, as is shown by the CTMC results in Fig. 3.4. Note that we are in the same  $\gamma$ -regime as in the example presented in Fig. 3.2, where we had  $\gamma = 2.0$ . In Fig. 3.4, the theory of YI leads to a sharp cut-off in the longitudinal momentum distribution, whereas the theory of Li yields more of a Gaussian-like profile.

Now that we obtained two different results from the two nonadiabatic theories, the obvious question is which one describes the physics of ionization more accurately. To this end, TDSE simulations were performed by Igor Ivanov, the technical details of which are described in [117, 164–166]. The result is shown in Fig. 3.4. As the TDSE result exhibits quantum interference which manifests itself as oscillations that cannot be captured in the CTMC calculations, we smooth the TDSE curve to guide the eye by replacing the TDSE result at each longitudinal momentum value by the average of all values that are found in a window that is centered at the respective momentum and has a total width of 0.28 a.u. along the longitudinal momentum axis. The window width was chosen in a way to smooth the oscillations while not being too broad to lose information about the averaged curve.

Comparing the smoothed TDSE result to the CTMC data in Fig. 3.4, it can be seen that the TDSE result exhibits the same Gaussian-like decay obtained in CTMC with the theory of Li, rather than the sharp cut-off we get using the theory of YI. To make this visual observation more quantitative, we look at the averaged absolute value of the difference between the smoothed TDSE and the CTMC results: the averaged deviation between the smoothed TDSE and the CTMC result with YI in the range of  $[-1, +1]$  on the momentum axis is 0.177 and thus more than twice as high as the averaged deviation between the smoothed TDSE and the CTMC result with Li, which is 0.070. As some may worry about the smoothing of the TDSE curve having biased that outcome, also the deviation between the unsmoothed TDSE (solid purple line in Fig. 3.4) and the

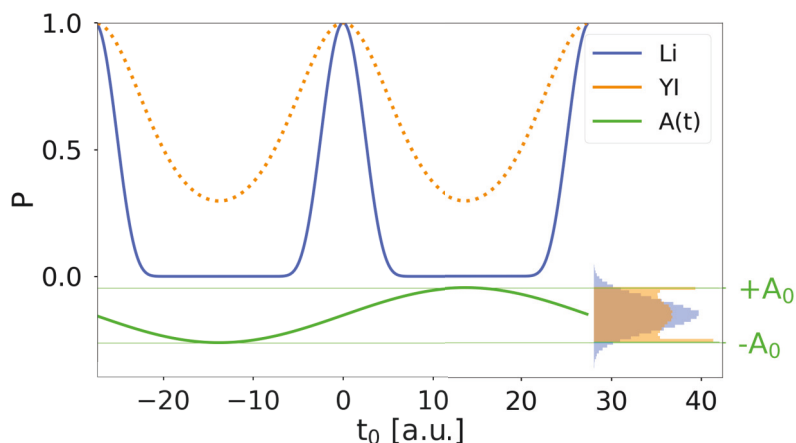


**Figure 3.5:** Normalized ionization probability  $P$  as a function of ionization time  $t_0$  for Li and YI, where for Li the initial transverse momentum was set to zero (YI sets the initial transverse momentum to zero already in the derivation of the ionization rate). The laser and atomic parameters are the same as in Fig. 3.4, except for the constant envelope used here. In the lower part also the vector potential  $A(t_0)$  is displayed as a green line. Since  $P(t_0)$  does not drop down to zero for YI, the maximal vector potential  $A_0$  gets sampled to a non-negligible amount. This leads to a sharp cut-off in the final longitudinal momentum distribution (orange histogram at the bottom right) if one performs CTMC calculations without the Coulomb force during propagation. The blue histogram, in contrast, was obtained in a CTMC simulation using the initial conditions according to Li (and again propagating without Coulomb potential). It retrieves the final longitudinal momentum distribution predicted by Bondar. The reason for the final distribution according to Li (blue histogram) having a tail that goes beyond  $\pm A_0$  is the non-zero initial longitudinal momentum.

CTMC with Li and YI, respectively, seem worth mentioning: The averaged<sup>4</sup> deviation between the TDSE and the CTMC result using Li is 0.1049, whereas the averaged deviation between the TDSE and the CTMC result using YI amounts to 0.2102 and is thus again about twice as large as for the CTMC with Li. We therefore find that the theory of Li is closer to the TDSE result, making it a more accurate theory to describe the situation at the tunnel exit. This observation not only corroborates the non-negligible longitudinal momenta at the tunnel exit, but it also implies that nonadiabaticity does not necessarily manifest itself in a time spread that is significantly broader than predicted by quasistatic theories, contrary to what is claimed in YI (see e.g. Fig. 3.3).

The observation of different momentum distributions at the detector using YI and Li obviously begs the question as to how this can be possible when we have just seen in the previous section (3.3) that the ionization times and initial longitudinal momenta can be obtained from the same theory (Bondar, [2]) which gives a unique probability distribution  $P(v_{||,f})$  for the final longitudinal momentum. One may think that this is due to the Coulomb effect playing a non-negligible role in this process, but as we will see this effect persists even without the Coulomb potential during propagation and the

<sup>4</sup>Note that averaged signifies that the the difference between TDSE and CTMC (=deviation) is calculated for each longitudinal momentum value, added up and then divided by the total number of longitudinal momentum bins. Thus, the term ‘averaged’ has nothing to do with the smoothing procedure described before.

reason is far more fundamental revealing the limits of shifting the final momentum spread arbitrarily to ionization time and initial longitudinal momentum distributions.

The key to understanding the different results obtained with Li and YI (Fig. 3.4) is the ionization time distribution displayed in Fig. 3.5. Since  $P(t_0)$  never drops down to zero for YI, the maximal vector potential  $A_0$  (green line) gets sampled to an appreciable amount leading to a considerable fraction of electrons ending up at  $|v_{||,f}| = \pm A_0$ . This results in a sharp cut-off at  $|v_{||,f}| = \pm A_0$  in the final momentum distribution (orange histogram at the bottom right panel of Fig. 3.5) for YI if one performs CTMC calculations without the Coulomb force during propagation. Including the Coulomb potential during propagation blurs this sharp line but does not destroy its basic characteristic, as we have seen in Fig. 3.4.

One consequence of the YI theory is that with its zero initial longitudinal velocity the resulting final momentum  $p_{||}$  is restricted to  $[-A_0, A_0]$  because we have to apply  $p_{||} = -A(t_0)$  (assuming no Coulomb potential). However, the final distribution given by Bondar in [2] predicts a non-negligible probability  $P(p_{||})$  at  $|p_{||}| > A_0$  at these specific parameters (The  $P(p_{||})$  predicted by Bondar at these parameters is shown as a light blue histogram in the inset at the bottom of Fig. 3.5). Therefore, the initial conditions of YI cannot retrieve  $P(p_{||})$  given by Bondar whereas Li can due to its non-zero initial longitudinal momentum. Actually, the light blue histogram at the bottom of Fig. 3.5 was calculated with the initial conditions from Li and is identical to the final momentum distribution predicted by Bondar. The reason for this is that, as mentioned above, Li's initial conditions can be obtained from Bondar's final momentum distribution. And after Coulomb-free propagation from the tunnel exit to the detector, Li's initial conditions directly result in Bondar's final momentum distribution again.

The obvious question now is why the same arguments are not valid for YI. Also the ionization time spread of YI can be obtained from Bondar's probability distribution  $P(v_{||,f})$ . This is done by setting  $v_{||,f} = -A(t_0)$  in  $P(v_{||,f})$ , corresponding to propagating the momentum distribution from the detector without Coulomb potential back to the tunnel exit, where the ensemble of trajectories exhibits zero momentum but a spread of ionization times. Nonetheless, we have witnessed that reversing this process and propagating these initial conditions from the tunnel exit to the detector, again neglecting the Coulomb potential, we do not recover the final momentum distribution  $P(v_{||,f})$  from which we started. Mathematically, this puzzling effect boils down to the following question: Why is

$$(A): P(v_{||,f}) \quad (3.14)$$

different from

$$(B): P(v_{||,f}(t_0(v_{||,f})))? \quad (3.15)$$

In (B),  $t_0(v_{||,f})$  is the ionization time obtained from propagating a trajectory with  $v_{||,f}$  at the detector back to the tunnel exit via

$$v_{||,f}(t_0) = A_0 \sin(\omega t_0) \Rightarrow v_{||,f}^{-1}(v_{||,f}) = t_0(v_{||,f}) = \frac{1}{\omega} \arcsin\left(\frac{v_{||,f}}{A_0}\right). \quad (3.16)$$

Therefore, one may think that one should be able to modify expression (B) as follows and obtain equality with expression (A):

$$P(v_{||,f}(t_0(v_{||,f}))) = P(v_{||,f}(v_{||,f}^{-1}(v_{||,f}))) = P(v_{||,f}). \quad (3.17)$$

However, from eq. (3.16) we can see that, on the one hand, we have  $v_{||,f}^{-1} : [-A_0, A_0] \rightarrow [-\infty, \infty]$ . On the other hand, we had  $P : [-A_0 - \zeta, A_0 + \zeta] \rightarrow [0, 1]$  with  $\zeta > 0$ , meaning we

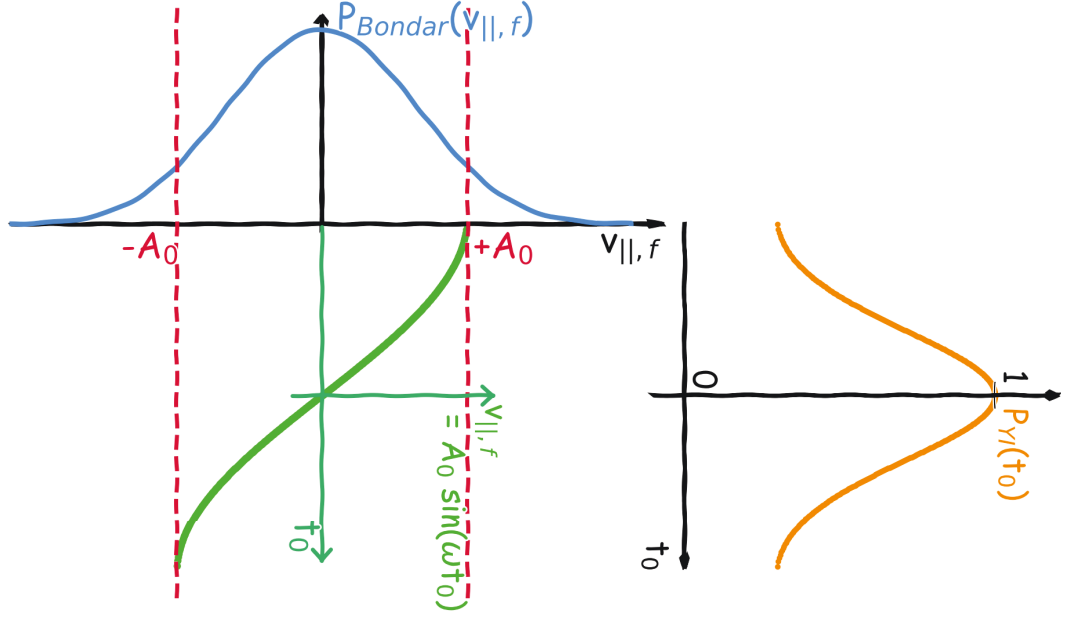


**Figure 3.6:** From  $P_{\text{Bondar}}(v_{\parallel, f})$  we can obtain  $P_{\text{YI}}(t_0)$  by replacing  $v_{\parallel, f}$  with  $A_0 \sin(\omega t_0)$ . This corresponds to backpropagation from the detector to the tunnel exit, where the Coulomb potential is neglected. However, reversing this process and propagating the electrons with ionization times that follow  $P_{\text{YI}}(t_0)$  without Coulomb to the detector, i.e. applying  $v_{\parallel, f} = A_0 \sin(\omega t_0)$ , we do not recover  $P_{\text{Bondar}}(v_{\parallel, f})$ . This is due to the fact that  $P_{\text{Bondar}}(v_{\parallel, f})$  has a non-zero probability for  $|v_{\parallel, f}| > A_0$  but no ionization time  $t_0$  leads to such a  $|v_{\parallel, f}| > A_0$  when applying  $v_{\parallel, f} = A_0 \sin(\omega t_0)$ . Mathematically, the problem is found in the fact that in  $P_{\text{Bondar}}(v_{\parallel, f})$  the domain of definition, i.e. the range of values  $v_{\parallel, f}$  one can plug into  $P_{\text{Bondar}}$ , goes beyond  $[-A_0, A_0]$ . In contrast, the domain of definition for  $t_0 = v_{\parallel, f}^{-1} = \arcsin(v_{\parallel, f}/A_0)/\omega$  is restricted to  $v_{\parallel, f} \in [-A_0, A_0]$ .

want to input  $|v_{\parallel, f}| > A_0$ , which is not defined for the  $v_{\parallel, f}^{-1}$  function in eq. (3.16). Consequently, the expressions (A) and (B) are different in their domain of definition, i.e. in the range of values  $v_{\parallel, f}$  one can plug into them. To put it another way, eq. (3.17) does not work because  $v_{\parallel, f}^{-1}$  as defined by eq. (3.16) is not defined for arguments (i.e.  $v_{\parallel, f}$  values) outside of  $[-A_0, A_0]$ , whereas  $P(v_{\parallel, f})$  (as given by Bondar in [2]) has  $P \neq 0$  for  $v_{\parallel, f} \notin [-A_0, A_0]$ . An illustration of this line of reasoning is given in Fig. 3.6.

All of this shows that one cannot replace the canonical momentum arbitrarily by ionization time and initial longitudinal momentum distributions, but that a physical justification for it, just as it is the case in Li, is crucial. In particular, it reveals that the assumption of a vanishing initial longitudinal momentum is not physical and can produce misleading results ‘at the detector’.

### 3.5 Conclusion and Outlook

In conclusion, it was shown that the nonadiabatic broadening of the time spread derived in YI is a direct consequence of setting the initial longitudinal momentum to zero. More generally, we saw that the strong coupling of the ionization time spread and the initial longitudinal momentum helps us understand why the theories of Li and YI, in



spite of their fundamentally different initial conditions, lead to approximately the same longitudinal momentum distribution at the detector if  $P(p_{||})$  is negligible for  $|p_{||}| > A_0$  and if the Coulomb potential during propagation can be neglected. As these conditions are widely met in strong field systems, we can now understand why the two nonadiabatic theories with their contrasting initial conditions were both successfully used to explain experiments in the nonadiabatic regime. This should account to some extent for the confusing character the discussions about nonadiabatic effects sometimes assume.

Despite the indistinguishability of the results obtained from the two theories in a wide range of typical nonadiabatic parameters, laser and atomic parameters were found that are still in the experimentally realizable and relevant regime for which the mentioned approximations break down and the two nonadiabatic theories yield experimentally distinguishable momentum distributions. The difference was understood by  $P(p_{||})$  (as given by Bondar in [2]) having a non-negligible probability for  $|p_{||}| > A_0$  at these parameters. Using the replacement of  $p_{||} = -A(t_0)$ , corresponding to a vanishing initial longitudinal momentum and thus shifting the spread completely to the ionization times as done in YI, only  $|p_{||}| \leq A_0$  can be obtained when propagating this initial condition to the detector again. Thus,  $P(p_{||})$  is not retrieved. Conversely, the use of non-zero initial longitudinal momenta in Li allows to reproduce  $P(p_{||})$  (as given by Bondar) and consequently, the momentum distribution at the detector obtained with the initial conditions of YI and Li differs at the detector for these parameters.

In line with this explanation, a ‘numerical experiment’ in the form of a TDSE simulation showed good agreement with the theory of Li, which uses a non-zero initial longitudinal momentum. With  $\lambda = 400$  nm,  $I = 1 \cdot 10^{14}$  W/cm<sup>2</sup> and  $I_p = 0.5$  a.u., the parameters of these calculations are in a regime that should be experimentally realizable. Therefore, this system is proposed for experimental testing of nonadiabatic effects on the initial conditions directly at the tunnel exit.

The strong evidence for the theory of Li being the more accurate one to describe the situation at the tunnel exit motivates, as a next step, to refine this theory. As already mentioned in section 3.1, the derivation of said nonadiabatic theory assumes a constant envelope. Consequently, envelope effects are so far accounted for only in an approximate fashion by replacing  $E_0$  by  $E_0 f(t)$  in the final result, with  $f(t)$  denoting the envelope. In principle, however, the derivation should also allow to include the envelope in the description of the field. It remains to be seen, though, whether analytical tractability can be maintained when fully including the envelope in the derivation and if not, one will have to think about numerical ways to solve the relevant equations efficiently.

Even though the Coulomb effect during propagation was not found to be the major effect to decide which of the two ionization theories describes the situation at the tunnel exit more accurately, it should be commented on briefly. The equivalence of YI and Li described in section 3.3 assumed that the Coulomb field is neglected. One may argue that, since the lack of initial longitudinal velocity is compensated by the earlier/later birth of the electron in YI directly at the beginning of propagation (see right panel of Fig. 3.2), the Coulomb effect can only be of relevance during that short time before the compensation is done. However, especially during that early time after the birth in the continuum the Coulomb potential matters due to the electron’s close location to the parent ion. The reason the Coulomb potential has a negligible effect in the parameter regime chosen in section 3.3 is mostly the fact that the low intensity leads to

a rather large tunnel exit. A smaller tunnel exit is achieved mainly with a larger intensity, which entails getting into the more adiabatic regime. Therefore, one usually does not have a small tunnel exit in the nonadiabatic regime. Consequently, to make use of the Coulomb potential to distinguish between the results of YI and Li one would need to evaluate a quantity that exhibits strong sensitivity to the Coulomb potential directly at the tunnel exit.





## Intensity and pulse duration dependence of Rydberg states

*"Problems worthy of attack prove their worth by fighting back."*

— Piet Hein (Danish mathematician, 1905-1996)

### Overview of this chapter

The investigation of Rydberg states that are created due to frustrated tunneling ionization in strong field processes has helped explain many strong field phenomena in the past decade. In this chapter, two new ways are presented for how to make use of and control the creation of Rydberg states:

Firstly, in section 4.2, the intensity dependence of the fraction of electrons that end up in a Rydberg state after strong field ionization with linearly polarized light is investigated numerically and analytically [71]. It is found that including the intensity-dependent distribution of ionization times and nonadiabatic effects leads to a better understanding of experimental results. This suggests that Rydberg yield measurements can be used as an independent test for nonadiabaticity in strong field ionization. Furthermore, using classical trajectory Monte Carlo simulations it is observed that the intensity dependence of the Rydberg yield changes with wavelength and that the previously observed power-law dependence breaks down at longer wavelengths.

In the second part, in section 4.3, it will be shown how the duration of the laser pulse can be used to control both the yield and principal quantum number distribution of Rydberg atoms [72]. An intuitive explanation for the underlying mechanism is provided and a scaling law for the position of the peak in the quantum number distribution on the pulse duration is derived. In particular, it will become clear that low principal quantum numbers are less likely to 'survive' longer pulses. This is relevant to studies and applications that rely on the principal quantum number distribution of Rydberg atoms like the recently developed method of creating coherent extreme-ultraviolet radiation from Rydberg atoms, in which the occupation of low principal quantum numbers is crucial. Furthermore, it will become clear that including the Coulomb potential during propagation is crucial for the understanding of pulse duration effects of Rydberg states and cannot be neglected as it was done so far in analytical descriptions of Rydberg states.

## 4.1 Introduction to Rydberg states

The liberation of an electron in the process of strong field ionization via tunneling does not necessarily lead to the electron leaving the atom for good [48, 49]. Rather, a considerable fraction of atoms survives the laser pulse in neutral excited states [48], so-called Rydberg states. The detection of excited neutral states in the multiphoton regime [167, 168] had been known long before the experiment of Ref. [48] presented neutral excited states in the tunneling regime and had been explained in the framework of a purely quantum mechanical picture as a stabilization process in multiphoton excitation. For the experiment in the tunneling region [48], a new mechanism to explain the creation of Rydberg states in this regime was required. As a consequence, the concept of ‘frustrated tunneling ionization’ (FTI) was born [48]. The idea behind FTI is based on the semiclassical model of tunneling ionization and subsequent propagation of the electron in the superposed laser and Coulombic field. The low kinetic energy of some electrons at the end of the laser pulse does not allow them to leave the Coulomb potential but results in their capture in a Rydberg state.

The relevance of FTI already becomes clear by the observation that under typical strong field conditions 10-20% of tunnel ionized electrons are trapped in Rydberg states [48], thus affecting many more electrons than other post-tunnel ionization mechanisms such as high-harmonic generation (HHG) or double ionization by collision [169, 170]. FTI not only explains the significant reduction of ionization rates [48] but can also be used to e.g. calibrate laser intensities [171], study nonadiabatic effects [71], probe the spatial gradient of the ponderomotive potential in a focused laser beam [172], or control the motion of neutral atoms in strong laser fields [170, 173].

There are some effects in strong field excitation, such as certain molecular effects or oscillations due to channel-closings in multiphoton excitation, that can only be understood based on the time-dependent Schrödinger equation [174–177]. However, especially the effect of FTI has been found to be described well in models that treat the propagation step and the capture in a Rydberg state classically [48–52, 178–180] and CTMC simulations have proven to be a powerful tool in the study of Rydberg state creation by FTI.

As the electron in a Rydberg state forms a bound state, this situation is characterized by a total energy that is negative after the pulse has passed

$$E = \frac{v^2}{2} - \frac{1}{r} < 0. \quad (4.1)$$

In CTMC simulations the Rydberg yield is computed by evaluating this relation at the end of the pulse and calculating the ratio of the number of electrons in a Rydberg state relative to the total number of electrons that have tunneled out of the atom. The Rydberg yield strongly depends on the intensity and pulse duration of the laser pulse, as has been pointed out before [48, 49]. In this chapter, we will continue the research along these lines, which will lead to a better understanding of Rydberg state creation via FTI and, in turn, give birth to completely new applications. For example, studying the intensity dependence of Rydberg states will open up a new way to detect nonadiabatic effects in strong field ionization [71], and the mechanism that is found to explain the pulse duration dependence of the yield can also be used to control the distribution of the principal quantum number of Rydberg states [72].

## 4.2 Intensity dependence

The content of this section has been published in a similar way in Phys. Rev. A 98, 033415 (2018) and a corresponding correction in Phys. Rev. A 99, 019901(E) (2019) (see Refs. [71, 181]). The copyrights of contents from those articles lie with the American Physical Society.

Already the first experiment that detected Rydberg state creation in the tunneling regime and introduced the concept of frustrated tunneling ionization (FTI) measured the intensity dependence of Rydberg states [48]. The takeaway from this measurement was that even though both the number of atoms in a neutral excited state (Rydberg state) and the number of ionized atoms grow with increasing intensity, the relative number of Rydberg states is smaller for higher intensities. Only a few months later an analytical model was proposed in Ref. [49] to explain not only the dependence of the Rydberg yield on the intensity but also on the wavelength and the pulse duration.

Below, we build on this work of Ref. [49] by including nonadiabatic effects, as well as introducing further corrections and expansions to the intensity-dependence of this theory. An analytical dependence of the Rydberg yield on intensity is presented that agrees better with the experimental results in Ref. [48]. Additionally, wavelength dependent effects in the intensity dependence are found which have not been predicted before and should be experimentally measurable. As we will see, especially the inclusion of nonadiabatic effects promises to be a new tool to study nonadiabaticity using Rydberg states instead of the momentum distribution of ionized electrons at the detector. This new approach to test nonadiabatic features does not depend on absolute intensity calibration that other nonadiabaticity studies struggle with (for a discussion see [154]).

### 4.2.1 Prior analytical estimates

In this section, the analytical tools that are developed and employed in Ref. [49] to estimate the Rydberg yield are explained and reviewed before they are modified in the following sections. The Rydberg yield, as defined in the present thesis, is the ratio of the number  $N^*$  of electrons which are captured in a Rydberg state and the number  $N_t$  of all electrons which tunneled through the potential barrier<sup>1</sup>. The key idea behind the analytical work in [49] is to assume a uniform distribution of electrons in the plane of initial conditions  $(t_0, v_{\perp,0})$  and to estimate the Rydberg yield to be proportional to the area  $\Sigma^*$  in this plane that contains those initial conditions that end up in a Rydberg state divided by the area  $\Sigma_t$  containing all ionization events

$$\frac{N^*}{N_t} \propto \frac{\Sigma^*}{\Sigma_t}. \quad (4.2)$$

In Fig. 4.1, we can observe the characteristic crescent-like shape of the Rydberg area  $\Sigma^*$  marked in shades of blue. In this plot, just as in the analytical estimate, we only consider ionization in the central half-cycle for the sake of analytical tractability. To estimate the area of the crescent it is instructive to look at the sketch in Fig. 4.2, where

<sup>1</sup>Note that in [49] the Rydberg yield is defined as the ratio  $N^*/N^+$ , with  $N^+$  the number of finally ionized atoms. Since  $N_t = N^* + N^+$ , the two definitions coincide only in the limit of  $N^* \ll N_t$ . In the corresponding analytical calculations in [49] we find a measure proportional to  $N_t$  in the denominator. Therefore, the definition of  $N^*/N_t$  as Rydberg yield would have been more accurate also in [49].

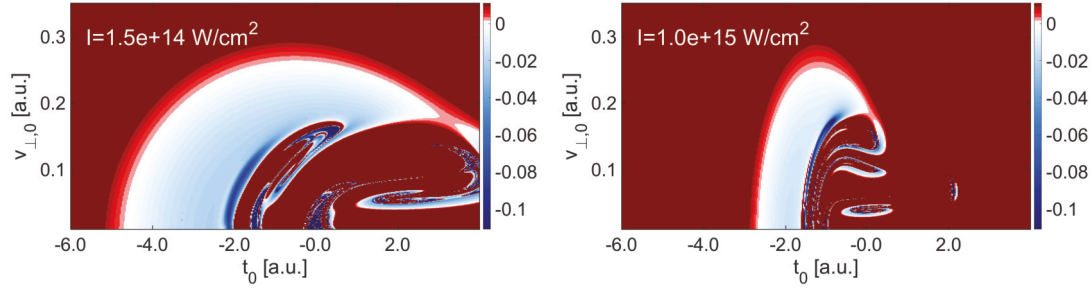


**Figure 4.1:** The total energy (see colorbar) at the end of the pulse for electrons ionized at time  $t_0$  in the central half-cycle with initial transverse momentum  $v_{\perp,0}$ , and propagated in the superposed laser and Coulomb potential. All quantities are given in atomic units. The laser pulse was chosen to have a wavelength of  $\lambda = 800$  nm and 8 cycles for two different intensities  $I$  specified in the plots. Rydberg states have a total energy that is negative (colored in shades of blue) and one can see how the Rydberg area shrinks for larger intensities.

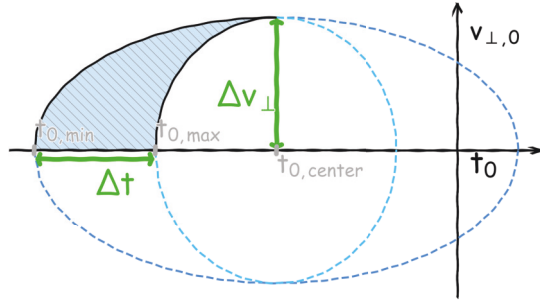


**Figure 4.2:** Illustration for why the crescent-like Rydberg area can be approximated by the relative complement of two ellipses with equal height but different widths and why, as a consequence, the Rydberg area can be approximated to scale linearly with  $\Delta t$  and  $\Delta v_{\perp}$ .

the crescent-shaped area is approximated by the relative complement of two ellipses of equal height (i.e. along the  $v_{\perp,0}$ -axis) but different widths (i.e. along the  $t_0$ -axis). As a consequence, we can assume that the crescent-shaped Rydberg area scales linearly with  $\Delta v$  and  $\Delta t$ , the range of  $v_{\perp,0}$  and  $t_0$  as defined in Fig. 4.2, respectively. This should become clear from the following calculation:

$$\begin{aligned}
 A_{\text{crescent}} &= \frac{1}{4} (A_{\text{large ellipse}} - A_{\text{small ellipse}}) \\
 &= \frac{1}{4} \left| \pi \cdot \Delta v_{\perp} \cdot (t_{0,\text{center}} - t_{0,\text{min}}) - \pi \cdot \Delta v_{\perp} \cdot (t_{0,\text{center}} - t_{0,\text{max}}) \right| \quad (4.3) \\
 &= \frac{\pi}{4} \cdot (t_{0,\text{max}} - t_{0,\text{min}}) \cdot \Delta v_{\perp} = \frac{\pi}{4} \cdot \Delta t \cdot \Delta v_{\perp}.
 \end{aligned}$$

Consequently, to estimate the Rydberg area it is sufficient to estimate the minimal and maximal ionization times  $t_{0,\text{min}}$  and  $t_{0,\text{max}}$  when  $v_{\perp,0} = 0$  and the initial velocities  $v_{\perp,0,\text{min}}$  and  $v_{\perp,0,\text{max}}$  that lead to a Rydberg state. Determining those four boundaries requires propagation in the superposed laser and Coulomb field. To keep this step analytically tractable, the electron trajectory is calculated without the Coulomb potential, which is further justified by the observation that including the Coulomb potential per-

turbatively does not affect the intensity-dependence of the size of the Rydberg area<sup>2</sup>. The Coulomb potential is only ‘turned on’ at the end of the pulse by means of eq. (4.1), which contains the Coulomb potential and which is evaluated in the limit of setting the total energy to 0. All in all, this results in the following estimate for the Rydberg area, as given in [49]:

$$\Sigma^* \propto \Delta\phi \cdot \Delta v \approx \frac{\omega}{E_0} \left( \frac{2}{\tau} \right)^{2/3}, \quad (4.4)$$

where  $\tau$  is the time at which the pulse has passed. As the center of the pulse is defined to be at  $t = 0$ ,  $2\tau$  equals the pulse duration  $\tau_L$ .

What still remains to be done is to estimate the ionization area. In Ref. [49], this is done by assuming that the ionization area scales linearly with the width of the distribution of the initial transverse velocity. The transverse velocity is estimated to scale as  $\sqrt{E_0}$  since the width of the Gaussian transverse velocity distribution of eq. (2.24) scales as  $\sqrt{E_0}$

$$\Sigma_t \propto \sigma_{v_\perp} \propto \sqrt{E_0}. \quad (4.5)$$

Combining eq. (4.4) and (4.5), one then obtains

$$\frac{N^*}{N_t} \propto \frac{\Sigma^*}{\Sigma_t} \propto \frac{\omega}{E_0^{3/2} \tau^{2/3}}. \quad (4.6)$$

Another point worth mentioning concerns the interpretation of this result. Even though  $\Sigma^* \propto 1/E_0$  agrees with the observation of the Rydberg area getting smaller with increasing intensity in Fig. 4.1, at first glance this does not seem to tally with the experimental observation of the number of neutral excited atoms increasing with increasing intensity [48]. This seeming contradiction is resolved by the fact that eq. (4.2) only holds in the relative sense, meaning under evaluation of the ratio rather than separate evaluation of the nominator and the denominator. Details concerning this point are presented in Appendix A.3.

## 4.2.2 Including the ionization time width

A vigilant reader may have noticed that in the estimation of  $\Sigma_t$  in eq. (4.5) only the width of the velocity spread was used, while the width of the ionization time spread was neglected. As the time width also depends strongly on the intensity, this shall be rectified in this section, thus introducing the first modification to the result presented in Ref. [49].

As we have already seen in eq. (2.28), the adiabatic ADK distribution for ionization phases  $\phi = \omega \cdot t_0$  [1, 182] can be approximated as a Gaussian function with an intensity-dependent width  $\sigma_\phi$  that is proportional to  $\sqrt{E_0}$ . Consequently, we should set

$$\Sigma_t \propto \sigma_{v_\perp} \cdot \sigma_\phi \propto \sqrt{E_0} \cdot \sqrt{E_0} = E_0 = \sqrt{I} \quad (4.7)$$

<sup>2</sup>In Ref. [49], the Coulomb force is taken account of in a perturbative manner by calculating the change of the momentum due to the Coulomb force accrued along the path of a trajectory that is propagated in only the laser field. However, the Coulomb correction cancels out in  $\Delta\phi = \omega\Delta t$  since it enters  $\phi_{latest}$  and  $\phi_{earliest}$  in the form of the exact same summand. For details see eqs. (10) to (12) in [49], where Coulomb effects are hidden in the parameter  $\lambda$ , which is not the wavelength there:  $\phi_{earliest} = \omega t_{0<} \approx -\lambda - \frac{\omega}{E_0} \left( \frac{4}{\tau_L} \right)^{1/3}$  and  $\phi_{latest} = \omega t_{0>} \approx -\lambda$ . Thus, in  $\Delta\phi = \phi_{latest} - \phi_{earliest}$ , the Coulomb-correction contained in  $\lambda$  cancels out and only shifts the Rydberg area along the  $\phi$ -axis but does not affect its size.

obtaining

$$\frac{N^*}{N_t} \propto \frac{\Sigma^*}{\Sigma_t} \propto I^{-1}. \quad (4.8)$$

This result enables a better understanding of the adiabatic CTMC simulation results displayed in Fig. 4.3 where a power law fit to the intensity-dependent Rydberg yield gives an exponent of  $-1.02$ . Note that even though the Coulomb effect is neglected in the propagation in the analytical estimates made in this chapter, the Coulomb potential is fully taken into account during propagation in the CTMC simulations. The observation that the CTMC result and the analytical estimate agree so well shows us that neglecting the Coulomb force during the propagation and the other approximations introduced above work well in the study of the intensity dependence of Rydberg states.

### 4.2.3 Nonadiabatic effects

From the experiment reported in [48], the ratio  $N^*/N_t$  can be extracted for various intensities. These values exhibit an intensity dependence that can be fitted very well by a power law function  $a \cdot I^b$  with fitting parameters  $a$  and  $b$ . The fit yields

$$\frac{N^*}{N_t} \propto I^{-0.86}, \quad (4.9)$$

displayed as a blue line in Fig. 4.3. So, even though taking into account the intensity-dependent ionization phase width in the analytical estimation in the preceding section, which shifted the power law exponent from  $b = -0.75$  as obtained in [49] to  $b = -1$ , was well captured by the adiabatic CTMC simulations giving  $b = -1.02$ , we still do not fully understand the experimental result of  $b = -0.86$  in this framework. However, when looking at the adiabaticity parameter  $\gamma = \omega\sqrt{2I_p}/E_0$  [89], we find that – for the intensity regime of  $I = 1.4 \cdot 10^{14} - 10^{15}$  W/cm<sup>2</sup> at  $\lambda = 800$  nm and  $I_p = 0.9$  –  $\gamma$  ranges from 0.5 to 1.2. This is the typical strong field ionization regime where the relevance of nonadiabatic effects is still under debate [57, 154, 161, 163].

We now show that nonadiabatic effects can be observed in Rydberg yield measurements from the power-law dependence alone. This eliminates the concerns about intensity calibration that have haunted prior experiments attempting to observe nonadiabatic effects by measuring electron momenta distributions [57, 154]. At this point, it seems important to emphasize that the factor correcting for the decay of neutral excited atoms into metastable states, which had to be applied in [48] to match theoretical and experimental results, does not depend on the intensity. Therefore it only affects the prefactor of the power law, but not its exponent, which makes the anyway high robustness of the exponent of a power law fit even less subject to issues arising from calibration of the absolute intensity.

In Fig. 4.3, CTMC simulation results are shown where on the one hand the nonadiabatic ionization theory described by Li et al. [3] (LI) was used and, on the other hand, the time spread by Yudin and Ivanov [7] (YI) combined with the transverse velocity spread of PPT<sup>3</sup>. A power law fit to the resulting intensity-dependent Rydberg yield

<sup>3</sup>The YI/PPT version, in short labeled as YI, was implemented using the theory of Bondar [2] where the final longitudinal momentum was replaced such that the ionization time distribution of YI was obtained (see chapter 3 for details). The initial transverse momentum distribution of Bondar matches that of PPT, which is shown in Fig. A.1 in Appendix A.1 for the two intensities that limit the intensity range considered in this chapter.



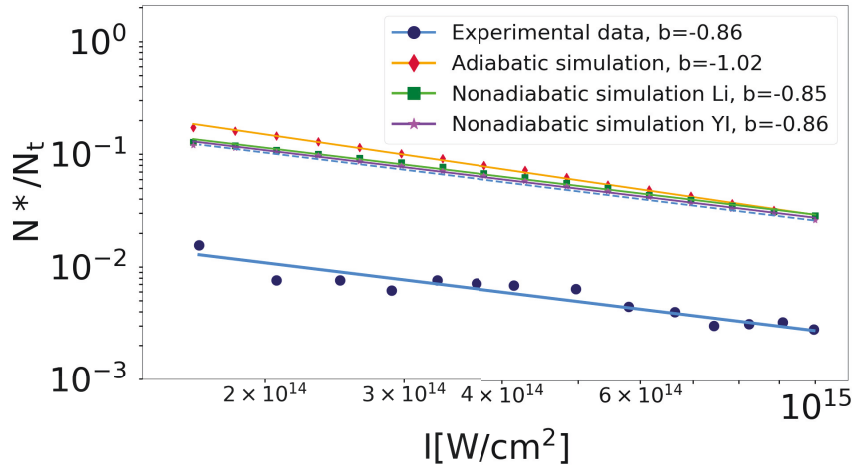


**Figure 4.3:** Rydberg yield for the parameters found in [48]:  $I = 1.4 \cdot 10^{14} - 10^{15} \text{ W/cm}^2$ , the FWHM of the pulse envelope is 30 fs,  $\lambda = 800 \text{ nm}$ , a helium atom with  $I_p = 0.9$  is ionized. The experimental yield (blue dots) was extracted from [48]. The adiabatic CTMC simulation (red diamonds) was performed using the ADK distribution [1, 182] and the nonadiabatic simulations are based on [4, 7] (YI, purple stars) and [3] (Li, green squares), respectively. The power law used for fitting is described by  $N^*/N_t = a \cdot I^b$  with  $b$  given in the legend. The fitting results are represented by lines. Note that the lower absolute values of the experimental yields are due to the decay of the excited states which is not accounted for here (for details see [48]). The correction factor that takes account of this effect and was applied in [48] for comparison between theory and experiment is found to be independent of the laser intensity. Therefore, it affects only the prefactor of the power law (and thus the offset on a log-log scale), but not the power law exponent (corresponding to the slope in the log-log plot) we are interested in here. For better visual comparison of the experimental result with the simulation data, the dashed blue line shows the experimental data artificially shifted closer to the simulation data.

gives an exponent of  $-0.86$  and  $-0.85$  for YI and Li, respectively. The good agreement between Li and YI is not surprising given the compensation effects that were described in chapter 3.3. More importantly, both nonadiabatic results are in much better quantitative agreement with the experimental value of  $b = -0.86$  than the adiabatic model.

Qualitatively, the nonadiabatic effect on the intensity dependence of the Rydberg yield observed here can be explained by the width in the distributions of the starting velocity and the ionization phase, which both increase more slowly with increasing intensity in the nonadiabatic case than in the adiabatic one. The slower growth with intensity can be understood qualitatively by the nonadiabatic broadening of the distributions of initial conditions at lower intensities, which makes these spreads of initial conditions drop less fast with decreasing intensity than in the adiabatic case. This shallower intensity dependence affects the denominator of the Rydberg yield, resulting in a less negative exponent in the power law.

In order to estimate the extent of the nonadiabatic effect quantitatively, we first evaluate how the spread of initial transverse velocities changes with intensity. Since the theory of Li and PPT agree in their description of the initial transverse velocity to a very good approximation (see e.g. the comparison in Fig. 3.1 (b) or in Fig. A.1 in Appendix A.1), we do not have to worry about which nonadiabatic theory to choose. We will

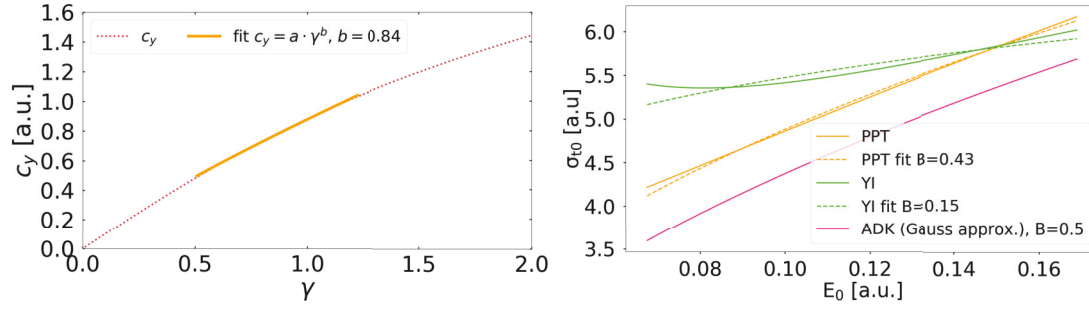


**Figure 4.4:** Left panel:  $c_y(\gamma)$  as given in [136] with the respective power law fits in the  $\gamma$ -regime defined by the parameters listed in Fig. 4.3. Right panel: Fit to the standard deviation  $\sigma_{t_0}$  of the ionization time spread as they are obtained from Gaussian fits to the theory of Refs. [4, 58, 136] (orange, PPT) and of Ref. [7] (green, YI). A power law fit  $A \cdot E_0^B$  was performed with the resulting exponents shown in the legend. For comparison, also the adiabatic case is shown which scales as  $\sqrt{E_0}$  according to eq. (2.28).

work with PPT here as it is easier to handle analytically. The transverse width of PPT is given in eq. (3.1) or equivalently in [136], where in the latter we find the notation  $\sigma_{v_\perp} = \sqrt{\omega/(2c_y)}$  for the width of the transverse velocity distribution with

$$c_y = \tau_0 = \sinh^{-1}(\gamma), \quad (4.10)$$

which in the adiabatic limit,  $\gamma \ll 1$ , reduces to

$$c_y = \tau_0 \approx \gamma \propto 1/E_0 \propto I^{-0.5} \Rightarrow \sigma_{v_\perp} \propto E_0^{0.5} \propto I^{0.25} \quad (4.11)$$

in accordance with eq. (4.5). For the nonadiabatic regime used here we fit a power law to eq. (4.10) (see left panel of Fig. 4.4) and obtain  $c_y \propto \gamma^{0.84}$  and thus

$$\sigma_{v_\perp} \propto \gamma^{-0.84/2} \propto E_0^{0.84/2} \propto I^{0.84/4}. \quad (4.12)$$

Concerning the second quantity of interest, the ionization time spread, the nonadiabatic effects described in YI and Li are different from each other, where in the latter we also saw effects on the initial longitudinal velocity spread (see ch. 3). In the following, we use the theory of YI rather than the theory of Li to describe nonadiabaticity. The reason for this choice is found in the fact that in the theory of Li the non-zero longitudinal velocity plays a crucial role. However, this quantity is not included in the model we use here, which focuses solely on the ionization time and initial transverse velocity spread. In chapter 3 we have seen that over a wide range of nonadiabatic parameters the lack of initial longitudinal momentum in YI is compensated to a good approximation by a broader ionization time spread and therefore yields almost identical results for the final longitudinal momentum spread as Li. This approximation is also valid at the parameters used in this chapter and, therefore, we use YI to estimate the extent of nonadiabatic effects here even though we found in chapter 3 that Li can be considered a more general nonadiabatic theory than YI.

The right panel of Fig. 4.4 shows how the ionization time spread of YI changes significantly less with intensity than in the adiabatic case. One feature of the YI-curve that may seem unexpected at first glance is that the width does not grow monotonically with increasing intensity but that there is a minimum around  $E_0 \approx 0.08$  a.u.. This can be understood as follows: In the adiabatic limit the ionization time width decreases



monotonically when the field strength becomes smaller. Smaller intensities, however, are related to the more nonadiabatic regime where nonadiabatic broadening of the ionization time distribution is found. As this nonadiabatic broadening is strong in YI, it dominates at small intensities, resulting in the curve going up for  $E_0 \lesssim 0.08$  a.u. in the right panel of Fig. 4.4. Despite the resulting minimum, we perform a power law fit to the field strength dependence of the ionization time spread of YI since it still reflects the fact that the nonadiabatic curve has a much more shallow intensity dependence than the adiabatic case. The resulting power law exponent is 0.15 and combining this with the result from eq. (4.12) we obtain

$$\frac{N^*}{N_t} \propto \frac{1/I^{0.5}}{I^{0.84/4+0.15/2}} = I^{-0.79}, \quad (4.13)$$

At this point, it seems important to highlight that the aim of the estimate in eq. (4.13) is not to attain a perfect match with the power law exponent of the CTMC simulation, but to qualitatively understand the CTMC simulation result. Even though the exponents do not match perfectly, we can learn from the above analysis that the main reason for the strong nonadiabatic effect lies in the much shallower intensity-dependence of the ionization time spread in the nonadiabatic case.

In the right panel of Fig. 4.4 the time-dependence as it was introduced into PPT in [58] is also included since this approach was used when the results shown here were originally published in [71, 181]. In the following, it is explained why in this thesis the nonadiabatic theory of YI is used instead. As outlined in the introduction to chapter 3, the PPT result is cycle-averaged and does not include instantaneous time-dependence. Even though the way the time-dependence is included into PPT in [58] worked well in the context it was applied to there, the right panel of Fig. 4.4 reveals that in the parameter regime used here, the theory of PPT and YI strongly differ in the ionization time spread. Since YI, in contrast to PPT, is designed to include instantaneous time-dependence, applying this theory of YI here seems more appropriate. This argument is corroborated by the nonadiabatic simulation results with YI yielding a power law exponent of  $b = -0.86$  that matches the experimental result of  $b = -0.86$  better than the exponent of  $b = -0.95$  [71, 181] obtained in the simulation with PPT with the time-dependence included following [58].

The results presented in this section do not only highlight the relevance of taking account of nonadiabatic effects, but it also shows in what way FTI can be used to investigate the initial conditions at the tunnel exit. In particular, as the discussed effects concern the denominator of the Rydberg yield and thus the total number of tunneled electrons, they are not only relevant for Rydberg related studies but for tunnel ionization in general. For example, the slower growth of the momentum width with intensity when applying nonadiabatic theories as compared to adiabatic theories can also be seen in the data presented in [154, 161].

The nonadiabatic observation made here now opens the door to use this effect for testing nonadiabaticity in a way that complements the tests employing momentum distributions. The latter is the way nonadiabaticity is usually studied: The quantity under scrutiny is typically the width of the momentum distribution [3, 57, 93, 154, 161, 183], which differs in adiabatic and nonadiabatic theories. The problem with this approach is that the momentum distribution is sensitive to the exact absolute value of the intensity. And this intensity is difficult to measure and is usually calibrated a posteriori by applying either an adiabatic or nonadiabatic theory on the photoelectron momen-

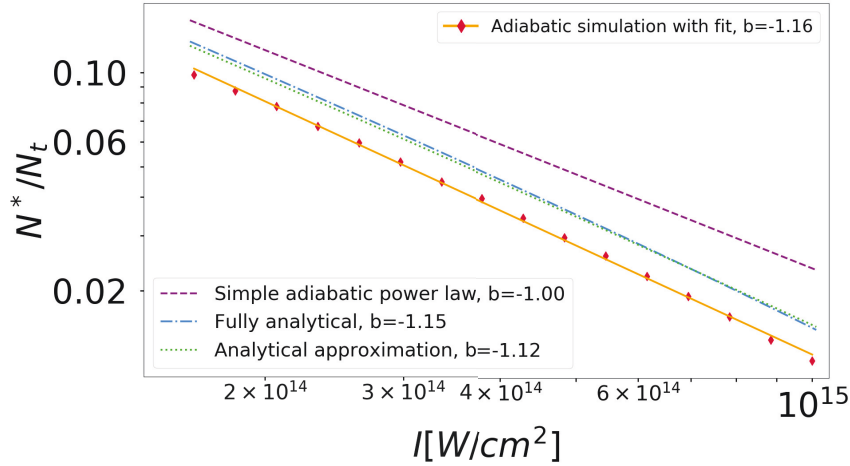


**Figure 4.5:** Intensity-dependent Rydberg yield at  $\lambda = 1200$  nm (all other parameters are chosen as listed in Fig. 4.3). Purple dashed line: The adiabatic power law with  $b = -1$  (see eq. (4.8)). Red diamonds: Adiabatic CTMC simulation data with power law fit (orange line) to it. Blue dashed-dotted line: Estimation by solving eq. (4.18) and (4.20) exactly, Green dotted line: Approximation given by eq. (4.33).

tum distribution, finding different intensity values depending on which framework is chosen. So, the theory under test is already used for calibration, which is certainly problematic [154]. Here, in contrast, we do not look at the momentum distribution of ionized electrons at all but study only the Rydberg yield. In this study of Rydberg states we are not interested in total but only in relative intensities, which can be controlled and measured independently of the mentioned calibration issues. Therefore, Rydberg states can be used for testing nonadiabaticity effects independent of the absolute intensity, thus complementing the way nonadiabaticity is tested using momentum distributions.

#### 4.2.4 Wavelength correction

For a wavelength of  $\lambda = 800$  nm the estimation of a power law with exponent  $b = -1$  matched the adiabatic simulation results rather well (see Fig. 4.3,  $b = -1.02$  for the adiabatic CTMC simulations). Even though eq. (4.6) contains  $\omega$ , the exponent of the power law of the *intensity dependence* in this adiabatic theory is wavelength-independent and we would expect the same power law scaling with about  $b = -1$  to hold for larger wavelengths as well – or even better since the system would be more adiabatic. However, the Rydberg yield from adiabatic CTMC simulations at  $\lambda = 1200$  nm shows a faster drop with intensity, which is reflected in the more negative exponent of  $b = -1.16$  in the power law fit (red diamonds with orange line in Fig. 4.5). For larger wavelengths, the drop increases even faster with increasing intensity. In the following, a theory is derived that explains this effect and that allows to make predictions about observing this effect in experimental data as well.

As expounded in section 4.2.1, we need the maximal initial transverse velocity  $v_{\perp,0,max}$  and the range  $\Delta\phi$  of ionization phases (at  $v_{\perp,0} = 0$ ) for estimating the area of initial events in the  $v_{\perp,0} - \phi$  plane which end up in a Rydberg state. The Coulomb force is neglected during propagation, as explained in section 4.2.1, and therefore we only use the Coulomb potential at the end of the pulse for the evaluation of eq. (4.1).

Moreover, the tunnel exit is set to  $x_e = 0$ . The position and velocity at a time  $\tau$  just when the pulse has passed are then approximated by

$$x(\tau) \approx \frac{E_0}{\omega^2} \cos(\phi) - \frac{E_0}{\omega} \sin(\phi) \cdot \tau \quad (4.14)$$

$$y(\tau) \approx v_{\perp,0} \cdot \tau \quad (4.15)$$

$$v_x = -\frac{E_0}{\omega} \sin(\phi) \quad (4.16)$$

$$v_{\perp} = v_{\perp,0}, \quad (4.17)$$

where a CEP of  $\pi$  was assumed (see Appendix A.4 for an explanation) and  $\tau = \tau_L/2$  is the time at the end of the pulse because  $\tau_L$  denotes the pulse duration and the ionization phase of  $\phi = 0$  is defined to correspond to ionization at the central field extremum. The detailed derivation of these equations along with an explanation of the approximations applied here are given in Appendix A.4. The important point about these equations is that they differ from the ones used in [49] in that they include the term  $\frac{E_0}{\omega^2} \cos(\phi)$  in  $x(\tau)$ . The wavelength effect in the intensity dependence that is derived in the following arises from this discrepancy. Therefore, the mentioned effect is weakened for longer pulses where the second term in  $x(\tau)$  dominates and the term  $\frac{E_0}{\omega^2} \cos(\phi)$  is less relevant.

For the calculation of  $v_{\perp,0,max}$ , we can plug eqs. (4.14) and (4.15) into eq. (4.1) in the limit of  $E = 0$  and set  $\phi = 0$

$$E = \frac{v_{\perp,0,max}^2}{2} - \frac{1}{\sqrt{\frac{E_0^2}{\omega^4} + v_{\perp,0,max}^2} \cdot \tau^2} = 0. \quad (4.18)$$

Analogously, we set  $v_{\perp,0} = 0$  in the calculation of  $\phi_{earliest}$  in eq. (4.1), which leads to:

$$\frac{1}{2} \left( \frac{E_0}{\omega} \right)^2 \cdot \sin^2(\phi_{earliest}) - \frac{1}{\frac{E_0}{\omega^2} \cos(\phi_{earliest}) - \frac{E_0}{\omega} \sin(\phi_{earliest}) \cdot \tau} = 0. \quad (4.19)$$

This expression can be approximated by

$$\frac{1}{2} \left( \frac{E_0}{\omega} \right)^2 \cdot \phi_{earliest}^2 - \frac{1}{\frac{E_0}{\omega^2} - \frac{E_0}{\omega} \phi_{earliest} \cdot \tau} = 0 \quad (4.20)$$

since  $\phi_{earliest} < 0.1$  for the parameters used here. Equations (4.18) and (4.20) can be solved analytically for  $v_{\perp,0,max}$  and  $\phi_{earliest}$ , respectively. The solutions are

$$v_{\perp,0,max} = \sqrt{\frac{-\frac{E_0^2}{\omega^4} + \frac{E_0^4}{\omega^8 \cdot h} + h}{3\tau^2}} \quad (4.21)$$

with

$$h = \left( -E_0^6 + 6\omega^6 \left( 9\tau^4 \omega^6 + \sqrt{-3E_0^6 \tau^4 + 81\tau^8 \omega^{12}} \right) \right)^{1/3} / \omega^4 \quad (4.22)$$

and

$$|\phi_{earliest}| = \frac{1 + g + \frac{1}{g}}{3\tau\omega} \quad (4.23)$$

with

$$g = E_0^3 / \left( E_0^9 - 27E_0^6 \tau^2 \omega^6 + 3 \sqrt{-6E_0^{15} \tau^2 \omega^6 + 81E_0^{12} \tau^4 \omega^{12}} \right)^{1/3}. \quad (4.24)$$

As before, the Rydberg yield is then estimated by plugging these results into

$$\frac{N^*}{N_t} \propto \frac{|\phi_{earliest}| \cdot |v_{\perp,0,max}|}{E_0}. \quad (4.25)$$

The resulting intensity dependence at  $\lambda = 1200$  nm can be seen in Fig. 4.5 (blue line), a power law fit to which gives an exponent of  $b = -1.15$ . This analytical derivation matches the simulation data (red diamonds), yielding  $b = -1.16$ , very well. As the lengthy, full analytical solutions of (4.18) and (4.20) given above do not allow for a deeper understanding of which parameters dominate this wavelength effect in the intensity dependence, an approximation for them is derived in the next paragraph.

The idea is to plug the approximate and simpler results  $v_{\perp,0,*} = (2/\tau)^{1/3}$  and  $\phi_* = -(\frac{2}{\tau})^{1/3} \cdot \frac{\omega}{E_0}$  from [49] into the Coulomb term of eq. (4.1) but not into its kinetic energy term. For  $v_{\perp,0,max}$ , this means

$$\frac{v_{\perp,0,max}^2}{2} - \frac{1}{\sqrt{\frac{E_0^2}{\omega^4} + v_{\perp,0,*}^2 \cdot \tau^2}} \approx 0 \Rightarrow v_{\perp,0,max} \approx \frac{\sqrt{2}}{\left(\frac{E_0^2}{\omega^4} + 2^{2/3} \cdot \tau^{4/3}\right)^{1/4}}. \quad (4.26)$$

And for the phase we obtain

$$\frac{1}{2} \left( \frac{E_0}{\omega} \right)^2 \cdot \phi^2 - \frac{1}{\frac{E_0}{\omega^2} - \frac{E_0}{\omega} \phi_* \cdot \tau} \approx 0, \quad (4.27)$$

from which follows

$$|\phi_{earliest}| \approx \frac{\omega/E_0 \cdot \sqrt{2}}{\sqrt{\frac{E_0}{\omega^2} - \frac{E_0}{\omega} \left(-(\frac{2}{\tau})^{1/3} \cdot \frac{\omega}{E_0}\right) \tau}} = \frac{\omega/E_0 \cdot \sqrt{2}}{\sqrt{\frac{E_0}{\omega^2} + 2^{1/3} \cdot \tau^{2/3}}}. \quad (4.28)$$

Setting  $m = \frac{E_0}{\omega^2}$  and  $n = 2^{1/3} \cdot \tau^{2/3}$ , the Rydberg yield can be expressed as follows:

$$\frac{N^*}{N_t} \propto \frac{\Sigma^*}{\Sigma_t} = \frac{|v_{\perp,0,max}| \cdot |\phi_{earliest}|}{E_0} \quad (4.29)$$

$$= \frac{\sqrt{2}}{(m^2 + n^2)^{1/4}} \cdot \frac{\sqrt{2} \cdot \omega/E_0}{(m + n)^{1/2}} \cdot \frac{1}{E_0} \quad (4.30)$$

$$= \frac{2\omega}{E_0^2 \cdot \sqrt{n} \cdot \left(1 + \frac{m^2}{n^2}\right)^{1/4} \cdot \sqrt{n} \cdot \left(1 + \frac{m}{n}\right)^{1/2}} \quad (4.31)$$

$$\approx \frac{2\omega}{E_0^2 \cdot \sqrt{n} \cdot \sqrt{n} \cdot \left(1 + \frac{1}{2} \frac{m}{n}\right)} \quad (4.32)$$

$$\propto \frac{\omega}{2^{1/3} \cdot E_0^2 \cdot \tau^{2/3} \left(1 + \frac{E_0}{2^{4/3} \cdot \omega^2 \cdot \tau^{2/3}}\right)}, \quad (4.33)$$

where eq. (4.32) is expanded in a Taylor series around  $m/n \approx 0$  neglecting terms with  $\mathcal{O}(m^2/n^2)$ . This expansion to first order seems reasonable since for the studied parameter regime  $m < n$  holds true. For the case of  $\lambda = 1200$  nm, the approximation is

plotted in Fig. 4.5 (green line) and a power law fit to it gives an exponent of  $b = -1.12$ . This approximation makes clear that for large wavelengths and small pulse durations the Rydberg yield as a function of intensity is less well described by a power law than for small wavelengths and longer pulses. It bears repeating that this discrepancy between the description in [49] and the one derived above stems from the fact that here the term  $\frac{E_0}{\omega^2} \cos(\phi)$  is included in the equation of motion whereas it is omitted in [49].

### 4.2.5 Conclusion and Discussion

In conclusion, it was found that taking account of the ionization time width into the analytical model describing the intensity dependence of the power law explains adiabatic CTMC simulations more accurately. In a next step, it became clear that nonadiabatic CTMC simulations match the experimental results better. The less negative power law exponent in the nonadiabatic case could be understood by the shallower intensity dependence of the spread of the initial transverse momentum and, in particular, of the ionization times. As the two mentioned corrections affect the denominator of the Rydberg ratio and thus the total number of electrons that tunneled out of the atom, these insights and approximations can be used beyond studies of Rydberg atoms when one is interested in the intensity dependence of tunnel ionization in a more general context. Moreover, we saw that the power law intensity dependence observed for infrared light breaks down for longer wavelengths. This correction is based on and highlights the importance of including the offset term  $E_0/\omega^2 \cos(\phi)$  in the approximation of the position of an electron that is driven by a laser field.

All in all, these results show new ways to use Rydberg atoms for retrieving information about the tunneling and propagation step in strong field ionization processes. In particular, measuring the Rydberg yield can be used as an independent test for nonadiabatic effects in strong field ionization. So far, the question of the importance of nonadiabatic effects in strong field ionization was addressed by investigating photoelectron momenta distributions [57, 61, 154, 161]. These investigations, however, have proved to be inconclusive, with some experiments confirming adiabatic assumptions [57, 161] and others pointing to relevance of nonadiabatic effects under typical strong field ionization conditions [61, 154]. As we have seen here, the intensity dependence of the Rydberg yield can be described by a power law, with nonadiabaticity affecting the exponent. Since the absolute value of intensity is therefore not important, the results do not depend on the calibration procedure which has been a serious issue in prior studies [154].

Thinking about pushing the nonadiabatic study of Rydberg states presented above deeper into the nonadiabatic regime, we need to be aware of the fact that multiphoton excitation effects become relevant and a description that is restricted to the tunneling picture is insufficient. As a consequence, CTMC simulations are expected to fall short when penetrating deeper into the nonadiabatic regime. For example, the yield of strong field excited atoms exhibits modulations in the vicinity of channel-closings in the multiphoton regime [184], which cannot be captured in the framework of CTMC. While adapting the SFA allows for a unified description of strong field excitation in the multiphoton *and* tunneling regime [184], this ansatz fails to include the Coulomb potential during propagation. This may not be a problem in cases where the Coulomb potential has a negligible effect on the observed quantity and can be treated perturbatively, but will be problematic in e.g. studying pulse duration effects

where the Coulomb potential plays a key role, as we will see shortly in section 4.3. A future challenge therefore seems to lie in finding a trajectory-based method that captures strong field excitation effects in the multiphoton regime while at the same time including Coulomb effects during propagation.

### 4.3 Pulse duration dependence

As the title suggests, this section deals with the pulse duration dependence of Rydberg states. Just like the intensity in the previous section, also the pulse duration affects the Rydberg yield. To those who read the previous section carefully this might not even come as a surprise since eq. (4.6) already predicted a drop of the Rydberg yield with increasing pulse duration, which was qualitatively corroborated by the experimental observations in Ref. [48]. However, the mechanism that led to this relation in Ref. [49] neglected the Coulomb potential during propagation. In the following we will see that, even though we arrive at a similar law to describe the decrease of the Rydberg yield with increasing pulse duration, the Coulomb potential is vital in the explanation of pulse duration effects on Rydberg states and that the underlying mechanism cannot be captured in a model with Coulomb-free propagation. It will thus become clear that the mechanism for the pulse duration dependence identified here is fundamentally different from the one suggested in [49].

Moreover, it will be found that the pulse duration changes the distribution of the principal quantum numbers of Rydberg states. So far, the principal quantum number populations are generally believed to be determined primarily by the field strength and wavelength, shifting to higher values for larger intensities and longer wavelengths of the laser pulse [176, 177, 185, 186]. Here, in contrast, it will be shown that the pulse duration offers an independent control knob, which allows to increase the relative occupation of low quantum number states without affecting other properties of the pulse. Understanding and controlling the principal quantum numbers is relevant as this quantity is crucial in characterizing excited neutral atoms, e.g. in terms of their lifetime before decaying into metastable states [48]. In the past decade, the distribution of principal quantum numbers has helped understand the stability of excited states under the influence of a second laser pulse [170, 171], ionization channels and their closings [184, 187] as well as the effect of spatial gradients in the laser field [188].

Most recently, a new source of coherent extreme-ultraviolet light emission was demonstrated [189] based on Rydberg states created by FTI. In this radiation scheme, atoms are coherently excited into a Rydberg state  $\Psi_R$  by the interaction with the incoming laser field. There can then be a spatial overlap of this excited state  $\Psi_R(\mathbf{r})$  with the ground state  $\Psi_0(\mathbf{r})$  and this superposition state can emit coherent extreme ultraviolet (XUV) light. One may interpret the radiation as due to the beating of the Rydberg state  $\Psi_R$  and the ground state  $\Psi_0$  (for an illustration of the mechanism, see Fig. 1a in [189]). This novel technique is expected to find applications in imaging with nanometer resolution, next-generation lithography for high precision circuit manufacturing, and ultrafast spectroscopy [190]. Interestingly, this new XUV light source relies on Rydberg states that occupy low principal quantum numbers [189]. Therefore, the insights gained about the control of the quantum number distribution via the pulse duration should prove helpful in tuning the XUV radiation scheme. Even though an adapted strong field approximation (SFA) model was developed and successfully applied to explain certain features of the mentioned XUV radiation [191], this description can-



not capture the Coulomb-dependent pulse duration effect presented here. Employing CTMC simulations, which fully include the Coulomb potential during propagation, the importance of using short pulses for the newly developed XUV scheme is revealed by showing that the excited states of small principal quantum numbers, which contribute significantly to that radiation scheme, cease to be a Rydberg state first when the pulse duration is increased.

More generally and beyond the specific application to the XUV radiation scheme, the mechanism that is identified to explain both the depletion of small quantum numbers and the overall reduction of the Rydberg yield with longer pulses will teach us more about fundamental post-ionization dynamics: We will see a counter-intuitive effect at work, with deeply bound Rydberg states being less likely to survive longer pulses than loosely bound Rydberg states due to the electron's interaction with the Coulomb potential.

### 4.3.1 A primer on principal quantum numbers of Rydberg states

In this section, the way principal quantum numbers of Rydberg states have been commonly dealt with so far is explained in a brief summary. The basic idea behind introducing principal numbers of Rydberg states is Bohr's model. Since the Rydberg electron's motion can be well described by a classical Kepler orbit around the parent ion after the laser pulse has passed, one can assign a principal quantum number to that Rydberg state in the following way [49, 179],

$$\text{Energy} = -\frac{0.5}{n^2} \quad (4.34)$$

where the factor of 0.5 is the Rydberg constant in atomic units. In addition, invoking the Virial theorem gives the following relations for the time-averaged kinetic energy  $\langle T \rangle$  and potential energy  $\langle U \rangle$  for the motion in a Coulomb potential

$$\begin{aligned} \langle T \rangle &= -\frac{1}{2} \langle U \rangle \\ \Rightarrow \langle T \rangle + \langle U \rangle &= \frac{1}{2} \langle U \rangle = -\frac{0.5}{\langle r \rangle} = -\frac{0.5}{n^2} \\ \Rightarrow n &= \sqrt{\langle r \rangle}, \end{aligned} \quad (4.35)$$

where for the last equality in the second line the total average energy  $\langle T \rangle + \langle U \rangle$  was set equal to eq. (4.34). Assuming that the average position  $\langle r \rangle$  can be approximated by the quiver amplitude  $E_0/\omega^2$  of the electron in the laser field the most probable principal quantum number is estimated to be

$$n \approx \frac{\sqrt{E_0}}{\omega}, \quad (4.36)$$

which is found in [49, 176].

### 4.3.2 Simulation results for the principal quantum number distribution

The relation given in eq. (4.36) states that the principal quantum number of Rydberg states increases with laser intensity and wavelength, which is in line with prior results

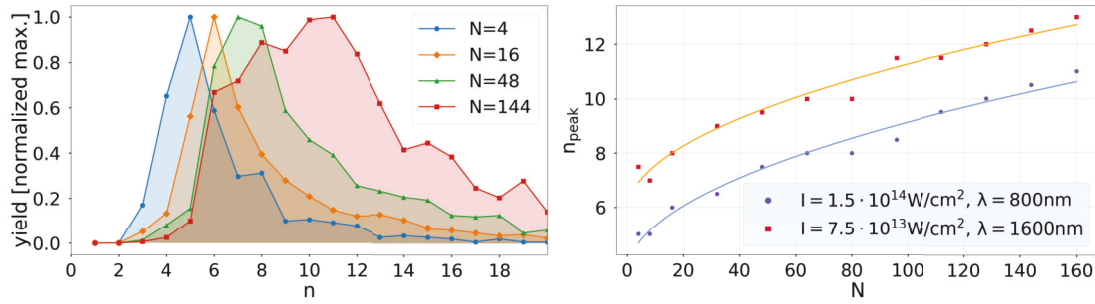


**Figure 4.6:** Left panel: Distribution of principal quantum numbers for various pulse durations specified by the number of cycles  $N$  in the legend. The maximal yield of each distribution is normalized to 1. The result was obtained for ionization of hydrogen at a laser intensity of  $I = 1.5 \cdot 10^{14} \text{ W/cm}^2$  and a central wavelength of  $\lambda = 800 \text{ nm}$ . Right panel: Position of the peak in the distribution of the principal quantum number vs. pulse duration for ionization of hydrogen at two different laser parameters that are specified in the legend. The lines represent fits according to eq. (4.42).

[48, 176, 177, 185, 186]. However, no dependence on the pulse duration is mentioned. As can be seen in Fig. 4.6, though, CTMC simulations reveal that the distribution of principal quantum numbers also depends on the pulse duration. These results make clear that the quantum number distribution in general and its peak in particular shift to larger  $n$  for longer pulse durations. The fit to the peak position presented in the right panel of Fig. 4.6 shows that the growth of the peak position of the principal quantum number distribution can be well described by a function that scales like  $\sqrt{N}$ , where  $N$  is the total number of cycles in the laser pulse.

### 4.3.3 Physical interpretation of the pulse duration effect

Before trying to understand the reason for that particular scaling, we want to obtain a qualitative and intuitive understanding for the growth of  $n$  with increasing pulse duration. To this end, we look at Fig. 4.7 showing the dependence of the final energy on the ionization time  $t_0$  and initial transverse velocity  $v_{\perp,0}$  at the tunnel exit, where the final energy was converted into the principal quantum number  $n$  according to eq. (4.34). The Rydberg area, the area in the plane of initial conditions  $(t_0, v_{\perp,0})$  that corresponds to electron capture into a Rydberg state, is crescent-shaped, in accordance with the findings presented in section 4.2 (see e.g. Fig. 4.1). At the inner edge of the crescent, we find those initial conditions that lead to Rydberg states of small principal quantum numbers, with  $n$  increasing towards the outer edge of the crescent. This makes sense as the earlier and thus farther away from the field maximum the electron is born, the more it is accelerated by the laser field<sup>4</sup>. Consequently, at the outer edge of the crescent we find electrons with a relatively large kinetic energy due to acceleration in the laser field and/or due to a large initial transverse velocity. Thus, the total energy is higher (less negative) here, corresponding to larger principal quantum numbers.

More importantly, Fig. 4.7 reveals that the position of the quantum numbers in the crescent does not change significantly with pulse duration, but that for increas-

<sup>4</sup>This can be seen, for example, from eq. (2.7), where, for a quick estimate, we can approximate  $A(t_0) \approx -E_0/\omega \sin(\omega t_0) \approx -E_0 t_0$ . Assuming  $v_x(t_0) \approx 0$ , the longitudinal momentum at the detector is  $v_x(t_f) \approx -A(t_0) \approx E_0 t_0$ .



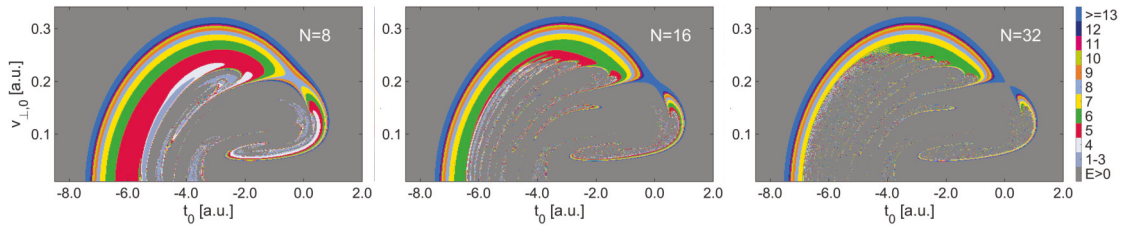


**Figure 4.7:** Map of the principal quantum number  $n$  depending on the ionization time  $t_0$  and the initial transverse velocity  $v_{\perp,0}$ . Initial conditions which do not end up in a Rydberg state (positive total energy,  $E > 0$ ) are marked in gray. The pulse duration is given by the number of cycles  $N$ . The increasing pulse duration leads to the crescent-shaped Rydberg area waning from the inside.

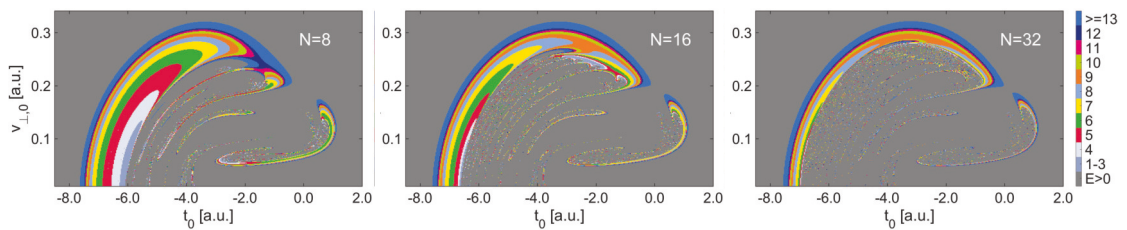


**Figure 4.8:** Same as Fig. 4.7, except for the constant envelope of the pulse used here. Even though there are minor differences to Fig. 4.7, the basic features persist. This reveals that the total time the electron spends in the laser field, rather than the different shapes of the envelope that different pulse durations imply, is responsible for the ‘waning of the moon’ with increasing pulse duration.

ing pulse duration the inner part of the crescent no longer comprises a Rydberg state. With increasing pulse duration, the small principal quantum numbers thus cease to be part of the Rydberg area, which matches our observation made in Fig. 4.6 about the principal quantum number distribution shifting to larger values for longer pulses. Moreover, the smaller overall size of the Rydberg area for longer pulses is in agreement with previous findings on Rydberg yield exhibiting a decline for increasing pulse durations [48, 49, 192]. Nevertheless, we will see shortly that the underlying mechanism we identify is different from the one that has explained this effect so far [49].

#### 4.3.4 Testing the effect of the envelope shape

To conclusively establish whether the loss of Rydberg electrons for longer pulses is caused by the longer time the electron spends in the laser field or by the different shapes of the envelope that the different pulse durations imply, additional simulations are performed. Replacing the  $\cos^2$ -term in eq. (2.4) by a heaviside step function in the interval  $[-N/2, N/2] \cdot 2\pi/\omega$ , we get almost the same crescents as the ones obtained using the full envelope (compare Figs. 4.7 and 4.8), with significant discrepancies only for very small pulse durations in the regime of  $N \leq 4$ . This shows that the reason for the loss of low quantum number Rydberg states with longer pulse durations is the long time the electrons spend in the laser field rather than a particular envelope shape.

### 4.3.5 Analysis of trajectories

Even though the plots of the Rydberg areas in Figs. 4.7 and 4.8 gave us some idea of the effect the pulse duration has on Rydberg states, it did not tell us *why* these effects are observed. To address this question, a closer look at trajectories with initial conditions around the inner edge of the crescent is enlightening. Fig. 4.9 shows such exemplary trajectories from around the inner edge of the crescent for two different pulse durations – one that still allows the electron to end up in a Rydberg state ( $N = 16$ ) and one that doesn't do so any more ( $N = 17$ ). A constant envelope is used since it simplifies the following considerations without a loss of generality, as just discussed. In the central panel of Fig. 4.9, we can see that during the first optical cycles the electron is – on cycle average – driven away from the residual ion and comes closer to it later on, approximately following a parabola-like curve.

How can we understand that the electron is – on cycle average – moving along a parabola-like curve? Loosely speaking, this is due to two competing effects: On the one hand, the laser field drives the electron away from the parent ion and, on the other hand, the Coulomb force of the residual ion has an attractive effect on the electron. For a deeper understanding, let us look at the bottom panel of Fig. 4.9, from which it becomes clear that the oscillation of the electron's position around a parabola-like curve is directly linked to the approximately linear function with positive slope that the velocity  $v_x(t)$  follows on cycle average. As we will see, the positive slope of this linear function is entirely due to the pull of the Coulomb potential in the direction of the residual ion. If the electron were driven merely by the laser field and were not influenced by the Coulomb potential, then the velocity of the electron would be given by

$$v_x(t) = -\frac{E_0}{\omega}(\sin(\omega t) - \sin(\omega t_0)) \quad (4.37)$$

for a constant envelope<sup>5</sup>. This function oscillates around the mean value of  $E_0/\omega \sin(\omega t_0)$ , which can be approximated by  $E_0 t_0$  and is thus negative for ionization times before the peak of the optical cycle, which is the time regime in which Rydberg electrons are typically born (the negative ionization time of Rydberg states can also be seen from Figs. 4.7 and 4.8). This negative offset in the velocity, when only considering the laser field and neglecting the Coulomb potential, explains why the electron is initially – on cycle average – slightly driven away from the residual ion (see center panel of Fig. 4.9). Now, as one can see in the central panel of Fig. 4.9, even though the change of the 'mean' position – the position of the electron in the  $x$ -direction that the electron oscillates around (green line) – is vital in the understanding of the electron's return, it changes rather slowly. Consequently, as the Coulomb force merely depends on the electron's position, the Coulomb force averaged over one optical cycle also does not change quickly and can be considered almost constant. A constant force, which is proportional to a constant acceleration, then leads to a linearly changing velocity, which agrees with what we observe numerically. The slope of this linear function is positive since the Coulomb potential exerts an attractive force on the electron. The linearly scaling velocity, in turn, leads to the cycle-averaged elongation following an approximate parabola, which tallies with the numerically obtained result (see central

<sup>5</sup>This equation differs from eq. 4.16 in the sign of the prefactor because here we use a CEP of 0, whereas for eq. 4.16 a CEP of  $\pi$  was used, which is explained in Appendix A.4.

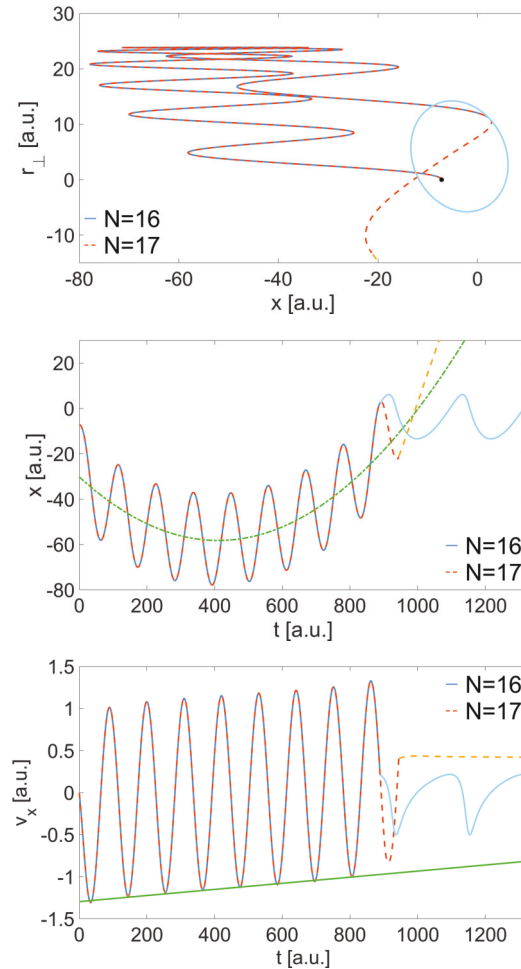


**Figure 4.9:** Data for trajectories released at  $t_0 = -6.4$  with  $v_{\perp,0} = 0.09$  from a hydrogen atom and propagated in a laser field with  $I = 1.5 \cdot 10^{14}$  W/cm<sup>2</sup> and  $\lambda = 800$  nm that has a constant envelope with a total number of cycles  $N = 16$  and  $N = 17$ , respectively. The fact that the electron experiences only about half of the respective numbers of optical cycles is due to the electron being born in the central cycle. Top panel: Coordinates  $x$  and  $r_{\perp} = \sqrt{y^2 + z^2}$ . Central and bottom panel: Position  $x$  and velocity  $v_x$  along the polarization axis as a function of propagation time, respectively. After the pulse is over, the respective trajectory is displayed in a lighter shade (i.e. orange and light-blue) of the color it had while the pulse was still on (i.e. red and dark blue).

and bottom panel of Fig. 4.9). At this point, one may be wondering why considering the cycle-averaged trajectory should be sufficient. Concerning that question, the reader is referred to Refs. [193, 194], which provide a detailed elaboration on the power of cycle-averaged descriptions of post-ionization dynamics, in particular in the context of including Coulomb effects during propagation.

The observation that the averaged position approximately follows a parabola now helps us explain why certain initial conditions lead to a Rydberg state for a short pulse but not for a longer one: If a critical number of optical cycles ( $N = 16$  in Fig. 4.9) is exceeded, the electron comes back so close to the ion that it ‘recollides’ gaining a lot of kinetic energy and therefore does not end up in a Rydberg state. In the return process, the cycle-averaged motion described approximately by the parabola is more relevant than the amplitude of the oscillation which strongly depends on the envelope. Thus,

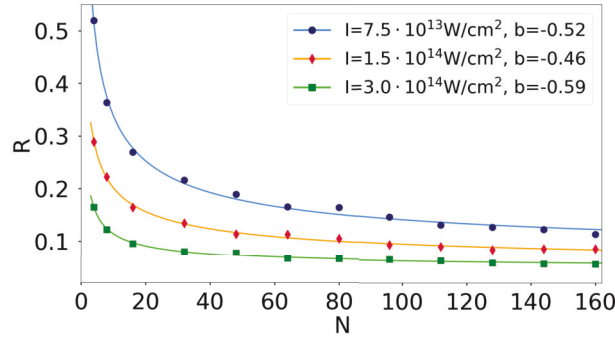


**Figure 4.10:** The dots represent the Rydberg yield  $R$  numerically obtained in CTMC simulations as a function of the pulse duration, encoded in the number of cycles  $N$ , for ionization from a hydrogen atom in a laser field as defined by eq. (2.4) at a central wavelength of  $\lambda = 800$  nm for three different intensities that are specified in the legend. The solid lines represent the fit results using the function given in eq. (4.38), where the crucial fitting parameter  $b$  is given in the legend.

we can now understand why we found in section 4.3.4 that the time the electron spends in the laser field is the relevant parameter rather than the different shapes of the envelope.

### 4.3.6 Dependence of the Rydberg yield on pulse duration

The described effect of the electron being ‘scattered out’ for too long pulses and the consequently shrinking Rydberg area leads to the Rydberg yield decreasing with increasing pulse duration. In order to give a more quantitative description, CTMC simulations are performed for various intensities and the Rydberg yield  $R$ , defined as the number  $N^*$  of electrons that end up in a Rydberg state divided by the number  $N_t$  of all electrons that tunneled out of the atom, is plotted as a function of pulse duration in Fig. 4.10. The Rydberg yield as a function of the pulse duration,  $\tau_L = 2\tau$ , which is encoded in the number of cycles  $N$ , is fitted by

$$R(N) = a \cdot N^b + c \quad (4.38)$$

with fitting parameters  $a$ ,  $b$ , and  $c$ . In all cases,  $b \approx -0.5$  is found, corresponding to  $R \propto \tau_L^{-0.5}$ .

To better understand this finding, we assume that the crescent-shaped Rydberg area in the central cycle of the pulse is proportional to the number of Rydberg states (just as in section 4.2 and in Ref. [49]). As also shown in section 4.2, the size of the crescent-shaped Rydberg area can be assumed to be proportional to the boundaries of the area in the  $t_0$  direction (see eq. (4.3) and Fig. 4.2):

$$R \propto (t_{0,max} - t_{0,min}), \quad (4.39)$$

where  $t_{0,min}$  is the earliest ionization time that leads to a Rydberg state and that can safely be assumed to be independent of the pulse duration (see e.g. Fig. 4.7).  $t_{0,max}$  defines the pulse duration dependent maximal initial time that leads to a Rydberg state.

When the pulse duration reaches its critical length, the total area under the  $v_x$  curve, which corresponds to the position of the electron, becomes approximately zero (see central and bottom panel in Fig. 4.9). This entails that the electron gets into the

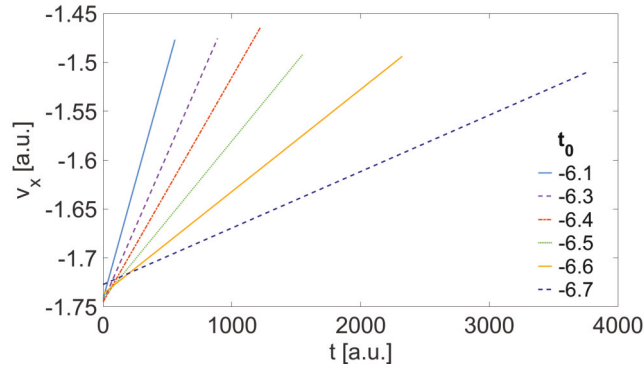


**Figure 4.11:** Linear fit to the minima of  $v_x$  (see e.g. the bottom panel of Fig. 4.9) obtained for ionization from hydrogen at a laser intensity of  $I = 3.0 \cdot 10^{14}$  W/cm<sup>2</sup>, a central wavelength of  $\lambda = 800$  nm, and an initial transverse velocity  $v_{\perp,0} = 0.15$  a.u. for different ionization times  $t_0$ . The pulse duration differs in each case and is chosen in a way that one optical cycle more would cause a strong Coulomb interaction that would accelerate the electron such that it would not be captured in a Rydberg state.

immediate vicinity of the residual ion and is strongly accelerated, gaining enough energy in the scattering process to leave the atom for good. In Fig. 4.11, linear fits to the minima of  $v_x$  (in analogy to the green line in the bottom panel of Fig. 4.9) are shown for different ionization times in the central cycle at a fixed intensity, wavelength, and initial transverse velocity. The parameter that is varied is the pulse duration, which is chosen in each case as the maximal pulse duration,  $N_{max}$ , that will still lead to a Rydberg state, meaning one additional optical cycle would bring the electron so close to the ion that the Coulomb potential would strongly accelerate the electron such that it would not be captured in a Rydberg state. From Fig. 4.11 we can see that the different ionization times mainly affect the slope of these lines<sup>6</sup> but both the offset and the range of  $v_x$ ,  $\Delta v_x$ , are almost constant with variations below 1% for the offset and below 15% for  $\Delta v_x$  from the respective mean value. Therefore, the following approximation is done

$$\Delta v_x \approx \text{const} = d(t_{0,max}) \cdot N_{max}(t_{0,max}), \quad (4.40)$$

where  $d$  is the slope of  $v_x$ . Furthermore, we find numerically for the dependence of  $t_{0,max}$  on the slope  $d$  that we can fit it nicely to a function

$$t_{0,max} = p \cdot d^\beta + q \quad (4.41)$$

with fitting parameters  $p$ ,  $q$ , and  $\beta$  (Fig. 4.12). In particular, we find similar values for  $\beta$  for the different laser parameter sets shown in Fig. 4.12 (which are the same laser parameters as in Fig. 4.10 that we try to understand):  $\beta \approx 0.6$ .

How can we understand this result? As has already been discussed in the context of the explanation of the approximately parabola-shaped elongation, the electron is, on cycle average, exposed to an approximately constant force that pulls it closer to

<sup>6</sup>Note that the different slopes of the linear cycle-averaged velocity curve correspond to different curvature radii of the parabola-like function the position is oscillating around. A steeper velocity slope corresponds to a smaller curvature radius of the parabola-like position curve and thus means the electron returns to the parent ion in fewer optical cycles. Also see Fig. 4.13, from which the relation between ionization time, parabola curvature and the maximal pulse duration that still leads to a Rydberg state becomes clear.



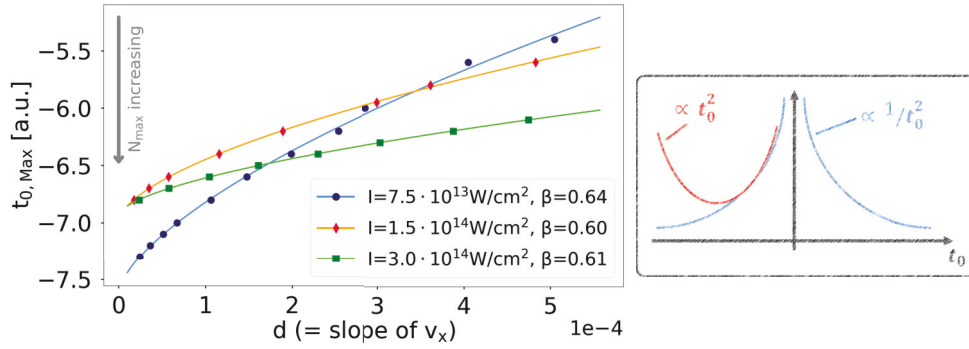


**Figure 4.12:** Left panel: The markers represent slopes of the linear fits to the minima of  $v_x$  (see e.g. Fig. 4.11) versus the maximal ionization times that still lead to the electron ending up in a Rydberg state for different intensities specified in the legend. A laser with a central wavelength of  $\lambda = 800$  nm was used for ionization of hydrogen, and the trajectories were started at an initial transverse velocity of  $v_{\perp,0} = 0.15$ . Note that, as in Fig. 4.11, the maximal pulse durations  $N_{max}$  that still lead to a Rydberg state were chosen for each point separately and thus vary in the plot.  $N_{max}$  grows as  $t_{0,Max}$  becomes more negative, as indicated by the arrow. The solid lines represent the corresponding fit of eq. (4.41) to the data, with the crucial fitting parameter  $\beta$  given in the legend. Right panel: Sketch showing how one can understand that a  $1/t_0^2$  scaling can locally be approximated by a  $t_0^2$  scaling.

the ion. This Coulomb force is represented as the slope  $d$  in eq. (4.40) and it obviously depends on how far the electron is away from the ion on average. The drift momentum imposed by the laser field is  $E_0/\omega \cdot \sin(\omega t_0) \approx E_0 t_0$  and can be used as a quantifier for how far away from the residual ion the electron is pushed on cycle average. So, the Coulomb force, which scales as  $-1/r^2$  with distance  $r$ , can be assumed to scale as  $-1/t_0^2$  with the ionization time, meaning  $d \propto 1/t_0^2$ . This seems to contradict our finding of  $d \propto t_{0,max}^{1/0.6} \approx t_{0,max}^2$  from the fit at first glance. However, as one can understand by the sketch in the right panel of Fig. 4.12, the approximate  $1/t_0^2$  drop of the Coulomb force can be further approximated around the typical values of  $t_0$ , i.e. slightly negative values, by a function that scales like a parabola  $t_0^2$ .

Thus, we have seen that in order to quantify how the Rydberg yield decreases with increasing pulse duration it is sufficient to quantify how fast the inner edge of the Rydberg area, i.e. the maximal ionization time that still leads to a Rydberg state, is shifted further away from the field maximum. We have learned that ionization closer to the field maximum leads to a steeper slope in the cycle-averaged linear velocity curve, corresponding to a smaller curvature radius the position is oscillating around and resulting in a return to the parent ion after fewer optical cycles. This was understood by ionization times further away from the field maximum leading to a larger drift by the laser field and hence the Coulomb force pulling the electron back more slowly.

### 4.3.7 Comparison to other models

Even though the scaling of  $R \propto \tau_L^{-1/2}$  is not dramatically different from prior results [48, 49], which gave a  $\tau_L^{-2/3}$  dependence, it offers a completely different explanation for the underlying mechanism. Prior treatments neglected the Coulomb potential, which was viewed as a higher-order correction, during propagation [49, 180]. Only after the pulse

was over, the Coulomb potential was accounted for by including it when checking if the total energy was negative [49]<sup>7</sup>. Our analysis, however, shows that including the Coulomb potential during propagation is vital in explaining that for sufficiently long pulses the electron is driven back to the parent ion, which leads to ionization. Without the Coulomb potential, the electron that can potentially form a Rydberg state (and is therefore born before the peak of the laser field) would be, on cycle average, monotonically driven away from the residual ion. Consequently, the electron would never, on cycle average, slowly move back to the ion and strongly interact with its Coulomb potential when a critical pulse duration is exceeded. Yet even sophisticated models like the modified SFA [191] that explains many features of the mentioned newly developed XUV radiation scheme [189] do not include the Coulomb effect during propagation and thus do not take this effect of ‘ionization through scattering’ into account and, as a consequence, cannot capture the pulse duration effects described here.

Furthermore, the analysis in Ref. [49] builds on the assumption that the ‘outer edge’ of the Rydberg area, corresponding to minimal ionization times and maximal transverse velocities, is affected by the pulse duration and the Rydberg area ‘shrinks from the outside’. The outer edge of the Rydberg area defines the limit  $E = 0$  when checking if the total energy  $E$  is negative according to eq. (4.1). Therefore, focusing on  $E = 0$  seems intuitively reasonable as close to this limit we find the most loosely bound Rydberg states, which one would intuitively (if wrongly) expect to be least stable and to survive only short pulses. In section 4.2, we have successfully applied this criterion of  $E = 0$  in the intensity dependence study. The pulse duration, in contrast, barely affects this outer edge of the Rydberg area but makes the Rydberg crescent wane from the inner edge, as we have seen above, e.g. in Fig. 4.7. Thus, the deeply bound Rydberg states found at the inner edge only survive short pulses, whereas the loosely bound Rydberg states close to the outer edge (corresponding to  $E = 0$ ) stay bound even for longer pulses. This counter-intuitive effect of loosely bound Rydberg states being more stable against pulse duration changes can only be explained in a model that includes the above-described effect of the electron returning to the parent ion and being accelerated in a scattering process. All of this highlights the importance of including the Coulomb effect when studying the pulse duration dependence of Rydberg states, which is further backed by the study by Dubois et al. that was published most recently in [195] (sec. IV. therein).

#### 4.3.8 Dependence of the principal quantum number distribution on pulse duration

The observation that the inner edge of the crescent scatters out first when the pulse duration increases is also crucial for understanding the effect of the pulse duration on the principal quantum number distribution (Fig. 4.6). The Rydberg states that are found at this inner edge have a more negative energy, corresponding to smaller quantum numbers. The fact that these smaller principal quantum numbers cease to be a Rydberg state first when the pulse duration increases is in agreement with the principal quantum number distribution shifting to larger  $n$  for longer pulses (see Fig. 4.6). To understand why the pulse duration affects small and large quantum numbers differently, it is instructive to look at two trajectories for the same initial transverse velocity but dif-

<sup>7</sup>Even though in Ref. [49] the Coulomb potential was accounted for in a perturbative manner, the effect cancels out in this description, as was explained in section 4.2.1.



ferent ionization times, where the smaller principal quantum number corresponds to an ionization time that is closer to the field maximum ( $t_0 = 0$ ), being found at the inner edge of the crescent. Fig. 4.13 shows such a comparison and we can see that being born closer to  $t_0 = 0$ , the electron moves along a smaller parabola-shaped curve. This is mainly due to the smaller vector potential of the laser field closer to the field maximum. Therefore, the acceleration by the laser field driving the electron away from the ion is weaker and the Coulomb potential pulls the electron back faster. Consequently, the critical number of optical cycles for which the electron recollides with the parent ion and ceases to be a Rydberg state is smaller for initial conditions corresponding to smaller principal quantum numbers.

To make these findings more quantitative, we look again at the right panel of Fig. 4.6. As indicated by the lines in this plot, we find that the principal quantum number  $n$  peaks at values  $n_{peak}$  that can be fitted by the following function

$$n_{peak} = A + B\sqrt{N} \quad (4.42)$$

with fitting parameters  $A$  and  $B$ . We can understand that the increase can be described by such a  $\sqrt{N}$ -scaling by looking at the parabola that  $x$  oscillates around (e.g. in Fig. 4.9 or 4.13). As mentioned before, we expect  $n \approx \sqrt{\langle r \rangle}$  (see eq. (4.35)). Similarly to section 4.3.6, we are again interested in  $N_{max}$ , the maximal number of cycles in the pulse that still leads to a Rydberg state (e.g.  $N_{max} = 16$  in Fig. 4.9) since it is directly linked to the zero-crossing of the parabola and its value depends strongly on the initial conditions ( $t_0, v_{\perp,0}$ ). We find that  $N_{max}$  depends linearly on the extreme value of the parabola, which we call  $x_{max}$ . This relation will be explained in the next paragraph, but now let us first look at the consequence: Since  $x_{max}$  depends linearly on  $N_{max}$ , also the mean elongation  $\langle x \rangle$  of the parabola depends approximately linearly on  $N_{max}$ , hence  $\langle x \rangle$  depends linearly on  $N_{max}$ . Also the motion transverse to the polarization axis happens along a parabola and an analogous line of reasoning can be applied here and we find that  $\langle r_{\perp} \rangle$  depends linearly on  $N_{max}$ . Therefore, we obtain  $n \approx \sqrt{\langle r \rangle} \approx \sqrt{\langle x \rangle^2 + \langle r_{\perp} \rangle^2}$ , which then depends linearly on  $\sqrt{N_{max}}$ . As the maximal number of cycles  $N_{max}$  defines the inner edge of the crescent and also the most likely  $n$  value, we can replace  $N_{max}$  by  $N$  and obtain eq. (4.42).

Now, back to the question of how we can understand that numerically it is found that the maximal number of optical cycles  $N_{max}$  that the pulse can have for a specific initial condition so that the electron still ends up in a Rydberg state depends linearly on the maximal elongation  $x_{max}$  of the parabola that we fit to the  $x(t)$  curve. Let us assume that the approximate parabola which  $x$  oscillates around returns to  $x = 0$  after propagation for about  $N_{max}/2$  cycles, which should become clear from Fig. 4.13 and from the fact that for  $x$  close to zero the recollision is increasingly likely<sup>8</sup>. In Fig. 4.13 we see that the maximal value  $x_{max}$  is found after a propagation time of about  $N_{max}/4$ . If we define the parabola fit function as  $x_{fit}(t) = d \cdot (e - t)^2 + f$  with fitting parameters  $d$ ,  $e$ , and  $f$ , then we realize that  $e \approx N_{max}/4$  and  $f \approx x_{max}$ . So, mathematically the question is why we find approximately that  $e$  depends linearly on  $f$ . As we can see in Fig. 4.13, the parabolas for different  $t_0$  are noticeably similar directly after ionization. In terms of the parabolic fit function, we can therefore write

$$\begin{aligned} x_{fit}(0) &= de^2 + f = P_1 \approx \text{const} \\ x'_{fit}(0) &= -2de = P_2 \approx \text{const} \end{aligned} \quad (4.43)$$

<sup>8</sup>Note that we assume that the electron is born in the central cycle and that thus the pulse is on only for about  $N_{max}/2$  cycles after ionization.

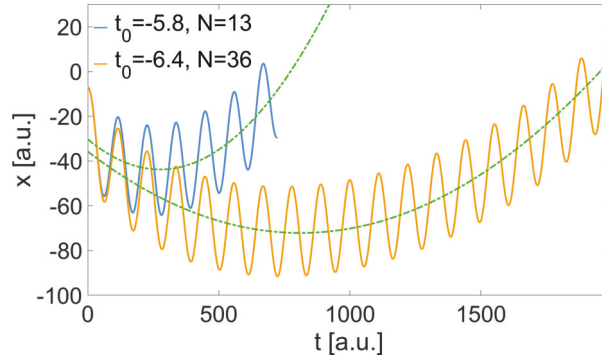


**Figure 4.13:** Position  $x$  vs. propagation time  $t$  for trajectories ionized from hydrogen in a laser field of an intensity  $I = 1.5 \cdot 10^{14} \text{ W/cm}^2$  and a central wavelength  $\lambda = 800 \text{ nm}$  with an initial transverse velocity  $v_{\perp,0} = 0.15$  for two different ionization times  $t_0$  and correspondingly two different pulse durations, which are chosen such that a pulse duration of one optical cycle more would have led to the electron not ending up in a Rydberg state anymore. The dashed lines show a parabolic fit through the value that  $x$  oscillates around.

and thus it follows

$$f = P_1 - de^2 = P_1 + P_2/2 \cdot e, \quad (4.44)$$

which means that  $f$  depends linearly on  $e$  and which tallies with our numerical observations described above.

Thus, similar to the analysis in section 4.3.6, we have used that an ionization time close to the field maximum leads to an earlier return to the parent ion. Instead of quantifying this in terms of a steeper slope of the cycle-averaged linear velocity curve as in section 4.3.6, here we used that, correspondingly, the parabola-like curve the position oscillates around has a smaller curvature radius. Focusing on the position allowed us to make a connection to the principal quantum number via  $n = \sqrt{\langle r \rangle}$ . Consequently, we could quantify approximately how an ionization time closer to the field maximum – corresponding to a smaller parabola and hence a smaller  $n$  – can only lead to a Rydberg state for shorter pulses.

### 4.3.9 Conclusion and Discussion

In summary, using CTMC simulations it was found that an increase in the pulse duration of the laser shifts the principal quantum number  $n$  of Rydberg states to larger values and that this increase scales approximately like the square root of the pulse duration. Moreover, we observed a decrease in the fraction of electrons that end up in a Rydberg state with increasing pulse duration. We could understand this general drop of the Rydberg yield by finding that the attractive Coulomb potential slowly drives the electron back to the parent ion. If the propagation is too long, the electron gets so close to the parent ion that the strong interaction causes a significant acceleration preventing the electron from forming a Rydberg state. We have seen that electrons ending up in Rydberg states of small quantum numbers return to the parent ion more quickly and are thus ‘scattered out’ already for shorter pulse durations. This explains the shift of the principal quantum number distribution to larger quantum numbers for longer pulse

durations. As the mechanism that explains these pulse duration effects stands in contrast to the mechanism found in a model that neglects the Coulomb force during the propagation in the laser field [49], the results presented here show that the Coulomb force has important consequences for the yield and quantum number distribution of Rydberg states.

The insights gained in the study of pulse duration effects allow us to not only understand but also control the distribution of principal quantum numbers, which will prove helpful in studies and applications that are based on this distribution, such as those presented in Refs. [170, 171, 184, 187–189, 196, 197]. Interestingly, the effect of the longer pulse duration ionizing Rydberg states of low principal quantum number reported in this work is similar to the effect reported in recent studies that used a second laser pulse to investigate the stability of Rydberg atoms [170, 171] since also the use of a second laser pulse leads to ionization of Rydberg states of low principal quantum numbers. Thinking in terms of control of the principal quantum number of Rydberg states the study presented in this chapter might prove helpful as modifying the pulse duration might be easier to implement than installing a second laser pulse in certain systems. One particular application for which the control of the quantum number distribution is vital is the recently developed scheme that uses radiation from Rydberg excited states created via FTI to generate coherent XUV emission [189]. As the XUV emission yield is larger if Rydberg states with low principal quantum numbers are populated, choosing a short pulse duration is vital here since we have seen that the low principal quantum number states are the ones affected most severely when the pulse duration becomes longer.

Stepping back and considering this chapter about Rydberg states as a whole, one open question seems to be why the intensity dependence in section 4.2 gave reasonable results in a model that neglected the Coulomb potential during propagation whereas in the pulse duration dependence in section 4.3 including the Coulomb potential was indispensable. The key to resolve this problem lies in the observation that the Rydberg area decreases from the ‘outside’ for increasing intensity and from the ‘inside’ for increasing pulse duration. In other words, the initial conditions that lead to Rydberg states for only small intensities or only short pulse durations have an energy that is close to zero or deeply negative, respectively. Thus, as the Rydberg states which cease to be a Rydberg state upon increasing the intensity are loosely bound anyway, the recollision mechanism is not the dominant process that leads to the decrease in Rydberg states and neglecting the Coulomb potential during propagation worked well. This stands in contrast to the deeply bound Rydberg states that cease to be a Rydberg state when the pulse duration increases because of the above-explained return to and rescattering at the parent ion.

## Emergence of a Higher Energy Structure in inhomogeneous fields

*"One sometimes finds what one is not looking for."*

—Alexander Fleming (Nobel Prize Laureate in 1945)

### Overview of this chapter

This chapter reports on the emergence of a prominent higher energy peak [73] in the spectrum of photoelectrons that were ionized from the gas phase in a laser pulse with time-varying spatial dependence as it is typically found in the vicinity of a nanostructure. The higher energy structure (HES) originates from direct electrons released in a narrow time-window and is separated from all other ionization events, with its location and width highly dependent on the strength of the spatial inhomogeneity. Hence, the HES can be used as a sensitive tool for near-field characterization in the “intermediate regime”, where the electron’s quiver amplitude is comparable to the field’s decay length. Moreover, the large accumulation of electrons with tuneable energy suggests a promising method for creating a localized source of electron pulses of attosecond duration using tabletop laser technology. In section 5.3, closed-form expressions are derived [74] to describe the movement in this “intermediate regime”, which is notoriously difficult to describe analytically. These descriptions will help us understand how the spectral position and width of the HES depends on the inhomogeneity of the field and thus how to control the parameters to obtain a spectrally narrow electron pulse of tunable energy.

In section 5.4, it will be shown that the recently reported experimental finding of a low energy peak (LEP) can be understood in the same theoretical framework as the theoretically predicted emergence of the HES. Even though the two peaks were observed in different energy regimes, and despite the LEP being detected for electrons that were released from a nanotip whereas the HES was found for electrons ionized from a gas that is placed in the vicinity of a nanotip, a single mechanism that causes the peak formation is identified. Based on this mechanism, a more general analytical model is derived to describe the energy upshift electrons experience in inhomogeneous electric fields. It will also explain the experimentally observed linear scaling of the peak energy of the LEP with the intensity of the incident laser pulse. Moreover, parameters are found at which electrons ionized directly from a nanostructure, the setting in which the LEP was found, form a prominent and narrow peak at higher energies as it was described in the framework of the HES. As ionization from the tip is experimentally better established than ionization from the gas phase near a nanostructure, this should pave the way for the experimental realization of almost monoenergetic electron beams of attosecond duration as they are predicted for the HES in the gas phase.

## 5.1 Introduction to inhomogeneous fields in the vicinity of a nanostructure

### 5.1.1 Introduction to nano-attophysics

In this chapter, we will leave the regime of ‘pure’ strong field attosecond science that focuses on lasers and atoms and include nanostructures that enhance the fields and introduce a spatial inhomogeneity. Of course, also ionizing ‘just’ atoms introduces an inhomogeneity via the Coulomb potential that cannot always be neglected, as we have seen in the previous chapter and which will also play a crucial role in chapter 6. In this chapter, however, the dominant inhomogeneity is produced by a nanostructure and thus much more extreme resulting in completely different effects.

‘Traditional’ nano-optics, i.e. using electromagnetic fields that are neither particularly strong nor short-pulsed, describes optical phenomena that arise at the nanometer scale [198]. This involves using solid state structures that are of nanometer size or at least exhibit edges and protrusions at this scale. These scales cannot be spatially resolved by typical wavelengths of several hundred nanometers, due to the diffraction limit [198]

$$\Delta x \geq \frac{1}{2\Delta k_x}. \quad (5.1)$$

Now, the clue and mathematical trick that the field of nano-optics is based on and that facilitates subwavelength resolution after all is the fact that we can increase the spread in  $k_x$  beyond  $k$  as long as we make sure that the relation

$$k = \sqrt{k_x^2 + k_y^2 + k_z^2} \quad (5.2)$$

is fulfilled. Choosing for example  $k_z$  to be imaginary, thus finding  $k_z^2 < 0$ , we can afford  $k_x > k$  and still satisfy eq. (5.2). However, having an imaginary  $k_z$  results in an exponentially decaying field  $\exp(-|k_z|z)$  in the positive  $z$ -direction, commonly referred to as an evanescent wave. In the opposite  $z$ -direction, the field would grow exponentially, which is unphysical and cannot be true. If, however, we are not in an infinitely extended space but at a surface between two different media, then the exponential decay can exist in one half-space while in the other half-space the other material and refractive index result in a different solution that does not necessarily lead to the exponential growth [198].

This principle of achieving subwavelength spatial resolution by introducing an imaginary wavevector and thus an evanescent wave has led to many powerful tools and applications in the field of nano-optics [199–206]. Prominent examples include scanning near-field optical microscopy (SNOM) [207], tip-enhanced Raman scattering (TERS) [208–210], photon scanning tunneling microscopy (PSTM) [211, 212] or total internal reflection fluorescence (TIRF) microscopy [213, 214], to mention but a few. The interest in nano-optics has certainly been boosted by the miniaturization and integration of electronic circuits for the computer industry [198] and nano-optics is therefore relevant beyond the realms of basic research with many applications in e.g. opto- or microelectronics [215–217].

Although nano-optics is a well-researched and mature field on its own, its merger with ultrafast strong fields is relatively new. This ‘marriage’ is interesting on (at least) two counts: Firstly, the local field enhancement that is found near nanostructures al-



lows the incident laser beam to have a relatively small intensity which – after enhancement – is in the typical strong field intensity regime [162]. And secondly, when the high spatial resolution of nano-optics teams up with the high temporal resolution of ultrashort pulses, the resulting system becomes a promising contender in the quest of achieving higher spatio-temporal resolution [218, 219].

Analyzing the electron dynamics in strongly enhanced, short-pulsed near-fields has allowed to characterize the near-field with subcycle resolution [220–222], which – in turn – opened up new perspectives to control electron dynamics in such near-fields and thus to create new electron sources. The extreme localization of electrons in space and time allows to use nanostructures illuminated by short pulses as femtosecond electron sources with outstanding beam qualities [223–226]. The highly coherent electron pulses from nanotips are, for example, exploited in studies of fundamental matter-wave quantum optics [226–228] or are used in exploring implementations of time-resolved point-projection microscopy (PPM), in which magnification is achieved by placing a field emission tip close to a specimen [229–231].

Speaking of coherent emission, one obvious question that arises is whether high-harmonic generation (HHG) in a system containing a nanostructure is possible and can be used as a coherent source of e.g. XUV light, which is discussed and reviewed in the following since it played an important role and shaped the field of nano-attosecond science in the past decade. At this point, it is crucial to distinguish between the two main paths that were chosen when trying to attain HHG using nanostructures:

- (i) HHG using electrons that were released from atoms or molecules in a gas that is located close to a nanostructure and therefore feels the near-field of it.
- (ii) HHG using electrons that were emitted directly from the nanotip.

Concerning mechanism (i), there was an early experiment in 2008 that claimed to have produced HHG light from argon atoms that were placed in the strongly enhanced field in between a bow-tie structure [232]. While indeed XUV radiation had been produced, the origin of the radiation remained contentious [233–235] and it is now generally believed that it was atomic line emission (ALE), rather than HHG, that was the underlying mechanism that produced the radiation [236, 237]. Even though the produced XUV light can be used in applications where spatial and temporal coherence are not essential, for example in implementations of near-field XUV lithography [236], the incoherent nature of the dominant ALE process clearly distinguishes it from a coherent HHG source. Despite many attempts to produce HHG at yields and repetition rates that are comparable to those achieved from the gas phase in homogeneous strong fields, so far this aim was not attained [238]. On the upside, though, the quest for HHG from atoms or molecules in the vicinity of a nanostructure has sparked further experimental and theoretical results along these lines [239–249], which helped develop the field of nanoattophysics.

Similarly, also the second category of attempts, (ii), which tried to produce HHG by emitting electrons directly from the nanotip, proved futile. Even though theoretical works made optimistic predictions about the feasibility of that method [250], as of yet no ‘direct HHG’ from metal tips, or any other nanostructure for that matter, has been reported [226]. The following estimate presented in Ref. [226] makes the problem with this approach to produce HHG clear: The surface of a typical nanotip consists of about  $10^3$ - $10^4$  atoms. In contrast, the number of gas atoms in the laser focus is of the order of

$10^{10}$ . Thus, on a nanostructure surface the number of potential emitters is too low to lead to a reasonable HHG yield via strong field emission and recollision.

In the midst of all of these vain attempts to generate HHG employing nanostructures, a silver lining appeared in the horizon. In 2016, the very group who set the discussion about HHG with nanostructures off with their contentious results in 2008 [232] achieved HHG radiation employing solid tips that are made of monocrystalline sapphire surrounded by a gold thin-film layer [251]. The underlying mechanism, though, is not found in either of the two categories presented above but coherent XUV light is created by means of inter- and intraband processes. This mechanism is the one that is also used to describe the HHG radiation from bulk solids and it does not involve photoemission but the radiation promotes the electron from the valence to the conduction band. Anharmonic oscillations and recombination then lead to intra- and interband radiation, respectively [27, 28, 252–257]. The main difference between HHG from bulk solids and this experiment therefore stems from the enhancement of the incident laser field at the metal-sapphire nanostructure in the latter. This enhancement was further improved upon by Vampa et al., who used a nanoantenna array of gold embedded in a layer of silicon [258]. The nanoantenna array produces localized surface plasmons and thus complements the experiment reported in Ref. [251] in which surface plasmon-polaritons enhanced the field [259]. Using localized surface plasmons has the advantage that the geometry of the nanoarray can be adapted to engineer e.g. the polarization of the harmonic beam [258].

Also, even though processes (i) and (ii) have not led to satisfactory HHG production, the theoretical studies that emerged around this discussion made clear that the strong field enhancement and field inhomogeneity near a nanostructure significantly influence the electrons' post-ionization dynamics [243, 244, 260] thus also affecting processes like double ionization [47]. Most directly, though, the effect of the nanostructure on an ionized electron can be observed by analyzing the photoelectron momentum spectrum: Shifts and suppression of peaks in the photoelectron spectrum and the extension of the rescattering cutoffs have been reported in the presence of a nanostructure [162, 218, 221, 261–264]. These effects were suggested to be used for the characterization of both the incident laser pulse, especially the carrier-envelope phase, and the near-field of the nanostructure [162, 218, 222, 263, 265].

The effect of the inhomogeneity on the photoelectron momentum spectrum will also be at the center of the discussions in this chapter. We will see how photoemission of atoms that are placed in the vicinity of a nanostructure is followed by electron dynamics that is characterized by acceleration due to the inhomogeneous field and how the resulting high-energetic electrons accumulate in a peak that we will name 'higher energy structure' (HES) [73, 74]. Moreover, we will realize that the motion of photoelectrons released directly from the tip bears great similarity to the dynamics underlying the HES and that it can be captured in the same theoretical framework.

### 5.1.2 Mathematical description of inhomogeneous fields

In the following, common theoretical models to describe the electric field in the vicinity of a nanostructure upon irradiation with a laser pulse are reviewed and discussed, thus setting the stage for the calculations that will be performed later in this chapter. Even though the nanostructures employed in nano-attophysics rarely are close to perfect spheres in free space and even though in certain cases taking into account the



exact geometry of the nanostructure matters [266–268], the electric fields near the nanostructure are often found to be well approximated by that of a sphere. Typically, the minimal radius of curvature of the nanotip's apex or of the protruding edges in more elaborate nanogeometries determines the size of the corresponding sphere in the theoretical model [198]. The electric field close to a dielectric sphere in a quasi-static approximation is a common example in undergraduate physics courses on theoretical electrodynamics [269, 270] and we will now see that this system does not only serve as a nice pedagogical tool to introduce the expansion in Legendre polynomials but that the result can help us model real-life nanosystems. For a sphere of radius  $R$  and dielectric constant  $\epsilon_s$  positioned at the origin in a medium with  $\epsilon_m = 1$ , the electric field at position  $\mathbf{r}$  reads [271, 272]

$$\mathbf{E}(\mathbf{r}) = \begin{cases} \frac{3}{\epsilon_s + 2} \mathbf{E}_i & \text{if } |\vec{r}| < R, \\ \mathbf{E}_i + \frac{3\hat{\mathbf{r}}(\hat{\mathbf{r}} \cdot \mathbf{p}) - \mathbf{p}}{|\mathbf{r}|^3} & \text{if } |\vec{r}| > R, \end{cases} \quad (5.3)$$

where  $\hat{\mathbf{r}}$  is the unit vector in space and  $\mathbf{E}_i$  denotes the spatially homogeneous incident field that is assumed to change so slowly that the system can adapt adiabatically to the change. The dipole moment  $\mathbf{p}$  is given by

$$\mathbf{p} = R^3 \frac{\epsilon_s - 1}{\epsilon_s + 2} \mathbf{E}_i. \quad (5.4)$$

As becomes clear from eq. (5.3), the electric field close to the sphere exhibits a strong spatial inhomogeneity. The maximal field strength is obtained directly at the surface of the sphere at the poles along the polarization direction of the incident field. The corresponding field enhancement is [238]

$$\left| \frac{\mathbf{E}(\mathbf{r} = R\hat{\mathbf{e}}_x)}{\mathbf{E}_i} \right| = \left| 1 + 2 \frac{\epsilon_s - 1}{\epsilon_s + 2} \right|, \quad (5.5)$$

where linear polarization in x-direction was assumed. For a gold sphere at  $\lambda = 720$  nm the dielectric constant is  $\epsilon_s = -16.41 + 1.38i$  [238] and the field enhancement amounts to 3.4, corresponding to an intensity enhancement by a factor of 11.6. Even though that may appear to be a large enhancement already, compared to other nanostructures it is considered relatively low [273] and typical enhancement factors can be one or two orders of magnitude larger [241, 267]. For a more intuitive understanding of the enhancement and inhomogeneity it is instructive to be aware of the fact that the second line of eq. (5.3) is the superposition of the incident field  $\mathbf{E}_i$  and the general expression for an electric field of a dipole with dipole moment  $\mathbf{p}$ . Here the dipole moment, as expressed by eq. (5.4), is induced by displacement of charges in the dielectric sphere by dint of the exposure to the incoming electric field. The resulting local positive charge surplus at one pole of the sphere and the concomitant local negative charge surplus at the other pole lead to the mentioned dipole.

The underlying assumption so far was that the charges follow the incident field instantaneously. However, the collective electronic response of the medium leads to a phase shift between the incident and the induced field at typically used parameters [221, 226, 274, 275]. The retardation does not only depend on the nanostructure's material but also on its geometry. As a consequence, the absolute phase profile of the resulting near-field cannot be directly determined from the incident pulse. In principle,

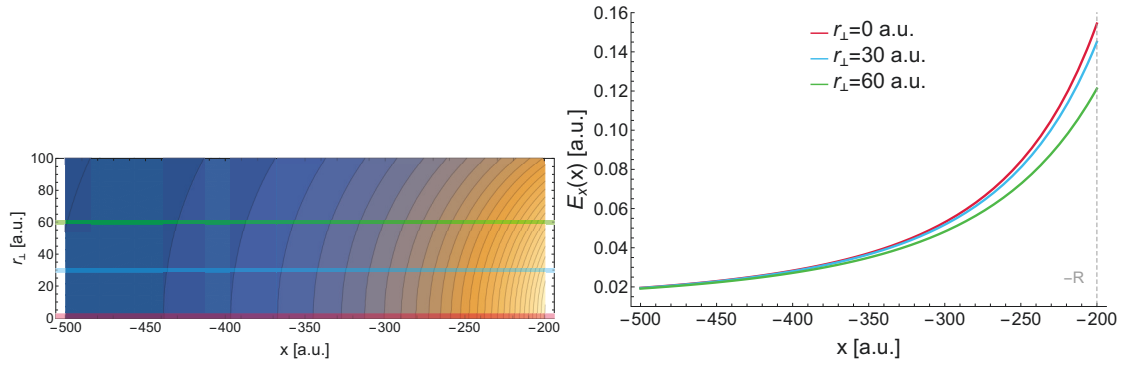


**Figure 5.1:** Electric field close to a sphere of a radius of 200 a.u. ( $= 10.6$  nm) in the polarization direction. The maximal induced field strength (at the poles,  $x = -R$ ,  $y = z = 0$ ) is  $E = 0.15$  a.u. and the incident field is  $E_i = 0.01$  a.u., corresponding to an enhancement factor of 15 (corresponding to e.g.  $\epsilon = -2.5$  in eq. (5.5)). Left panel: 2D plot with the  $x$ -axis being parallel to the polarization axis of the incident light and  $r_{\perp}$  denoting the direction perpendicular to it. One can see that the inhomogeneity is mainly found along the polarization axis of the incident light and is smaller perpendicular to it. Right panel: Three cuts through the field profile with constant  $r_{\perp}$  values that are highlighted as lines in the corresponding color in the left panel.

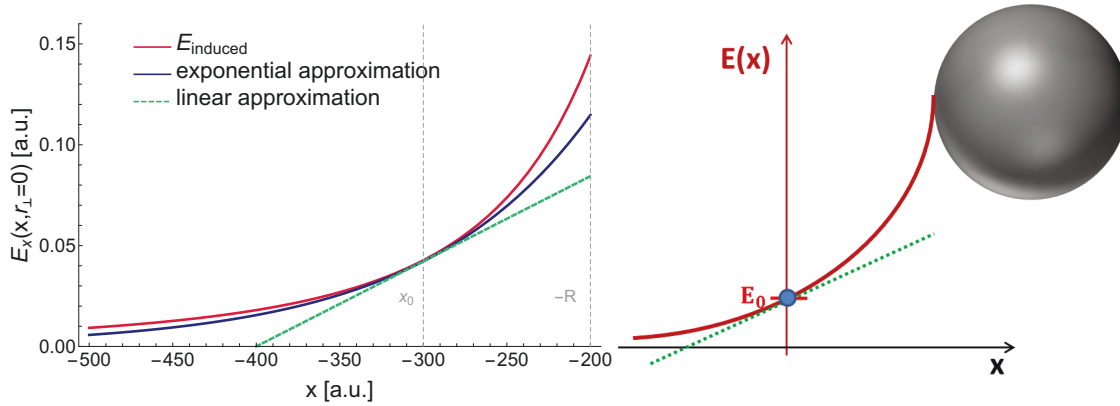


**Figure 5.2:** Left panel: Exponential and linear approximation at  $x = x_0$  to the induced part of the field presented in Fig. 5.1 (with  $r_{\perp} = 0$ ). Right panel: Sketch showing the notation presented in eq. (5.7), which is used to describe the ionization of gas atoms located at  $x = 0$  and  $E_0$  is defined as the field strength an atom is exposed to at this position.

the superposition of the incident and phase-shifted, enhanced induced field can lead to a complicated temporal pulse profile. Usually, though, the induced field dominates the resulting near-field and the resulting total field bears strong resemblance with the temporal profile of the incident field up to the mentioned phase shift, as numerical simulations show [221, 275].

As Fig. 5.1 shows, the inhomogeneity in the vicinity of a nanostructure is most pronounced along the polarization axis and is relatively small in the direction perpendicular to it. Therefore, it is common to theoretically model the movement of the ionized electron in a one-dimensional system along the polarization axis [75, 219, 222, 238, 241, 246, 248, 273, 276–281].

Furthermore, a common way to approximate the spatial decay of the induced dipole field is to use an exponential function

$$E(x) = E(0)e^{-|x|/l_f}, \quad (5.6)$$

as it is done in the example shown in the left panel of Fig. 5.2. Note that the field that is approximated here does not contain the incident field. Neglecting the ‘small offset’ of the incident field is usually a good approximation as it is significantly weaker than the enhanced field of the induced dipole, particularly in the regime where the inhomogeneity is strong and where the relevant effects that we are interested in here happen. Therefore, eq. (5.6) is often used to describe the full near-field close to a nanostructure. The scale at which the exponential function decays is determined by the constant  $l_f$ . In the example presented in Fig. 5.1 and the left panel of Fig. 5.2,  $l_f = 100$  a.u. was used. This decay length is thus in the same order of magnitude as the size of the nanostructure ( $R = 200$  a.u.) – a relation which is often used to estimate the decay length of the near-field [238].

The exponential approximation for the field close to a nanostructure is frequently applied [75, 219, 222, 273]. In some cases, however, even further approximations are used and only the linear term in the Taylor expansion of the exponential field is taken into account, thus making the equations easier to handle numerically and also analytically [238, 241, 246, 248, 276–281]. In sections 5.2 and 5.3 of this chapter, such a linear approximation will be used in the following notation:

$$E(x, t) = E_0(1 + 2\beta x)f(t) \cos(\omega t + \phi_{CEP}), \quad (5.7)$$

where  $\phi_{CEP}$  is the carrier-envelope phase (CEP) and  $f(t) = \cos^2\left(\frac{\omega t}{2N}\right)$  describes the pulse envelope, with  $N$  being the number of optical cycles in the pulse. This notation assumes a shift of the system along the  $x$ -axis as compared to the notation presented in Fig. 5.1 and the left panel of Fig. 5.2 such that now  $x = 0$  does not determine the center of the nanostructure anymore but is a point in its near-field at which we find a field strength  $E_0$ . At this point in space, atoms to be ionized are positioned and here the slope of the linear approximation matches the actual near-field drop, as is depicted in the sketch in the right panel of Fig. 5.2. This linear approximation does not only allow TDSE simulations of inhomogeneous fields with reasonable computational effort but will also open the door to an analytical description of the electron’s movement in the inhomogeneous field, as we will see in section 5.3.

The linear approximation brings about one important restriction though: If the term  $(1 + 2\beta x)$  changes sign due to sufficiently large negative values of  $x$ , the force that acts on the electron also changes its sign, which is unphysical. The parameters in this chapter ensure that this zero-crossing does not happen, mainly by choosing short pulses. One may, of course, argue that also close to the mentioned zero-crossing the linear approximation gets increasingly worse and does not reflect the actual inhomogeneity very well any more. While it is true that indeed the linear approximation becomes increasingly worse close to the sign change of  $(1 + 2\beta x)$ , the pulse envelope is usually already reduced considerably when the electron gets into that regime and the main acceleration effects due to the inhomogeneous nature of the near-field happen around the central cycle when the pulse envelope is maximal, as we will see. A more exhaustive discussion about the extent to which the linear approximation captures the effects observed in the more accurate description of the exponentially decaying field will follow in section 5.4.

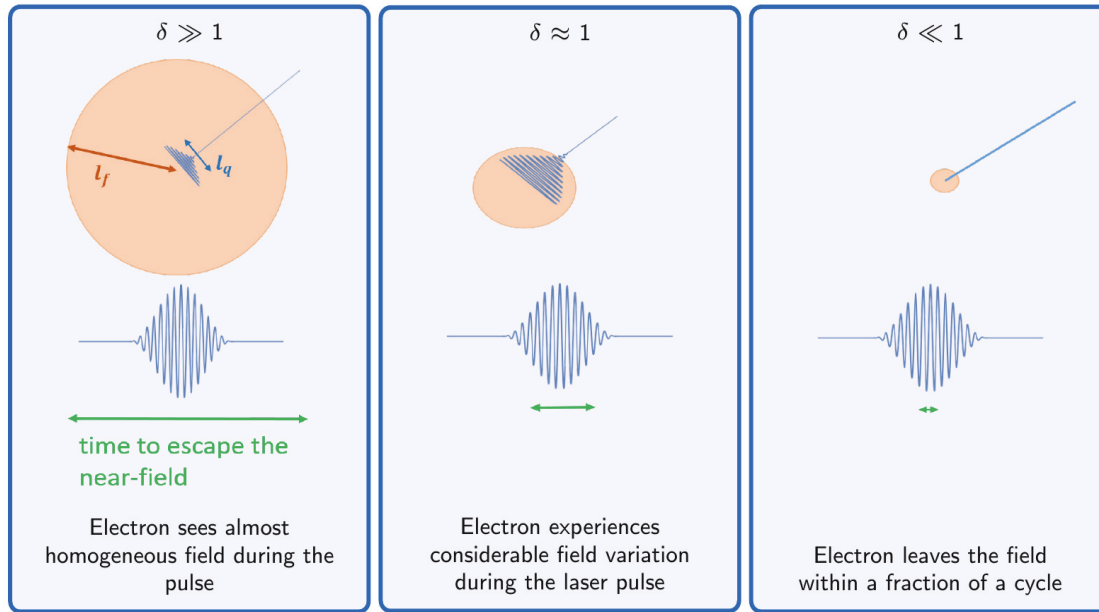


**Figure 5.3:** The different inhomogeneity regimes are defined by the different ratios of the decay length  $l_f$  of the near-field and the quiver amplitude of the electron  $l_q$ . The figure follows the ideas presented in Fig. 1 in [282].

### 5.1.3 Three different inhomogeneity regimes

When talking about electrons moving in the near-field of a nanostructure, driven by a short laser pulse, it has proven helpful to introduce the following parameter in order to quantify how much of the inhomogeneity is explored by the electron, and at what relative time scales [218]:

$$\delta = \frac{\text{decay length of the electric field}}{\text{quiver amplitude of the electron}} = \frac{l_f}{l_q} = \frac{l_f \omega^2}{E_0}. \quad (5.8)$$

Here,  $l_f$  is the decay length we became acquainted with in eq. (5.6) and the quiver amplitude is estimated by the amplitude  $E_0/\omega^2$  of an electron moving in a homogeneous field with maximal field strength  $E_0$  and angular frequency  $\omega$ .

As illustrated in Fig. 5.3, for  $\delta \gg 1$  the electron explores so little of the near-field while the pulse is on that it sees an almost homogeneous field. This is easy to describe since we can draw on the physics developed in plain strong fields without nanostructures, but at the same time we cannot expect any interesting new effects due to the spatial structure of the near-field here.

In the opposite limit of small  $\delta$ , the electron sees so much of the inhomogeneity within a fraction of an optical cycle that it leaves the inhomogeneity almost immediately. As the escape from the near-field happens on a subcycle time scale, the near-field itself can be described by a quasistatic approximation to explain the results in this regime [218, 283].

In the intermediate regime of  $\delta \approx 1$ , the decay length of the near-field is of the same order as the quiver amplitude and the electron explores a considerable part of the inhomogeneous spatial profile during multiple oscillatory cycles. According to Ref. [238] ‘the other two regimes are most desirable’ (i.e.  $\delta \ll 1$  and  $\delta \gg 1$ ) since the intermediate regime of  $\delta \approx 1$  ‘requires extensive modeling’. In this chapter, we will venture into this less understood intermediate regime and find that it is indeed a nontrivial task to

describe systems at such parameters theoretically. In particular, finding an analytical description will pose a genuine challenge. However, our efforts will be well-rewarded as we will see new effects arise in this regime.

## 5.2 Emergence of a higher energy structure

The content of this section has been published in a similar way in *Phys. Rev. Letters* 119, 053204 (2017) (see Ref. [73]). The copyright of content from said article lies with the American Physical Society.

### 5.2.1 Choosing the parameters

As already announced in the previous section, the regime in which we will work in this chapter is the intermediate  $\delta$ -regime, where the electron explores a lot of the inhomogeneity of a nanostructure's near-field while the pulse is on. According to eq. (5.8) we have three control knobs to adjust the  $\delta$  parameter.

The first parameter is the field strength and we choose it to correspond to an intensity of  $I = 1 \cdot 10^{14}$  W/cm<sup>2</sup>. Note that this intensity neither defines the maximum intensity of the incident nor the enhanced field but describes the intensity that the atom is exposed to when placed in the vicinity of the nanostructure (see the right panel of Fig. 5.2). For the time being, we will use the linear approximation of the near-field presented in eq. (5.7), meaning the atom we ionize from is defined to be found at  $x = 0$  and  $E_0$  is the field strength it experiences there. The choice of  $I = 1 \cdot 10^{14}$  W/cm<sup>2</sup> is therefore motivated by the ionization potential of atoms typically used in strong field ionization and leads to ionization in the tunneling regime, which we will be able to quantify after having set the wavelength in the next paragraph.

The wavelength  $\lambda$  is the second parameter and rather than working at the typical 800 nm produced by the ubiquitous Ti:sapphire laser, a wavelength of  $\lambda = 2 \mu\text{m}$  is chosen here. Extending the wavelengths used for strong field ionization experiments into this mid-infrared (mid-IR) regime is a relatively recent development [284–287]. The larger excursion amplitude the electron has at larger wavelengths should lead to a system in which spatial inhomogeneities due to the Coulomb potential should be particularly small. Thus, one may think, if such a mid-IR field is spatially homogeneous, it should be a perfect system for applying the strong field approximation. However, as the discovery and explanation of the low energy structure (LES) in the mid-IR range has shown, the small spatial dependence introduced by the  $1/r$  Coulomb potential can lead to surprising and clearly experimentally measurable effects at these wavelengths. This unexpected finding stimulated a great amount of experimental [55, 286, 288–290] and theoretical work [53, 55, 290–294], and highlighted the dramatic impact that even a small spatial inhomogeneity in force can have on electron dynamics after strong field ionization. In the following we will go one step further and, while still working in the mid-IR, add a significantly stronger inhomogeneity to the system by means of a nanostructure. As we will see, this leads again to another interesting feature in the photoelectron momentum spectrum. A wavelength in the mid-IR in combination with nanostructures has the advantage of enabling the electron to explore a lot of the inhomogeneity while still using nanostructures that do not need to be too small. Working in the mid-IR has the added benefit that at an intensity of  $I = 1 \cdot 10^{14}$  W/cm<sup>2</sup> we are in the tunneling regime, e.g. we have  $\gamma = 0.4$  if we ionize hydrogen. Thus, we can apply an



adiabatic ionization theory as described in chapter 2.3.2.1 and as often referred to as ADK. This makes things easier to describe analytically and, moreover, we do not need to worry about nonadiabatic effects as they were e.g. described in chapter 3 but can focus on studying effects originating from the spatial field inhomogeneity.

The third and last parameter to tune is the decay length  $l_f$  of the nanostructure. For  $\delta$  to be in the intermediate regime, we choose two different decay lengths of  $l_f = 8.8 \text{ nm} = 167 \text{ a.u.}$  and  $l_f = 13.2 \text{ nm} = 250 \text{ a.u.}$ , corresponding to  $\delta = 1.62$  and  $2.43$ , respectively. Since the decay length can be estimated to be in the same order of magnitude as the extent of the nanostructure [238], this implies the use of a nanostructure of a size as it is readily available for such experiments [162, 218, 220]. With  $\delta \propto l_f/\lambda^2$ , we can understand the advantage of using a rather long wavelength, in the mid-IR, even better now as it allows us to employ larger decay lengths and hence larger nanostructures that are fabricated more easily, while still being in the intermediate  $\delta$ -regime. As we want to apply the linear approximation given in eq. (5.7), the decay length needs to be converted to the inhomogeneity parameter  $\beta$  using  $\beta = 1/(2l_f)$ , which yields  $\beta = 0.002$  and  $\beta = 0.003$  for the above-mentioned values.

## 5.2.2 Simulations

Using the linearly approximated near-field described by eq. (5.7), TDSE simulations, run by Jose Pérez-Hernández, and CTMC simulations are performed. The number of optical cycles is chosen to be  $N = 2$  and the CEP, denoted by  $\phi_{CEP}$  in eq. (5.7), is set to  $\pi$ . Note that even though TDSE and CTMC simulations are solved in a three-dimensional framework, the one-dimensional approximation of the near-field implies that the following calculations should match experimental results best for those electrons whose direction of propagation is along the direction of the polarization of the incident electric field. Such electrons can be isolated experimentally by measuring electrons emitted within a narrow cone around the polarization axis. The 3D-TDSE is considered in the length gauge,

$$i\frac{\partial\Psi(\mathbf{r}, t)}{\partial t} = H\Psi(\mathbf{r}, t) = \left(-\frac{\nabla^2}{2} + V(r) + V_I(\mathbf{r}, t)\right)\Psi(\mathbf{r}, t), \quad (5.9)$$

and is solved following the method described in [262], where  $V(r)$  is the atomic Coulomb potential and  $V_I(\mathbf{r}, t) = -\int^{\mathbf{r}} d\mathbf{r}' \mathbf{E}(\mathbf{r}', t)$  represents the interaction with the laser field given in eq. (5.7). The single active electron approximation is applied, using the potentials given in [295] and starting from the ground-state wave function.

Figure 5.4 shows photoelectron momentum spectra for hydrogen, helium, and argon atoms obtained in the 3D-TDSE simulations just described for two different decay lengths,  $l_f = 8.8 \text{ nm}$  ( $\beta = 0.003$ ) and  $l_f = 13.2 \text{ nm}$  ( $\beta = 0.002$ ). As expected, the electron yield from helium is significantly lower than from hydrogen and argon due to a higher ionization potential. What is far more interesting here, though, is that in each case the electrons accumulate around a prominent peak, which we call Higher Energy Structure (HES) as it goes beyond two times the ponderomotive potential  $U_p$  (here:  $U_p = 37 \text{ eV}$ ), which would be the classical limit for direct electrons in homogeneous fields.

Prior theoretical work using inhomogeneous fields in the infrared regime [246, 262, 276] found a large enhancement in electron yield forming an extended high energy *tail*. This enhancement resulted in a substantial extension in the maximum cutoff energy, well above the usual  $10U_p$  cutoff for rescattered electrons [296, 297]. The HES

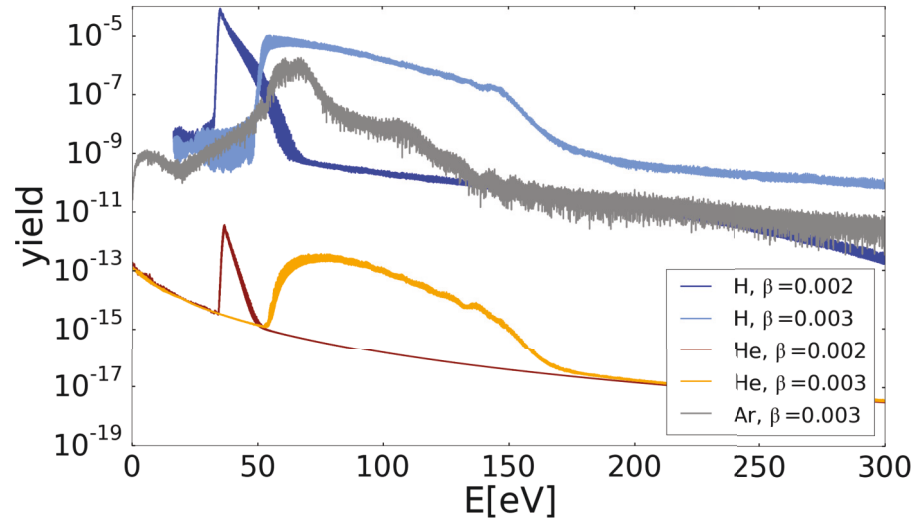


**Figure 5.4:** 3D-TDSE photoelectron spectra for hydrogen, helium, and argon atoms generated by laser pulses described in eq. (5.7) for different values of the inhomogeneity parameter  $\beta$ . The laser intensity at the atom is  $I = 1 \cdot 10^{14} \text{ W/cm}^2$  (corresponding to  $E_0 = 0.0534 \text{ a.u.}$ ), the wavelength is  $\lambda = 2 \mu\text{m}$ , the number of cycles  $N = 2$ , and the CEP is set to  $\phi_{CEP} = \pi$ .

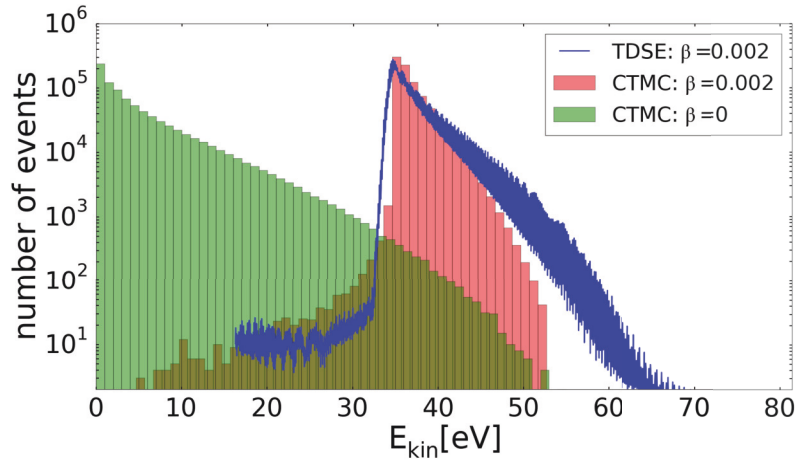
emerging here, in contrast, is found near  $2U_p$  and rather than extending a plateau it is characterized by a prominent hump. The location near  $2U_p$  also hints at the electrons comprising the HES being direct electrons [82, 298, 299], i.e. no significant interaction with the Coulomb potential of the ion has occurred and rather than returning close to the parent ion and being deflected the electrons get to the detector ‘directly’. The ‘direct’ nature of the HES electrons is also corroborated by CTMC simulations in which the Coulomb potential is turned off and which still yield the HES.

At first glance, the higher energy structure may look like a resonance. However, as becomes clear from Fig. 5.4, its location is independent of the atomic species and is mainly determined by the inhomogeneity of the near-field instead. This dependence on the inhomogeneity will be analyzed in depth in section 5.3.

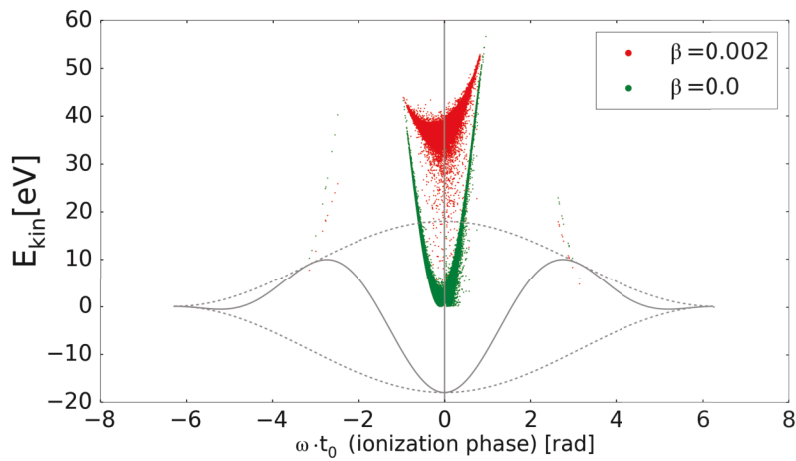
To gain a better understanding of the origin of the HES, CTMC simulations are performed as well. Single trajectories are launched at a starting phase  $\varphi_0 = \omega t_0$ , with velocity  $v_{\perp,0}$  perpendicular to the laser polarization direction. The probability distribution of these initial conditions at the tunnel exit is described by the Ammosov-Delone-Krainov (ADK) formula given in eq. (2.24), which is typically used to model strong field ionization in the tunneling limit. The tunnel exit radius is obtained using parabolic coordinates, as described by eq. (2.25). Note that the ionization step in the CTMC simulation, in which the initial conditions are determined, is the same as in a homogeneous field. In the propagation step, in contrast, the inhomogeneity of the electric field is taken account of by using the electric field of eq. (5.7) in the equation of motion given in eq. (2.30).

Figure 5.5 shows the electron yield as a function of energy resulting from such CTMC simulations. As can be seen, the prominent higher energy peak starting around 40 eV that is observed in the TDSE simulation (blue curve) is well reproduced by the CTMC result. The surprising accuracy of the adiabatic ADK approximation is due to the large wavelength of the laser light, which results in a Keldysh adiabaticity parameter of  $\gamma = 0.4$ , well within the tunnel ionization regime. The figure also includes the photo-





**Figure 5.5:** Histogram of the photoelectron yield as a function of the final kinetic energy obtained in a CTMC calculation for hydrogen with the same laser parameters as given in Fig. 5.4 for two different values of  $\beta$ , where  $\beta = 0$  corresponds to a homogeneous field. The blue line shows the photoelectron yield obtained in a 3D-TDSE calculation for the same parameters and equals the dark blue curve in Fig. 5.4.



**Figure 5.6:** Kinetic energy of photoelectrons as a function of the ionization phase from a CTMC calculation for hydrogen for the same homogeneous ( $\beta = 0$ ) and inhomogeneous ( $\beta = 0.002$ ) electric fields as used in Figs. 5.4 and 5.5. Each dot corresponds to a single trajectory. For visual guidance, the time-dependence of the homogeneous field is plotted in the background in gray in arbitrary units.

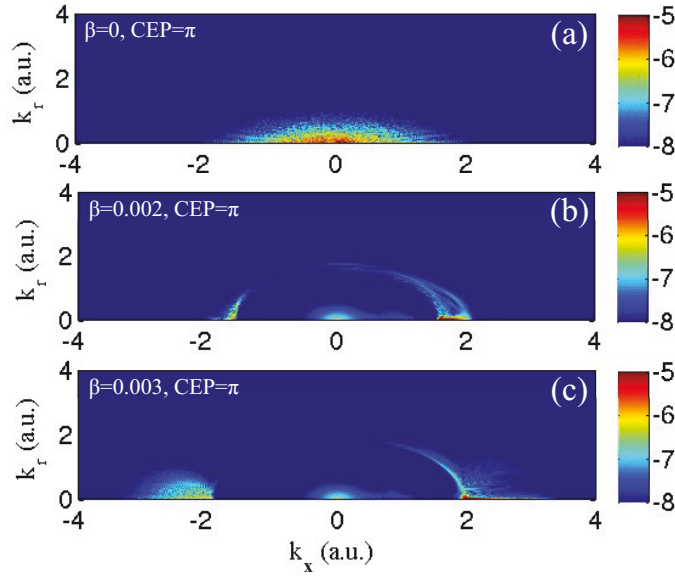
electron energy distribution in the absence of field inhomogeneity ( $\beta = 0$ ), which peaks close to zero energy. This stands in contrast to the distribution obtained with  $\beta = 0.002$ , which peaks around 40 eV. Thus, we can see how the field inhomogeneity significantly accelerates a large fraction of the electrons.

Figure 5.6 establishes the physical origin of the HES further by comparing the final electron kinetic energy as a function of ionization time,  $t_0$ , for homogeneous and inhomogeneous fields. By far the most dramatic influence of the spatial inhomogeneity occurs in the central cycle, corresponding to the maximum probability of ionization, along the direction of increasing field. As Fig. 5.6 shows, field inhomogeneity causes electrons ionized near the laser field maximum to get accelerated to over 30 eV, whereas these same electrons have much smaller energies in homogeneous fields. In fact, the electrons ionized near the peak by homogeneous fields are known to have low final energies (see also Fig. 5.5), thereby contributing to Rydberg states [180] and the zero energy structure [55, 286, 287]. This also suggests, in agreement with prior findings [242], a depletion of long trajectory contributions to high harmonic generation in inhomogeneous fields, since these trajectories are made up of electrons ionized shortly after the peak of the laser field. Importantly, in addition to accelerating, the field inhomogeneity also significantly narrows the electron energy distribution, leading to a well-defined peak observed in CTMC and TDSE simulations (see Fig. 5.5). This can be understood from Fig. 5.6, in which we can see that the inhomogeneity has a huge effect on the electrons ionized directly at the center of the pulse but a comparatively low effect on the electrons ionized before or after the central peak thus leading to an accumulation of electrons in a narrow energy regime.

Moreover, we can see that even though a few electrons are also ionized in the non-central half-cycles, they are distinctly separated in energy from the ionization events in the central half-cycle. A better understanding of this separation will be obtained in the framework of the unifying theory presented in section 5.4.

Based on the above analysis, the appearance of a HES should coincide with a depletion of low energy electrons, which get accelerated by the field inhomogeneity. This depletion can be clearly observed in Fig. 5.7, which shows 3D-TDSE simulations of electron momentum distributions for hydrogen for homogeneous and inhomogeneous electric fields. The high energy electrons with positive (negative) momentum along the x-axis come from a narrow time window before (after) the peak of the laser pulse. This narrow time window is a feature of the tunnel ionization regime, which is characterized by a strong exponential dependence in ionization probability on the laser field strength. The striking accumulation of electrons near  $k_x = 2$  a.u., combined with the knowledge that these electrons come from a narrow time window, given by the low- $\gamma$  tunnel ionization regime, suggests a new method for producing tightly focused electron beams of subfemtosecond duration.

Moreover, CTMC simulations show that the photoelectron spectrum obtained with inhomogeneous fields strongly depends on whether the electron is born when the electric field has a positive or a negative sign. For short pulses this results in a strong CEP dependence. This effect is at the center of the unifying theory that will be developed in section 5.4 and the discussion of CEP effects is therefore deferred to this later section. It seems to be worth mentioning already now, though, that the strong CEP dependence of the HES can be used as a tool to characterize the near-field. Strong influence of the CEP on the photoelectron momentum distribution has been reported for electrons released from a nanopip [162, 218, 261, 263]. The HES can play a similar role in measuring



**Figure 5.7:** Two-dimensional electron momentum distributions ( $k_x, k_r$ ) ( $x$ : along polarization axis,  $r$ : perpendicular to it) obtained in 3D-TDSE simulations for hydrogen at the laser parameters given in Fig. 5.4 for three different inhomogeneity parameters  $\beta$ , where  $\beta = 0$  corresponds to a homogeneous field.

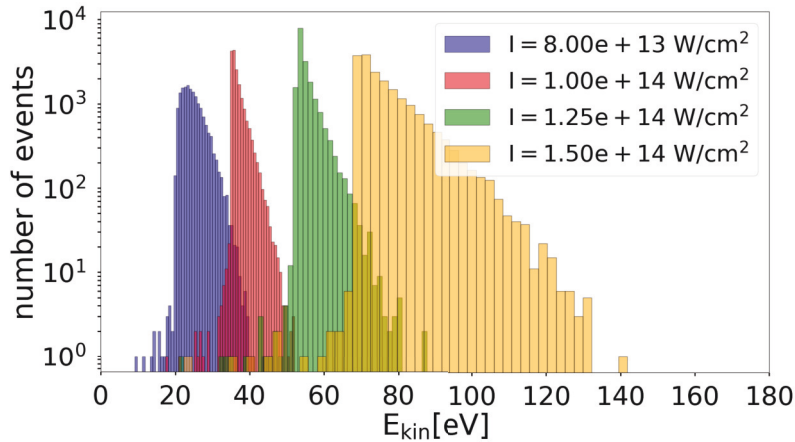


**Figure 5.8:** CTMC simulations of the HES for different laser intensities, for a fixed spatial inhomogeneity of  $\beta = 0.002$  using hydrogen and with all other parameters as described above (see e.g. the caption of Fig. 5.4). Increasing the laser intensity broadens the peak and shifts it to higher energies.

the CEP in a system that ionizes the gas-phase.

In terms of characterizing the near-field, it seems worth mentioning that the spectral position and width of the HES also strongly depend on the field strength and inhomogeneity parameter  $\beta$ , as can be seen from Fig. 5.8 and 5.9, respectively. Therefore, the HES promises to be suited for characterizing the field enhancement and decay length of the near-field, which in turn gives information about material properties and the geometry of the nanostructure.

Let us conclude this section with a short recap: We have seen a prominent higher

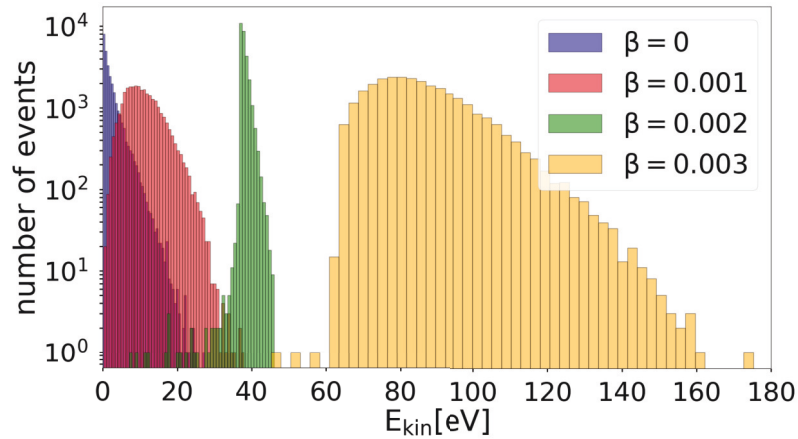


**Figure 5.9:** Histograms of the final electron energy shows the accumulation of electrons at higher energies in an inhomogeneous field, where the inhomogeneity is quantified by the parameter  $\beta$  given in the legend. The intensity is chosen to be  $I = 1 \cdot 10^{14}$  W/cm<sup>2</sup>, the central wavelength is  $\lambda = 2$   $\mu$ m in a 2-cycle pulse ( $N = 2$ ) with a CEP of  $\phi_{CEP} = \pi$  in helium ( $I_p = 0.9$  a.u.).

energy peak emerge in the ‘intermediate’ regime where the spatial decay length,  $l_F$ , of the electric fields is comparable to the electron quiver amplitude. The sensitive dependence of the location and width of the HES on the intensity, field decay length, and CEP suggests a new precise tool for near-field characterization. Finally, the fact that the prominent higher energy peak comes from a narrow time window, well within a single half-cycle of the laser pulse, may be used to create localized sources of monoenergetic electron beams of sub-femtosecond duration. Such sources would take the techniques of classical electron diffraction into the attosecond domain, enabling the investigation of dynamic changes of electron distribution in complex systems, such as nanostructures and biological molecules [300, 301].

### 5.3 Analysis and optimization of the higher energy structure

The content of this section has been published in a similar way in Phys. Rev. A 97, 023420 (2018) (see Ref. [74]). The copyright of content from said article lies with the American Physical Society.

In the previous section, we have witnessed the emergence of a higher energy structure (HES) due to a spatial inhomogeneity in the laser electric field. For practical applications, such as the characterization of near-fields or the creation of almost monoenergetic electron beams with tuneable energies, further insight into the nature of this higher energy structure is needed.

In Fig. 5.9 the HES is displayed for four different degrees of inhomogeneity. The energy at which this peak is located turns out to be very sensitive to the inhomogeneity of the field. This allows to tune the energy around which the electrons accumulate by varying the geometry of the nanostructure. In addition, it is important for certain applications to have a narrow energy distribution in the HES peak in order to generate ultrashort and nearly monoenergetic electron beams. So at which inhomogeneity does

the HES peak appear at minimal width? Both issues, the position and width of the HES peak, were only touched on qualitatively in the previous section. However, a deeper and, in particular, analytic understanding for the dependence of the HES on field inhomogeneity is still missing but is vital in order to tailor the parameters for potential applications. The presence of inhomogeneous electric fields considerably complicates the equations of motion, making tractable analytic approximations difficult, especially in the intermediate  $\delta$ -regime.

In this section, two different ways to describe the movement of the electron in the inhomogeneous electric field in closed-form analytical approximations are presented [74]. Based on these descriptions a simple scaling law for the location of the HES peak will be derived and a scheme for tuning the width of the peak will be given, both of which will prove useful in optimizing the nanostructure size or geometry for creating the HES in experimental settings [74].

The comparison between TDSE and CTMC simulations in the previous section (see Fig. 5.5) revealed that the sizeable gain in electron energy can be explained classically by the movement of the electron in the inhomogeneous field. Consequently, it is sufficient to solve Newton's equation of motion

$$\ddot{\mathbf{r}}(t) = -\mathbf{E}(x, t) - \frac{\mathbf{r}}{r^3} \quad (5.10)$$

in order to investigate the HES further. Moreover, we will neglect the Coulomb force, which is usually a good approximation in strong field ionization anyway and here in particular as the inhomogeneity of the electric field is significantly stronger than the inhomogeneity of the Coulomb field. This approximation will also be validated later by comparing CTMC simulations with and without the Coulomb potential included (see Fig. 5.13). Neglecting the Coulomb force, the motion along the different coordinates decouples, with non-trivial motion being driven by the laser electric field along the x-direction:

$$\ddot{x}(t) = -E_0 f(t) \cos(\omega t + \phi_{CEP}) \cdot (1 + 2\beta x) \quad (5.11)$$

with the envelope  $f(t) = \cos^2\left(\frac{\omega t}{2N}\right)$ . Thus, we also neglect the spread of transverse velocities, which approximately stays constant during propagation as it is not influenced by the inhomogeneity of the laser field and would not modify the shape of the higher energy structure in a significant way as the corresponding velocities are much smaller than those along the direction of polarization.

In the following, two different ways are suggested to describe the motion of the electron in the inhomogeneous field analytically. The first way draws on Mathieu differential equations having an exact solution [279, 302, 303] and the second path follows a perturbative approach.

### 5.3.1 Analytical approximation via Mathieu equations

The differential equation presented in eq. (5.11) is easier to handle after a coordinate transformation in which the x-coordinate is shifted such that the position-dependent potential is centered around zero. The shift  $x_M = x + 1/(2\beta)$  does the trick and yields

$$\ddot{x}_M(t) = -E_0 f(t) \cos(\omega t + \phi_{CEP}) \cdot (2\beta x_M). \quad (5.12)$$

For a slowly varying envelope relative to the laser frequency, or  $1/(2N) \ll 1$ , we can neglect the time-dependence in the envelope,  $f(t)$ , when solving the equation of motion.

In this case, the solution is given by Mathieu functions [302]. Using initial conditions of  $x_M(t_0) = -I_p/E(x=0, t_0) + 1/(2\beta)$  and  $\dot{x}_M(t_0) = 0$  at the time of ionization  $t_0$  (with  $t_0 = 0$  corresponding to ionization at the center of the pulse) the solution to equation (5.12) under the described approximations reads

$$x_M(t) \approx \frac{(M'_C(\eta_0)M_S(\eta) - M_C(\eta)M'_S(\eta_0))D}{2\beta E_0(M'_C(\eta_0)M_S(\eta_0) - M_C(\eta_0)M'_S(\eta_0))}, \quad (5.13)$$

where  $\eta_0 = (0, \alpha, \zeta_0)$  and  $\eta = (0, \alpha, \zeta)$  denote the three arguments of the even and odd Mathieu functions,  $M_C$  and  $M_S$  (respectively), as they are defined in Mathematica [304] and where  $\alpha = -\frac{4\beta E_0}{\omega^2}$ ,  $\zeta = \frac{1}{2}(\phi_{CEP} + \omega t)$ ,  $\zeta_0 = \frac{1}{2}(\phi_{CEP} + \omega t_0)$ , and  $D$  is defined as

$$D = \left( E_0 - 2\beta I_p \sec^2 \left( \frac{\omega t_0}{2N} \right) \sec(\phi_{CEP} + \omega t_0) \right). \quad (5.14)$$

Moreover, the prime denotes the derivative of the Mathieu function with respect to time, which can, just as the Mathieu functions themselves, be evaluated with the help of standard libraries.

### 5.3.1.1 Analytical approximation for the acceleration and thus the inhomogeneous field

Plugging this solution  $x_M$  of the Mathieu equation into the original differential equation with no envelope approximations (eq. (5.12)), we obtain an expression for the acceleration

$$\begin{aligned} a_{approx}(t) &= -E_0 f(t) \cos(\omega t + \phi_{CEP}) \cdot (2\beta x_M(t)) \\ &= a_M(t) \cdot f(t). \end{aligned} \quad (5.15)$$

The same result can be obtained by calculating the second derivative of  $x_M$  and multiplying it by the pulse envelope, which is shown by the expression in the second line of eq. (5.15), where  $a_M$  denotes the second order time derivative of eq. (5.13).

Fig. 5.10 compares the approximation of the acceleration according to eq. (5.15) with the full numerical solution of eq. (5.11) for two different ionization times. The agreement between the numerical result and the analytical approximation is surprisingly good, given that only a two-cycle ( $N = 2$ ) pulse is used. An even better agreement should be expected for longer pulses, where the slowly-varying envelope assumption is more valid. At this point, it seems important to emphasize that even though we neglect the envelope in solving the differential equation assuming a slowly varying envelope in eq. (5.13), envelope effects are included later on in refining the approximation by plugging  $x_M$  back into the original differential equation containing the envelope, which should also become clear by the relation given in the second line of eq. (5.15).

Also, note that eq. (5.15) serves as a closed-form approximate analytic expression for the time-dependent force experienced by the electron following ionization or the inhomogeneous field strength (the latter is obtained by multiplying the acceleration by -1). Up till now, due to the spatial field inhomogeneity, force and field could only be calculated by numerically solving the equation of motion (eq. (5.11)) first. Having a closed-form expression for force and field at our hands now, paves the way for further investigations of inhomogeneous fields.



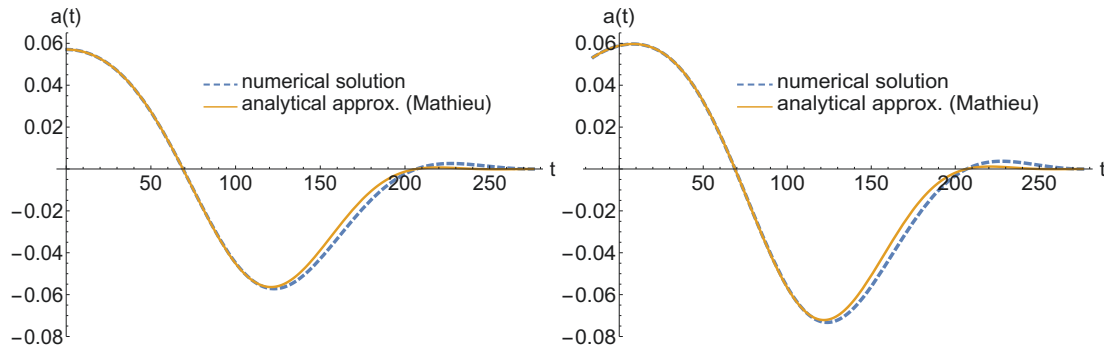


**Figure 5.10:** Full numerical solution of eq. (5.12) for the acceleration  $a$  (dashed blue line) compared to the approximate analytical solution (solid orange line) according to eq. (5.15) as a function of time for two different ionization times,  $t_0 = 0$  (left panel) and  $t_0 = -16$  a.u. (right panel). As approximately 96% of all electrons forming the HES should be launched between about  $t_0 = -16$  a.u. and  $t_0 = 16$  a.u., the good agreement between the depicted curves shows that this approximation should yield good results for all relevant trajectories. The depicted quantities are given in atomic units. The parameters are chosen as before in Fig. 5.9 and the inhomogeneity is given by  $\beta = 0.002$ .

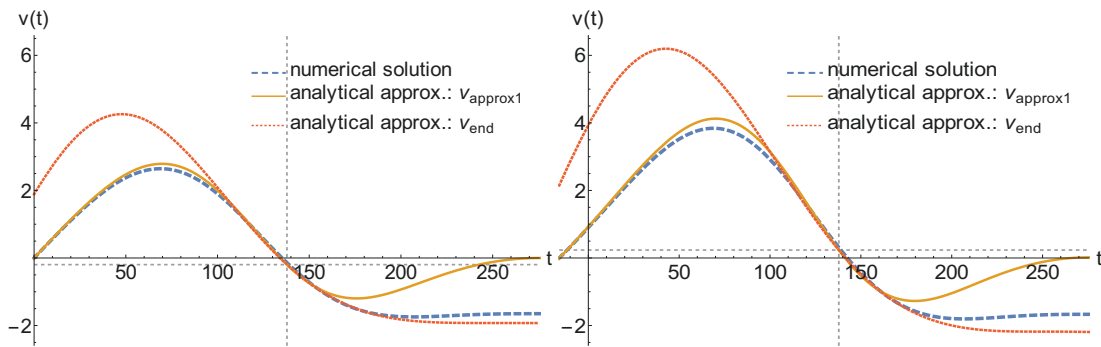


**Figure 5.11:** Numerical solution for the velocity  $v$  (dashed blue line, solution of eq. (5.11)) compared to the approximate analytical solution for the first part of propagation (solid orange line, eq. (5.18)) and for the second part of propagation (dotted red line, eq. (5.21)) as a function of time for two different ionization times  $t_0 = 0$  (left panel) and  $t_0 = -16$  a.u. (right panel). The depicted quantities are given in atomic units. All parameters were chosen to be the same as those in Fig. 5.10 and as before (see e.g. caption of Fig. 5.9). The initial conditions for eq. (5.21) were chosen at time  $t^* = \pi/\omega$ , one half-cycle away from the center of the pulse. The dashed gray vertical and horizontal lines mark the parameters  $t^*$  and  $v^*$ , respectively.

### 5.3.1.2 Analytical approximation for the velocity

The acceleration approximation invoking the analytical solution of Mathieu's equation has worked out quite nicely. However, for the velocity things turn out to be not equally easy. Since the velocity at the end of the pulse determines the final energy of electrons forming the HES, an analytical description of the velocity would be of great help, though. This motivates us to take on the velocity description as well.

A first approximation of the velocity is to merely derive the approximation of the



position according to eq. (5.13) with respect to time, which yields

$$v_M(t) = \omega \frac{(M'_C(\eta_0)M'_S(\eta) - M'_C(\eta)M'_S(\eta_0))D}{2\beta E_0(M'_C(\eta_0)M_S(\eta_0) - M_C(\eta_0)M'_S(\eta_0))} \quad (5.16)$$

following the same notation as in eq. (5.13). As this result poorly matches the numerical solution for the velocity, further refinement is needed. To this end, we approximate the velocity by integrating the acceleration we obtained in eq. (5.15), using integration by parts and dropping the terms that contain higher order derivatives of the envelope  $f(t)$ , assuming a slowly-varying envelope:

$$\begin{aligned} v_{approx1}(t) &= \int_{t_0}^t a_M(t') \cdot f(t') dt' \\ &= [v_M(t') \cdot f(t')]_{t_0}^t - \int_{t_0}^t v_M(t') \cdot \frac{d}{dt'} f(t') dt' \\ &\approx [v_M(t') \cdot f(t')]_{t_0}^t - \int_{t_0}^t (v_M \cdot f(t')) \cdot \frac{d}{dt'} f(t') dt' \\ &= [v_M(t') \cdot f(t')]_{t_0}^t - \left( \left[ x_M(t') \cdot f(t') \cdot \frac{d}{dt'} f(t') \right]_{t_0}^t - V \right), \end{aligned} \quad (5.17)$$

where, for further improvement of the approximation, in the third line  $v_M$  was replaced by  $v_M \cdot f$  as the latter is the lowest order approximation (first summand in lines 2 to 4) of  $v_{approx1}$ . Moreover,  $V$  denotes  $\int x_M(t') \left( f(t') \cdot \frac{d^2}{dt'^2} f(t') + \left( \frac{d}{dt'} f(t') \right)^2 \right) dt'$ , which we drop assuming a slowly-varying envelope. As a result, we obtain the following approximation for the velocity of the electron

$$v_{approx1}(t) = \left[ v_M(t') \cdot f(t') - x_M(t') \cdot f(t') \cdot \frac{d}{dt'} f(t') \right]_{t_0}^t. \quad (5.18)$$

The result of this approximation is depicted as a solid orange line in Fig. 5.11 for two different ionization times  $t_0 = 0$  (left panel) and  $t_0 = -16$  a.u. (right panel). We find that this approximation matches the numerical solution of eq. (5.11) (dashed blue line) nicely in the first half of propagation, but deviates considerably in the second half. The reason for this is the breakdown of the slowly-varying envelope assumption for short-cycle pulses. Our assumptions work well near the center of the pulse envelope where the time derivative is small but breaks down for sufficiently short pulses later on, as the derivative of  $f(t)$  becomes larger. To take account of this, we include the time-dependence of the pulse envelope at later times in electron propagation but drop the primary oscillation of the laser field, so as to keep the equation analytically tractable:

$$\ddot{x}_{end}(t) = -E^* \cdot (2\beta x_{end}(t)) \cdot \cos^2(\omega^* t) \quad (5.19)$$

with initial conditions  $v^* = \dot{x}_{end}(t^*) = v_{approx1}(t^*)$  and  $x^* = x_{end}(t^*) = x_M(t^*) - 1/(2\beta)$ , where  $t^*$  is chosen as the time where the first part of the solution  $v_{approx1}$  starts to deviate considerably from the numerical solution of eq. (5.11).  $E^*$  is chosen such that the solutions  $v_{approx1}$  and  $v_{end}$  match at  $t^*$  and, consequently, is given by

$$E^* = -a_M(t^*)f(t^*)/(2\beta x_{end}(t^*) \cos^2(\omega^* t^*)) \quad (5.20)$$

with  $a_M$  denoting the second time derivative of  $x_M$  and  $\omega^*$  is determined by the frequency of the envelope given by  $\omega/(2N)$ . The solution  $x_{end}$  of eq. (5.19) is again obtained by employing the Mathieu functions and this solution for the electron's position can be easily derived with respect to time,  $v_{end} = d/dt x_{end}$ , thus obtaining the following approximation for the velocity of the electron at the end of the pulse:

$$v_{end}(t) = \frac{(-v^* M_C(\zeta_0) + \omega^* x^* M'_C(\zeta_0)) \cdot M'_S(\zeta) + M_C(\zeta) \cdot (v^* M_S(\zeta_0) - \omega^* x^* M'_S(\zeta_0))}{M'_C(\zeta_0) M_S(\zeta_0) - M_C(\zeta_0) M'_S(\zeta_0)}, \quad (5.21)$$

where  $\zeta$  denotes the following three arguments of the respective Mathieu function  $\left(\frac{\beta E^*}{\omega^{*2}}, -\frac{\beta E^*}{2\omega^{*2}}, \omega^* t\right)$  and analogously  $\zeta_0$  replaces  $\left(\frac{\beta E^*}{\omega^{*2}}, -\frac{\beta E^*}{2\omega^{*2}}, \omega^* t^*\right)$ . As Fig. 5.11 shows, this approximate solution (dotted red line) matches well the second part of the electron's propagation in the laser field and, in particular, it also allows us to calculate the final kinetic energy at the end of the pulse. Hence we find that an analytic approximation given by eq. (5.21), where the explicit time-dependence of the laser field is approximated by the pulse envelope, gives an accurate estimate for the final electron energy independent of the ionization time, even though it may deviate considerably from the exact solution during the propagation.

### 5.3.2 Analytical approximation using a perturbative approach

Although using Mathieu equations worked nicely to approximate the acceleration and thus the inhomogeneous field itself and even though an approximation for the velocity at the end of the pulse was obtained in that framework as well, the latter required a two-step approach and is rather cumbersome to handle. Therefore, in the following, a perturbative model is presented for the analytical description of the velocity which will provide a more direct access to the  $\beta$ -dependence of the final velocity. The starting point for this approach is the differential equation presented in eq. (5.11), which is written out fully here again for easier reading

$$\ddot{x}(t) = -E_0 \cos^2\left(\frac{\omega t}{2N}\right) \cos(\omega t + \phi_{CEP}) \cdot (1 + 2\beta x). \quad (5.22)$$

The first step, or zeroth order step if you will, is to integrate the homogeneous part of the equation to obtain the zeroth order solution for the velocity:

$$v_0(t) = \int_{t_0}^t \left(-E_0 \cos^2\left(\frac{\omega t}{2N}\right) \cos(\omega t + \phi_{CEP})\right) dt. \quad (5.23)$$

One more integration step yields the zeroth order position, where the offset is determined by the tunnel exit  $x_{tunnel}$ :

$$x_0(t) = \int_{t_0}^t v_0(t) dt + x_{tunnel}. \quad (5.24)$$

Using this result for the position in the RHS of eq. (5.22) one can calculate the first order velocity:

$$v_1(t) = \int_{t_0}^t \left(-E_0 \cos^2\left(\frac{\omega t}{2N}\right) \cos(\omega t + \phi_{CEP}) \cdot x_0(t)\right) dt. \quad (5.25)$$

And then, we can put it together as follows

$$v_{approx,perturb}(t) = v_0(t) + 2\beta v_1(t) \quad (5.26)$$

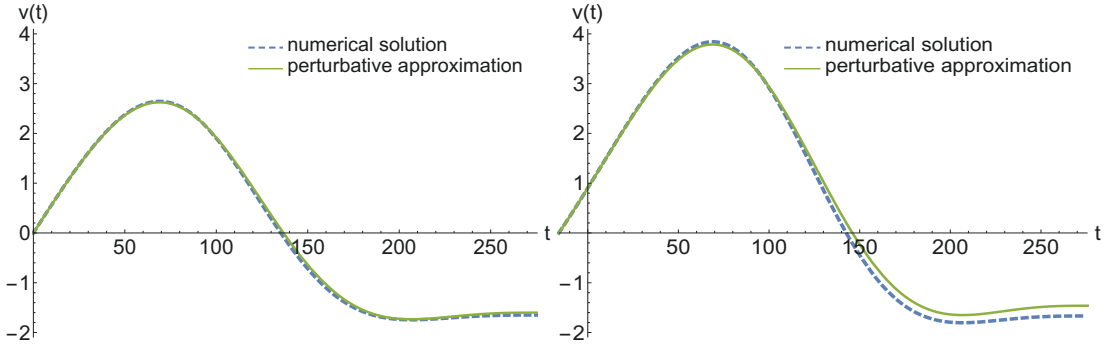


**Figure 5.12:** Numerical solution for the velocity  $v$  (dashed blue line, solution of eq. (5.11)) compared to the perturbative analytical solution of first order (solid green line, eq. (5.26)). The depicted quantities are given in atomic units. The parameters are chosen as before in Fig. 5.9, with  $\beta = 0.002$  here. The ionization time is chosen to be  $t_0 = 0$  (left panel, corresponding to ionization at the center of the pulse) and  $t_0 = -16$  (right panel).

since the underlying assumption of the perturbative ansatz was that we can express the position as  $x(t) = \sum_i^\infty (2\beta)^i x_i(t)$  and thus the velocity should have the form  $v(t) = \sum_i^\infty (2\beta)^i v_i(t)$ , where we went only up to first order here. The comparison with the numerical solution shows very good agreement for different ionization times, as can be seen from Fig. 5.12.

While the above equations look neat and innocuous enough, one needs to keep in mind that despite all the integrals being analytically tractable, the analytical expressions of those terms are lengthy and not as easy to handle as one would hope. To make this point clearer the solutions for  $x_0$  and  $v_0$  are written out here, and the even more unwieldy expression for  $v_1$  is given in appendix A.5:

$$v_0(t) = -\frac{E_0}{4(-1+N^2)\omega} \left\{ 2(-1+N^2) \sin(\phi_{CEP} + \omega t) + 2N^2 \sin\left(\phi_{CEP} + \frac{(-1+N)\omega t}{N}\right) - 2(-1+N^2) \sin(\phi_{CEP} + \omega t_0) - 2N^2 \sin\left(\phi_{CEP} + \frac{(-1+N)\omega t_0}{N}\right) \right\}, \quad (5.27)$$

$$x_0(t) = x_{tunnel} - \frac{E_0}{4(-1+N^2)\omega} \left\{ \frac{2(-1+N^2)(-\cos(\phi_{CEP} + \omega t) + \cos(\phi_{CEP} + \omega t_0))}{\omega} + \frac{N^2(1+N)(-\cos(\phi_{CEP} + \frac{(-1+N)\omega t}{N}) + \cos(\phi_{CEP} + \frac{(-1+N)\omega t_0}{N}))}{(-1+N)\omega} + \frac{(-1+N)N^2(-\cos(\phi_{CEP} + \frac{(1+N)\omega t}{N}) + \cos(\phi_{CEP} + \frac{(1+N)\omega t_0}{N}))}{(1+N)\omega} - 2(-1+N^2)(t-t_0) \sin(\phi_{CEP} + \omega t_0) - N(1+N)(t-t_0) \sin\left(\phi_{CEP} + \frac{(-1+N)\omega t_0}{N}\right) - (-1+N)N(t-t_0) \sin\left(\phi_{CEP} + \frac{(1+N)\omega t_0}{N}\right) \right\}. \quad (5.28)$$

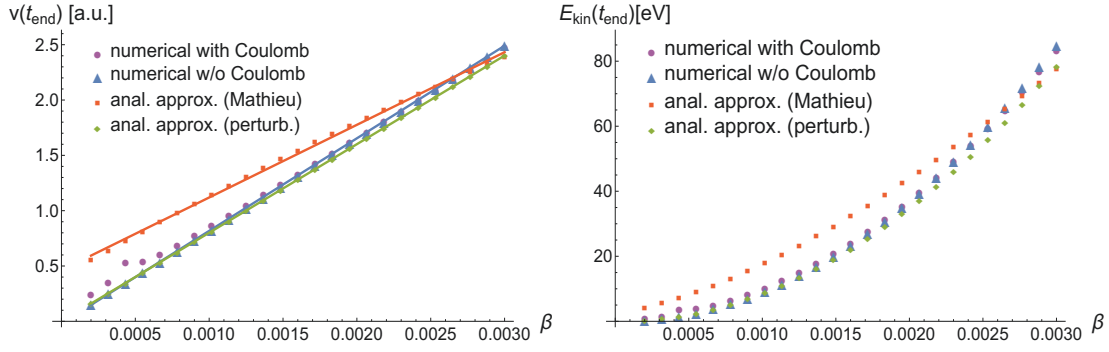


**Figure 5.13:** Final velocity (left panel) and kinetic energy (right panel) as a function of the inhomogeneity parameter  $\beta$  for an electron that is released at  $t_0 = 0$  (center of the pulse, corresponding to the time of most likely ionization) and the remaining parameters are chosen as before in Fig. 5.9. One can clearly see the linear dependence of the final velocity and equivalently the quadratic dependence of the final kinetic energy on  $\beta$ .

### 5.3.3 Spectral position of the HES

Having obtained analytical descriptions of the velocity during any time during propagation and thus also at the end of the pulse, we can use this as a tool to estimate how the HES, its spectral position and width, depends on the inhomogeneity parameter  $\beta$ .

Concerning the spectral position of the peak, we look at those trajectories that were released at the center of the pulse, at  $t_0 = 0$ , where the ionization probability is maximal. Fig. 5.13 shows the final velocity and the kinetic energy calculated from this central trajectory as a function of the inhomogeneity parameter  $\beta$  obtained from four different calculations. The two numerical results with and without the Coulomb potential included were obtained from numerically solving eq. (5.10) and (5.11), respectively, for initial conditions  $t_0 = 0$ ,  $\mathbf{v}_0 = 0$  and a TIPIS tunnel exit according to eq. (2.25). Comparing these results we can see that they hardly differ, with maximal deviations of 2.2 eV in the kinetic energy plot, which reassures us that neglecting the Coulomb potential approximates the system well.

Moreover, we can see from Fig. 5.13 that both the estimate for the final velocity obtained using Mathieu functions (see section 5.3.1.2) and with a perturbative ansatz (see section 5.3.2) show good agreement with the numerical solution not only for the case of  $\beta = 0.002$  that was used to test those approximations before but over a wider range of  $\beta$ . The perturbative approximation matches the numerical particularly well and, as we will see shortly, this can be used to further describe the inhomogeneity dependence of the peak position.

From the data depicted in the left panel of Fig. 5.13, we can already guess that the scaling of the final velocity as a function of field inhomogeneity,  $\beta$ , has a linear dependence. To investigate this further, we perform a power law fit  $A\beta^B$  with fitting parameters  $A$  and  $B$  on the numerical solution of eq. (5.11) for the final electron velocity (blue triangles in Fig. 5.13). Note that this power law is consistent with the fact that for  $\beta = 0$ , the case of a homogeneous field, we expect that an electron launched at the center of the pulse will end up with a negligibly small velocity. We find that such a power law fit gives  $B = 1.01$ , which substantiates the assumption of a linear dependence of the final velocity on the inhomogeneity parameter.

The insights gained from the analytical approximations in the previous sections

can now help us understand this linear scaling of the final velocity, or equivalently the quadratic scaling of the spectral position of the peak. In fact, the perturbative approach has the linear scaling already encoded in its description of the velocity: Taking another look at the equations in section 5.3.2, we can see that neither  $v_0$  nor  $v_1$  contains any  $\beta$ -dependence and the inhomogeneity enters eq. (5.26) only by the obvious factor of  $\beta$  in front of  $v_1$ . Thus, the linear dependence of the final velocity on  $\beta$  can be seen directly from eq. (5.26).

However, we should keep in mind that this prefactor of  $\beta$  in front of  $v_1$  is part of the perturbative approach up to first order by design, and going to higher orders would introduce higher order  $\beta$  prefactors. Thus, rather than explaining the linear dependence of the numerically obtained final velocity on  $\beta$  as being *due to* the linear prefactor of  $\beta$  in eq. (5.26) we should say that the fact of a perturbative approach of first order in  $\beta$  describing the velocity so well concurs with the numerically observed linear scaling of the final velocity with  $\beta$ .

With that said, we are still looking for an intuitive physical explanation for why the final velocity grows with  $\beta$ , and does so in a linear fashion. To this end, we first take a look at how the acceleration  $a(t)$  depends on  $\beta$ , keeping in mind that the final velocity corresponds to the area under this curve. As the top panel in Fig. 5.14 shows, the zeros of  $a(t)$  are scarcely affected by  $\beta$  and the inhomogeneity mainly influences the amplitude of the oscillation in between. As the ‘second hump’, the curve between the two zeros (around  $t \approx 125$  a.u.), bears a strong resemblance to a sine function, the area under this half-cycle part of the curve approximately scales linearly with the amplitude. (For an intuitive understanding of this concept one may think of the integral over a half-cycle sine function with amplitude  $C$ ,  $\int_0^\pi C \sin(x) dx = C \cdot 2$ , which obviously depends linearly on the amplitude  $C$ .)

Fig. 5.15 shows that indeed the final velocity scales linearly with the amplitude of the ‘second hump’, the minimum of the acceleration  $a_{min}$ , which determines the area under the second hump and thus the final velocity

$$v(t_{end}) \propto a_{min}. \quad (5.29)$$

Looking at eq. (5.12), it is clear that the acceleration is proportional to the inhomogeneity  $\beta$  at times where the position is independent of  $\beta$ . At the time where the acceleration is minimal (and the position is around its maximum), the position is indeed approximately independent of the inhomogeneity parameter as becomes clear from the bottom panel of Fig. 5.14. Therefore, we can use the relation

$$a_{min} \propto \beta \quad (5.30)$$

and combining this with eq. (5.29) we can infer the approximate proportionality

$$v(t_{end}) \propto \beta \quad (5.31)$$

or equivalently

$$E_{kin}(t_{end}) \propto \beta^2, \quad (5.32)$$

which confirms above findings. Thus, we have seen that the linear dependence of the final velocity on  $\beta$  is due to the amplitude of the acceleration curve approximately scaling linearly with  $\beta$ .

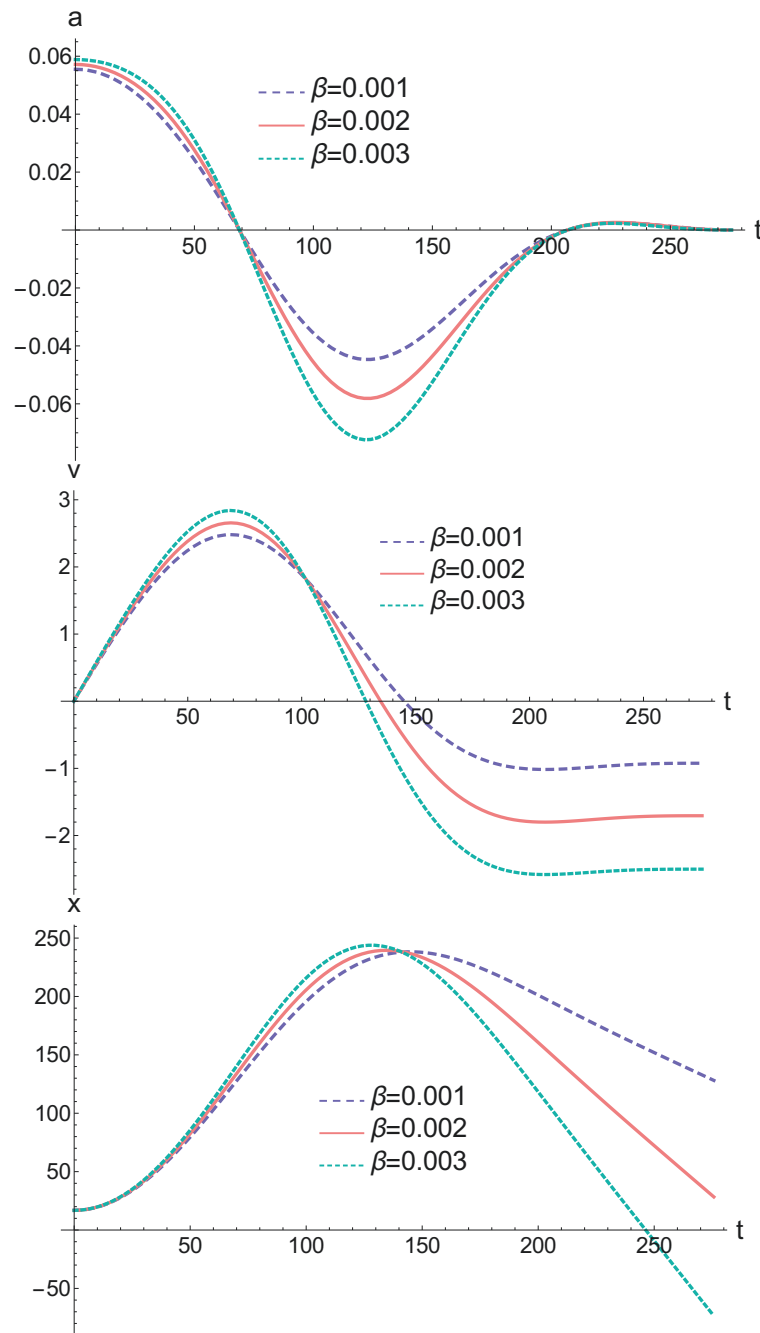


**Figure 5.14:** Top panel: The numerical solution for  $a(t)$  according to eq. (5.11) for three different  $\beta$  values where all the other parameters were chosen as in Fig. 5.9. The area under this curve, which equals the electron's final velocity, is influenced by  $\beta$  mainly via the amplitude of the oscillations in  $a(t)$ . Central and bottom panel: Same as the top panel but with velocity  $v$  (central panel) and position  $x$  (bottom panel) instead of the acceleration  $a$ . The parameters were chosen as before in Fig. 5.9. All depicted quantities are given in atomic units.



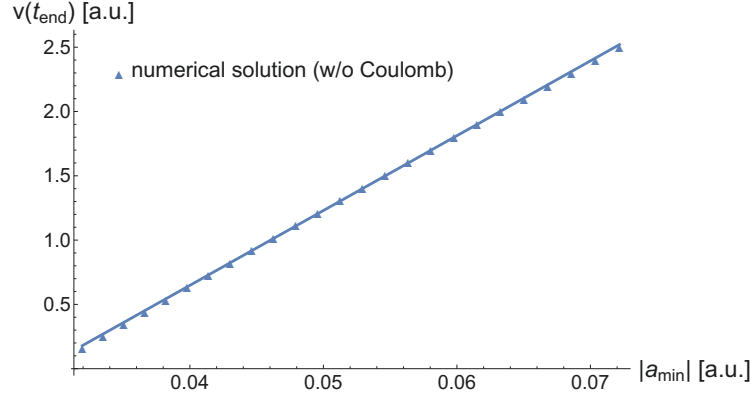


**Figure 5.15:** The final ( $t = t_{end}$ ) electron velocity as a function of the absolute value of the amplitude  $a_{min}$  of  $a(t)$  according to the numerical solution of eq. (5.11). The straight line represents a linear fit which confirms that the final velocity can be approximated to depend linearly on  $a_{min}$ .

### 5.3.4 Spectral width of the HES

As Fig. 5.9 already revealed in a qualitative fashion, not only the center of the HES but also its width strongly depends on the inhomogeneity parameter  $\beta$ . Reducing the HES width is potentially of great importance when using the HES in the creation of near monoenergetic electron beams. For the determination of the energy at which the HES peak is centered in section 5.3.3, we had a closer look at trajectories of electrons launched at the center of the pulse  $t_0 = 0$  as here the ionization probability is largest. To estimate the width of the peak, it is relevant to describe how different ionization times lead to different final energies. A minimized peak width is attained when the different ionization times lead to a range of final energies as small as possible.

The distribution of ionization times in the adiabatic ionization rate can be approximated by a Gaussian function, as derived in eq. (2.28). Its standard deviation

$$\sigma = \sqrt{\frac{3E_0}{2^{5/2} I_p^{3/2}} \frac{1}{\omega}} \quad (5.33)$$

helps us estimate the width of the time span in which the majority of trajectories are launched. We analyze electrons that are launched at  $t_0 = -\sigma$  and  $t_0 = +\sigma$  in order to be able to quantify how deviating from  $t_0 = 0$  changes the final energy. It is worth repeating that we want a deviation from  $t_0 = 0$  to have the least effect on the final energy in order to minimize the HES peak width.

The central plot in Fig. 5.16 shows the final energy for the three mentioned ionization times over a range of inhomogeneity parameters. Here, the three curves intersect at about  $\beta \approx 0.002$ . Note that the fact that all three curves intersect in one point does not imply that the peak is infinitely sharp. As Fig. 5.9 shows for the case of  $\beta = 0.002$ , even though the peak is narrow, it has finite width. The evaluation of the final energy of trajectories starting at  $t_0 = \pm\sigma$  does not provide us with a reasonable measure for the absolute width of the HES, it merely tells us at which inhomogeneity different ionization times have the least effect on the final energy, which should be the very inhomogeneity at which the HES width is minimized.

So, how can we understand that the HES peak width does not depend monotonically on  $\beta$  but that there is an inhomogeneity at which the width is minimized? To



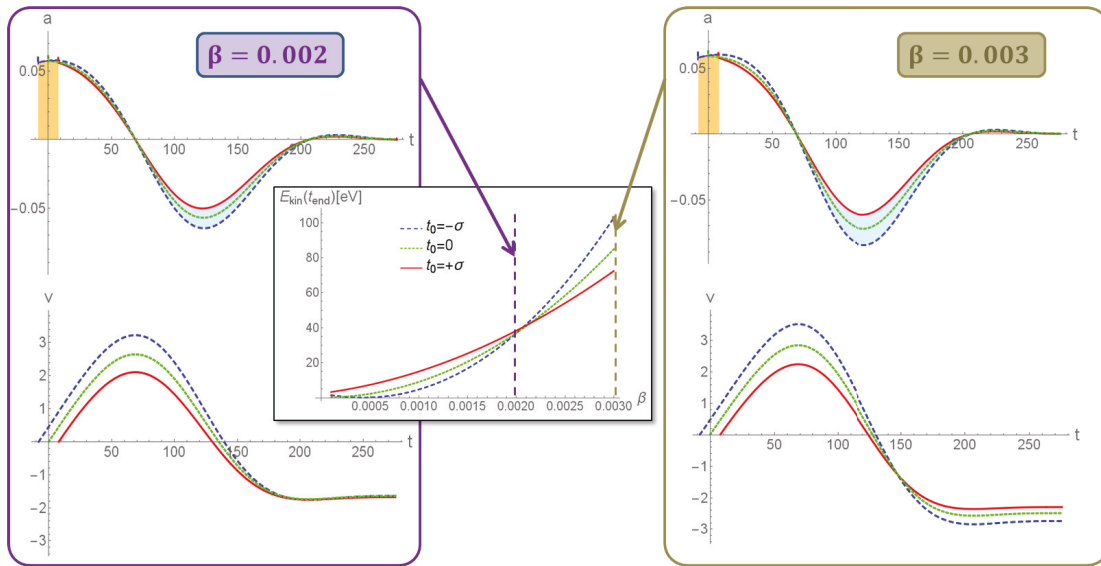


**Figure 5.16:** The final kinetic energy (central panel), the acceleration (upper panels) and the velocity (lower panels) as a function of time according to the numerical solution of eq. (5.11). The electrons are launched at  $t_0 = 0$  (dotted green lines),  $t_0 = -\sigma$  (dashed blue lines), and  $t_0 = +\sigma$  (solid red lines). Note that velocity, acceleration, and time are given in atomic units, whereas the kinetic energy in the central panel is given in electron volts (eV). Both panels on the left show results for  $\beta = 0.002$ , whereas on the right-hand side  $\beta = 0.003$  was used. In the central panel the final energy is shown over a large range of inhomogeneities. The HES peak width is assumed to be minimal at the inhomogeneity for which ionization before or after the center of the pulse has the least effect on the final kinetic energy, which is the case for  $\beta \approx 0.002$  here.

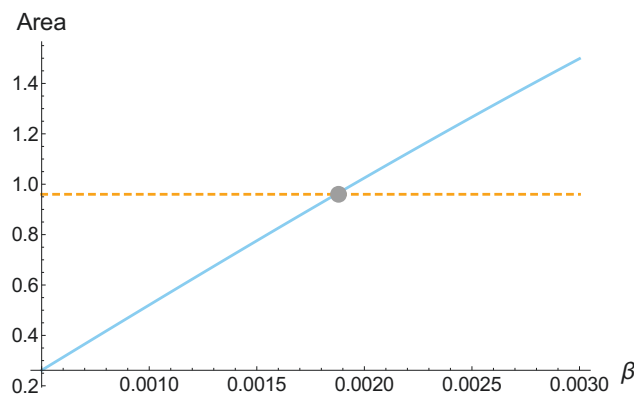


**Figure 5.17:** Scheme for estimating graphically the  $\beta$  value which minimizes the HES peak width. It is found at the intersection of the dashed orange line representing the initial additional positive area  $A_{pos}$  of the head start trajectory and the solid blue curve, which represents the additional negative area  $A_{neg}$  the head start trajectory accrues later on. Here, both curves intersect at  $\beta \approx 0.002$ . For details see appendix A.6.

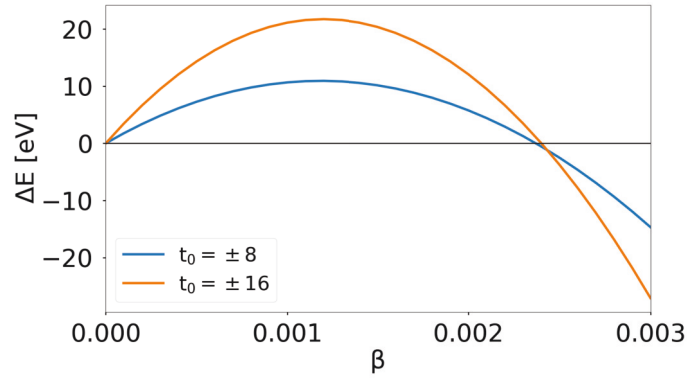


**Figure 5.18:** Difference of the final energy of two trajectories born at  $t_0 = 8$  and  $t_0 = -8$  (blue curve) or  $t_0 = 16$  and  $t_0 = -16$  (orange curve). The minimum of the (absolute value of the) energy difference, given by the zero-crossing, can be used as an estimate for the  $\beta$  yielding the narrowest HES. The figure shows that this zero-crossing has a negligible dependence on the choice of ionization times.

answer this question, it is instructive to look at the acceleration and velocity during propagation for electrons launched at  $t_0 = 0$  and  $t_0 = \pm\sigma$ . For  $\beta = 0.002$ , these quantities are depicted in the left panel of Fig. 5.16. Now, it is easy to see that the head start of the electron released at  $t_0 = -\sigma$  will initially add a positive area (marked in orange) under the acceleration curve as compared to the trajectory launched at  $t_0 = +\sigma$ . However, later on this head start trajectory also gains an additional negative area (light blue shaded area) under the second hump. In the case of  $\beta = 0.002$ , which optimizes the peak width, the additional positive area and the additional negative area cancel out each other and the total area under the acceleration curve and thus the final velocity is the same for all three trajectories. So we can understand the appearance of the minimal peak width as due to cancellation of two competing effects: Electrons ionized earlier will be initially accelerated more, but will experience greater deceleration later on in the pulse.

For other inhomogeneities either the initial orange head start area or the blue negative area will dominate and different ionization times will lead to more different final velocities. This can be seen in the example of  $\beta = 0.003$ , which is shown in the right panel of Fig. 5.16. Here, the positive area due to the head start of the electron launched at  $t_0 = -\sigma$  as compared to the one launched at  $t_0 = +\sigma$ , shaded in orange, is of approximately the same size as it was the case for  $\beta = 0.002$ . In contrast, the difference in the negative area under the second hump of the acceleration curve (shaded in blue) has grown with  $\beta$ . As a consequence, the overall area under the acceleration curve for  $t_0 = -\sigma$  is more negative than it is for  $t_0 = +\sigma$  and, thus, the latter ends up at a smaller kinetic energy.

The same concept can be used for arbitrary inhomogeneities: The initial orange head start area adding a positive area,  $A_{pos}$ , can be approximated to be independent of  $\beta$ , represented by the dashed orange horizontal line in Fig. 5.17. The negative area,  $A_{neg}$ , under the second hump is shown by a linearly growing solid blue curve in Fig. 5.17 (for details concerning this figure see appendix A.6). The minimum width of HES occurs where the dashed orange and the solid blue curve intersect, near  $\beta \approx 0.002$ , signifying the convergence in energy of trajectories starting at different ionization times.

Having established the origin of the minimum peak width, we want to proceed

from the visual approach above to a more quantitative way to determine the  $\beta$  that minimizes the width. To this end, we employ the perturbative model introduced in section 5.3.2. As one argument in the expression for the velocity is the initial time  $t_0$ , we change the notation from  $v(t)$  to  $v(t_0, t)$ . We are now interested in how different initial times lead to different final energies, where – again – we want to minimize that difference in order to obtain a minimal peak width. The difference in energy for two different ionization times  $t_{0,1}$  and  $t_{0,2}$  can be written as

$$\begin{aligned}\Delta E &= \frac{1}{2} \left( v_0(t_{0,1}, t_f) + \beta v_1(t_{0,1}, t_f) \right)^2 - \frac{1}{2} \left( v_0(t_{0,2}, t_f) + \beta v_1(t_{0,2}, t_f) \right)^2 \\ &= \frac{1}{2} \left( v_0^2(t_{0,1}, t_f) - v_0^2(t_{0,2}, t_f) + \beta^2 \left( v_1^2(t_{0,1}, t_f) - v_1^2(t_{0,2}, t_f) \right) \right. \\ &\quad \left. + 2\beta \left( v_0(t_{0,1}, t_f) \cdot v_1(t_{0,1}, t_f) - v_0(t_{0,2}, t_f) \cdot v_1(t_{0,2}, t_f) \right) \right) \\ &= a + b\beta + c\beta^2,\end{aligned}\tag{5.34}$$

where  $t_f$  denotes the time when the pulse has passed and

$$\begin{aligned}a &= \frac{1}{2} \left( v_0^2(t_{0,1}, t_f) - v_0^2(t_{0,2}, t_f) \right) \\ b &= v_0(t_{0,1}, t_f) \cdot v_1(t_{0,1}, t_f) - v_0(t_{0,2}, t_f) \cdot v_1(t_{0,2}, t_f) \\ c &= \frac{1}{2} \left( v_1^2(t_{0,1}, t_f) - v_1^2(t_{0,2}, t_f) \right).\end{aligned}\tag{5.35}$$

$\Delta E(\beta)$  is a parabola and we are interested in the minimum of its absolute value, i.e. the zero-crossing, which is found at

$$\beta_{\text{minimal peak width}} = -\frac{b}{2c} \pm \sqrt{\left(\frac{b}{2c}\right)^2 - \frac{a}{c}}.\tag{5.36}$$

Fig. 5.18 shows two parabolas for the cases of  $\{t_{0,1} = +\sigma = +8, t_{0,2} = -\sigma = -8\}$  and  $\{t_{0,1} = 2\sigma = 16, t_{0,2} = -2\sigma = -16\}$ . The symmetric choice of ionization times results in  $A(t_{0,1}) = -A(t_{0,2})$  and therefore  $|v_0(t_{0,1}, t_f)| = |v_0(t_{0,2}, t_f)|$ , which gives  $a = 0$  and finally  $\beta_{\text{minimal peak width}} = \frac{b}{c}$ . For the two parabolas depicted in Fig. 5.18, we find

$$\begin{aligned}\beta_{\text{minimal peak width}} &= 0.00237 \quad \text{for } \{t_{0,1} = +\sigma, t_{0,2} = -\sigma\} \\ \beta_{\text{minimal peak width}} &= 0.00240 \quad \text{for } \{t_{0,1} = +2\sigma, t_{0,2} = -2\sigma\}.\end{aligned}\tag{5.37}$$

Thus, we can see that our approach of finding the inhomogeneity which leads to the minimum peak width is not particularly sensitive to the choice of ionization times. Also, we get about the same result as obtained from numerically solving the equations of motion and looking at the intersection of energies for different ionization times in Fig. 5.16, which gave  $\beta \approx 0.002$ .

### 5.3.5 Summary of the analysis of the HES

In this section, we have seen that describing the electron's motion in an inhomogeneous laser field in the intermediate regime of  $\delta \approx 1$ , which is known to be notoriously difficult to handle mathematically [238], is not only possible numerically but that also analytical approximations can be attained and even allow to estimate relevant quantities such as the spectral position and width of the HES.

Observing numerically that the inhomogeneity of the laser field dominates over the inhomogeneity of the Coulomb potential of the ionized atom, we could neglect the Coulomb potential in the equation of motion. Making use of the pulse envelope varying more slowly than the primary oscillation of the laser field, the equations of motions could be reduced to Mathieu differential equations that can be solved analytically. Including the shape of the envelope perturbatively after solving the Mathieu differential equation, a closed-form expression for the acceleration was found. This serves also as an analytical description of the inhomogeneous field that the electron experiences, which otherwise needs to be computed numerically.

Although the ansatz of Mathieu equations also led to an analytical description of the velocity of the electron, it was found that a perturbative approach yields better agreement with the numerical solution. The fact that the perturbative ansatz up to first order is sufficient to describe the electron's velocity in the inhomogeneous field, i.e. it has the form  $v_0 + \beta v_1$ , also helped us derive a simple scaling law stating that the final velocity of an electron born at the center of the pulse scales linearly with the inhomogeneity and, equivalently, that the spectral position of the HES peak scales quadratically with  $\beta$ .

Moreover, it was found that there is an inhomogeneity at which the width of the HES peak is minimal and a scheme to estimate this optimal inhomogeneity based on the analytical descriptions of the velocity was presented.

Being able to estimate the dependence of both the spectral width and position of the HES on the inhomogeneity should help tune the parameters to realize the HES experimentally and to control, for example, the spectrum of potentially resulting femtosecond electron beams.

## 5.4 Unifying effects in strong inhomogeneous fields in the intermediate regime

Only briefly after the emergence of the HES was discovered, the appearance of another peak was reported in the spectrum of electrons that move in the inhomogeneous field of a nanostructure [75]. The latter was named 'low-energy peak' (LEP) and, as the name suggests, was found at rather low energies of about 1 eV, whereas the HES was located at about 40 to 80 eV. Additionally, the HES was produced in a system where electrons are ionized from a gas target that is placed in the inhomogeneous field of a nanotip, whereas the LEP is formed of electrons that are released directly from the surface of a nanotip. Moreover, the HES was a theoretical prediction while the LEP was measured experimentally.

Given the diametrically opposed nature and naming of the HES and LEP, one may wonder why we should bother to compare them to each other at all. The objections insinuated by such a question are further supported by the fact that the publication which reported on the LEP [75] does not even mention the HES. However, both the LEP and HES emerged in the intermediate regime of  $\delta \gtrsim 1$  and in both cases the electron's motion in the inhomogeneous laser field was claimed to cause the accumulation of electrons in the respective peaks. From what we have learned about the HES above, we should therefore expect that similar effects are at play.

Indeed, we will see that even though the two peaks were observed in different energy regimes, we can identify one mechanism in which both observations are explained.

We thus unify the theories behind LEP and HES, finding that LEP and HES are two manifestations of the same energy upshift due to propagation in an inhomogeneous field. It will then become clear that the sole difference between HES and LEP is that in the setting in which the HES was observed the electrons initially move towards the nanostructure whereas the electrons that form the LEP leave the nanostructure directly after liberation. Even though this difference leads to a slightly larger energy gain of electrons that initially approach the nanotip than of those directly leaving it, we find that this effect is small and does not explain why the LEP was found at much lower energies, of about 1 eV, than the HES, which was found to peak at around 40 to 80 eV. Rather, we establish that the underlying dynamics are the same and that the main reason for the different final energies is the different parameters that were chosen in the observation of the HES and LEP. This insight is of particular interest as it allows us to propose a modification of the setting in which the *low* energy peak (LEP) was experimentally observed such that it leads to a photoelectron distribution at energies as high and as spectrally confined as it was observed in the HES. This promises the still outstanding experimental realization of almost monoenergetic electron bunches as they were described in the framework of the HES.

### 5.4.1 An intuitive model for the energy upshift observed in the HES

As a first step, we need to understand why electrons experience an energy upshift at all when moving in inhomogeneous fields. Even though the analysis of the HES in section 5.3 already provided some insights into how one can describe the electron movement mathematically and we understood how the spectral position and width changes with the inhomogeneity of the field, a simple and physically intuitive model for why the electrons accumulate in a prominent peak was not given in the previous section, or any other publication for that matter.

For a better understanding of the upshift mechanism, we look at the dynamics of an electron in a typical inhomogeneous field that leads to a HES, presented in Fig. 5.19. It is important to note that we now use an exponential description of the inhomogeneous field

$$E(x, t) = E_0 \cos\left(\frac{\omega t}{2N}\right)^2 \cos(\omega t + \phi_{CEP}) \exp\left(-\frac{x}{l_f}\right) \quad (5.38)$$

and not the linear approximation of it (see eq. (5.7)) anymore. Thus, we do not need to worry about zero-crossings of the  $(1 + 2\beta x)$  term and can include longer pulses in our study as well. Moreover, in order to make things easier mathematically, we focus on the field-decay along the positive x-axis rather than having the field decay along the negative x-axis as was the case before (see e.g. Fig. 5.2). This entails that the final velocity  $v_x$  is positive rather than negative now (compare e.g. Fig. 5.12 and 5.19) and that a CEP of  $\pi$  (at which the HES was observed in the linearly approximated field) needs to be converted to a CEP of 0. The advantage of moving to the positive x-axis is that we do not have to deal with evaluating the absolute value of  $x$  in the exponential term (see eq. (5.6)) and the concomitant mathematical problems.

Now, to understand the energy upshift due to the movement in the inhomogeneous field, we first look at the acceleration curve of an exemplary trajectory plotted in Fig. 5.19. After all, the area under this curve determines the final velocity. For an electron born at the center of the pulse and propagated in a *homogeneous* field (case not shown in Fig. 5.19), the acceleration curve would oscillate symmetrically around zero



(when neglecting envelope effects) leading to equally large positive and negative areas and thus to zero velocity at the end of the pulse [39, 305]. The spatial inhomogeneity, in contrast, introduces an asymmetry in the acceleration curve, which we can evaluate better by splitting the pulse in half-cycles (see the striped background in Fig. 5.19) and looking closer at the acceleration amplitudes of varying height that lead to a non-zero area under the acceleration curve in the individual half-cycles.

At the beginning of the propagation, it is very clear that in each half-cycle (corresponding to one stripe) the amplitude is larger for the acceleration with a positive sign than for the one with a negative sign because for the positive sign the electron is closer to the nanotip. As a consequence, we gain ‘positive area’ under the acceleration curve and thus positive final velocity in each of these early half-cycles<sup>1</sup>. Later on, however, the electron has already gained so much energy that it does not change the sign of its velocity anymore and is only leaving the tip. Then, in the half-cycles highlighted in white, where the negative acceleration comes prior to the positive one, we have an energy loss since here the negative acceleration is larger than the positive acceleration. In the blue half-cycles, though, where the positive acceleration part comes first, we still gain energy. Now, the key to understanding the overall energy upshift is that the loss during the white half-cycle is always smaller than the gain in the neighboring blue half-cycle and consequently there is an energy gain during one *full* optical cycle. This effect is due to the fact that the velocity during the white half-cycle is moving around its minimum. Consequently, the distance gained during that half-cycle is smaller and the difference in the amplitudes of  $a < 0$  and  $a > 0$  is much smaller than in the blue half-cycle where the velocity is around its maximum and the gain in distance and thus the difference of the amplitudes at  $a > 0$  and  $a < 0$  is larger.

Consequently, we can understand the energy upshift as due to the asymmetry which the inhomogeneous field introduces in the acceleration curve such that we obtain a non-zero total area under it even for electrons ionized at the center of the pulse. Even though there are half-cycles in which we lose a little energy, the half-cycles in which we gain energy (blue stripes in the background) always dominate. And in the beginning, while the electron has gained so little energy that it still oscillates back and forth and approaches the tip in the white half-cycles we even have an energy gain in every half-cycle, which explains the particularly fast energy gain at the beginning of the propagation.

### 5.4.2 Unified model for HES and LEP

An important point in the above mechanism is that it does not only explain the energy upshift in the setting that was employed in [73] for the HES, which was used in Fig. 5.19, but equally explains the energy upshift at the parameters that led to the LEP [75]. This should become clear from Fig. 5.20, in which the parameters were chosen to coincide with those used for the experimental realization of the LEP [75]. Even though these parameters differ considerably from those in Fig. 5.19, which are in the regime where the HES was predicted theoretically, the overall shape of the curves does not greatly differ. The main reason for the strong resemblance of the curves in Fig. 5.19 (HES) and Fig. 5.20 (LEP) is the fact that both are in the intermediate  $\delta$ -regime.

<sup>1</sup>For an illustration of this concept, see the top panel of Fig. 5.24, where the green quarter-cycle area contributes positively and the red quarter-cycle area negatively, yielding a total positive area for that half-cycle.



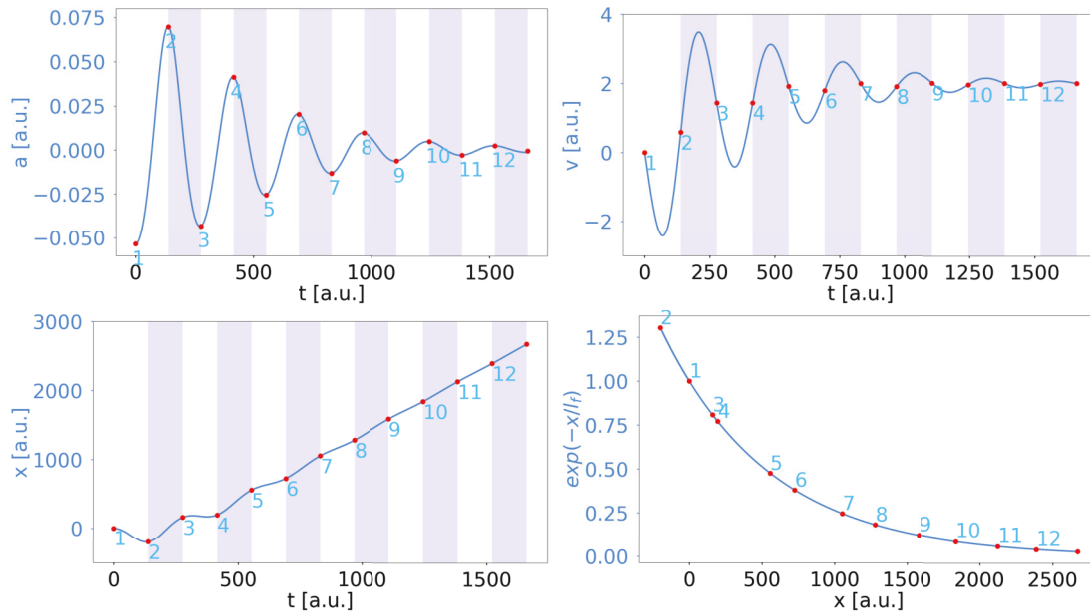


**Figure 5.19:** Acceleration  $a$ , velocity  $v$ , position  $x$  as a function of time  $t$ , and the exponential decay factor  $\exp(-x/l_f)$  for an electron released from an atom in an electric field as described by eq. (5.38) at the center of a 12 cycles pulse with  $\lambda = 2 \mu\text{m}$ ,  $\text{CEP} = 0$ ,  $l_f = 750$  a.u. and where the atom is exposed to a maximal intensity of  $I = 1 \cdot 10^{14} \text{ W/cm}^2$  ('HES setting'). The numbered red dots are plotted at every half-cycle of the laser pulse for visual guidance.

In terms of the mechanism outlined in section 5.4.1, which explained the gain of kinetic energy in the inhomogeneous field by the asymmetry of the field and thus acceleration amplitudes, there is one major difference between Fig. 5.19 and Fig. 5.20, though. In the framework of the HES (Fig. 5.19), the electron is ionized from atoms placed in the vicinity of a nanostructure and the electron initially moves *towards* the nanotip, thus initially exploring fields that are even higher than during the ionization process. Consequently, these electrons gain more energy than in the LEP case, where the electrons are ionized directly from the nanostructure and initially move *away* from the tip. Even though electrons that initially leave the nanostructure gain less energy than electrons initially approaching the nanostructure, they are still upshifted considerably in energy due to the mechanism explained in section 5.4.1.

In a setting where the initial movement both towards and away from the tip is allowed, one may think of HES and LEP as two manifestations of the same energy upshift that are found in neighboring half-cycles, where the higher energy upshift (HES) is found in the half-cycle in which the electron initially moves towards the tip and the lower energy upshift (LEP) is found in the half-cycle in which the electron initially leaves the tip. This is illustrated in Fig. 5.21, from which it should also become clear that one can switch between HES and LEP in one fixed half-cycle by changing the carrier-envelope phase by  $\pi$ .

Even though the electrons ionized in the 'LEP half-cycle' (orange dots in Fig. 5.21) and the 'HES half-cycle' (blue dots) end up at different energies, it becomes clear from Fig. 5.21 that the energy difference due to the opposed initial directions of the electron is not several orders of magnitude but only a factor of about 3. This is important to note since the fact that the LEP was experimentally observed at about 1 eV [75] and the

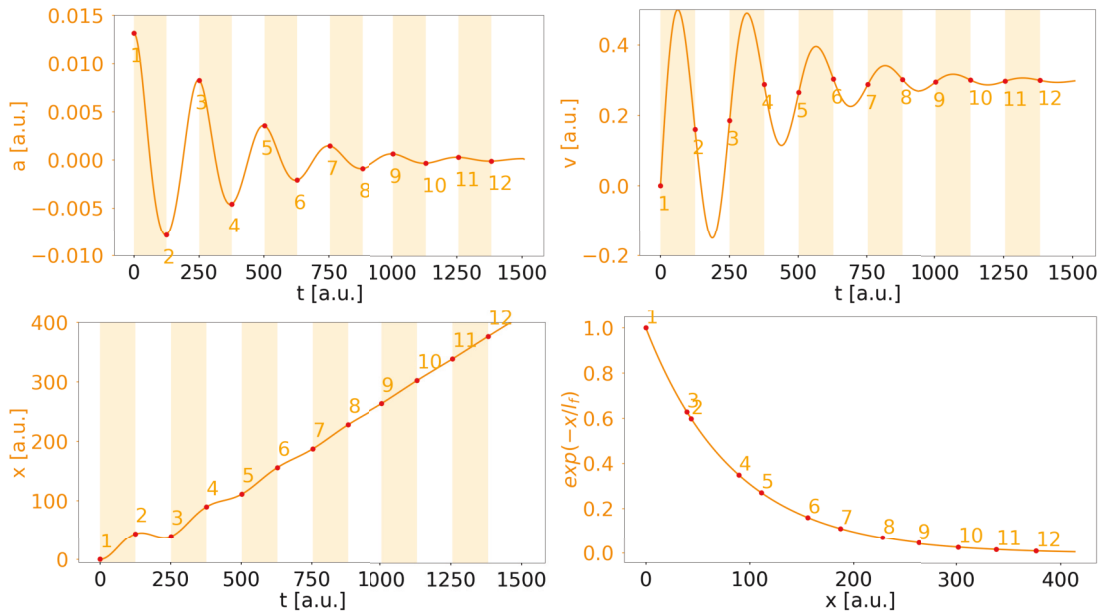


**Figure 5.20:** Acceleration  $a$ , velocity  $v$ , position  $x$  as a function of time  $t$ , and the exponential decay factor  $\exp(-x/l_f)$  for a trajectory ionized from a nanotip in an electric field as described by eq. (5.38) at the center of a 12 cycles pulse with  $\lambda = 1.8 \mu\text{m}$ ,  $\text{CEP} = \pi$ ,  $l_f = 85 \text{ a.u.}$  where the maximal (enhanced) intensity is  $I = 6.05 \cdot 10^{12} \text{ W/cm}^2$  (corresponding to an incident intensity of  $I_{0,inc} = 2 \cdot 10^{11} \text{ W/cm}^2$  and a field enhancement factor of 5.5). The numbered red dots are plotted at every half-cycle of the laser pulse for visual guidance. The mechanism underlying the energy gain in the inhomogeneous field is the same as in the HES case since the only difference to Fig. 5.19 is the initial movement in the opposite direction, which only leads to a slightly weaker energy gain, particularly in the first half-cycles. The reason for that slightly weaker energy gain is that the maximal field strength the electron sees is higher in case of initial movement towards the tip (compare the plots of  $\exp(-x/l_f)$  in Fig. 5.19 and Fig. 5.20 for that).

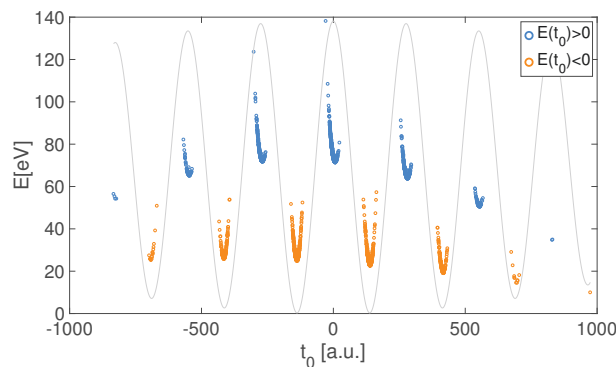


**Figure 5.21:** Final kinetic energy as a function of ionization time for electrons ionized at a maximal intensity of  $I = 1 \cdot 10^{14} \text{ W/cm}^2$ . The decay length of the field is  $l_f = 500 \text{ a.u.}$ , the wavelength is  $\lambda = 2 \mu\text{m}$ , the pulse has  $N = 24$  cycles and  $\text{CEP} = 0$ . The equation for the inhomogeneous electric field is given by eq. (5.38). For visual guidance the field strength of the incident homogeneous laser pulse is plotted in the background in arbitrary units for the time window in which ionization happens.

HES was theoretically calculated at 40 eV up to 120 eV [73], might create the illusion of a large energy gap between those two effects. Most of this large difference in energies in [75] and [73], though, is due to the choice of disparate parameters: For the HES in [73], an enhanced intensity of  $I = 1 \cdot 10^{14}$  W/cm<sup>2</sup> and an inhomogeneity parameter corresponding to a decay length of about  $l_f = 170 - 500$  a.u. and a wavelength of  $\lambda = 2 \mu\text{m}$  was used, whereas the experimental observation of the LEP was made at  $I = 1 \cdot 10^{12}$  W/cm<sup>2</sup>,  $l_f = 85$  a.u. and  $\lambda = 1.8 \mu\text{m}$  [75].

Thus, there are two effects that explain the energy difference of the HES reported in [73] and the LEP in [75]: First, in [73], the electron initially moves towards the tip and sees a larger maximal electric field, which accounts only for about a factor of 2-3 to energies of electrons that directly leave the tip, as it is the case in [75]. Second, the choice of laser and nanotip parameters differs significantly, which accounts for most of the discrepancy in energy. These parameters we can change, though. And as the mechanism of energy gain is in principle the same, independent of the initial direction of the electron, we should be able to create confined photoelectron distributions also at high energies for electrons ionized directly from the nanotip, which initially leave the nanotip, if we choose our parameters appropriately.

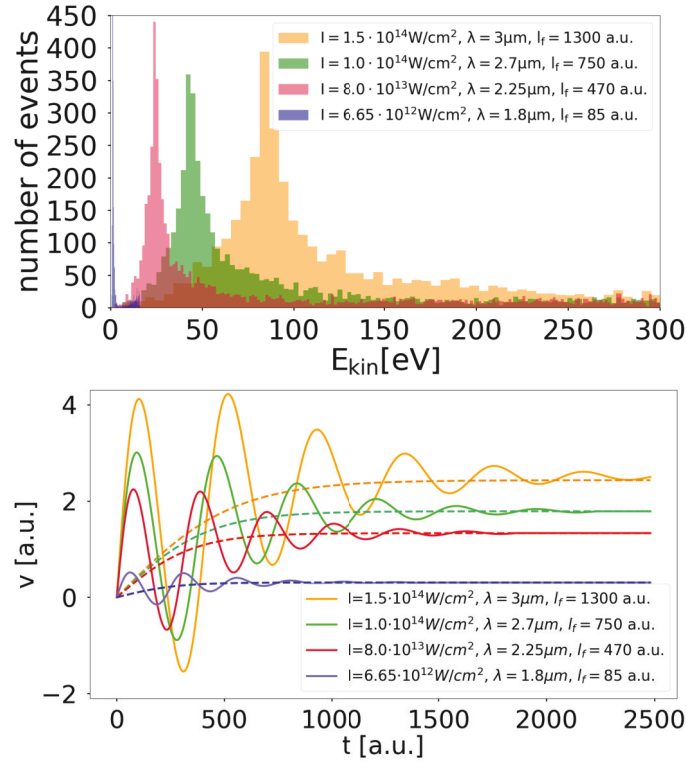
Fig. 5.22 shows that indeed such parameters exist. The top panel depicts CTMC simulation results for ionization directly from the nanotip where we follow the model applied in [75] using the one-dimensional exponentially decaying field of eq. (5.6). The ionization probability is described by the Fowler-Nordheimer tunneling formula [218, 220, 306], which gives the ionization current from the tip (with exponential accuracy) as

$$J(t) \propto \exp\left(-\frac{2(2W)^{3/2}}{3E(t)}\right), \quad (5.39)$$

where  $W$  denotes the work function of the nanotip. Comparing this function to the adiabatic ionization rate for the gas phase (see eq. (2.21)), we can see that it is identical save for the ionization potential  $I_p$  which is replaced by the work function  $W$ . Following Ref. [307], we only allow electrons to be born during half-cycles of negative field strength, as only then the field drives the electrons from the inside towards the surface of the nanotip and allows ionization (assuming that only emission in positive  $x$ -direction is possible). Moreover, we model the electrons to be born at the surface of the tip with zero initial velocity and rescattering at the tip is implemented as elastic scattering with a reflection coefficient of 1 [75, 307].

In the top panel of Fig. 5.22, the lowest peak reproduces the LEP peak at about 1 eV that was reported in [75]. However, at other intensities, wavelengths and decay lengths the peak is shifted to higher energies, while still being spectrally confined. In particular, we can even reach energies as high as they were so far only reported for the HES, while now being produced in a LEP setting, i.e. by ionization from a tip and not from the gas phase in the vicinity of the tip.

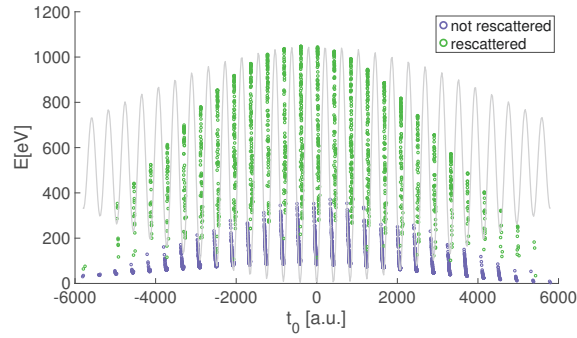
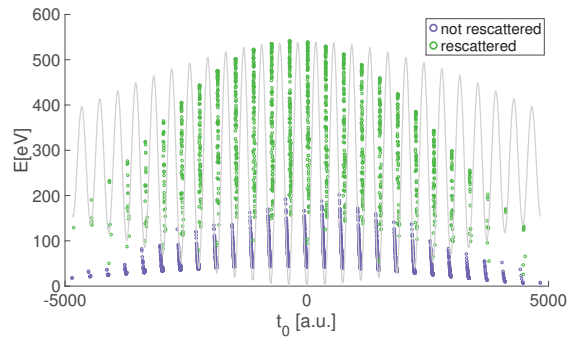
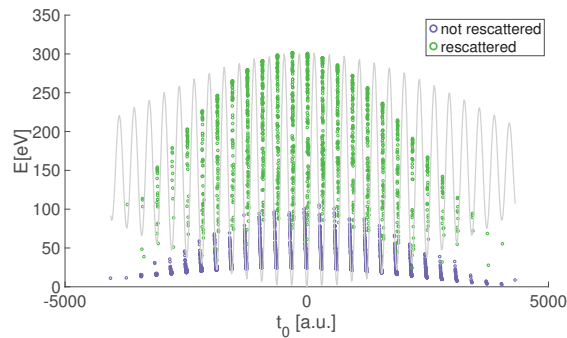
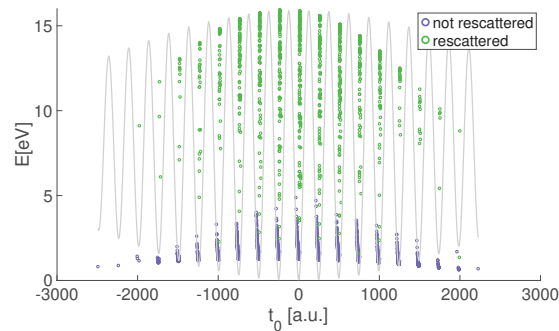
To get a better understanding of the spectra shown in the top panel of Fig. 5.22, it is instructive to analyze in which part of the laser pulse the electrons are born. Such an analysis is presented in Fig. 5.23, where the electrons are color-coded according to having been rescattered at the nanostructure (green dots) and not having undergone rescattering (purple dots). From this it becomes clear that the high energetic long tails of the electron distributions in Fig. 5.22 are due to rescattering events and that the prominent peak that arises in the spectral electron distribution is formed by direct electrons, which is in agreement with the findings in [75] and in line with the



**Figure 5.22:** Top panel: Final kinetic energy of photoelectrons ionized directly from a nanostructure for various laser and nanostructure parameters specified in the legend, where a 48 cycle pulse was used. The peak at small energies (blue) reproduces the experimental result reported in [75] and is found at about 1 eV. These simulations also show how we can obtain considerably higher energies in the same setup when choosing other parameters. The electrons that form the tail are from rescattering events, which becomes clear from Fig. 5.23. Bottom panel: Velocity as a function of time for a trajectory ionized at the center of the pulse at the surface of the nanostructure with zero initial velocity for the same parameters as in the top panel. The dashed lines are analytical approximations according to eq. (5.45).

mechanism outlined in section 5.4.1 where the energy gain is due to movement in the inhomogeneous fields and not rescattering.

Obviously, the question of experimental realizability arises at this point. There is reason to be optimistic that the parameters that led to the high-energetic peaks in the top panel of Fig. 5.22 can indeed be used experimentally, mainly since similar parameters have been used before. Not only the LEP around 1 eV has already been measured [75] but also a sharp peak at about 10 eV has already been experimentally realized [141] where enhanced field strengths and decay lengths were applied that are in the regime used for the high-energetic peaks in the top panel of Fig. 5.22. In [141], though, a wavelength of  $\lambda = 800$  nm is used and going to longer wavelengths at similar intensities promises to lead to higher absolute photoelectron energies that are in the regime of energies as they were predicted for the HES in [73] and as they are found in the top panel of Fig. 5.22. Using a setting where the electrons are released directly from the nanostructure should be easier to implement experimentally than ionization from atoms in the vicinity of the nanostructure. The latter was the setting in which the HES was predicted theoretically (see section 5.2 and [73]) but has the disadvantage that the

(a)  $I = 1.5 \cdot 10^{14} \text{ W/cm}^2$ ,  $\lambda = 3 \mu\text{m}$ ,  $l_f = 1300 \text{ a.u.}$ (b)  $I = 1 \cdot 10^{14} \text{ W/cm}^2$ ,  $\lambda = 2.7 \mu\text{m}$ ,  $l_f = 750 \text{ a.u.}$ (c)  $I = 8 \cdot 10^{13} \text{ W/cm}^2$ ,  $\lambda = 2.25 \mu\text{m}$ ,  $l_f = 470 \text{ a.u.}$ (d)  $I = 6.65 \cdot 10^{12} \text{ W/cm}^2$ ,  $\lambda = 1.8 \mu\text{m}$ ,  $l_f = 85 \text{ a.u.}$ 

**Figure 5.23:** Final kinetic energies of photoelectrons as a function of ionization times for the parameters specified below each panel, corresponding to the results shown in Fig. 5.22. Even though in all cases the same number of optical cycles ( $N = 48$ ) was chosen, the part of the pulse which contributes significantly to ionization differs depending on the laser intensity.

theoretically assumed precise location of the atoms in the inhomogeneous field is difficult to realize experimentally and the spread of the atoms would probably result in a broadening of the HES. With ionization directly from the nanotip, in contrast, the initial position of the electron after ionization can be controlled better and is locally more confined, consequently reducing blurring effects.

Thus, it seems expedient to use the setting in which the *low* energy peak was observed to produce electron distributions as they were theoretically predicted for the *high* energy structure, where the seeming contradiction due to the different names is resolved by the fact that both effects have the same underlying mechanism for the energy upshift in the inhomogeneous field but have so far been investigated at strongly different parameter sets.

### 5.4.3 A new analytical description of the energy upshift

Based on the cycle-averaged model that was described qualitatively above, we can now also derive a quantitative analytical description for the energy that an electron gains while moving in an inhomogeneous field. Following the same basic idea as the one underlying the explanation of Figures 5.19 and 5.20, we can calculate the change of velocity  $v$  during every half-cycle by calculating the change of the area under the acceleration curve in the corresponding half-cycle:

$$\ddot{x} = \frac{\Delta v}{\Delta t} = \frac{|A_1| - |A_2|}{T/2} \quad (5.40)$$

with  $A_1$  and  $A_2$  being the area under the acceleration curve in the first and second half of the half-cycle under consideration, respectively (see top panel of Fig. 5.24 for a visualization). Denoting  $g(x) = \exp(-x/l_f)$  and using  $\int_0^{T/4} E_0 \cos(\omega t) dt = E_0/\omega$ , we can thus approximate:

$$\ddot{x} = \frac{|A_1| - |A_2|}{T/2} = \frac{\frac{1}{\omega} (|E_{0,1}| - |E_{0,2}|)}{\pi/\omega} = \frac{(|E_{0,1}| - |E_{0,2}|)}{\pi} = \frac{E_0 \Delta g}{\pi} = \frac{E_0 \Delta x}{\pi l_f}. \quad (5.41)$$

In the second equality in eq. (5.41), the assumption is that the amplitude of the acceleration curve in the half-cycle of interest determines the area. This ‘local’ amplitude of the acceleration curve can easily be expressed by the amplitudes of the field strength,  $E_{0,1}$  and  $E_{0,2}$ . In the last step in eq. (5.41), a local linear approximation to the exponentially decaying field was assumed (see central panel of Fig. 5.24), where  $\Delta x$  is the local amplitude of the oscillation, which depends on the local value of the electric field  $E_{0,loc}$

$$\Delta x = E_{0,loc}/\omega^2 = E_0 \exp(-x/l_f)/\omega^2 \quad (5.42)$$

and also  $1/l_f$ , the absolute value of the slope of the local linear approximation, varies locally:

$$\frac{1}{l_f} \rightarrow \frac{1}{l_f} \exp(-x/l_f), \quad (5.43)$$

which corresponds to the derivative of  $g(x)$  with respect to  $x$ . Plugging eqs. (5.42) and (5.43) into eq. (5.41) we obtain

$$\ddot{x} = \frac{E_0 (E_0 \exp(-x/l_f)/\omega^2)}{\pi l_f \exp(x/l_f)} = \frac{E_0^2 \exp(-2x/l_f)}{l_f \pi \omega^2}. \quad (5.44)$$



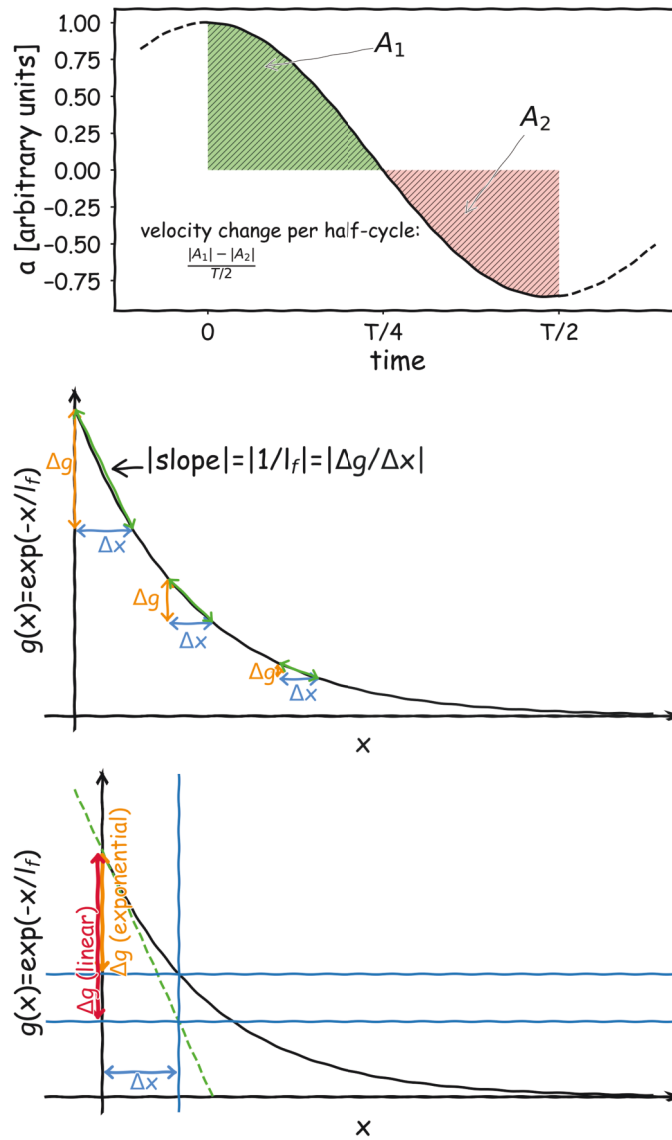


**Figure 5.24:** Top panel: The half-cycle averaged velocity change is calculated as the difference of the areas under two adjacent quarter-cycles of the acceleration curve. Central panel: This illustration of the local linear approximation shows how the difference in the acceleration amplitudes ( $\approx E_0 \cdot \Delta g$ ) and the slope of the corresponding local linear approximation depend on the position of the electron and, in turn, on the oscillation amplitude  $\Delta x$ . The absolute value of the slope can be approximated to be  $1/l_f$  at  $x = 0$ , but becomes smaller for increasing distance  $x$  from the nanotip according to eq. (5.43). Bottom panel: Visualization of how the linear approximation overestimates  $\Delta g$  and thus the difference between the acceleration amplitudes in subsequent quarter-cycles, leading to an overestimation of the energy the electron gains in the inhomogeneous field. The effect is most pronounced for large intensities, where a local linear approximation for one half-cycle fails since the electron's oscillation amplitude is too large.

This differential equation is analytically solvable:

$$\begin{aligned}
 x_{approx} &= l_f \log \left( \cosh \left( \frac{E_0 t}{l_f \sqrt{\pi} \omega} \right) \right) \\
 \Rightarrow v_{approx} &= \frac{dx_{approx}}{dt} = l_f \frac{1}{\cosh \left( \frac{E_0 t}{l_f \sqrt{\pi} \omega} \right)} \sinh \left( \frac{E_0 t}{l_f \sqrt{\pi} \omega} \right) \frac{E_0}{l_f \sqrt{\pi} \omega} = \frac{E_0 \tanh \left( \frac{E_0 t}{l_f \sqrt{\pi} \omega} \right)}{\sqrt{\pi} \omega} \\
 \Rightarrow E_{kin,approx} &= \frac{v_{approx}^2}{2} = \frac{E_0^2 \tanh^2 \left( \frac{E_0 t}{l_f \sqrt{\pi} \omega} \right)}{2\pi\omega^2}.
 \end{aligned} \tag{5.45}$$

The validity of the approximation can be seen in the bottom panel of Fig. 5.22. Note, though, that the model is restricted to the applicability of the ‘linear local approximation’, which implies that the electric field the electron experiences within one half-cycle can be well approximated by a linear function. The breakdown of this assumption will be further addressed in section 5.4.4.

Also, even though this cycle-averaged description is a powerful and simple estimate of how the electron’s velocity, and thus energy, changes while moving in the inhomogeneous field, it does not resolve the subcycle dynamics and is thus also insensitive to, for example, variations in the ionization time. However, crucial properties of the peak, such as its width, depend strongly on how different ionization times lead to different energies, as we have seen in the analysis of the HES width in section 5.3.4. This motivates the derivation of an analytical approximation for the subcycle dynamics, which will be done in the following subsection. It seems important to emphasize already now, though, that the cycle-averaged nature of the above description also leads to the fact that eq. (5.45) does not capture the difference between the electrons that are ionized at a positive or negative sign of the electric field. This difference may be included in the model by using the maximal field strength the electron sees during propagation rather than the field strength during ionization for  $E_0$ .

#### 5.4.3.1 An analytical description including subcycle effects

One way to include subcycle effects is found in combining the cycle-averaged description derived in the preceding section with the perturbative model derived in section 5.3.2. The perturbative model in its pure form worked well in section 5.3.2, where the short pulse duration allowed to describe the inhomogeneous field by a linear model. Now, however, we use longer pulses and a more accurate approximation of the inhomogeneous field by applying the exponential description of eq. (5.38) is required. Technically, we could approximate this by the linear model again, of course, in order to apply the perturbative approach, which would then read

$$v_{perturb}(t) = v_0(t) - \frac{1}{l_f} v_1(t). \tag{5.46}$$

Note that this is the same perturbative ansatz as in eq. (5.26), the only difference being the notation of  $-1/l_f$  corresponding to  $2\beta$  in eq. (5.26). Therefore, this linear approximation of the exponential case also has the same problem as the linear ansatz in eq. (5.26): We need to avoid the zero crossing of  $(1 - x/l_f)$ , which requires short pulses.

One way to make use of the perturbative approach that is based on the linear approximation after all is to realize that eq. (5.46) can be improved upon by adapt-

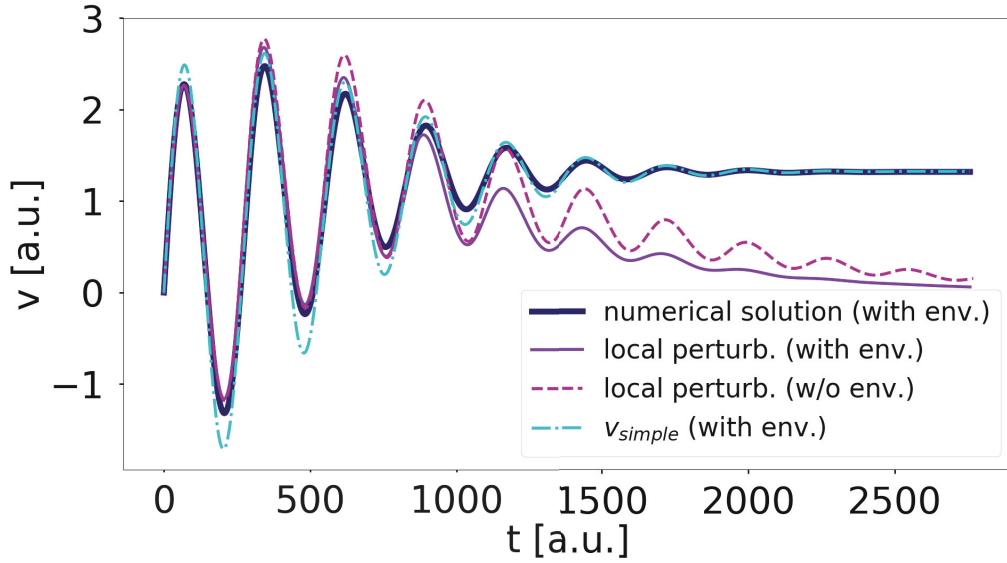


**Figure 5.25:** Velocity as a function of time for an electron. The maximal enhanced intensity of the electric field is  $I = 1 \cdot 10^{14} \text{ W/cm}^2$  at the position where the electron is released, the wavelength is  $\lambda = 2 \mu\text{m}$ ,  $\phi_{CEP} = \pi$ , and the decay length of the field is  $l_f = 750 \text{ a.u.}$ . The number of optical cycles is  $N = 20$  and the electron is born at the center of the pulse at  $t_0 = 0$ . The local perturbative solution according to eq. (5.47) (solid purple line) matches the numerical solution (solid dark blue line) well in the first few cycles, but diverges considerably later on. One can see that neglecting the envelope, i.e. using eqs. (5.50) to (5.52) (dashed pink line), gives a similarly good approximation. Note that even though the approximation  $v_{simple}$  according to eq. (5.49) (dash-dotted turquoise line) gives a better overall agreement with the numerical solution, the local perturbative model describes the subcycle dynamics more accurately in the first few cycles. Moreover, for other parameters the local perturbative model can also be the more accurate approximation for the final velocity than  $v_{simple}$  as becomes clear from Fig. 5.26.

ing the field strength in the zeroth order terms. This is done by replacing  $E_0$  by  $E_0 \exp(-x_{approx}(t)/l_f)$  in the zeroth order terms  $x_0$  and  $v_0$ , where  $x_{approx}$  is the cycle-averaged approximation according to eq. (5.45). We are thus taking into account that the maximal field strength the electron sees during one particular half-cycle decays with increasing distance from the nanostructure. As the zeroth order term  $x_0$  is also used in the calculation of the first order velocity, this modification introduces a factor of  $\exp(-x_{approx}(t)/l_f)$  also in the first order velocity  $v_1$ , leading to

$$v_{perturb,improved}(t) = \left( v_0(t) - \frac{1}{l_f} v_1(t) \right) \cdot e^{-x_{approx}(t)/l_f}. \quad (5.47)$$

In the following, this model is called the local perturbative model since it corresponds to the slope of the linear approximation being adapted locally. This can be seen from comparing the prefactor of  $v_1$  in eq. (5.46) and (5.47) realizing that

$$\frac{1}{l_f} \rightarrow \frac{1}{l_f} e^{-x_{approx}(t)/l_f} \quad (5.48)$$

was applied, which corresponds to the local linear approximation presented in eq. (5.43) of the previous section (also see the central panel of Fig. 5.24 for a visualiza-

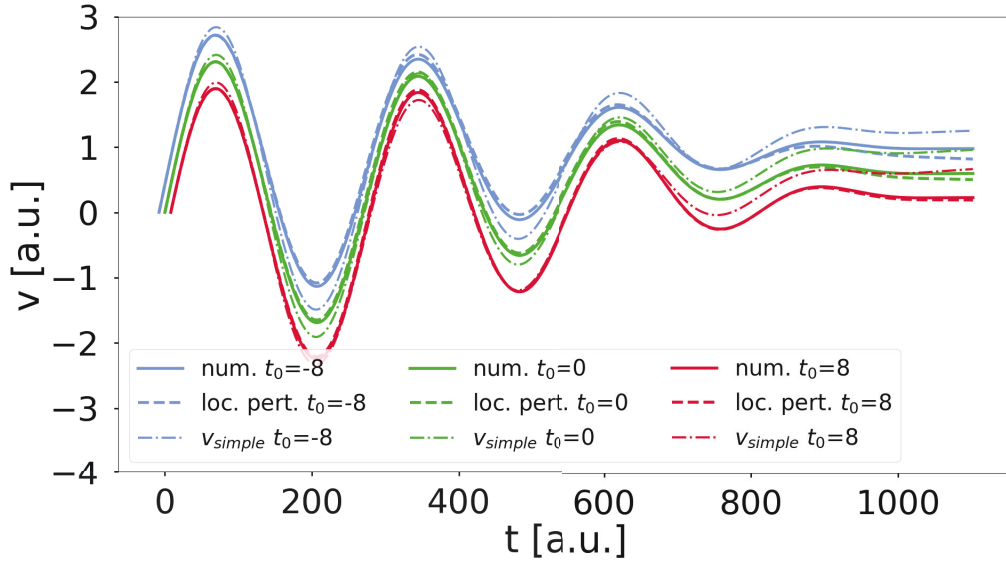


**Figure 5.26:** Velocity as a function of time. The maximal enhanced intensity of the electric field is  $I = 1 \cdot 10^{14}$  W/cm<sup>2</sup> at the position where the electron is released, the wavelength is  $\lambda = 2$   $\mu$ m,  $\phi_{CEP} = \pi$ , and the decay length of the field is  $l_f = 1600$  a.u.. The number of optical cycles is  $N = 8$  and the electron is born at times  $t_0$  specified in the legend. Here, the subcycle dynamics is resolved better with the local perturbative approach ('loc. pert.', eq. (5.47)) than with the approximation according to eq. (5.49) (' $v_{simple}$ '). This is the case over a wide range of  $t_0$ , which are chosen to be  $t_0 = \pm\sigma = 8$  (see eq. (5.33)) and  $t_0 = 0$ .

tion and eq. (5.41) for the derivation). In contrast to eq. (5.43), the position is directly estimated by the cycle-averaged position  $x_{approx}$  described in eq. (5.45) here. With increasing distance from the nanostructure, the slope of the local linear function gets progressively shallower and we do not need to worry about the zero-crossing of this local linear function.

An exemplary velocity curve approximated by eq. (5.47) is shown as a solid purple line in Fig. 5.25, where we can see that it matches the numerical solution (solid dark blue line) well in the first few cycles but deviates later on. At the point where the approximation starts to deviate, however, the approximation is already close to the velocity the full numerical solution converges to. Therefore, one may still use the perturbative approach of eq. (5.47) to estimate the final velocity by evaluating it at the point where it diverges e.g. from the cycle-averaged velocity  $v_{approx}$  given in eq. (5.45).

In Fig. 5.25 we find another approximation, which in that case matches the numerical solution better at the end of the pulse. It is described by

$$v_{simple} = v_0(t)e^{-x_{approx}(t)/l_f} + v_{approx}. \quad (5.49)$$

Here, the first term equals the first term of eq. (5.47) but the second term is replaced by  $v_{approx}$  (eq. (5.45)), based on the assumption that  $v_{approx}$  approximates the final velocity well. Note that even though the approximation  $v_{simple}$  according to eq. (5.49) (dash-dotted turquoise line) gives a better overall agreement with the numerical solution in Fig. 5.25, the local perturbative model describes the subcycle dynamics more accurately in the first few cycles. Moreover, for other parameters the local perturbative model can also be the more accurate approximation than  $v_{simple}$ . Fig. 5.26 presents

a case where the local perturbative model according to eq. (5.47) approximates the numerical solution better than eq. (5.49) over a wide range of ionization times  $t_0$ . In particular, this figure shows how the effect of the different ionization times on the final velocity can be approximated in the subcycle models, which is vital in studying the width of the resulting peak in the photoelectron spectrum, as we learned in section 5.3.4.

The fact that with the exponentially decaying field we are now able to use longer pulses than in the linear approximation in sections 5.2 and 5.3 opens the door to neglecting envelope effects. This has the advantage that the lengthy, albeit analytical, expressions of the perturbative approach from section 5.3.2 can be reduced to a more convenient size. Neglecting the envelope we obtain the following expressions:

$$v_0(t) = - \int_{t_0}^t E_0 \cos(\omega t' + \phi_{CEP}) dt' = \frac{E_0(\sin(\omega t_0 + \phi_{CEP}) - \sin(\omega t + \phi_{CEP}))}{\omega} \quad (5.50)$$

$$\begin{aligned} x_0(t) &= \int_{t_0}^t v_0(t') dt' \\ &= - \frac{E_0(\cos(\omega t_0 + \phi_{CEP}) - \cos(\omega t + \phi_{CEP}))}{\omega^2} + \frac{E_0 \sin(\omega t_0 + \phi_{CEP})(t - t_0)}{\omega} \end{aligned} \quad (5.51)$$

$$\begin{aligned} v_1(t) &= - \int_{t_0}^t E_0 \cos(\omega t' + \phi_{CEP}) x_0(t') dt' \\ &= \frac{E_0^2}{4\omega^3} \left( 2\omega(t_0 - t) + 4 \sin(\omega(t - t_0)) \right. \\ &\quad \left. + 2\omega(t_0 - t)(\cos(\omega(t_0 - t)) - \cos(2\phi_{CEP} + \omega(t_0 + t))) \right. \\ &\quad \left. + \sin(2(\phi_{CEP} + \omega t_0)) - \sin(2(\phi_{CEP} + \omega t)) \right). \end{aligned} \quad (5.52)$$

Comparing this version of  $v_1$  with the unwieldy expression in appendix A.5 shows that neglecting the envelope significantly reduces the length of this term. The dashed pink line in Fig. 5.25 shows how using eqs. (5.50) to (5.52) in the local perturbative approach given in eq. (5.47) is a reasonable approximation which starts deviating from the numerical solution at about the same point as the local perturbative solution with the envelope included.

#### 5.4.4 Explaining the experimentally observed linear intensity scaling

In the framework of the cycle-averaged approximation introduced in section 5.4.3 we can now also understand directly the linear scaling of the energy of the LEP with intensity reported in [75]. As can be seen from the approximate description in eq. (5.45), the final energy should scale as  $E_0^2$  since  $\tanh \rightarrow 1$  for large  $t$ . Note that this statement differs from the widely known effect that the cycle-averaged kinetic energy of an electron in a homogeneous field scales with  $E_0^2$ . In homogeneous fields this statement pertains to the quiver motion during propagation whereas the statement made here for the inhomogeneous fields concerns the final energy at the end of the pulse for an electron born at the center of the pulse. Such an electron has zero energy at the end of propagation in a homogeneous laser pulse, but undergoes an energy upshift in an inhomogeneous field due to the mechanism that is qualitatively described in section 5.4.1 and mathematically captured in eq. (5.45).

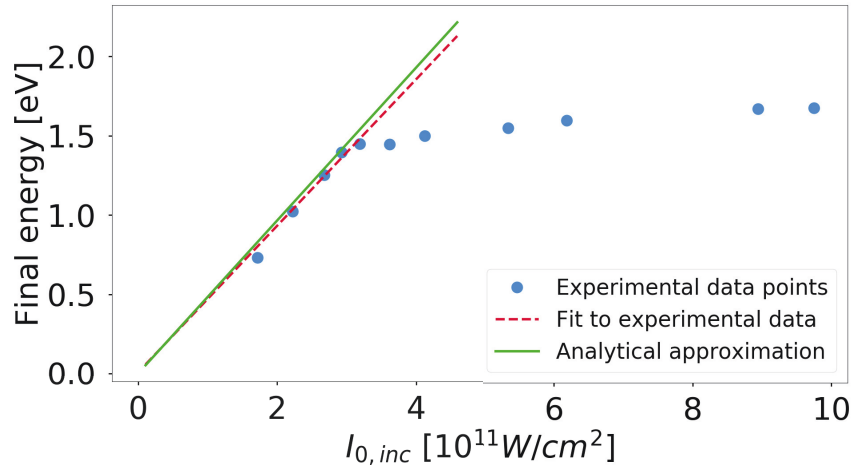


**Figure 5.27:** Final photoelectron energy as a function of the incident laser intensity (note that the enhanced intensity is significantly larger). The experimental data and the linear fit to it were extracted from [75]. The analytical result is described by eq. (5.45) where a field enhancement factor of 5 was assumed, which lies in the regime estimated in [75].

The theoretically predicted linear scaling of the final energy with intensity was indeed observed in the experiment of the LEP in [75] for not too large intensities. The experimental results are depicted in Fig. 5.27 along with the linear fit done in [75] and the estimation according to eq. (5.45), which matches the experimental result nicely. Moreover, we can understand intuitively why the experiment in [75] exhibits a breakdown of the linear scaling for larger intensities: The local linear approximation over one half-cycle overestimates the amplitude of  $\Delta g$  and thus overestimates the energy gain (see bottom panel of Fig. 5.24). This effect becomes stronger with increasing oscillation amplitudes  $\Delta x$ , which we get for larger  $E_0$ , and explains why our model overestimates the spectral position of the peak for large intensities.

Furthermore, from the visualization in Fig. 5.24 it becomes clear that the breakdown of the linear scaling with intensity also marks the regime where the electron explores very different parts of the inhomogeneous fields during one half-cycle and where changes during one half-cycle are so strong that they cannot be approximated linearly and the cycle-averaged approach fails. This makes clear that the approximate description derived in section 5.4.3 is restricted to  $\delta$ -parameters in the intermediate regime. Thus, we can also understand the seemingly odd feature of eq. (5.45) according to which the final energy depends only on  $E_0$  and  $\omega$  but not on  $l_f$ . The decay length  $l_f$  only determines how fast the final velocity is reached in this approximation. However, via the  $\delta$ -parameter,  $E_0$  and  $\omega$  implicitly contain (approximate) information about  $l_f$ , which explains why the approximation of eq. (5.45) works so well to describe the final energy, as we have seen e.g. in Fig. 5.22. In this figure, all combinations of the strongly different intensities, wavelengths and decay lengths correspond to a  $\delta$ -parameter of about 4.

### 5.4.5 Conclusion and Outlook

This last section 5.4 in the chapter on inhomogeneous fields was devoted to showing that the seemingly different effects dubbed low-energy peak (LEP) and higher energy



structure (HES) can be understood in one unified theory in which the different observed peaks emerge because of an upshift in energy due to the motion of the electron in the inhomogeneous field. In both the LEP and HES setting the asymmetric amplitude profile of the acceleration curve, introduced by the inhomogeneity of the field, leads to a systematic energy gain in the inhomogeneous field. Two reasons for the HES having appeared at high energies in [73] and the LEP having been measured at low energies in [75] were identified: First, the LEP was measured in a spectrum of photoelectrons that were released directly from the nanotip leading to an initial movement away from the tip, towards smaller field strengths. In contrast, the HES was predicted in a setting where the electrons are ionized from an atom in the near-field of a nanotip with the electron initially approaching the nanostructure. The higher maximum field the electron therefore sees in the HES setting than in the LEP setting accounts for a factor of the order of two to three in the final energy. The more important reason for the different energy scales at which the HES and LEP were reported previously, though, is the fact that vastly different intensities and decay lengths were chosen in the corresponding publications.

As for both the HES and LEP the combination of intensity, decay length, and wavelength was nonetheless in the same intermediate  $\delta$ -regime, we have seen that the overall dynamics is the same at the different energy scales and can be described by the same theory. Closed-form expressions were derived to describe the cycle-averaged energy gain in the inhomogeneous field, which also explain the linear scaling of the spectral position of the peak with intensity that was reported for the experimentally observed LEP.

Unifying the electron dynamics for high and low energies on the one hand, and for the different settings of electrons being released directly from the nanotip and from the gas phase on the other hand, paves the way of experimentally realizing the favorable features that have been theoretically predicted for the HES [73, 74]. One problem with realizing the HES in the way it was described in sections 5.2 and 5.3 is the fact that the ionization happened from the gas phase. While our theoretical model allowed us to neatly place the atom at a clearly defined position thus experiencing a well-defined field strength and decay length, a real system would not allow such precise atom location. Rather, one would need to employ an atomic beam with a finite spread in space. The atoms in that beam would consequently be exposed to different field strengths and slopes thereof, which would lead to blurring and thus broadening of the HES peak. Now, however, we have seen that we can use the LEP setting, i.e. ionization from the tip, to create spectrally narrow peaks at energies as formerly only reported for the HES (top panel of Fig. 5.22). The advantage of using ionization from a tip is not only that it is a well-established experimental technique but, more importantly, that here the electron position upon ionization and thus the field strength and decay length the electron experiences after its birth in the continuum are more clearly defined and controllable and can be kept almost constant for a large ensemble of photoelectrons. Thus, we can be optimistic about the experimental realization of creating almost monoenergetic electron beams of tuneable energy in the higher-energetic regime using inhomogeneous fields.

## Tracking the ionization site in a neutral diatomic molecule

*“A diatomic molecule is a molecule with one atom too many.”*

— Arthur Leonard Schawlow (Nobel Prize Laureate in 1981)

### Overview of this chapter

Coulomb explosion has proven to be a powerful technique to investigate the effect of ionization enhancement and to track the ionization site in molecules. However, this technique does not allow to determine the ionization site in neutral homonuclear molecules. Here, a new method is proposed for quantitatively retrieving the ratio of ionization happening at the up- and downfield atomic site in a neutral diatomic molecule from experimental data by means of comparison with numerical simulations. The key mechanism is based on the deflection of the electron in the asymmetric Coulomb potential of a tilted diatomic molecule, which introduces an asymmetry in the final photoelectron momentum distribution. As the degree of asymmetry depends on whether the electron is born at the up- or downfield atom and as the ionization site ratio can be controlled in trajectory-based simulations, this information can be used to quantify the ratio of ionization from the up- and downfield site from experimental photoelectron momentum distributions.

### 6.1 Goals and challenges in describing molecular effects

After having studied the effect of field inhomogeneities as they are typically found in the vicinity of a nanostructure in the previous chapter, this chapter deals with inhomogeneities that arise in a more natural way: the inhomogeneities of the molecular potential. Despite of, and maybe even because of, the inhomogeneities in molecular systems not being as extreme as near nanostructures, we will find that describing the resulting effects is a challenging task and requires numerical treatment.

As we have seen, for instance in chapter 3, already superposing an atomic Coulomb potential and a homogeneous laser field is challenging to describe theoretically. Entering the regimes of molecules, however, we have to handle far more degrees of freedoms that play a role at different time scales: The rotational degree of freedom is relevant on the picosecond timescale, vibrational freedoms are observed on a femtosecond scale and the electronic movement happens on the attosecond scale [308]. Even in seemingly benign diatomic molecules the symmetry of molecular orbitals [309–314], the

possibility to dissociate into atomic fragments [315–318], and variable internuclear distances [319–321] already complicate matters considerably. This makes it all the more surprising that molecular targets in strong field ionization have been studied from the early days on [322–330] – beginning in the late 1980s. Even though we are still discussing the description of the ionization process in the hydrogen atom (see chapter 3 or Refs. [116, 117, 331, 332]), strong field ionization is already employed as a tool to understand molecular effects better [308, 333, 334]. For example, in Ref. [335] strong field holography [336–338] is used to resolve the difference of the nuclear dynamics of  $H_2$  and  $D_2$  with subangstrom spatial and subcycle temporal resolution. Other publications helped understand how the phase of the electron depends on the atomic site the electron is born at [130, 339].

The key to success in investigating molecular systems with strong field pulses is often based on a concept one may describe as the ‘molecule taking a selfie’ [20], i.e. the very electron that was ionized can, on its way to the detector, return (close) to the remaining molecular ion. Thus, information about the molecule itself is encoded in the ionized electron. Among these ‘self-interrogating’ techniques, methods referred to as laser-induced electron diffraction (LIED) [16–19] and photoelectron holography [336–338] have been particularly successful in recovering information about the molecular structure and dynamics [130, 131, 339–348]. Similarly, high-harmonic generation spectra from molecules contain information about the molecule the electron has accrued before recombination, i.e. during ionization and propagation [310, 311, 349–353].

Despite all of this success in dealing with molecules, even nature’s simplest molecule,  $H_2^+$ , isn’t fully understood yet [308]. A great deal of the problems arising in the context of molecules is due to the difficulties in modeling molecules theoretically. The additional degrees of freedom of a molecule are difficult to capture by numerical solutions of the TDSE [354–356] and this method is therefore usually only used for either very small molecules like  $H_2^+$  or in proof-of-principle calculations with model orbitals [357, 358]. Resorting to other popular techniques such as SFA and CTMC using ADK rates often yields surprisingly good results for a large variety of molecules [357, 359–367] but does not make things less contentious. For example, the molecular expansion of SFA (MO-SFA) including Stark corrections [98] predicts a maximized ionization rate for a CO molecule when the laser field points in the C-O direction whereas the molecular expansion of ADK (MO-ADK) that includes Stark corrections [368, 369] predicts such a maximum for the laser field being directed in the O-C direction [370]. An experiment devised to test these predictions indicated that double ionization of CO is more likely to occur when the laser field is pointing from C to O [371] and that more generally the linear Stark effect plays a minor role in this system.

The importance of taking account of traits of the molecular orbital one is ionizing from, e.g. its symmetry [309–314], makes information from quantum chemistry calculations beneficial for many theoretical models. But, again, while including orbital information is relatively straight forward in the atomic case and can, for example, be described in a method called partial Fourier transform [372], it is less clear how to expand this theory for the molecular case [131, 373–375]. Therefore, even though theory was able to make experimentally validated predictions about molecular effects (see e.g. [319, 326, 376, 377] or [378–381]), it seems even more vital for molecular theories than for atomic theories to be backed up by experimental results, which is the path we also chose for the present chapter.

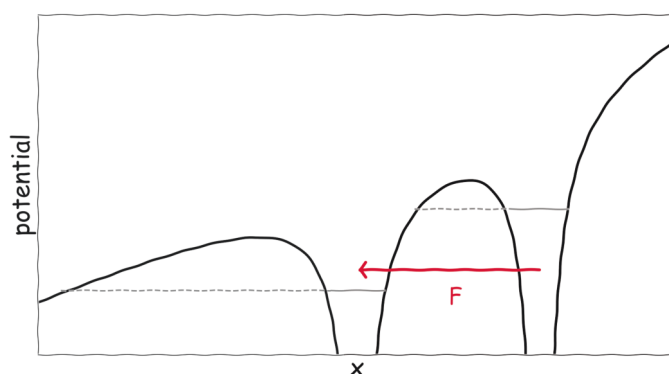


**Figure 6.1:** Illustration of a diatomic potential for alignment of the internuclear axis along the polarization axis. The horizontal gray lines represent the linearly Stark-shifted ionization potential (see e.g. eq. (1) and Fig. 2 in [384] or Fig. 1(c) and the equations on p. 043002-4 in [123]). The ionization barrier for the upper well is considerably narrowed by the influence of the lower well, which can lead to ionization enhancement, provided electron localization at the upfield atom is significant. However, the force  $F$  of the electric field can drive the electron towards the downfield well, which is expected to play a role if the electron position adapts adiabatically to the laser field and which would result in the downfield atom to be the dominant ionization site.

## 6.2 The problem of tracking the ionization site in a molecule

This chapter is devoted to answering the question at which atomic site in a molecule the electron is born. More precisely, we are interested in the ratio at which the electrons are born from the upfield and downfield atom, where upfield and downfield refer to the atom where the potential is heightened or lowered due to the laser field, respectively. Knowledge about the site the electron is born at is not only vital in understanding the tunneling process in molecules itself but is relevant for theoretically modeling, and thus the analysis and interpretation, of molecular imaging techniques [382] such as molecular orbital tomography [21, 383], photoelectron holography [336–338], or laser-induced electron diffraction (LIED) [16–19].

This problem of identifying the tunneling site in molecules is usually addressed in the context of an effect called charge resonance enhanced ionization (CREI), sometimes also referred to as ionization enhancement. Therefore some introductory words on this effect seem warranted.

The experimentally observed effect of ionization being larger when the molecular axis of a diatomic molecule is aligned along the polarization axis of the electric field when compared to the perpendicular orientation [322, 385] was explained by Codling et al. in 1989 [326]. They proposed a mechanism in which the internuclear barrier is suppressed for certain internuclear distances. Thus, the barrier that an electron located in the upfield well has to tunnel through is narrower than the barrier in perpendicular orientation and ionization is enhanced (see Fig. 6.1). Even though this model was introduced decades ago, doubts about its validity haunted physicists for a long time [318, 386] and only recently various major breakthroughs were obtained in this debate [123, 374, 382, 387–391]. The dominant tool in the study of CREI is the mechanism of Coulomb explosion since the enhancement depends strongly on the internu-

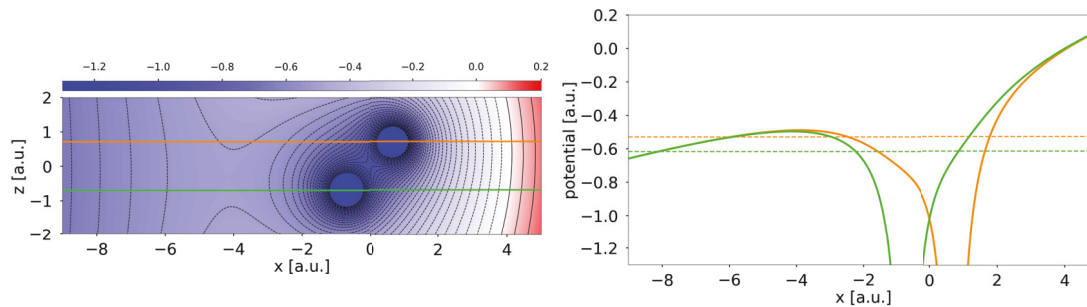


**Figure 6.2:** Left panel: Equipotential lines of the Coulomb potential of a  $N_2$  molecule tilted by  $45^\circ$  against the polarization axis under the influence of a constant electric field ( $E_0 = 0.061$  a.u.  $\leftrightarrow I = 1.3 \cdot 10^{14}$  W/cm $^2$ ). Right panel: Cuts through the potential surface of the left panel parallel to the polarization axis through the upfield atom (orange line, also marked in the left panel) or downfield atom (green line), respectively. The horizontal dashed lines in the right panel represent the linearly Stark-shifted ionization potential (similar to the dashed gray lines in Fig. 6.1).

clear distance which can be easily determined from the kinetic energy release (KER) during Coulomb explosion by invoking Coulomb's law telling us that the KER is inversely proportional to the distance between the atoms at the time of defragmentation [392].

While more and more experiments have validated that there are indeed internuclear distances at which ionization is enhanced, the underlying mechanism remains under debate [378, 379, 393]. One path to understanding the ionization mechanism in molecules better is the determination of the tunneling site and recent studies along this line have provided strong evidence for the suppressed upfield barrier at certain internuclear distances leading to the enhancement [123, 374, 382, 387–391]. An important step was achieved in Ref. [391], where the dominance of ionization from the upfield atom in an ionization enhancement setting was measured. This experiment relied again on the mechanism of Coulomb explosion and could distinguish between the ionization ratios from the up- and downfield atom by making use of the fact that the ionization of  $ArXe^+$  happened at the Ar atom. Thus, this method is not only restricted to doubly charged ionization products but also requires a diatomic molecule of different atomic species.

Ionization enhancement is explained by the idea that the electron is born at the upfield atom, escaping through the lowered internuclear barrier, as can be seen from the sketch in Fig. 6.1 of a molecule whose internuclear axis is parallel to the polarization axis. However, as also becomes clear from this sketch, the field should drive the electron cloud towards the downfield atom. This effect plays a role if the electron position adapts to the laser field adiabatically, which is expected to happen if the internuclear distance is small and the laser field changes relatively slowly. Therefore, for the electron to escape over the suppressed internuclear barrier, the potential barrier is required to move sufficiently fast to allow trapping of the electron in the upper well in the first place [319, 333, 377, 384, 394–396]. Since this effect only happens at internuclear distances that lead to ionization enhancement, studying it does not provide information on what atomic site the electron is born at when the molecule is found at other internuclear distances.

Obviously, things are further complicated if the molecular axis is tilted with respect



to the laser polarization axis (see Fig. 6.2). Such a system will be discussed in the following: A neutral  $N_2$  molecule that is tilted against the laser polarization axis by 45 degrees is (single) ionized. This setup equals the one described in [339], the experimental data of which will be used for comparison later on. This system does not result in defragmentation via Coulomb explosion, which is usually drawn on when investigating the atomic site at which the electron is born in a molecule. Even though a recently proposed method for the determination of the tunneling site [382] does not use the concept of Coulomb explosion and could be applied to neutral molecules, it does not allow *quantitative* insights into the likelihood of electrons being ionized from the two different atomic sites. Below, we develop an approach to quantize ionization rates from the up- and downfield site in the tilted diatomic molecule.

## 6.3 A new method for tracking the ionization site in a molecule

### 6.3.1 Experimental results

The fact that electrons that are born at the two different atomic sites and should thus explore different Coulombic potentials, which in addition are asymmetric with respect to the polarization axis of the laser, is expected to lead to an asymmetry of the photoelectron momentum distribution at the detector. However, looking at the experimentally detected photoelectron momentum distribution of a tilted  $N_2$  molecule in Fig. 6.3 no asymmetry is visible, to the bare eye, in the holographic fringes. The effect only becomes perceptible when averaging over the  $v_z$ -values for each  $v_x$  in the following way

$$v_{z,mean}(v_x(i)) = \frac{\sum_{j=1}^n w(i, j) v_z(j)}{\sum_{j=1}^n w(i, j)}, \quad (6.1)$$

where  $w(i, j)$  is the momentum distribution at the detector in the  $i$ th bin of  $v_x$  and the  $j$ th bin of  $v_z$ . This quantity, as directly extracted from the experimental data shown in Fig. 6.3, is plotted as a blue line in Fig. 6.4 and we can see that it exhibits an asymmetry, meaning it is not a horizontal line located at  $v_{z,mean} = 0$ . Surprisingly, also the cases of  $0^\circ$ ,  $90^\circ$ , and even the orientation-averaged curve show an asymmetry. Theoretically, one would expect the photoelectron momentum distribution in these cases to be symmetric resulting in a (almost) horizontal line at  $v_{z,mean} = 0$ , which is observed in QTMC simulations of these systems. The fact that the asymmetry found in these three experimental systems where one would expect no asymmetry ( $0^\circ$ ,  $90^\circ$ , and orientation-averaged) is about the same in all of these cases points to a systematic tilt of the experimental setting, which needs to be corrected. This is done following the idea that was already successfully applied in Ref. [339], where these data sets were previously used, by subtracting the orientation-averaged case from the 45-degree case. The corrected curve is shown in green in Fig. 6.4 and in the following will be referred to as the experimental curve. This curve can also be found as a bold green line in Fig. 6.6.

We can see that for  $v_x < 0$  the mean value  $v_{z,mean}(v_x)$  is mostly negative for that curve, whereas for  $v_x > 0$  this quantity is found primarily in the positive regime. This effect will be further explained in section 6.3.3 on the basis of QTMC simulations, the details of which will be given first in section 6.3.2.



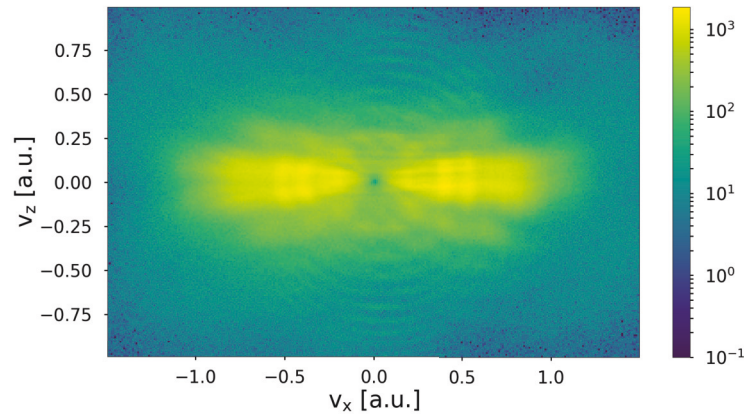


**Figure 6.3:** Experimental 2D photoelectron momentum distribution for the  $45^\circ$  case. The data was previously published in [339].

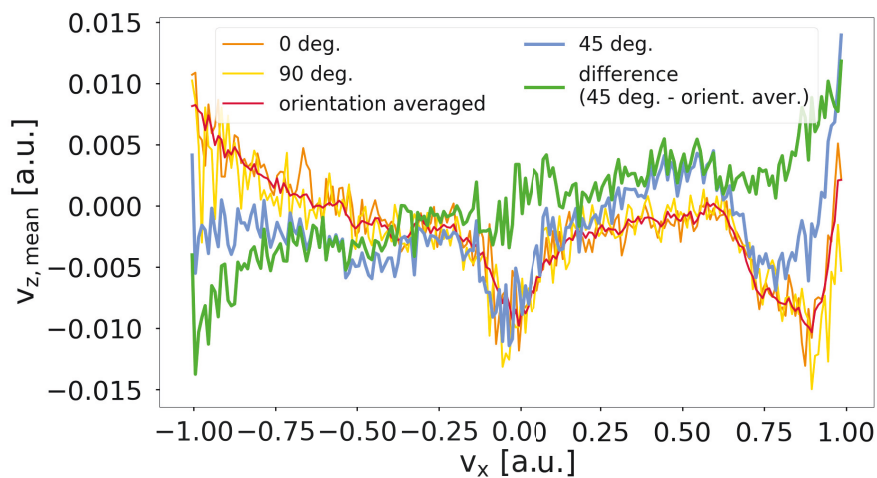


**Figure 6.4:**  $v_{z,\text{mean}}$  as a function of  $v_x$  calculated by applying eq. (6.1) to the experimental data published in [339] and shown in Fig. 6.4 for the case of  $45^\circ$ . One can see that not only the  $45^\circ$  data (blue curve) exhibits an asymmetry in  $v_{z,\text{mean}}$  but also the orientations of  $0^\circ$ ,  $90^\circ$ , and the orientation-averaged curve are asymmetric (i.e. they are not a flat curve at  $v_{z,\text{mean}} = 0$ ). As the asymmetry is about the same in all of these three cases for which one would expect no asymmetry (i.e.  $0^\circ$ ,  $90^\circ$  and averaged orientation), this effect is interpreted as due to a systematic tilt in the experimental setup that needs to be corrected for. This is done by subtracting the orientation-averaged curve from the curve for  $45^\circ$  (green line).

### 6.3.2 Performing molecular QTMC simulations

To understand the asymmetry observed in the experimental data, Quantum Trajectory Monte Carlo (QTMC) simulations are performed [62], where the corrections proposed in [60] and the phase depending on the atomic positions with respect to the polarization direction introduced in [130] are included. The peak intensity is set to  $I = 1.3 \cdot 10^{14}$  W/cm<sup>2</sup> and the wavelength is 800 nm, just as in the experiment [339, 397].

As we want to compare our results directly to experimental results now, assuming a constant intensity, as we have done up till now, is not sufficient but we have to take into account that there is a spatial variation of the intensity in the focal volume. This intensity profile is commonly described by a Lorentzian along the laser beam axis, which for the sake of consistency with the nomenclature of cylindrical coordinates we will set to  $z$  for the following derivation, and by a Gaussian profile in  $\rho$ , the distance perpendicular to the beam axis [398]. It reads

$$I(\rho, z) = I_0 \left( \frac{w_0}{w(z)} \right)^2 \exp\left(-\frac{2\rho^2}{w^2(z)}\right), \quad (6.2)$$

where  $I_0$  denotes the maximal intensity in the focus and  $w(z) = w_0 \sqrt{1 + (z/z_0)^2}$  is the  $z$ -dependent waist with the minimal waist  $w_0$  and with  $z_0 = \pi w_0^2 / \lambda$  denoting the Rayleigh range. The rate of electrons generated within the focal volume is given by [399]

$$\frac{dN}{dt} = \int d^3r R(I(\rho, z)), \quad (6.3)$$

where  $R(I) = d^4N/(d^3r dt)$  denotes the number of electrons generated per volume and time at the constant intensity  $I$ . In order to transform the integral in eq. (6.3) into an integral over intensity, we need the contour surface of constant intensity  $I$ , a visualization of which can be found in Fig. 1a in [400]. More specifically, we need the volume between two intensity surface shells with constant intensities  $I$  and  $I + dI$  [401]

$$V_{FV}(I, I_0) = \pi z_0 w_0^2 \left[ \frac{4}{3} \left( \frac{I_0 - I}{I} \right)^{1/2} + \frac{2}{9} \left( \frac{I_0 - I}{I} \right)^{3/2} - \frac{4}{3} \tan^{-1} \left( \frac{I_0 - I}{I} \right)^{1/2} \right]. \quad (6.4)$$

Thus, we can transform eq. (6.3) into an integral over intensity [400, 402]

$$\frac{dN}{dt} = \int R(I(\rho, z)) d^3r = \int R(I) dV(I, I_0) = \int_0^{I_0} R(I) \left| \frac{\partial V_{FV}}{\partial I}(I, I_0) \right| dI, \quad (6.5)$$

where we can use eq. (6.4) to obtain

$$\left| \frac{\partial V_{FV}}{\partial I}(I, I_0) \right| = \frac{\pi z_0 w_0^2}{3} \frac{2I + I_0}{I^{5/2}} \sqrt{I_0 - I}. \quad (6.6)$$

Consequently, the relative weight of each intensity is given by [130, 402]

$$\frac{2I + I_0}{I^{5/2}} \sqrt{I_0 - I}. \quad (6.7)$$

This is implemented as follows: Prior to the sampling process described in chapter 2.3.2, intensities are sampled according to eq. (6.7) using a reject-sampling algorithm. For each intensity a batch of trajectories (typically 500 trajectories) is sampled such

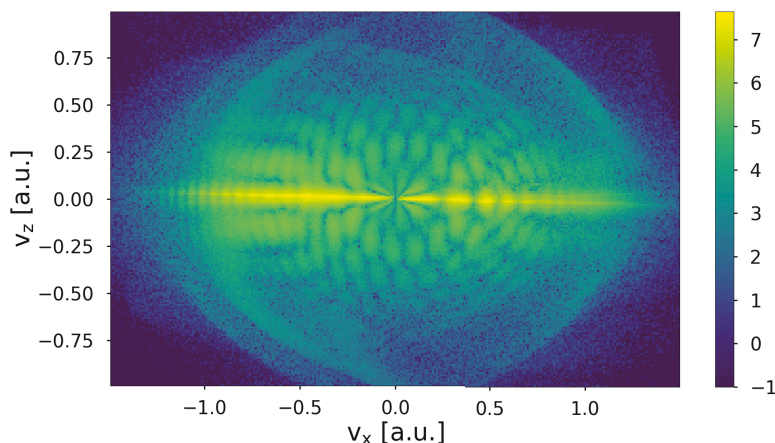


**Figure 6.5:** 2D momentum distribution obtained in a QTMC simulation as described in section 6.3.2 for the case of an ionization site ratio of  $q = 0.6$  (as defined in eq. 6.8). The color bar is given on a logarithmic scale.

that the initial times and momenta follow a probability distribution which treats this specific intensity as the maximal intensity.

Furthermore, in order to take into account that the shape of the molecular orbital changes the probability distribution of the initial transverse momentum, we modify the probability distribution by a prefactor obtained in a partial Fourier transform [372] analogously to the way it is described in [131]. The molecular orbital that is needed for this method was computed in the STO-6G Gaussian basis with the restricted Hartree-Fock (RHF) method using the quantum chemistry package GAMESS [403]. In the basis set name, STO stands for 'Slater Type Orbitals' and 6G signifies that each atomic Slater-type orbital is represented by six Gaussian basis functions. The accuracy of the RHF/STO-6G calculation is supported by the fact that the ionization potential, computed according to Koopmans' theorem [404] as minus the energy of the highest-occupied molecular orbital, is  $0.57 \text{ a.u.} = 15.5 \text{ eV}$ . This value is very close to the experimentally observed ionization potential of  $15.6 \text{ eV}$  [405].

The laser is polarized along the  $x$ -axis and is six cycles long under a  $\cos^2$ -envelope (see eq. (2.4)). The ionization potential is chosen to be  $I_p = 15.6 \text{ eV}$  [339, 405]. Since we are in the intermediate nonadiabatic regime ( $\gamma = 0.9994$ ), the nonadiabatic ionization theory of Li et al. [3] is used to describe the initial conditions at the tunnel exit (for details also see chapter 3). The Coulomb potential used during propagation is the same as the one described in the supplementary of [339] and in [130], where the positive charge that the molecule has after ionization is distributed equally between the two atomic centers. However, we do not adapt the internuclear distance as it was done in [339] to obtain a more pronounced effect of the phase offset studied there but stick to the physical distance of  $2 \text{ a.u.}$  [406, 407].

As can be seen from Fig. 6.2 and as already mentioned, one of the main challenges is that the tunneling barrier is not only modified by the laser field but also by the Coulomb potential from the other nucleus. From the bottom panel of Fig. 6.2 one can see that the mutual distortion of the Coulomb wells is so weak at the tunnel exit that it is a good approximation to employ the atomic theory of Ref. [3] with the unshifted ionization potential of  $I_p = 15.6 \text{ eV}$  to calculate the initial spatial conditions. Subsequently, as this theory assumes an atom placed at the origin, we merely shift this result

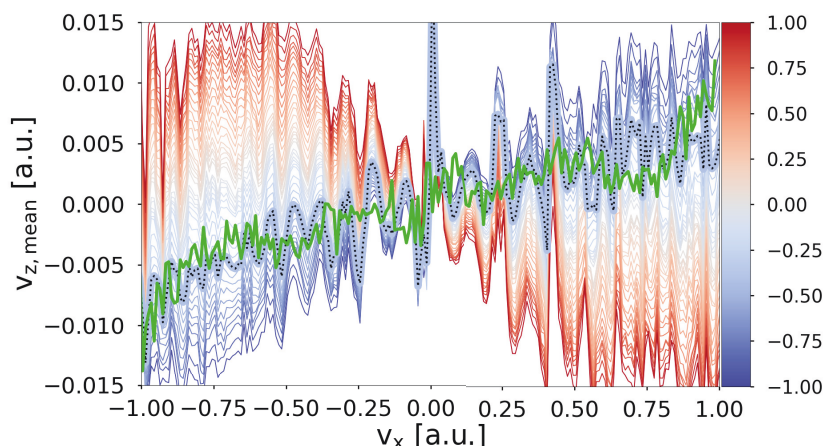


**Figure 6.6:**  $v_{z,mean}$  as a function of  $v_x$ . The green line represents the values extracted from the experimental data. The ensemble of curves was obtained from QTMC simulations over a range of ionization ratios  $q$ , which is specified by the color of the curve (see colorbar). The theoretical curve that matches the experimental data best according to the comparison of the asymmetry parameter  $a$  (see Fig. 6.9) is printed in bold with a dotted black line on top of it. In both the theoretical and experimental evaluation the photoelectron momentum distribution was restricted to  $v_z \in [-1, 1]$  and  $v_x \in [-1, 1]$ .

by the central position of the respective atom the electron is born at. Thus, we calculate the tunnel *exits*.

In contrast, the tunnel *width* that mainly determines the tunneling probability is strongly affected by the internuclear Coulomb distortion and we cannot simply employ an atomic ionization theory that does not properly account for this effect when calculating the rates. Since solving this problem of the ratio of ionization from the up- and downfield well is the aim of this work, we scan through different ionization ratios. This will lead to different degrees of asymmetry, which can then be compared to the asymmetry obtained from the experiment. To this end, we define the ratio  $q$  of ionization from the two different sites as

$$q = \frac{\#up - \#down}{\#up + \#down}, \quad (6.8)$$

where #up and #down are the number of electrons born upfield and downfield, respectively. The limits of  $q = -1$  and  $q = +1$  therefore correspond to the electrons being born exclusively downfield or upfield, respectively. Note that the two different atoms change being the up- and downfield atom several times during the pulse as the sign of the electric field changes.

A sample momentum distribution obtained in the described QTMC simulation can be found in Fig. 6.5.

### 6.3.3 Explanation for the asymmetry via trajectory analysis

Fig. 6.6 shows  $v_{z,mean}(v_x)$  of QTMC results over a range of ionization ratios  $q$  specified in the colorbar. The evaluation of the final momentum distribution was done in the same way as in the experiment, which also does integration over  $v_y$  that is limited to an out-of-plane angle of  $\theta < 10^\circ$  before calculating  $v_{z,mean}(v_x)$  [339]. The  $v_{z,mean}(v_x)$

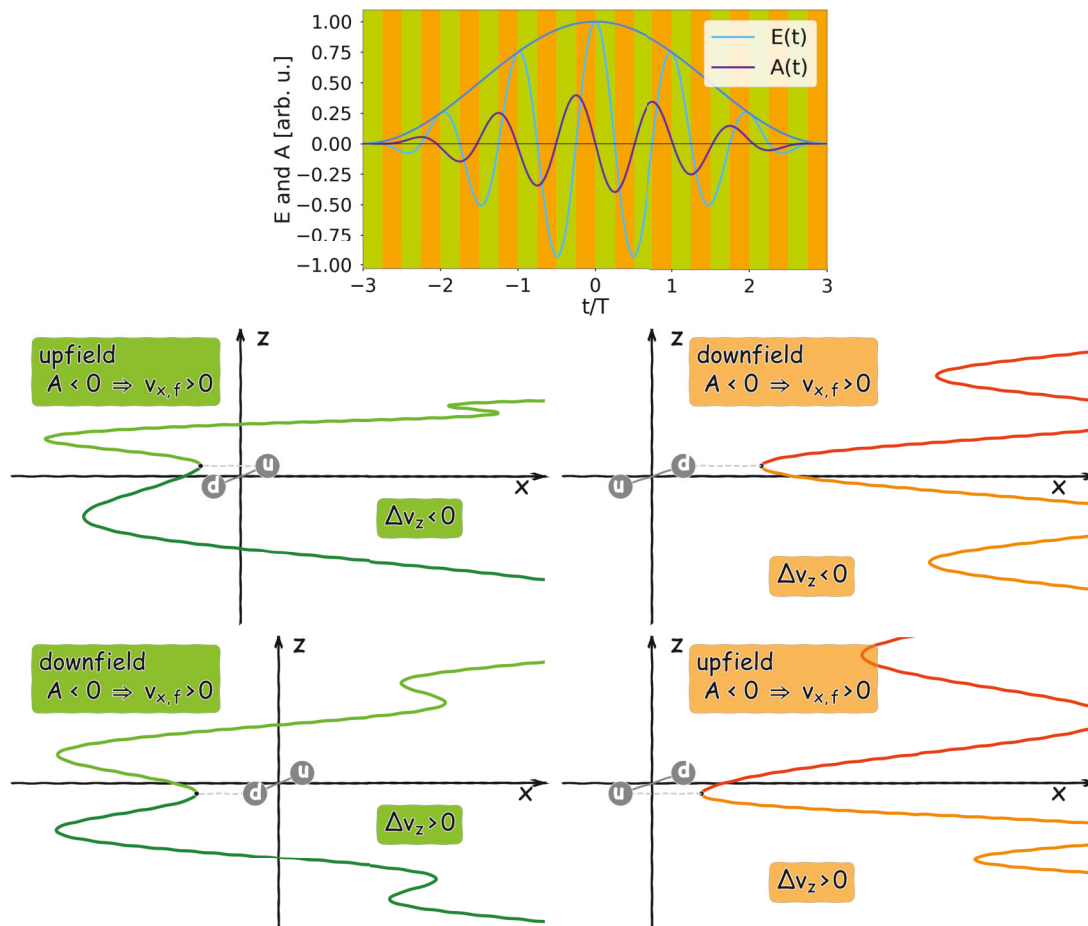


**Figure 6.7:** Top panel: Field strength and vector potential in the pulse. Quarter cycles with decreasing absolute field strength are highlighted in green, whereas increasing absolute field strengths are orange. Bottom left panels: Field  $> 0$  and the final velocity is positive. The electrons fly around the parent molecular ion and accrue much asymmetric Coulomb deflection. Bottom right panels: Field  $< 0$  but the final velocity is again positive because the same sign of the vector potential  $A$  is chosen. The electrons fly directly to the detector and are less deflected by the asymmetric Coulomb potential. Note that these trajectories were calculated with an oversized molecule for illustrative purposes. For an accurate calculation with trajectories of the real system see Fig. 6.8 and Table 6.1.



curves in Fig. 6.6 exhibit a clear pattern: The more electrons are released from the upfield atom (redder on the colorbar), the more positive  $v_{z,mean}$  is for  $v_x < 0$  and the more negative for  $v_x > 0$ . If the majority of electrons are born at the downfield atom, qualitatively the same effect is observed with the signs of  $v_{z,mean}$  reversed.

How can we understand this effect? Analyzing the QTMC trajectories, the deflection of the trajectories in the asymmetric Coulomb potential is identified as the origin of the asymmetry in  $v_{z,mean}(v_x)$ . Fig. 6.7 displays an illustration of the mechanism that is explained in the following. Note that these trajectories were calculated with an oversized molecule for illustrative purposes and a quantitative description with trajectories that are propagated in the system with the correct parameters is deferred to the subsequent paragraph.

Without loss of generality, we focus on those electrons that end up at  $v_x > 0$ . They were born at a time when the vector potential,  $A$ , was negative (which is true under the assumption that the trajectories under consideration do not interact strongly with the Coulomb potential). As the depiction of the pulse in the top panel of Fig. 6.7 shows, this can happen at a positive field strength that is decreasing (green stripes) or at a negative field strength whose absolute value is increasing (orange stripes). The four lower panels each show two trajectories with a transverse velocity of opposite sign but same absolute value. In all cases, the absolute value of the transverse velocity is reduced during propagation due to general Coulomb focusing. However, we are interested only in the asymmetric deflection due to the asymmetric Coulomb potential which is obtained as the *sum* of the change in  $v_z$  during propagation of both of those trajectories with opposite signs, denoted  $\Delta v_z$ .

In the left half of the lower panels (green, corresponding to a positive field strength that is decreasing) the asymmetric deflection  $\Delta v_z$  of electrons born at the upfield atom is negative due to the pull from the downfield atom. Vice versa, if the electron is born at the downfield atom, the overall deflection is positive. Alternatively, one can understand the sign of the overall deflection  $\Delta v_z$  by checking whether the electron is born below or above the center of charge along the  $z$ -axis, which leads to  $\Delta v_z > 0$  or  $\Delta v_z < 0$ , respectively. For  $v_x > 0$ , a deflection of  $\Delta v_z > 0$  for electrons born at the downfield atom and of  $\Delta v_z < 0$  for electrons born at the upfield atom is also in line with the signs of  $v_{z,mean}(v_x)$  observed in Fig. 6.6.

But what about the trajectories born when the field strength is inverted? Then, the atom that was formerly the downfield atom is the upfield one, and vice versa. Consequently, also the signs of the overall deflections  $\Delta v_z$  are inverted: positive for a birth at the upfield atom and negative for a start at the downfield atom (see right (orange) bottom panels of Fig. 6.7). However, since in the case of the absolute value of the field strength increasing (orange) the electrons directly leave the parent ion, the asymmetric deflection is weaker than in the case when the electron goes around the parent ion (green). Therefore, even though the overall deflections  $\Delta v_z$  have opposite signs in adjacent quarter-cycles with the same sign of  $A$ , they do not compensate each other as the deflection in the ‘green’ quarter-cycles dominates since in these cases the electron goes around the parent ion and is affected by the asymmetric Coulomb potential more strongly than in the ‘orange’ quarter-cycles. An analogous line of reasoning can be applied to  $v_x < 0$ , where the signs of the deflections need to be swapped. This explains qualitatively the asymmetric shifts observed in Fig. 6.6.

To also get a more quantitative impression of the asymmetry of the electron’s deflection, let us take a look at the trajectories depicted in Fig. 6.8. Here, the laser and



$t_0$	$v_{z,0}$	upfield (u) / downfield (d)	final $v_z$	$dv_z$	$\Delta v_z$ ( $dv_z$ summed up separately for u and d)
4	0.3	u	0.090	-0.210	u: $-0.210 + 0.176 = -0.034$ d: $-0.148 + 0.163 = +0.015$
		d	0.152	-0.148	
	-0.3	u	-0.124	0.176	
		d	-0.137	0.163	

$t_0$	$v_{z,0}$	upfield (u) / downfield (d)	final $v_z$	$dv_z$	$\Delta v_z$ ( $dv_z$ summed up separately for u and d)
-4	0.3	u	0.205	-0.095	u: $-0.095 + 0.072 = -0.023$ d: $-0.056 + 0.062 = +0.006$
		d	0.244	-0.056	
	-0.3	u	-0.228	0.072	
		d	-0.238	0.062	

**Table 6.1:** Changes of  $\Delta v_z$  for the trajectories depicted in Fig. 6.8. For  $t_0 = 4$  the electrons go around the molecular ion and end up at  $v_x > 0$ . For  $t_0 = -4$  the electrons fly directly to the detector and end up at  $v_x < 0$ . The corresponding trajectories are displayed in Fig. 6.8.

atomic parameters applied in the simulations shown in Fig. 6.6 are used. The scenarios depicted in Fig. 6.8 differ from each other in the following parameters. Electrons are either released ...

- ... from the up- or downfield atom.
- ... at a transverse velocity  $v_{z,0} = -0.3$  or  $v_{z,0} = 0.3$ .
- ... at  $t_0 = -4$  (before the peak of the pulse, increasing positive field strength) or at  $t_0 = 4$  (after the peak, decreasing positive field strength).

The resulting  $2^3 = 8$  combinations are depicted as trajectories of different colors in Fig. 6.8. One can directly see from the insets  $v_z(t)$  that for the trajectory that goes around the parent ion (upper panel) the Coulomb deflection is much larger than when the electron directly leaves the ion (lower panel). The quantitative change of  $v_z$  for a single trajectory from the birth in the continuum till after the pulse has passed, denoted  $dv_z$ , is listed in Table 6.1. From these values the following can be seen: The asymmetry in the deflection, expressed as  $\Delta v_z$  in the last column, is larger (in absolute values) when the electron has to go around the molecular ion ( $t_0 = 4$ ) than when it directly leaves it ( $t_0 = -4$ ). This is the case for birth at both the up- and downfield atom and thus corroborates the qualitative arguments for the asymmetric deflection given above.

### 6.3.4 Comparison of theoretical and experimental results to identify the ionization site

In order to describe the asymmetry observed in the experiment and in the QTMC simulations quantitatively, we define the asymmetry parameter  $a$  as follows

$$a = \frac{\sum_{i=1}^m \text{sign}(v_x(i)) \cdot v_{z,\text{mean}}(v_x(i))}{m}. \quad (6.9)$$

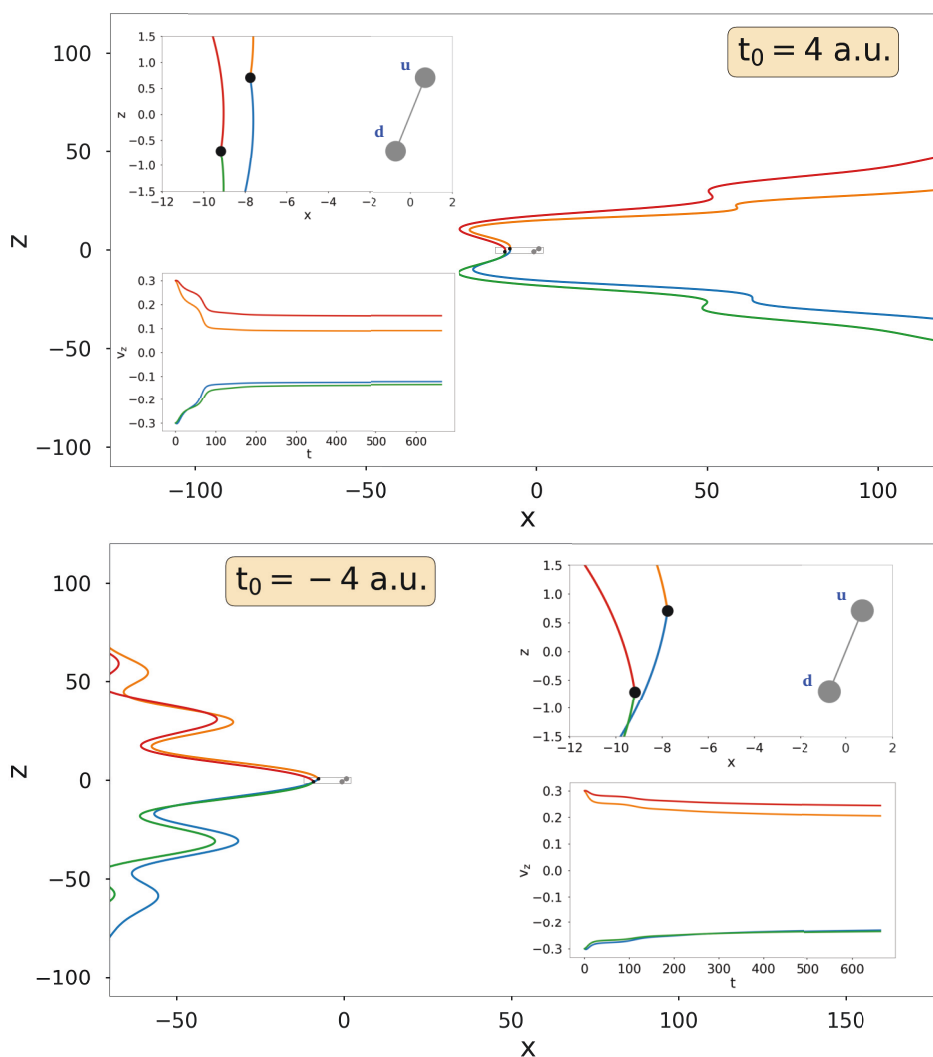


**Figure 6.8:** Trajectories for different scenarios showing that the asymmetric deflection is larger when the electron goes around the parent ion (top panel) than when it directly leaves the molecule (bottom panel). The quantitative description of the deflection is given in Tab. 6.1 and commented on in section 6.3.3. All depicted quantities are given in atomic units.

The multiplication with the sign of  $v_x$  enables us to distinguish between the corresponding  $v_{z,mean}$  curves rising or falling for increasing  $v_x$  and leads to a unique mapping between  $q$  and  $a$ . This quantity is calculated, on the one hand, for the range of ionization ratios in the QTMC simulation and, on the other hand, for the single experimental data set. The results are depicted in Fig. 6.9. Comparing the experimental value of  $a = 0.0031$  with the theoretical curve now allows us to estimate the ionization ratio  $q$  of the up- and downfield atom in the experiment. The value obtained is  $q = -0.377$ , which means that for every 100 electrons born downfield 45 electrons are born upfield. Thus, this result indicates that ionization from the downfield well is favored. According to the introductory discussion in section 6.2 (also see Fig. 6.1), this hints at an adiabatic adaption of the electron location as the electric field changes sign.

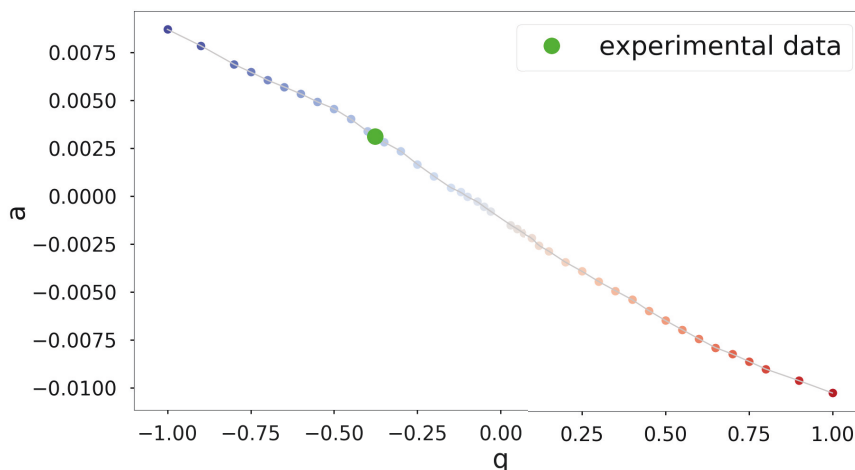


**Figure 6.9:** Asymmetry parameter  $a$  according to eq. (6.9) as a function of the ionization site ratio  $q$  according to eq. (6.8). The colors of the theoretically obtained dots are chosen according to the color-coding for  $q$  in the colorbar of Fig. 6.6. The experimental value is plotted as a larger green dot.

## 6.4 Conclusion and Outlook

To conclude, it was found that the experimental photoelectron momentum distribution of electrons ionized from a neutral diatomic nitrogen molecule that is tilted by  $45^\circ$  against the laser polarization direction exhibits an asymmetry. QTMC simulations reproduced this asymmetry and revealed that the extent and sign of the asymmetry depend strongly on the fraction of atoms born at the up- and downfield atom. Trajectory analysis made clear that the asymmetry of the momentum distribution is due to the asymmetric Coulomb potential that the electron explores on its way to the detector.

Sweeping over the ionization ratio in QTMC simulations, we obtained a unique map of the ionization site ratio onto the asymmetry parameter. Locating the experimental asymmetry parameter on this theoretical map allows to estimate the ratio at which the electrons were released from the up- and downfield well from the experimental data. The result indicates that ionization from the downfield well is favored in the studied system. Asymmetries like the one described here can be expected to be observed in any system that exhibits a notable asymmetry in the molecular potential with respect to the axis of polarization direction and thus to have a wide range of applications. The method presented here stands out in that it tracks the ionization site for single ionization of neutral molecules, where the technique of analyzing Coulomb explosion, that has so far been used to track ionization sites in diatomic molecules, is not applicable.

As the asymmetry in the momentum distribution is due to the asymmetry in the Coulomb potential, this work also stands in line with those recent publications that highlight the importance of including the Coulomb effect as accurately as possible when theoretically describing holographic effects [65, 135, 408–412]. In particular, this study is a case in point for the strength of QTMC simulations over using SFA theories. As highest accuracy is required in terms of the Coulomb potential here, it is not sufficient to include the Coulomb potential perturbatively as it is, for example, done in Coulomb-corrected SFA theories [69, 70].

Improvement of the theory presented in this chapter could be achieved by higher accuracy in the theoretical description of the diatomic model. For example, it is not clear whether it is a good approximation to distribute the ionic charge evenly to the two atomic centers after ionization. Even though the model of even charge distribution has been successfully applied in the theoretical interpretation of the very experimental data that are again used here, in the TDSE simulations presented in (the supplementary of) [339] and the QTMC simulations in [130], a deeper study along these lines seems warranted, in particular if the theory is applied to other molecular systems.

Speaking of other systems, it seems important to emphasize that the theory presented in this chapter can be applied to other molecules and laser parameters as well. A larger bond length of the molecule would be expected to lead to a more pronounced asymmetry in the photoelectron momentum distribution, as long as the underlying assumptions of our model are satisfied. However, one should keep in mind that a larger bond length might change the whole underlying process, for example, of how the remaining positive charge is distributed to the ionic cores. Varying the bond length would be interesting in particular in that one might observe the transition from the electron being primarily born at the downfield atom to the electron being localized at the upfield well. Whereas dominant ionization from the downfield atom is expected in small molecules in which adiabatic adaption of the electron position plays a dominant role, as it was found to be the case for the  $N_2$  molecule presented in this chapter, the electron can be localized at the upfield well in larger molecules due to nonadiabatic effects that are crucial in the phenomenon of ionization enhancement (CREI).



---

## Conclusions and Outlook

*“The whole strenuous intellectual work of an industrious research worker would appear, after all, in vain and hopeless, if he were not occasionally through some striking facts to find that he had, at the end of all his criss-cross journeys, at last accomplished at least one step which was conclusively nearer the truth.”*

— Max Planck in his Nobel Lecture in 1920

At the end of this thesis we can look back on a ‘journey’ through a variety of ways to apply trajectory-based models in strong field ionization. Let us take the time to recapitulate what we have learned on our ‘exploration’ – especially for future ventures into these realms.

We have ‘departed’ from the question that haunts every trajectory Monte Carlo method: What probability distribution should the initial conditions of the trajectories follow? Focusing on nonadiabatic effects, we have revisited two popular theories that describe how nonadiabaticity manifests itself at the tunnel exit in a seemingly contradictory way. While one popular nonadiabatic theory claims a strong broadening of the ionization time spread and assumes zero longitudinal momentum at the tunnel exit [7] (YI), another prominent nonadiabatic theory [3] (Li) shows that the initial longitudinal momentum is by far not negligible and arrives at a significantly less broad time spread. The confusion about these discrepancies was resolved in chapter 3 by showing that the nonadiabatic broadening of the time spread derived in YI [7] is a direct consequence of setting the initial longitudinal momentum to zero. More generally, we saw that the strong coupling of the ionization time spread and the initial longitudinal momentum leads to the theories of Li and YI, in spite of their fundamentally different initial conditions, to end up at approximately the same longitudinal momentum distribution at the detector in an approximation that is valid for common experimental set-ups using 800 nm light. Thus, we can now understand why the two nonadiabatic theories with their contrasting initial conditions were both successfully used to explain experiments in the nonadiabatic regime. This should account to some extent for the confusing character the discussions about nonadiabatic effects sometimes assumed.

Despite the indistinguishability of the results obtained from the two theories in a wide range of typical nonadiabatic parameters, laser and atomic parameters were found that are still in the experimentally realizable and relevant regime for which the mentioned approximations break down and the two nonadiabatic theories yield clearly



distinguishable momentum distributions. Comparing TDSE simulations to the CTMC results obtained with the initial conditions of Li and YI gave much better agreement with the theory of Li [3]. The open question is whether experimental data can back this result. At this point, one 'take home' message is that any assumption about the initial longitudinal momentum directly and significantly affects the ionization time spread and that it is, therefore, important to physically motivate the choice of the initial longitudinal momentum.

Our journey then continued in the field of Rydberg state creation by frustrated tunnel ionization. Here, we picked up on the study of the intensity dependence of the Rydberg yield described in [49] and found that including (i) the intensity-dependent distribution of ionization times and (ii) nonadiabatic effects leads to a better understanding of experimental results. The latter point suggests that Rydberg states can be used to test nonadiabatic effects in a way that contrasts the commonly used methods for nonadiabaticity tests in that it does not use the momentum distribution at the detector. As the nonadiabatic effects can be observed in the slope of the power-law scaling of the intensity dependence of the Rydberg yield alone, this eliminates the concerns about the calibration of the absolute intensity that have haunted prior experiments attempting to observe nonadiabatic effects by measuring electron momenta distributions [57, 154].

Moreover, we have seen how an increase of the pulse duration shifts the principal quantum number distribution of Rydberg states to larger values and reduces the overall Rydberg yield. These effects could be understood by the observation that the electrons that potentially end up in a Rydberg state are slowly driven back to the parent ion by the attractive Coulomb potential. When the pulse duration exceeds a critical value, the electron gets so close to the ion that it gains too much kinetic energy in the interaction with the ionic potential to be a Rydberg state. As this critical pulse duration is smaller for more deeply bound Rydberg states (corresponding to small  $n$ ), low principal quantum numbers are less likely to 'survive' longer pulses. This is relevant to studies and applications that rely on the principal quantum number distribution of Rydberg atoms like the recently developed method of creating coherent extreme-ultraviolet radiation from Rydberg atoms, in which the occupation of low principal quantum numbers is crucial [189]. Also, this study is a case in point for showing the importance of including the Coulomb potential during the propagation process [72]. In particular, the mechanism presented here, which relies on the Coulomb potential, stands in contrast to prior explanations of the Rydberg yield dropping with increasing pulse duration which neglected the Coulomb potential during propagation.

The next stop on our journey were laser fields with a time-varying spatial dependence as it is typically found in the vicinity of nanostructures. We have seen the emergence of a prominent higher energy structure (HES) in the spectrum of photoelectrons that were ionized from the gas phase in such an inhomogeneous laser field. The laser and tip parameters were chosen to be in the 'intermediate regime' where the electron's quiver amplitude is of the same order as the decay length of the nearfield and the electron dynamics is therefore difficult to describe theoretically. Trajectory-analysis revealed that the electrons comprising the HES are born within a narrow time window and may therefore be used to create localized sources of monoenergetic electron beams of sub-femtosecond duration. Having such applications in mind, analytical ex-

pressions to describe the electrons' motion in the inhomogeneous field were derived. From this we have learned how the spectral position and width of the HES depend on the inhomogeneity parameter of the nearfield and can thus be optimized.

Moreover, we have seen that the recently reported experimental finding of a low energy peak (LEP) [75] can be understood in the same theoretical framework as the theoretically predicted emergence of the HES. Even though the two peaks were observed in different energy regimes, and despite the LEP being detected for electrons that were released from a nanotip whereas the HES was found for electrons ionized from a gas that is placed in the vicinity of a nanotip, a single mechanism that causes the peak formation was identified. Based on this mechanism, a more general analytical model was derived to describe the energy upshift that electrons experience in inhomogeneous electric fields. This theoretical description also explained the experimentally observed linear scaling of the peak energy of the LEP with the intensity of the incident laser pulse.

In particular, parameters were found at which electrons ionized directly from a nanostructure, the setting in which the LEP was found, form a prominent and narrow peak at higher energies as it was described in the framework of the HES. As ionization from the tip is experimentally better established than ionization from the gas phase near a nanostructure, this should pave the way for the experimental realization of almost monoenergetic electron beams of sub-femtosecond duration as they are predicted for the HES in the gas phase.

The last part of our journey led us into the realms of molecules. A new method was proposed for quantitatively retrieving the ratio of ionization happening at the up- and downfield atomic site. So far, such studies were restricted to ionization from charged molecules with Coulomb explosion ensuing the ionization process. Here, in contrast, a method was developed for the ionization of neutral molecules that makes use of the deflection of the electron in the asymmetric Coulomb potential of the tilted molecule, which introduces an asymmetry in the photoelectron momentum distribution at the detector. As the degree of asymmetry depends on whether the electron is born at the up- or downfield atom and as the ionization site ratio can be controlled in QTMC simulations, this asymmetry information can be used to quantify the relative ionization probabilities from the up- and downfield site from experimental photoelectron momentum distributions.

The site from which the electron is ionized also gives insights into the time scale on which the electronic distribution within the molecule adapts to the changing electric field. Therefore, one particularly interesting direction for future work is the variation of the bond length. Varying the bond length one might observe the transition from the electron being primarily born at the downfield atom to the electron being localized at the upfield well. Whereas dominant ionization from the downfield atom is expected in small molecules in which adiabatic adaption of the electron position plays a dominant role, as it was the case for the  $N_2$  molecule in this work, the electron can be localized at the upfield well in larger molecules due to nonadiabatic effects that are crucial in the phenomenon of ionization enhancement (CREI). In particular when changing the bond length, but not only then, the way the ionic charge is distributed among the atomic sites in the theoretical model needs to be reconsidered.

The molecular system also served as a case in point to show that including the Coulomb potential as accurately as possible is of utmost importance. Therefore, modeling this system using CTMC/QTMC simulations should be favored over SFA approaches in which Coulomb effects can, at best, be included perturbatively [69, 70]. Similarly, the relevance of fully including the Coulomb potential during propagation was relevant in the study of the pulse duration effects on Rydberg states presented in section 4.3. Speaking of the advantages of CTMC/QTMC over SFA simulations, we have come full circle to the motivation given in the introduction in chapter 1, where on page 11 the prerequisites for the application of SFA were listed. In addition to the spatial inhomogeneity of the atomic or molecular Coulomb potential, we have also seen the third point in said list being violated: In chapter 5, the strong inhomogeneity of the electric field in the vicinity of a nanostructure also revealed the power of a trajectory-based method such as CTMC in which the field inhomogeneity can be fully included in the equation of motion.

Considering the SFA prerequisites further, also the first point in the list on page 11, stating that the laser field should be strong enough for multiphoton or tunnel ionization to be the dominant ionization process, seems worth some consideration. After all, the flourishing field of streaking [413–421] often uses pump pulses that are of high frequency and low intensity resulting in *single*-photon ionization being the dominant liberation mechanism. The weakness of the high-frequency pump pulse ensures a negligible effect on the post-ionization dynamics, which is dominated by a second laser pulse, the probe pulse, that is stronger and of lower frequency. Scanning the delay between the two pulses has proven to be a powerful tool in the study of ionization delays. Modeling single-photon ionization semiclassically, in particular in combination with the stronger probe pulse, is far less common and mature than strong field ionization in attosecond science [422]. Nonetheless, semiclassical models provide several advantages over the numerical solution of the TDSE also here. Among those, the most notable is probably the insight which trajectory analysis allows into the streaking process, into the origin of and different contributions to the measured streaking delay [414, 423]. Moreover, the lower computational cost of semiclassical models relative to numerical solutions of the TDSE is becoming increasingly important as the field of attosecond spectroscopy, which until recently was dominated by experiments performed on rare gas atoms and metal surfaces [66, 424], is moving increasingly towards molecules [422]. In the following, a semiclassical method to simulate attosecond streaking experiments which is particularly suited to include information about the molecular potential is briefly summarized. In the framework of my PhD studies I was involved in work with and on this ‘Classical Wigner Propagation’ (CWP) method which is the brainchild of Dr. Tomáš Zimmermann and details about which can be found in Ref. [422].

The CWP method treats the ionization step quantum mechanically followed by classical propagation in the infrared probe field. The two key advantages of this method over other semiclassical approaches such as CTMC or QTMC are found in (i) the fully quantum mechanical treatment of the ionization step, where the weakness of the pump field allows to use perturbation theory and (ii) the description of the wavepacket by a Wigner quasi-probability distribution [422]. The latter serves as a distribution to sample initial conditions for trajectories and is not only a proper phase-space density distribution with well-defined classical limit of the dynamics but – even when propagated classically – it also incorporates (some) quantum effects through interference of pos-

itive and negative weights. Moreover, this method allows to include the electrostatic potential of the atomic or molecular ion, computed from the one-electron density matrix obtained in quantum chemistry calculations for the respective system.

As the electrostatic potential plays a crucial role in streaking delays [414, 425–429], a future model to simulate streaking experiments may combine the electrostatic atomic or molecular potential obtained from quantum chemistry calculations during propagation with a CTMC model for describing the initial conditions. Using CTMC instead of CWP for sampling the initial conditions would not only be easier to implement but would have the added benefit of a straight-forward trajectory analysis, which is more involved in the CWP due to the negative weights trajectories can have. Then, however, we need to think about appropriate initial conditions for the CTMC simulations. Even though models to describe such a weak(er) field single-photon ionization process in CTMC simulations have been developed and successfully applied in the past [274, 414, 418, 430], they are far less tested against experiments than it is the case for strong field ionization processes, and consequently may need to be adapted. For example, it is not clear where and with momenta in which direction to start. While [414, 418] just start with momenta in random directions, in [274, 430, 431] the initial momenta are chosen according to a cosine distribution. Moreover, using molecules we need to think about the atomic site at which to start the trajectories. In the CWP method, information about the ionization site was obtained from the Wigner function. In CTMC, in contrast, such information has to be included indirectly, e.g. from studies similar to the one presented in chapter 6 about the ionization site ratios in a molecule.

Dealing with more complicated molecular structures and nanostructures while still trying to answer basic questions in atomic systems has not only been a feature of this PhD thesis but is a more general attribute of ultrafast strong field physics. Hopefully, this thesis has shown that CTMC and QTMC simulations are a powerful and versatile tool that can contribute to discussions in many facets of this field.



# Appendix

## A.1 Tunnel exits and transverse momentum spreads in nonadiabatic theories

Here, it is shown that the tunnel exit obtained by Perelomov, Popov and Terent'ev (PPT) [4, 5] or Mur et al. [136] is the same as the one obtained in the theory of Li et al. [3]. The reason for this is that – as becomes most clear in chapter 3 – all nonadiabatic theories discussed in this work follow the same basic tools in their derivations (imaginary time and saddle point method). As the results in PPT/Mur and Li for the tunnel exit look different in notation, we show here that the equations are actually the same.

In PPT/Mur, the tunnel radius is given as

$$r_{\text{tunnel},PPT} = \left| \frac{E_0}{\omega^2} \left( \cosh(\operatorname{arctanh} \left( \sqrt{\frac{\gamma^2}{1+\gamma^2}} \right)) - 1 \right) \right|. \quad (\text{A.1})$$

Using the trigonometric relation

$$\cosh(\operatorname{arctanh}(a)) = 1/\sqrt{1-a^2}, \quad (\text{A.2})$$

which is valid for  $-1 < a < 1$ , we can recast this into

$$\begin{aligned} r_{\text{tunnel},PPT} &= \left| \frac{E_0}{\omega^2} \left( \frac{1}{\sqrt{1-\frac{\gamma^2}{1+\gamma^2}}} - 1 \right) \right| = \left| \frac{E_0}{\omega^2} \left( \frac{1}{\sqrt{\frac{1+\gamma^2-\gamma^2}{1+\gamma^2}}} - 1 \right) \right| \\ &= \left| \frac{E_0}{\omega^2} \left( \frac{1}{\sqrt{\frac{1}{1+\gamma^2}}} - 1 \right) \right| = \left| \frac{E_0}{\omega^2} \left( \sqrt{1+\gamma^2} - 1 \right) \right|. \end{aligned} \quad (\text{A.3})$$

Introducing instantaneous time-dependence,  $E_0 \rightarrow E_0 \cos(\omega t_0)$  and  $\gamma \rightarrow \gamma(t_0, v_\perp) = \frac{\omega \sqrt{I_p + v_\perp^2}}{E_0 \cos(\omega t_0)}$ , this matches the result from Li et al. [3]

$$r_{\text{tunnel},Li} = \left| \frac{E_0}{\omega^2} \cos(\omega t_0) (1 - \sqrt{1 + \gamma^2(t_0, v_\perp)}) \right|. \quad (\text{A.4})$$



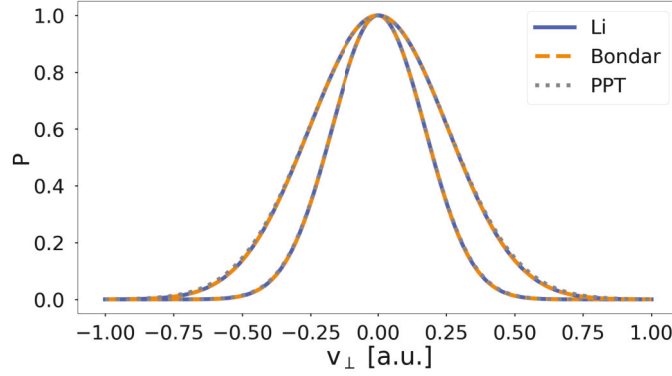


**Figure A.1:** Normalized ionization probability as a function of the initial transverse velocity. The three inner curves correspond to an intensity of  $I = 1.6 \cdot 10^{14} \text{ W/cm}^2$  and the three outer curves were obtained for an intensity of  $I = 1 \cdot 10^{15} \text{ W/cm}^2$ . In both cases helium was ionized at  $\lambda = 800 \text{ nm}$ . The initial longitudinal momentum and the ionization time were set to zero if these quantities appear in the respective theories.

Similarly, also the transverse momentum distribution is approximately identical for the theories of PPT, Li and Bondar [2]. This becomes clear from Fig. A.1, where the distribution of the initial transverse velocity is shown for two different intensities. The two intensities were chosen to correspond to the minimum and maximum intensity of the intensity range that is considered in chapter 4.2.

## A.2 Ionization time spreads of Yudin/Ivanov and Li as special cases of the theory of Bondar

In the following, the statement used in section 3.3 claiming that the distribution of ionization times presented by Yudin/Ivanov (YI) [7] and Li [3] can be obtained as special cases of the theory derived by Bondar [2] is shown.

Concerning YI, it can be referred directly to Ref. [2] by Bondar, where it is stated explicitly in the comment below eq. (16) that the result of YI is retrieved from the results in [2] by setting  $v_{\parallel}$  at the tunnel exit to 0, meaning the canonical momentum is expressed as  $p_{\parallel} = -A(t_0)$ . The only point one has to keep in mind when looking at Ref. [2] is that Bondar denotes the canonical momentum as  $\mathbf{k}$ . Therefore, when it is written in eq. (16) in Ref. [2] that the transformation  $k_{\parallel} \rightarrow k_{\parallel} - A(t)$  is done and then  $k = 0$  is set to zero, this corresponds to  $k_{\parallel} = -A(t)$  and thus to  $v_{\parallel,0} = v_{\perp,0} = 0$ , as in YI.

Moreover, Li [3] is a special case of [2] for the assumption of  $p_{\parallel} = v_{\parallel}(t_0) - A(t_0)$  as will become clear in the following. Even though both Li and Bondar use the saddle point equation and calculate the action

$$S(\mathbf{p}, t_s) = \int_{t_s}^{t_r} dt \left( \frac{1}{2} (\mathbf{p} + \mathbf{A}(t))^2 + I_p \right) \quad (\text{A.5})$$

and then the ionization probability

$$P \propto \exp(-2\text{Im}\{S\}) \quad (\text{A.6})$$

in the same way, the final equations and also intermediate results found in these two references look so different that it is not immediately obvious that just plugging in  $p_{\parallel} =$

$v_{\parallel}(t_0) - A(t_0)$  into Ref. [2] one obtains the result of Ref. [3]. On closer inspection, one can see that the differences mainly stem from the different trigonometric relations that are used to calculate the real and imaginary part of the saddle point  $t_s = t_0 + i t_i$ . In the following, it will be shown that starting from the result presented in eq. (6) in [2],

$$\omega t_s = \arcsin \left( \left( \frac{p_{\parallel}}{\sqrt{2I_p}} + i \sqrt{\frac{p_{\perp}^2}{2I_p} + 1} \right) \cdot \gamma \right), \quad (\text{A.7})$$

we obtain the same relations for  $t_i$ ,  $t_0$  and  $v_{\parallel}(t_0)$  (and thus  $p_{\parallel}$ ) as the ones presented in Li [3] when using  $p_{\parallel} = v_{\parallel}(t_0) - A(t_0)$ . Due to Li [3] and Bondar [2] using the same relations for  $S$  and  $P$  (see eq. (A.5) and (A.6)) this suffices for showing that the ionization time distribution of [3] is a special case of [2].

Using  $\gamma = \sqrt{2I_p} \frac{\omega}{E_0}$  and  $p_{\perp} = v_{\perp,0}$ , we can rearrange eq. (A.7) as follows

$$\sin(\omega t_s) = \left( \frac{p_{\parallel}}{\sqrt{2I_p}} + i \sqrt{\frac{v_{\perp,0}^2}{2I_p} + 1} \right) \cdot \sqrt{2I_p} \frac{\omega}{E_0} \quad (\text{A.8})$$

$$\Rightarrow \sin(\omega t_0) \cdot \cosh(\omega t_i) + i \cdot \cos(\omega t_0) \sinh(\omega t_i) = \frac{\omega}{E_0} p_{\parallel} + i \sqrt{\frac{v_{\perp,0}^2}{2I_p} + 1} \sqrt{2I_p} \frac{\omega}{E_0} \quad (\text{A.9})$$

where in the last step the trigonometric relation  $\sin(a+b) = \sin(a) \cos(b) + \cos(a) \sin(b)$  along with  $\sin(ix) = i \sinh(x)$  and  $\cos(ix) = \cosh(x)$  were applied. Now, we can extract the real and imaginary part of this equation:

$$\sin(\omega t_0) \cdot \cosh(\omega t_i) = \frac{\omega}{E_0} p_{\parallel} \quad (\text{A.10})$$

$$\cos(\omega t_0) \sinh(\omega t_i) = \sqrt{\frac{v_{\perp,0}^2}{2I_p} + 1} \sqrt{2I_p} \frac{\omega}{E_0} \quad (\text{A.11})$$

So far, this is simply Bondar's intermediate result from eq. (A.7) recast. Now, the assumption that is used in Li [3] is introduced, which is  $p_{\parallel} = v_{\parallel}(t_0) - A(t_0)$  with  $A(t_0) = -\frac{E_0}{\omega} \sin(\omega t_0)$ . For the real part we obtain

$$\sin(\omega t_0) \cdot \cosh(\omega t_i) = \frac{\omega}{E_0} \left( v_{\parallel}(t_0) + \frac{E_0}{\omega} \sin(\omega t_0) \right) \quad (\text{A.12})$$

$$\Rightarrow v_{\parallel}(t_0) = \frac{E_0}{\omega} \sin(\omega t_0) \cdot \cosh(\omega t_i) - \frac{E_0}{\omega} \sin(\omega t_0) \quad (\text{A.13})$$

$$\Rightarrow v_{\parallel}(t_0) = \frac{E_0}{\omega} \sin(\omega t_0) (\cosh(\omega t_i) - 1). \quad (\text{A.14})$$

And the imaginary part (eq. (A.11)) can be rewritten as

$$\sinh(\omega t_i) = \frac{\omega \sqrt{v_{\perp,0}^2 + 2I_p}}{E_0 \cos(\omega t_0)}. \quad (\text{A.15})$$

Combining eq. (A.14) and (A.15) and using  $\cosh^2 - \sinh^2 = 1$ , we obtain the same longitudinal momentum at the tunnel exit,  $v_{\parallel, Li}(t_0)$ , as given in eq. (5) in [3]:

$$\cosh^2(\omega t_i) - \sinh^2(\omega t_i) = 1 \quad (\text{A.16})$$

$$\Rightarrow \left( v_{\parallel}(t_0) \frac{\omega}{E_0 \sin(\omega t_0)} + 1 \right)^2 - \frac{\omega^2 (v_{\perp,0}^2 + 2I_p)}{E_0^2 \cos^2(\omega t_0)} = 1 \quad (\text{A.17})$$

$$\Rightarrow v_{\parallel}(t_0) \frac{\omega}{E_0 \sin(\omega t_0)} + 1 = \sqrt{1 + \frac{\omega^2 (v_{\perp,0}^2 + 2I_p)}{E_0^2 \cos^2(\omega t_0)}} \quad (\text{A.18})$$

$$\Rightarrow v_{\parallel}(t_0) = \frac{E_0}{\omega} \sin(\omega t_0) \left( \sqrt{1 + \frac{\omega^2 (v_{\perp,0}^2 + 2I_p)}{E_0^2 \cos^2(\omega t_0)}} - 1 \right) = v_{\parallel, Li}(t_0). \quad (\text{A.19})$$

In Li,  $t_0$  and  $t_i$  are not directly expressed in terms of  $E_0$ ,  $I_p$  and  $\omega$ , but as eqs. (A.15) and (A.19) agree with eqs. (4) and (5) in Li ([3]), respectively, this should suffice to reassure us that  $t_0$  and  $t_i$  relate to  $E_0$ ,  $I_p$  and  $\omega$  in the same way as in Li. In addition, we have also retrieved  $v_{\parallel, Li}(t_0)$  of Li from Bondar, and thus also  $p_{\parallel} = v_{\parallel}(t_0) - A(t_0)$  of Li. Consequently, using these results in eqs. (A.5) and (A.6), which are used not only in Bondar but also in Li, the ionization time distribution of Li is obtained.

### A.3 Interpretation of the intensity dependence of the Rydberg yield

In the following, we resolve the confusion that may arise from the fact that the Rydberg area is observed to become smaller with increasing intensity (see Fig. 4.1 and also e.g. eq. (4.4)) while it is experimentally observed in [48] that the number of Rydberg states is increasing with increasing intensity. The key to understanding these seemingly contradictory features lies in the correct interpretation of eq. (4.2). The arguments presented in the following use the result of eq. (4.6) but are equally valid for the modifications of this equation derived in sections 4.2.2 to 4.2.4.

The confusion arises from eq. (4.2) implicitly suggesting that  $N^* \propto \Sigma^*$  and  $N_t \propto \Sigma_t$ , which is not true. Eq. (4.2) only holds in the relative sense, meaning under evaluation of the ratio rather than separate evaluation of the nominator and the denominator. If one is interested in the total number of atoms that are ionized or end up in a Rydberg state, respectively, the intensity-dependent ionization rate has to be accounted for properly, e.g. by the adiabatic factor  $\exp(-2(2I_p)^{3/2}/(3E_0))$  (see eq.(2.21)):

$$\begin{aligned} N_t(E_0) &\propto \exp^{-\frac{2(2I_p)^{3/2}}{3E_0}} \Sigma_t(E_0) \propto \exp^{-\frac{2(2I_p)^{3/2}}{3E_0}} \sqrt{E_0} \\ N^*(E_0) &\propto \exp^{-\frac{2(2I_p)^{3/2}}{3E_0}} \Sigma^*(E_0) \propto \exp^{-\frac{2(2I_p)^{3/2}}{3E_0}} \frac{1}{E_0}. \end{aligned} \quad (\text{A.20})$$

Therefore, the dominant contribution to the total number of electrons captured in a Rydberg state comes from the intensity-dependent ionization rate factor, which is increasing with increasing intensity. Thus we can understand why with increasing intensity the area  $\Sigma^* \propto 1/E_0$  decreases despite the experimentally observed increase of Rydberg atoms. In the ratio  $N^*/N_t$ , the prefactor  $\exp(-2(2I_p)^{3/2}/(3E_0))$  cancels out and therefore we do not need to care about it. This concept is illustrated in Fig. A.2 and further explained in the corresponding caption.

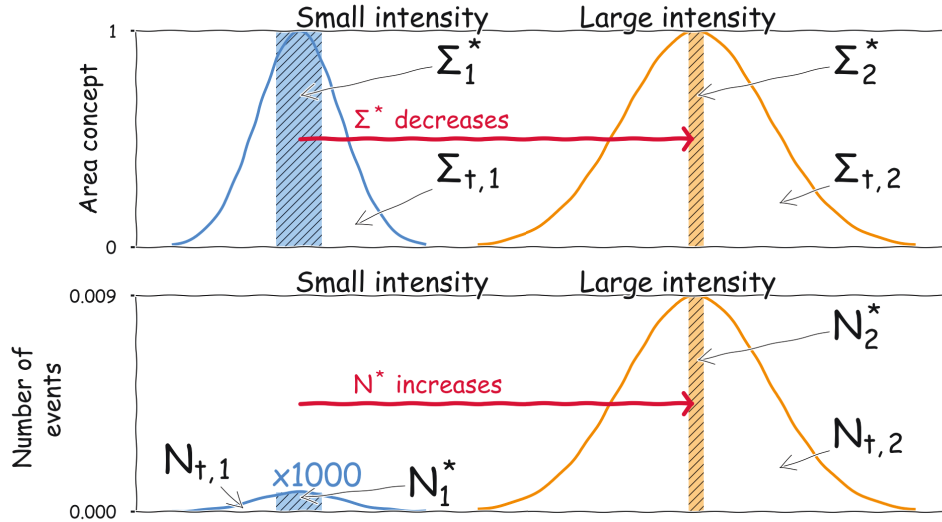


**Figure A.2:** Illustration of the difference between the area concept, which is applied in this work, and estimating total numbers of events. The unlabeled  $x$ -axes represent the initial conditions at which the electrons are born,  $t_0$  and  $v_{\perp,0}$ , which are abstractly represented in a single dimension for the sake of simplicity here. The depicted Gaussian-like curves show the ionization rate and the striped rectangular curves show the initial conditions that lead to a Rydberg state. Note that in all depictions above (area and total number concept) we are interested in the areas under the Gaussian and rectangular-like curves shown, not the curves themselves. In the area concept, the different ionization rates at different intensities is not accounted for. This is illustrated as equal heights of all curves in the upper panel. Here, only the widths of the curves matter. As  $\Sigma^* \propto 1/E_0$ , the Rydberg area decreases with increasing intensity. However, when one is interested in the total number of electrons that ever tunneled out ( $N_t$ ) or that end up in Rydberg states ( $N^*$ ) separately, one has to also account for the ionization rate increasing severely with increasing intensity, e.g. by weighting the height with  $\exp(-2(2I_p)^{3/2}/(3E_0))$ . Since the ratio of  $N^*$  and  $N_t$  is evaluated at each intensity individually, the height does not matter when we are interested in  $N^*/N_t$  because that weighting factor cancels out and  $N^*/N_t$  equals the ratio  $\Sigma^*/\Sigma_t$ .

## A.4 Equations of motion in the Coulomb-free electric field

In the following, an analytical description of the motion of an electron in a laser field without Coulomb potential is derived. We only consider the motion along the direction of polarization. In addition, approximations as they proved helpful in the context of studying the intensity dependence of Rydberg states in section 4.2.4 are included. The starting point is the following equation of motion:

$$\frac{\partial^2 x}{\partial t^2} = -E(t) = -E_0 f(t) \cos(\omega t + \pi) = E_0 f(t) \cos(\omega t). \quad (\text{A.21})$$

where  $f(t)$  denotes the envelope of the laser field. The choice of setting the CEP to  $\pi$  introduces a minus sign and is made here because thus the position  $x$  at the end of the pulse will be obviously positive for typical  $t_0$  that lead to Rydberg states (i.e.  $t_0$  slightly negative) and in the evaluation of  $r = |x|$  in eq. (4.19) we can directly insert  $x$

without having to change signs in order to obtain the absolute value  $|x|$ . Otherwise the different sign in the prefactor has no bearing on the calculations in section 4.2.4. Integrating eq. (A.21) once, the velocity is obtained as follows

$$\begin{aligned} \dot{x}(t) &= E_0 \int_{t_0}^t dt' f(t') \cos(\omega t') \\ &= E_0 \left( \left[ f(t') \frac{\sin(\omega t')}{\omega} \right]_{t_0}^t - \int_{t_0}^t dt' \underbrace{\frac{\partial f(t')}{\partial t'}}_{\approx 0} \frac{\sin(\omega t')}{\omega} \right) \\ &\approx \frac{E_0}{\omega} (f(t) \sin(\omega t) - f(t_0) \sin(\omega t_0)), \end{aligned} \quad (\text{A.22})$$

where in the second step the derivative of the envelope was neglected, which is justified in the application in section 4.2.4 as the pulse duration is rather long (30 fs) and consequently the envelope changes significantly more slowly than the primary oscillation of the field. Evaluating this result at  $t = \tau$ , i.e. after the pulse has passed, we can use  $f(\tau) = 0$ . Moreover, assuming ionization in the central cycle we can approximate  $f(t_0) \approx 1$  and thus obtain eq. (4.16)

$$v_x(\tau) \approx -\frac{E_0}{\omega} \sin(\omega t_0). \quad (\text{A.23})$$

Integrating once more with respect to time gives the position

$$\begin{aligned} x(t) &\approx \frac{E_0}{\omega} \int_{t_0}^t dt' (f(t') \sin(\omega t') - f(t_0) \sin(\omega t_0)) \\ &\approx \frac{E_0}{\omega} \left\{ \left[ -f(t') \frac{\cos(\omega t')}{\omega} \right]_{t_0}^t - \int_{t_0}^t dt' \left( -\underbrace{\frac{\partial f(t')}{\partial t'}}_{\approx 0} \frac{\cos(\omega t')}{\omega} \right) - f(t_0) \sin(\omega t_0)(t - t_0) \right\} \\ &\approx \frac{E_0}{\omega} \left\{ -f(t) \frac{\cos(\omega t)}{\omega} + \underbrace{f(t_0)}_{\approx 1} \frac{\cos(\omega t_0)}{\omega} - \underbrace{f(t_0)}_{\approx 1} \sin(\omega t_0)(t - t_0) \right\} \\ &\approx \frac{E_0}{\omega^2} (\cos(\omega t_0) - f(t) \cos(\omega t)) - \frac{E_0}{\omega} \sin(\omega t_0)(t - t_0). \end{aligned} \quad (\text{A.24})$$

Evaluating eq. (A.24) at  $t = \tau = \tau_L/2$ , at the time the pulse has passed, we have  $f(\tau) = 0$  and thus

$$x(\tau) \approx \frac{E_0}{\omega^2} \cos(\omega t_0) - \frac{E_0}{\omega} \sin(\omega t_0)\tau, \quad (\text{A.25})$$

where in the last term the approximation  $(\tau - t_0) \approx \tau$  was applied because of  $\tau \gg t_0$ . Setting  $\phi = \omega t_0$ , this result equals eq. (4.14).

## A.5 Term $v_1$ in the perturbative approach

Here, the term  $v_1$  of the perturbative approach presented in section 5.3.2 is written out in order to show that even though eq. 5.26 does look benign, the terms used in it, such as  $v_1$ , can be unwieldy. Note that, for the sake of brevity,  $\phi_{CEP}$  was replaced by  $\phi$ .

$$v_1(t) = -E_0 \left( \frac{E_0 \left( (2N+1) \sin\left(\frac{\omega t}{N}\right) + \sin\left(2\phi + \left(2 + \frac{1}{N}\right)\omega t\right) \right) N^3}{16(N+1)^2(2N+1)\omega^3} \right)$$

$$\begin{aligned}
& \frac{E_0 \left( \cos \left( \phi + \frac{(N+1)\omega t_0}{N} \right) (N-1)^2 + (N+1)^2 \cos \left( \phi + \frac{(N-1)\omega t_0}{N} \right) \right) \sin \left( \phi + \frac{(N-1)\omega t}{N} \right) N^3}{16(N-1)^3(N+1)^2\omega^3} \\
& - \frac{E_0 \cos \left( \phi + \frac{(N-1)\omega t_0}{N} \right) \sin \left( \phi + \frac{(N+1)\omega t}{N} \right) N^3}{16(N-1)^2(N+1)\omega^3} - \frac{E_0 \cos \left( \phi + \frac{(N+1)\omega t_0}{N} \right) \sin \left( \phi + \frac{(N+1)\omega t}{N} \right) N^3}{16(N+1)^3\omega^3} \\
& + \frac{E_0 \left( (2N-1) \sin \left( \frac{\omega t}{N} \right) + \sin \left( 2\phi + \frac{(2N-1)\omega t}{N} \right) \right) N^3}{16(N-1)^2(2N-1)\omega^3} + \frac{E_0 t_0 \sin^2 \left( \phi + \frac{(N+1)\omega t_0}{N} \right) N^2}{16(N+1)^2\omega^2} \\
& - \frac{E_0 \left( (2N+1) \sin \left( \frac{\omega t_0}{N} \right) + \sin \left( 2\phi + \left( 2 + \frac{1}{N} \right) \omega t_0 \right) \right) N^3}{16(N+1)^2(2N+1)\omega^3} \\
& + \frac{E_0 \cos \left( \phi + \frac{(N+1)\omega t_0}{N} \right) \sin \left( \phi + \frac{(N-1)\omega t_0}{N} \right) N^3}{16(N-1)(N+1)^2\omega^3} + \frac{E_0 \sin \left( 2 \left( \phi + \frac{(N-1)\omega t_0}{N} \right) \right) N^3}{32(N-1)^3\omega^3} \\
& + \frac{E_0 \cos \left( \phi + \frac{(N-1)\omega t_0}{N} \right) \sin \left( \phi + \frac{(N+1)\omega t_0}{N} \right) N^3}{16(N-1)^2(N+1)\omega^3} + \frac{E_0 \sin \left( 2 \left( \phi + \frac{(N+1)\omega t_0}{N} \right) \right) N^3}{32(N+1)^3\omega^3} \\
& - \frac{E_0 \left( (2N-1) \sin \left( \frac{\omega t_0}{N} \right) + \sin \left( 2\phi + \frac{(2N-1)\omega t_0}{N} \right) \right) N^3}{16(N-1)^2(2N-1)\omega^3} + \frac{E_0 t_0 \sin^2 \left( \phi + \frac{(N-1)\omega t_0}{N} \right) N^2}{16(N-1)^2\omega^2} \\
& - E_0 \left( \cos \left( \phi + \frac{(N+1)\omega t_0}{N} \right) (N-1)^2 + (N+1)^2 \cos \left( \phi + \frac{(N-1)\omega t_0}{N} \right) \right) \\
& \quad \cdot \frac{\cos \left( \phi + \frac{1}{2}(t+t_0)\omega \right) \sin \left( \frac{1}{2}(t-t_0)\omega \right) N^2}{4(N^2-1)^2\omega^3} \\
& + \frac{E_0 \left( N \sin \left( \frac{2\omega t}{N} \right) + \sin(2(\phi + \omega t)) \right) N^2}{64(N-1)^2\omega^3} + \frac{E_0 \left( N \sin \left( \frac{2\omega t}{N} \right) + \sin(2(\phi + \omega t)) \right) N^2}{64(N+1)^2\omega^3} \\
& + \frac{E_0 \left( -2\omega t + 2N(\phi + \omega t) + N \sin \left( 2 \left( \phi + \frac{(N-1)\omega t}{N} \right) \right) \right) N^2}{64(N-1)^3\omega^3} \\
& + \frac{E_0 \left( 2\omega t + 2N(\phi + \omega t) + N \sin \left( 2 \left( \phi + \frac{(N+1)\omega t}{N} \right) \right) \right) N^2}{64(N+1)^3\omega^3} \\
& - \frac{E_0 \left( N \sin \left( \frac{2\omega t_0}{N} \right) + \sin(2(\phi + \omega t_0)) \right) N^2}{64(N-1)^2\omega^3} - \frac{E_0 \left( N \sin \left( \frac{2\omega t_0}{N} \right) + \sin(2(\phi + \omega t_0)) \right) N^2}{64(N+1)^2\omega^3} \\
& - \frac{E_0 t_0 \sin \left( \phi + \frac{(N-1)\omega t}{N} \right) \sin \left( \phi + \frac{(N-1)\omega t_0}{N} \right) N^2}{16(N-1)^2\omega^2} \\
& + \frac{E_0 \left( N \cos \left( \phi + \frac{(N-1)\omega t}{N} \right) + (N-1)\omega t \sin \left( \phi + \frac{(N-1)\omega t}{N} \right) \right) \sin \left( \phi + \frac{(N-1)\omega t_0}{N} \right) N^2}{16(N-1)^3\omega^3} \\
& - \frac{E_0 t_0 \sin \left( \phi + \frac{(N+1)\omega t}{N} \right) \sin \left( \phi + \frac{(N-1)\omega t_0}{N} \right) N^2}{16(N^2-1)\omega^2} \\
& + \frac{E_0 \left( N \cos \left( \phi + \frac{(N+1)\omega t}{N} \right) + (N+1)\omega t \sin \left( \phi + \frac{(N+1)\omega t}{N} \right) \right) \sin \left( \phi + \frac{(N-1)\omega t_0}{N} \right) N^2}{16(N-1)(N+1)^2\omega^3} \\
& - \frac{E_0 \left( -2\omega t_0 + 2N(\phi + \omega t_0) + N \sin \left( 2 \left( \phi + \frac{(N-1)\omega t_0}{N} \right) \right) \right) N^2}{64(N-1)^3\omega^3}
\end{aligned}$$



$$\begin{aligned}
& - \frac{E_0 t_0 \sin\left(\phi + \frac{(N-1)\omega t}{N}\right) \sin\left(\phi + \frac{(N+1)\omega t_0}{N}\right) N^2}{16(N^2 - 1)\omega^2} \\
& + \frac{E_0 \left( N \cos\left(\phi + \frac{(N-1)\omega t}{N}\right) + (N-1)\omega t \sin\left(\phi + \frac{(N-1)\omega t}{N}\right) \right) \sin\left(\phi + \frac{(N+1)\omega t_0}{N}\right) N^2}{16(N-1)^2(N+1)\omega^3} \\
& - \frac{E_0 t_0 \sin\left(\phi + \frac{(N+1)\omega t}{N}\right) \sin\left(\phi + \frac{(N+1)\omega t_0}{N}\right) N^2}{16(N+1)^2\omega^2} \\
& + \frac{E_0 \left( N \cos\left(\phi + \frac{(N+1)\omega t}{N}\right) + (N+1)\omega t \sin\left(\phi + \frac{(N+1)\omega t}{N}\right) \right) \sin\left(\phi + \frac{(N+1)\omega t_0}{N}\right) N^2}{16(N+1)^3\omega^3} \\
& + \frac{E_0 t_0 \sin\left(\phi + \frac{(N-1)\omega t_0}{N}\right) \sin\left(\phi + \frac{(N+1)\omega t_0}{N}\right) N^2}{8(N^2 - 1)\omega^2} \\
& - \frac{E_0 \left( N \cos\left(\phi + \frac{(N-1)\omega t_0}{N}\right) + (N-1)\omega t_0 \sin\left(\phi + \frac{(N-1)\omega t_0}{N}\right) \right) \sin\left(\phi + \frac{(N+1)\omega t_0}{N}\right) N^2}{16(N-1)^2(N+1)\omega^3} \\
& - \frac{E_0 \left( 2\omega t_0 + 2N(\phi + \omega t_0) + N \sin\left(2\left(\phi + \frac{(N+1)\omega t_0}{N}\right)\right) \right) N^2}{64(N+1)^3\omega^3} \\
& + \frac{E_0 \left( (2N+1) \sin\left(\frac{\omega t}{N}\right) + \sin\left(2\phi + \left(2 + \frac{1}{N}\right)\omega t\right) \right) N}{16(2N+1)\omega^3} \\
& - \frac{E_0 \cos(\phi + \omega t_0) \sin\left(\phi + \frac{(N-1)\omega t}{N}\right) N}{8(N-1)\omega^3} - \frac{E_0 \cos(\phi + \omega t_0) \sin\left(\phi + \frac{(N+1)\omega t}{N}\right) N}{8(N+1)\omega^3} \\
& + \frac{x_{tunnel} \sin\left(\phi + \frac{(N+1)\omega t}{N}\right) N}{4(N+1)\omega} + \frac{E_0 \left( (2N-1) \sin\left(\frac{\omega t}{N}\right) + \sin\left(2\phi + \frac{(2N-1)\omega t}{N}\right) \right) N}{16(2N-1)\omega^3} \\
& - \frac{E_0 t_0 \sin\left(\phi + \frac{(N-1)\omega t}{N}\right) \sin(\phi + \omega t_0) N}{8(N-1)\omega^2} \\
& + \frac{E_0 \left( N \cos\left(\phi + \frac{(N-1)\omega t}{N}\right) + (N-1)\omega t \sin\left(\phi + \frac{(N-1)\omega t}{N}\right) \right) \sin(\phi + \omega t_0) N}{8(N-1)^2\omega^3} \\
& - \frac{E_0 t_0 \sin\left(\phi + \frac{(N+1)\omega t}{N}\right) \sin(\phi + \omega t_0) N}{8(N+1)\omega^2} \\
& + \frac{E_0 \left( N \cos\left(\phi + \frac{(N+1)\omega t}{N}\right) + (N+1)\omega t \sin\left(\phi + \frac{(N+1)\omega t}{N}\right) \right) \sin(\phi + \omega t_0) N}{8(N+1)^2\omega^3} \\
& - \frac{E_0 \left( (2N+1) \sin\left(\frac{\omega t_0}{N}\right) + \sin\left(2\phi + \left(2 + \frac{1}{N}\right)\omega t_0\right) \right) N}{16(2N+1)\omega^3} \\
& + \frac{E_0 \cos(\phi + \omega t_0) \sin\left(\phi + \frac{(N-1)\omega t_0}{N}\right) N}{8(N-1)\omega^3} + \frac{E_0 t_0 \sin(\phi + \omega t_0) \sin\left(\phi + \frac{(N-1)\omega t_0}{N}\right) N}{8(N-1)\omega^2} \\
& - \frac{E_0 \left( \cos(\phi + \omega t_0) + \omega t_0 \sin(\phi + \omega t_0) \right) \sin\left(\phi + \frac{(N-1)\omega t_0}{N}\right) N}{8(N-1)\omega^3} \\
& + \frac{E_0 \left( \cos(\phi + \omega t) + (t - t_0)\omega \sin(\phi + \omega t) + \omega t_0 \sin(\phi + \omega t_0) \right) \sin\left(\phi + \frac{(N-1)\omega t_0}{N}\right) N}{8(N-1)\omega^3}
\end{aligned}$$

$$\begin{aligned}
& - \frac{x_{tunnel} \sin\left(\phi + \frac{(N-1)\omega t_0}{N}\right) N}{4(N-1)\omega} \\
& - \frac{E_0 \left(2(N-1) \sin(\phi + \omega t_0) + N \sin\left(\phi + \frac{(N-1)\omega t_0}{N}\right)\right)}{16(N-1)^3 \omega^3} \\
& \cdot \left(N \cos\left(\phi + \frac{(N-1)\omega t_0}{N}\right) + (N-1)\omega t_0 \sin\left(\phi + \frac{(N-1)\omega t_0}{N}\right)\right) N \\
& + \frac{E_0 \cos(\phi + \omega t_0) \sin\left(\phi + \frac{(N+1)\omega t_0}{N}\right) N}{8(N+1)\omega^3} + \frac{E_0 t_0 \sin(\phi + \omega t_0) \sin\left(\phi + \frac{(N+1)\omega t_0}{N}\right) N}{8(N+1)\omega^2} \\
& - \frac{E_0 (\cos(\phi + \omega t_0) + \omega t_0 \sin(\phi + \omega t_0)) \sin\left(\phi + \frac{(N+1)\omega t_0}{N}\right) N}{8(N+1)\omega^3} \\
& + \frac{E_0 (\cos(\phi + \omega t) + (t - t_0)\omega \sin(\phi + \omega t) + \omega t_0 \sin(\phi + \omega t_0)) \sin\left(\phi + \frac{(N+1)\omega t_0}{N}\right) N}{8(N+1)\omega^3} \\
& - \frac{x_{tunnel} \sin\left(\phi + \frac{(N+1)\omega t_0}{N}\right) N}{4(N+1)\omega} + \frac{1}{2} x_{tunnel} \left(\frac{\cos(\omega t) \sin(\phi)}{\omega} + \frac{\cos(\phi) \sin(\omega t)}{\omega}\right) \\
& - \frac{E_0 \left(2(N^2 - 1) \sin(\phi + \omega t_0) + N(N+1) \sin\left(\phi + \frac{(N-1)\omega t_0}{N}\right) + (N-1)N \sin\left(\phi + \frac{(N+1)\omega t_0}{N}\right)\right)}{16(N-1)(N+1)^3 \omega^3} \\
& \cdot \left(N \cos\left(\phi + \frac{(N+1)\omega t_0}{N}\right) + (N+1)\omega t_0 \sin\left(\phi + \frac{(N+1)\omega t_0}{N}\right)\right) N \\
& - \frac{E_0 \left((2N-1) \sin\left(\frac{\omega t_0}{N}\right) + \sin\left(2\phi + \frac{(2N-1)\omega t_0}{N}\right)\right) N}{16(2N-1)\omega^3} \\
& - \frac{1}{2} x_{tunnel} \left(\frac{\cos(\omega t_0) \sin(\phi)}{\omega} + \frac{\cos(\phi) \sin(\omega t_0)}{\omega}\right) + \frac{E_0 (2(\phi + \omega t) + \sin(2(\phi + \omega t)))}{16\omega^3} \\
& + \frac{\frac{2N x_{tunnel} \sin\left(\phi + \frac{(N-1)\omega t}{N}\right) \omega^2}{N-1} - E_0 \sin(\omega(t - t_0)) + 2E_0 \cos\left(2\phi + \frac{1}{2}\omega(t + 3t_0)\right) \sin\left(\frac{1}{2}\omega(t_0 - t)\right)}{8\omega^3} \\
& - \frac{E_0 (2\phi + 2\omega t_0 - 2\omega(t - t_0) \cos(\omega(t - t_0)) + 2\omega(t - t_0) \cos(2\phi + \omega(t + t_0)))}{16\omega^3} \\
& - \frac{E_0 (+2 \sin(\omega(t - t_0)) + 3 \sin(2(\phi + \omega t_0)) - 2 \sin(2\phi + \omega(t + t_0)))}{16\omega^3}
\end{aligned}$$

## A.6 Graphically estimating $\beta$ for minimal HES width (details of Fig. 5.17)

In the following it is explained how the curves presented in Fig. 5.17 were obtained. Note, however, that even though the intersection of the blue and orange curve in Fig. 5.17 allows a graphical estimate for the  $\beta$  that leads to a minimal peak width, the quantitative method using the perturbative approach, presented in section 5.3.4, is recommended to be used for quantitative estimates of the  $\beta$  that leads to a minimized HES width. The purpose of Fig. 5.17 is to visualize the compensation effect presented in Fig. 5.16 and the way the exact numbers of that figure are obtained is of secondary relevance and are presented in the following for the mere sake of completeness.

The initial additional positive area  $A_{pos}$  of the head start trajectory, marked in or-

ange in Fig. 5.16, can be approximated to be independent of  $\beta$  as the acceleration (and consequently the field strength) is rather shallow around  $t = 0$  and, in particular, the field strength at the center of the pulse at the position of the atom is  $E_0$  per definition and thus also independent of  $\beta$ .  $A_{pos}$  can therefore be estimated by assuming a rectangle of a width in time of  $2\sigma$ . The rectangle's height can be estimated by  $|a(0)| = E_0$ .

The negative area,  $A_{neg}$ , under the second hump is depicted by a solid blue curve in Fig. 5.17. It grows linearly with  $\beta$  because  $|a_{min}| \propto \beta$  (see eq. (5.30)). Thus, in order to estimate the negative area  $A_{neg}$  under the second hump we do a trick similar to the one done to estimate the  $\beta$  dependence of the energy at which the HES peak is centered (see section 5.3.3): As the zeros of the acceleration are scarcely affected by  $\beta$  and as the function looks close to something like a sine or cosine, we can assume that the area scales linearly with the minimum  $a_{min}$  of the curve:  $A_{neg} \propto |(a_{t_0=-\sigma}(t_{min}) - a_{t_0=+\sigma}(t_{min}))|$ . We also need to determine the prefactor  $A_{ref}$ , which determines the slope:

$$A_{neg} = A_{ref} |a_{min,t_0=-\sigma}(t_{min}) - a_{min,t_0=+\sigma}(t_{min})|. \quad (\text{A.26})$$

As this equation calculates just the difference between the full area under the second hump for  $t_0 = -\sigma$  and the full area under the second hump for  $t_0 = +\sigma$ , this prefactor can be determined by the knowledge about the area under the second hump for a single ionization time. We choose  $t_0 = 0$  as for this case we can use eq. (5.18) and eq. (5.21) (velocity estimate from Mathieu functions) to determine the area under the second hump immediately as  $|v_{end}(t_{z,1}) - v_{Approx,1}(t_{z,2})|$  where  $t_{z,1/2}$  denote the limits in time of the negative hump, the zeros of  $a(t)$ . Thus, we obtain

$$A_{ref} \approx \frac{|v_{end}(t_{z,1}) - v_{Approx,1}(t_{z,2})|}{|a_{t_0=0}(t_{min})|}. \quad (\text{A.27})$$

Now, the inhomogeneity at which the additional positive area  $A_{pos}$  of the head start trajectory (dashed orange line) and the additional negative Area  $A_{neg}$  (solid blue line) intersect, should be a good estimate for the inhomogeneity leading to a minimal width in energy of the HES peak. In the case shown in Fig. 5.17, this graphical method gives  $\beta \approx 0.0019$  for the optimal inhomogeneity, which agrees well with  $\beta \approx 0.002$  that we got from solving eq. (5.11) numerically for  $t_0 = 0, \pm\sigma$  for various  $\beta$  (see central panel in Fig. 5.16).



---

## Bibliography

- [1] M. Ammosov, N. Delone, and V. Krainov. “Tunnel ionization of complex atoms and of atomic ions in an alternating electric field”. *Sov. Phys. JETP* 64 (1986), p. 1191.
- [2] D. I. Bondar. “Instantaneous multiphoton ionization rate and initial distribution of electron momentum”. *Physical Review A* 78.1 (2008), p. 015405.
- [3] M. Li, J.-W. Geng, M. Han, M.-M. Liu, L.-Y. Peng, Q. Gong, and Y. Liu. “Subcycle nonadiabatic strong-field tunneling ionization”. *Physical Review A* 93.1 (2016), p. 013402.
- [4] A. Perelomov, V. Popov, and M. Terent’ev. “Ionization of atoms in an alternating electric field”. *Sov. Phys. JETP* 23.5 (1966), p. 924.
- [5] A. Perelomov, V. Popov, and M. Terent’ev. “Ionization of atoms in an alternating electric field: II”. *Sov. Phys. JETP* 24.1 (1967), p. 207.
- [6] A. N. Pfeiffer, C. Cirelli, M. Smolarski, D. Dimitrovski, M. Abu-Samha, L. B. Madsen, and U. Keller. “Attoclock reveals natural coordinates of the laser-induced tunnelling current flow in atoms”. *Nature Physics* 8.1 (2012), p. 76.
- [7] G. L. Yudin and M. Y. Ivanov. “Nonadiabatic tunnel ionization: Looking inside a laser cycle”. *Physical Review A* 64.1 (2001), p. 013409.
- [8] D. Strickland and G. Mourou. “Compression of amplified chirped optical pulses”. *Optics Communications* 55.6 (1985), p. 447.
- [9] *Groundbreaking inventions in laser physics: optical tweezers and generation of high-intensity, ultra-short optical pulses. Scientific background on the Nobel Prize in Physics 2018. The Nobel Prize Committee in Physics (2018).*
- [10] T. Brabec and F. Krausz. “Intense few-cycle laser fields: Frontiers of nonlinear optics”. *Reviews of Modern Physics* 72.2 (2000), p. 545.
- [11] A. Scrinzi, M. Y. Ivanov, R. Kienberger, and D. M. Villeneuve. “Attosecond physics”. *Journal of Physics B: Atomic, Molecular and Optical Physics* 39.1 (2005), R1.

- [12] A. Baltuška, T. Udem, M. Uiberacker, M. Hentschel, E. Goulielmakis, C. Gohle, R. Holzwarth, V. Yakovlev, A. Scrinzi, T. W. Hänsch, et al. "Attosecond control of electronic processes by intense light fields". *Nature* 421.6923 (2003), p. 611.
- [13] S. T. Cundiff and J. Ye. "Phase stabilization of mode-locked lasers". *Journal of Modern Optics* 52.2-3 (2005), p. 201.
- [14] M. Kremer, B. Fischer, B. Feuerstein, V. L. B. de Jesus, V. Sharma, C. Hofrichter, A. Rudenko, U. Thumm, C. D. Schröter, R. Moshhammer, et al. "Electron localization in molecular fragmentation of  $H_2$  by carrier-envelope phase stabilized laser pulses". *Physical Review Letters* 103.21 (2009), p. 213003.
- [15] I. J. Sola, E. Mével, L. Elouga, E. Constant, V. Strelkov, L. Poletto, P. Villoresi, E. Benedetti, J.-P. Caumes, S. Stagira, et al. "Controlling attosecond electron dynamics by phase-stabilized polarization gating". *Nature Physics* 2.5 (2006), p. 319.
- [16] M. Meckel, D. Comtois, D. Zeidler, A. Staudte, D. Pavičić, H. Bandulet, H. Pépin, J. Kieffer, R. Dörner, D. Villeneuve, et al. "Laser-induced electron tunneling and diffraction". *Science* 320.5882 (2008), p. 1478.
- [17] T. Zuo, A. D. Bandrauk, and P. B. Corkum. "Laser-induced electron diffraction: a new tool for probing ultrafast molecular dynamics". *Chemical Physics Letters* 259.3-4 (1996), p. 313.
- [18] C. I. Blaga, J. Xu, A. D. DiChiara, E. Sistrunk, K. Zhang, P. Agostini, T. A. Miller, L. F. DiMauro, and C. Lin. "Imaging ultrafast molecular dynamics with laser-induced electron diffraction". *Nature* 483.7388 (2012), p. 194.
- [19] M. G. Pullen, B. Wolter, A.-T. Le, M. Baudisch, M. Hemmer, A. Senftleben, C. D. Schröter, J. Ullrich, R. Moshhammer, C.-D. Lin, et al. "Imaging an aligned polyatomic molecule with laser-induced electron diffraction". *Nature Communications* 6 (2015), p. 7262.
- [20] J. Yeston. "Acetylene's scission visualized by selfie". Comment in *Science* 354 (2016), p. 299.
- [21] J. Itatani, J. Levesque, D. Zeidler, H. Niikura, H. Pépin, J.-C. Kieffer, P. B. Corkum, and D. M. Villeneuve. "Tomographic imaging of molecular orbitals". *Nature* 432.7019 (2004), p. 867.
- [22] T. Morishita, A.-T. Le, Z. Chen, and C. D. Lin. "Accurate retrieval of structural information from laser-induced photoelectron and high-order harmonic spectra by few-cycle laser pulses". *Physical Review Letters* 100.1 (2008), p. 013903.
- [23] M. Lein, N. Hay, R. Velotta, J. P. Marangos, and P. L. Knight. "Interference effects in high-order harmonic generation with molecules". *Physical Review A* 66.2 (2002), p. 023805.
- [24] T. Kanai, S. Minemoto, and H. Sakai. "Quantum interference during high-order harmonic generation from aligned molecules". *Nature* 435.7041 (2005), p. 470.
- [25] S. Baker, J. S. Robinson, C. A. Haworth, H. Teng, R. A. Smith, C. C. Chirilă, M. Lein, J. W. G. Tisch, and J. P. Marangos. "Probing proton dynamics in molecules on an attosecond time scale". *Science* 312.5772 (2006), p. 424.
- [26] D. Shafir, H. Soifer, B. D. Bruner, M. Dagan, Y. Mairesse, S. Patchkovskii, M. Y. Ivanov, O. Smirnova, and N. Dudovich. "Resolving the time when an electron exits a tunnelling barrier". *Nature* 485.7398 (2012), p. 343.

- [27] S. Ghimire, A. D. DiChiara, E. Sistrunk, P. Agostini, L. F. DiMauro, and D. A. Reis. “Observation of high-order harmonic generation in a bulk crystal”. *Nature Physics* 7.2 (2011), p. 138.
- [28] S. Ghimire and D. A. Reis. “High-harmonic generation from solids”. *Nature Physics* 15.1 (2019), p. 10.
- [29] G. Vampa, T. J. Hammond, N. Thiré, B. E. Schmidt, F. Légaré, C. R. McDonald, T. Brabec, D. D. Klug, and P. B. Corkum. “All-optical reconstruction of crystal band structure”. *Physical Review Letters* 115.19 (2015), p. 193603.
- [30] A. Sommer, E. Bothschafter, S. Sato, C. Jakubeit, T. Latka, O. Razskazovskaya, H. Fattahi, M. Jobst, W. Schweinberger, V. Shirvanyan, et al. “Attosecond non-linear polarization and light–matter energy transfer in solids”. *Nature* 534.7605 (2016), p. 86.
- [31] Y. S. You, D. A. Reis, and S. Ghimire. “Anisotropic high-harmonic generation in bulk crystals”. *Nature Physics* 13.4 (2017), p. 345.
- [32] S. Han, L. Ortmann, H. Kim, Y. W. Kim, T. Oka, A. Chacon, B. Doran, M. Ciappina, M. Lewenstein, S.-W. Kim, et al. “Extraction of higher-order nonlinear electronic response to strong field excitation in solids using high harmonic generation”. *arXiv preprint* 1904.11103 (2019).
- [33] M. Y. Ivanov, M. Spanner, and O. Smirnova. “Anatomy of strong field ionization”. *Journal of Modern Optics* 52.2-3 (2005), p. 165.
- [34] K. Amini, J. Biegert, F. Calegari, A. Chacón, M. F. Ciappina, A. Dauphin, D. K. Efimov, C. F.d. M. Faria, K. Giergiel, P. Gniewek, et al. “Symphony on Strong Field Approximation”. *arXiv preprint* 1812.11447 (2018).
- [35] M. Lewenstein, P. Balcou, M. Y. Ivanov, A. L’Huillier, and P. B. Corkum. “Theory of high-harmonic generation by low-frequency laser fields”. *Physical Review A* 49.3 (1994), p. 2117.
- [36] B. Yang, K. J. Schafer, B. Walker, K. C. Kulander, P. Agostini, and L. F. DiMauro. “Intensity-dependent scattering rings in high order above-threshold ionization”. *Physical Review Letters* 71.23 (1993), p. 3770.
- [37] M. Lewenstein, K. C. Kulander, K. J. Schafer, and P. Bucksbaum. “Rings in above-threshold ionization: A quasiclassical analysis”. *Physical Review A* 51.2 (1995), p. 1495.
- [38] W. Becker, X. Liu, P. J. Ho, and J. H. Eberly. “Theories of photoelectron correlation in laser-driven multiple atomic ionization”. *Reviews of Modern Physics* 84.3 (2012), p. 1011.
- [39] P. B. Corkum. “Plasma perspective on strong field multiphoton ionization”. *Physical Review Letters* 71.13 (1993), p. 1994.
- [40] G. G. Paulus, W. Becker, W. Nicklich, and H. Walther. “Rescattering effects in above-threshold ionization: a classical model”. *Journal of Physics B: Atomic, Molecular and Optical Physics* 27.21 (1994), p. L703.
- [41] A. Staudte, C. Ruiz, M. Schöffler, S. Schössler, D. Zeidler, T. Weber, M. Meckel, D. M. Villeneuve, P. B. Corkum, A. Becker, et al. “Binary and recoil collisions in strong field double ionization of helium”. *Physical Review Letters* 99.26 (2007), p. 263002.



- [42] F. Lindner, M. G. Schätzel, H. Walther, A. Baltuška, E. Goulielmakis, F. Krausz, D. Milošević, D. Bauer, W. Becker, and G. G. Paulus. “Attosecond double-slit experiment”. *Physical Review Letters* 95.4 (2005), p. 040401.
- [43] T. Brabec, M. Y. Ivanov, and P. B. Corkum. “Coulomb focusing in intense field atomic processes”. *Physical Review A* 54.4 (1996), R2551.
- [44] B. HuP, J. Liu, and S.-G. Chen. “Plateau in above-threshold-ionization spectra and chaotic behavior in rescattering processes”. *Physics Letters A* 236.5-6 (1997), p. 533.
- [45] L.-B. Fu, J. Liu, J. Chen, and S.-G. Chen. “Classical collisional trajectories as the source of strong-field double ionization of helium in the knee regime”. *Physical Review A* 63.4 (2001), p. 043416.
- [46] K. I. Dimitriou, D. G. Arbó, S. Yoshida, E. Persson, and J. Burgdörfer. “Origin of the double-peak structure in the momentum distribution of ionization of hydrogen atoms driven by strong laser fields”. *Physical Review A* 70.6 (2004), p. 061401.
- [47] A. Chacón, L. Ortmann, F. Cucchietti, N. Suárez, J. A. Pérez-Hernández, M. F. Ciappina, A. S. Landsman, and M. Lewenstein. “Double-electron ionization driven by inhomogeneous fields”. *Exploring the World with the Laser*. Springer, 2018, p. 491.
- [48] T. Nubbemeyer, K. Gorling, A. Saenz, U. Eichmann, and W. Sandner. “Strong-field tunneling without ionization”. *Physical Review Letters* 101.23 (2008), p. 233001.
- [49] N. I. Shvetsov-Shilovski, S. P. Goreslavski, S. V. Popruzhenko, and W. Becker. “Capture into Rydberg states and momentum distributions of ionized electrons”. *Laser Physics* 19.8 (2009), p. 1550.
- [50] K.-y. Huang, Q.-z. Xia, and L.-B. Fu. “Survival window for atomic tunneling ionization with elliptically polarized laser fields”. *Physical Review A* 87.3 (2013), p. 033415.
- [51] W.-H. Xiong, X.-R. Xiao, L.-Y. Peng, and Q. Gong. “Correspondence of below-threshold high-order-harmonic generation and frustrated tunneling ionization”. *Physical Review A* 94.1 (2016), p. 013417.
- [52] H. Price, C. Lazarou, and A. Emmanouilidou. “Toolkit for semiclassical computations for strongly driven molecules: Frustrated ionization of  $H_2$  driven by elliptical laser fields”. *Physical Review A* 90.5 (2014), p. 053419.
- [53] C. Liu and K. Z. Hatsagortsyan. “Origin of unexpected low energy structure in photoelectron spectra induced by midinfrared strong laser fields”. *Physical Review Letters* 105.11 (2010), p. 113003.
- [54] C. Lemell, K. I. Dimitriou, X.-M. Tong, S. Nagele, D. V. Kartashov, J. Burgdörfer, and S. Gräfe. “Low-energy peak structure in strong-field ionization by midinfrared laser pulses: Two-dimensional focusing by the atomic potential”. *Physical Review A* 85.1 (2012), p. 011403.
- [55] B. Wolter, C. Lemell, M. Baudisch, M. G. Pullen, X.-M. Tong, M. Hemmer, A. Senftleben, C. D. Schröter, J. Ullrich, R. Moshhammer, et al. “Formation of very-low-energy states crossing the ionization threshold of argon atoms in strong mid-infrared fields”. *Physical Review A* 90.6 (2014), p. 063424.

- [56] M. Li, Y. Liu, H. Liu, Q. Ning, L. Fu, J. Liu, Y. Deng, C. Wu, L.-Y. Peng, and Q. Gong. “Subcycle dynamics of coulomb asymmetry in strong elliptical laser fields”. *Physical Review Letters* 111.2 (2013), p. 023006.
- [57] R. Boge, C. Cirelli, A. S. Landsman, S. Heuser, A. Ludwig, J. Maurer, M. Weger, L. Gallmann, and U. Keller. “Probing nonadiabatic effects in strong-field tunnel ionization”. *Physical Review Letters* 111.10 (2013), p. 103003.
- [58] C. Hofmann, A. S. Landsman, A. Zielinski, C. Cirelli, T. Zimmermann, A. Scrinzi, and U. Keller. “Interpreting electron-momentum distributions and nonadiabaticity in strong-field ionization”. *Physical Review A* 90.4 (2014), p. 043406.
- [59] X. Sun, M. Li, J. Yu, Y. Deng, Q. Gong, and Y. Liu. “Calibration of the initial longitudinal momentum spread of tunneling ionization”. *Physical Review A* 89.4 (2014), p. 045402.
- [60] N. I. Shvetsov-Shilovski, M. Lein, L. Madsen, E. Räsänen, C. Lemell, J. Burgdörfer, D. G. Arbó, and K. Tókési. “Semiclassical two-step model for strong-field ionization”. *Physical Review A* 94.1 (2016), p. 013415.
- [61] M. Li, M.-M. Liu, J.-W. Geng, M. Han, X. Sun, Y. Shao, Y. Deng, C. Wu, L.-Y. Peng, Q. Gong, et al. “Experimental verification of the nonadiabatic effect in strong-field ionization with elliptical polarization”. *Physical Review A* 95.5 (2017), p. 053425.
- [62] M. Li, J.-W. Geng, H. Liu, Y. Deng, C. Wu, L.-Y. Peng, Q. Gong, and Y. Liu. “Classical-quantum correspondence for above-threshold ionization”. *Physical Review Letters* 112.11 (2014), p. 113002.
- [63] M. Richter, M. Kunitski, M. Schöffler, T. Jahnke, L. P. Schmidt, M. Li, Y. Liu, and R. Dörner. “Streaking temporal double-slit interference by an orthogonal two-color laser field”. *Physical Review Letters* 114.14 (2015), p. 143001.
- [64] J.-W. Geng, L. Qin, M. Li, W.-H. Xiong, Y. Liu, Q. Gong, and L.-Y. Peng. “Nonadiabatic tunneling ionization of atoms in elliptically polarized laser fields”. *Journal of Physics B: Atomic, Molecular and Optical Physics* 47.20 (2014), p. 204027.
- [65] H. Xie, M. Li, Y. Li, Y. Zhou, and P. Lu. “Intra-half-cycle interference of low-energy photoelectron in strong midinfrared laser fields”. *Optics Express* 24.24 (2016), p. 27726.
- [66] L.-Y. Peng, W.-C. Jiang, J.-W. Geng, W.-H. Xiong, and Q. Gong. “Tracing and controlling electronic dynamics in atoms and molecules by attosecond pulses”. *Physics Reports* 575 (2015), p. 1.
- [67] X. Gong, C. Lin, F. He, Q. Song, K. Lin, Q. Ji, W. Zhang, J. Ma, P. Lu, Y. Liu, et al. “Energy-resolved ultrashort delays of photoelectron emission clocked by orthogonal two-color laser fields”. *Physical Review Letters* 118.14 (2017), p. 143203.
- [68] J.-P. Wang and F. He. “Tunneling ionization of neon atoms carrying different orbital angular momenta in strong laser fields”. *Physical Review A* 95.4 (2017), p. 043420.
- [69] S. Popruzhenko, G. G. Paulus, and D. Bauer. “Coulomb-corrected quantum trajectories in strong-field ionization”. *Physical Review A* 77.5 (2008), p. 053409.

- [70] S. Popruzhenko and D. Bauer. “Strong field approximation for systems with Coulomb interaction”. *Journal of Modern Optics* 55.16 (2008), p. 2573.
- [71] L. Ortmann, C. Hofmann, and A. Landsman. “Dependence of Rydberg-state creation by strong-field ionization on laser intensity”. *Physical Review A* 98.3 (2018), p. 033415.
- [72] L. Ortmann, C. Hofmann, and A. Landsman. “Controlling the quantum number distribution and yield of Rydberg states via the duration of the laser pulse”. *arXiv preprint* 1810.07164 (2018).
- [73] L. Ortmann, J. Pérez-Hernández, M. Ciappina, J. Schötz, A. Chacón, G. Zeraoui, M. F. Kling, L. Roso, M. Lewenstein, and A. Landsman. “Emergence of a higher energy structure in strong field ionization with inhomogeneous electric fields”. *Physical Review Letters* 119.5 (2017), p. 053204.
- [74] L. Ortmann and A. Landsman. “Analysis of the higher-energy structure in strong-field ionization with inhomogeneous electric fields”. *Physical Review A* 97.2 (2018), p. 023420.
- [75] J. Schötz, S. Mitra, H. Fuest, M. Neuhaus, W. Okell, M. Förster, T. Paschen, M. F. Ciappina, H. Yanagisawa, P. Wnuk, et al. “Nonadiabatic ponderomotive effects in photoemission from nanotips in intense midinfrared laser fields”. *Physical Review A* 97.1 (2018), p. 013413.
- [76] A. Einstein. “Über einen die Erzeugung und Verwandlung des Lichtes betreffenden heuristischen Gesichtspunkt”. *Annalen der Physik* 322.6 (1905), p. 132.
- [77] C. Müller. The structure of the lists describing single and multiphoton ionization in this dissertation is based on the slides of the “*Lecture on multiphoton physics*”. [https://www.mpi-hd.mpg.de/imprs-qd/fileadmin/user\\_upload/Internal\\_School\\_2013/IMPRS\\_2013\\_CMueller.pdf](https://www.mpi-hd.mpg.de/imprs-qd/fileadmin/user_upload/Internal_School_2013/IMPRS_2013_CMueller.pdf). 2013 (accessed March 14, 2019).
- [78] M. Göppert-Mayer. “Über Elementarakte mit zwei Quantensprüngen”. *Annalen der Physik* 401.3 (1931), p. 273.
- [79] P. A. Franken, A. E. Hill, C. W. Peters, and G. Weinreich. “Generation of optical harmonics”. *Physical Review Letters* 7.4 (1961), p. 118.
- [80] W. Kaiser and C. G. B. Garrett. “Two-photon excitation in  $CaF_2: Eu^{2+}$ ”. *Physical Review Letters* 7.6 (1961), p. 229.
- [81] P. Agostini, F. Fabre, G. Mainfray, G. Petite, and N. K. Rahman. “Free-free transitions following six-photon ionization of xenon atoms”. *Physical Review Letters* 42.17 (1979), p. 1127.
- [82] P. Agostini. “The Simple Rahman’s Theory”. *Universality And Diversity In Science: Festschrift in Honor of Naseem K Rahman’s 60th Birthday*. World Scientific, 2004, p. 1.
- [83] C. J. Joachain, N. J. Kylstra, and R. M. Potvliege. *Atoms in intense laser fields*. Cambridge University Press, 2012.
- [84] P. Kruit, J. Kimman, H. G. Muller, and M. J. Van der Wiel. “Electron spectra from multiphoton ionization of xenon at 1064, 532, and 355 nm”. *Physical Review A* 28.1 (1983), p. 248.

- [85] H. G. Muller, A. Tip, and M. J. Van der Wiel. "Ponderomotive force and AC Stark shift in multiphoton ionisation". *Journal of Physics B: Atomic and Molecular Physics* 16.22 (1983), p. L679.
- [86] B. J. Sussman. "Five ways to the nonresonant dynamic Stark effect". *American Journal of Physics* 79.5 (2011), p. 477.
- [87] P. Mulser, S. Uryupin, R. Sauerbrey, and B. Wellegehausen. "Ponderomotive potential and dynamical Stark shift in multiphoton ionization". *Physical Review A* 48.6 (1993), p. 4547.
- [88] P. Agostini and G. Petite. "Photoelectric effect under strong irradiation". *Contemporary Physics* 29.1 (1988), p. 57.
- [89] L. V. Keldysh. "Ionization in the field of a strong electromagnetic wave". *Sov. Phys. JETP* 20.5 (1965), p. 1307.
- [90] V. S. Popov. "Tunnel and multiphoton ionization of atoms and ions in a strong laser field (Keldysh theory)". *Physics-Uspekhi* 47.9 (2004), p. 855.
- [91] A. S. Landsman and U. Keller. "Attosecond science and the tunnelling time problem". *Physics Reports* 547 (2015), p. 1.
- [92] M. Klaiber, K. Z. Hatsagortsyan, and C. H. Keitel. "Tunneling dynamics in multiphoton ionization and attoclock calibration". *Physical Review Letters* 114.8 (2015), p. 083001.
- [93] J. Tian, X. Wang, and J. H. Eberly. "Numerical Detector Theory for the Longitudinal Momentum Distribution of the Electron in Strong Field Ionization". *Physical Review Letters* 118.21 (2017), p. 213201.
- [94] H. Ni, N. Eicke, C. Ruiz, J. Cai, F. Oppermann, N. I. Shvetsov-Shilovski, and L.-W. Pi. "Tunneling criteria and a nonadiabatic term for strong-field ionization". *Physical Review A* 98.1 (2018), p. 013411.
- [95] H. R. Reiss. "Limits on tunneling theories of strong-field ionization". *Physical Review Letters* 101.4 (2008), p. 043002.
- [96] F. Weinhold. *Discovering chemistry with natural bond orbitals*. John Wiley & Sons, 2012.
- [97] G. W. Drake. *Springer handbook of atomic, molecular, and optical physics*. Springer Science & Business Media, 2006.
- [98] D. Dimitrovski, C. P. Martiny, and L. B. Madsen. "Strong-field ionization of polar molecules: Stark-shift-corrected strong-field approximation". *Physical Review A* 82.5 (2010), p. 053404.
- [99] E. Pisanty Alatorre. "Electron dynamics in complex time and complex space". PhD thesis. Imperial College London, 2016.
- [100] T. Keil and D. Bauer. "Coulomb-corrected strong-field quantum trajectories beyond dipole approximation". *Journal of Physics B: Atomic, Molecular and Optical Physics* 50.19 (2017), p. 194002.
- [101] A. Ludwig, J. Maurer, B. W. Mayer, C. R. Phillips, L. Gallmann, and U. Keller. "Breakdown of the dipole approximation in strong-field ionization". *Physical Review Letters* 113.24 (2014), p. 243001.

- [102] P. Agostini and L. F. DiMauro. “Atomic and molecular ionization dynamics in strong laser fields: from optical to x-rays”. *Advances In Atomic, Molecular, and Optical Physics*. Vol. 61. Elsevier, 2012, p. 117.
- [103] R. R. Freeman, P. Bucksbaum, H. Milchberg, S. Darack, D. Schumacher, and M. E. Geusic. “Above-threshold ionization with subpicosecond laser pulses”. *Physical Review Letters* 59.10 (1987), p. 1092.
- [104] D. J. Tannor. *Introduction to quantum mechanics: a time-dependent perspective*. University Science Books, 2007.
- [105] P. Ehrenfest. “Bemerkung über die angenäherte Gültigkeit der klassischen Mechanik innerhalb der Quantenmechanik”. *Zeitschrift für Physik A Hadrons and Nuclei* 45.7 (1927), p. 455.
- [106] C. Hofmann. “Attosecond electron dynamics in strong-field ionization”. PhD thesis. ETH Zurich, 2016.
- [107] P. B. Corkum and F. Krausz. “Attosecond science”. *Nature Physics* 3.6 (2007), p. 381.
- [108] N. Shvetsov-Shilovski, D. Dimitrovski, and L. B. Madsen. “Ehrenfest’s theorem and the validity of the two-step model for strong-field ionization”. *Physical Review A* 87.1 (2013), p. 013427.
- [109] F. H. Faisal. “Multiple absorption of laser photons by atoms”. *Journal of Physics B: Atomic and Molecular Physics* 6.4 (1973), p. L89.
- [110] H. R. Reiss. “Effect of an intense electromagnetic field on a weakly bound system”. *Physical Review A* 22.5 (1980), p. 1786.
- [111] D. Bauer, D. Milošević, and W. Becker. “Strong-field approximation for intense-laser-atom processes: The choice of gauge”. *Physical Review A* 72.2 (2005), p. 023415.
- [112] R. Schlicher, W. Becker, J. Bergou, and M. Scully. “Interaction Hamiltonian in Quantum Optics”. *Quantum Electrodynamics and Quantum Optics*. Springer, 1984, p. 405.
- [113] P. Eckle, M. Smolarski, P. Schlup, J. Biegert, A. Staudte, M. Schöffler, H. G. Müller, R. Dörner, and U. Keller. “Attosecond angular streaking”. *Nature Physics* 4.7 (2008), p. 565.
- [114] P. Eckle, A. N. Pfeiffer, C. Cirelli, A. Staudte, R. Dörner, H. G. Müller, M. Büttiker, and U. Keller. “Attosecond ionization and tunneling delay time measurements in helium”. *science* 322.5907 (2008), p. 1525.
- [115] L. Torlina, F. Morales, J. Kaushal, I. Ivanov, A. Kheifets, A. Zielinski, A. Scrinzi, H. G. Müller, S. Sukiasyan, M. Ivanov, et al. “Interpreting attoclock measurements of tunnelling times”. *Nature Physics* 11.6 (2015), p. 503.
- [116] H. Ni, U. Saalman, and J.-M. Rost. “Tunneling ionization time resolved by backpropagation”. *Physical Review Letters* 117.2 (2016), p. 023002.
- [117] I. Ivanov, C. Hofmann, L. Ortmann, A. S. Landsman, C. H. Nam, and K. T. Kim. “Instantaneous ionization rate as a functional derivative”. *Communications Physics* 1.1 (2018), p. 81.
- [118] C. Hofmann, A. S. Landsman, and U. Keller. “Attoclock revisited on electron tunnelling time”. *arXiv preprint* 1901.07015 (2019).



- [119] S. Popruzhenko. “Keldysh theory of strong field ionization: history, applications, difficulties and perspectives”. *Journal of Physics B: Atomic, Molecular and Optical Physics* 47.20 (2014), p. 204001.
- [120] A. S. Landsman and U. Keller. “Tunnelling time in strong field ionisation”. *Journal of Physics B: Atomic, Molecular and Optical Physics* 47.20 (2014), p. 204024.
- [121] L. D. Landau and E. M. Lifshitz. *Quantum mechanics: non-relativistic theory*. Vol. 3. Pergamon press, 1958.
- [122] C. Hofmann, A. S. Landsman, C. Cirelli, A. N. Pfeiffer, and U. Keller. “Comparison of different approaches to the longitudinal momentum spread after tunnel ionization”. *Journal of Physics B: Atomic, Molecular and Optical Physics* 46.12 (2013), p. 125601.
- [123] J. Wu, M. Meckel, S. Voss, H. Sann, M. Kunitski, L. P. H. Schmidt, A. Czasch, H. Kim, T. Jahnke, and R. Dörner. “Coulomb asymmetry in strong field multielectron ionization of diatomic molecules”. *Physical Review Letters* 108.4 (2012), p. 043002.
- [124] N. Shvetsov-Shilovski, D. Dimitrovski, and L. B. Madsen. “Ionization in elliptically polarized pulses: Multielectron polarization effects and asymmetry of photoelectron momentum distributions”. *Physical Review A* 85.2 (2012), p. 023428.
- [125] S. Goreslavski, G. Paulus, S. Popruzhenko, and N. Shvetsov-Shilovski. “Coulomb asymmetry in above-threshold ionization”. *Physical Review Letters* 93.23 (2004), p. 233002.
- [126] N. Eicke and M. Lein. “Trajectory-free ionization times in strong-field ionization”. *Physical Review A* 97.3 (2018), p. 031402.
- [127] M. Magrakvelidze, F. He, S. De, I. Bocharova, D. Ray, U. Thumm, and I. Litvinyuk. “Angular dependence of the strong-field ionization measured in randomly oriented hydrogen molecules”. *Physical Review A* 79.3 (2009), p. 033408.
- [128] L. F. Shampine and M. W. Reichelt. “The matlab ode suite”. *SIAM Journal on Scientific Computing* 18.1 (1997), p. 1.
- [129] R. Ashino, M. Nagase, and R. Vaillancourt. “Behind and beyond the MATLAB ODE suite”. *Computers and Mathematics with Applications* 40.4-5 (2000), p. 491.
- [130] M.-M. Liu, M. Li, C. Wu, Q. Gong, A. Staudte, and Y. Liu. “Phase structure of strong-field tunneling wave packets from molecules”. *Physical Review Letters* 116.16 (2016), p. 163004.
- [131] S. G. Walt, N. B. Ram, M. Atala, N. I. Shvetsov-Shilovski, A. Von Conta, D. Baykushcheva, M. Lein, and H. J. Wörner. “Dynamics of valence-shell electrons and nuclei probed by strong-field holography and rescattering”. *Nature Communications* 8 (2017), p. 15651.
- [132] M.-M. Liu and Y. Liu. “Semiclassical models for strong-field tunneling ionization of molecules”. *Journal of Physics B: Atomic, Molecular and Optical Physics* 50.10 (2017), p. 105602.
- [133] Y. Shao, M. Li, M.-M. Liu, X. Sun, X. Xie, P. Wang, Y. Deng, C. Wu, Q. Gong, and Y. Liu. “Isolating resonant excitation from above-threshold ionization”. *Physical Review A* 92.1 (2015), p. 013415.



- [134] Y. Wang, S. Yu, X. Lai, H. Kang, S. Xu, R. Sun, W. Quan, and X. Liu. “Separating intracycle interferences in photoelectron momentum distributions by a polarization-gated pulse”. *Physical Review A* 98.4 (2018), p. 043422.
- [135] N. Shvetsov-Shilovski and M. Lein. “Effects of the Coulomb potential in interference patterns of strong-field holography with photoelectrons”. *Physical Review A* 97.1 (2018), p. 013411.
- [136] V. Mur, S. Popruzhenko, and V. Popov. “Energy and momentum spectra of photoelectrons under conditions of ionization by strong laser radiation (the case of elliptic polarization)”. *Journal of Experimental and Theoretical Physics* 92.5 (2001), p. 777.
- [137] M. Uiberacker, T. Uphues, M. Schultze, A. J. Verhoef, V. Yakovlev, M. F. Kling, J. Rauschenberger, N. M. Kabachnik, H. Schröder, M. Lezius, et al. “Attosecond real-time observation of electron tunnelling in atoms”. *Nature* 446.7136 (2007), p. 627.
- [138] A. Shiner, C. Trallero-Herrero, N. Kajumba, H.-C. Bandulet, D. Comtois, F. Légaré, M. Giguère, J. Kieffer, P. Corkum, and D. Villeneuve. “Wavelength scaling of high harmonic generation efficiency”. *Physical Review Letters* 103.7 (2009), p. 073902.
- [139] A. Rupenyan, P. M. Kraus, J. Schneider, and H. J. Wörner. “High-harmonic spectroscopy of isoelectronic molecules: Wavelength scaling of electronic-structure and multielectron effects”. *Physical Review A* 87.3 (2013), p. 033409.
- [140] S. Chelkowski and A. D. Bandrauk. “Asymmetries in strong-field photoionization by few-cycle laser pulses: Kinetic-energy spectra and semiclassical explanation of the asymmetries of fast and slow electrons”. *Physical Review A* 71.5 (2005), p. 053815.
- [141] P. Dombi, A. Horl, P. Racz, I. Marton, A. Trugler, J. R. Krenn, and U. Hohenester. “Ultrafast strong-field photoemission from plasmonic nanoparticles”. *Nano Letters* 13.2 (2013), p. 674.
- [142] P. M. Kraus, B. Mignolet, D. Baykusheva, A. Rupenyan, L. Horný, E. F. Penka, G. Grassi, O. I. Tolstikhin, J. Schneider, F. Jensen, et al. “Measurement and laser control of attosecond charge migration in ionized iodoacetylene”. *Science* 350.6262 (2015), p. 790.
- [143] A. Staudte, S. Patchkovskii, D. Pavičić, H. Akagi, O. Smirnova, D. Zeidler, M. Meckel, D. Villeneuve, R. Dörner, M. Y. Ivanov, et al. “Angular tunneling ionization probability of fixed-in-space  $H_2$  molecules in intense laser pulses”. *Physical Review Letters* 102.3 (2009), p. 033004.
- [144] L. Zhang, X. Xie, S. Roither, Y. Zhou, P. Lu, D. Kartashov, M. Schöffler, D. Shafir, P. B. Corkum, A. Baltuška, et al. “Subcycle control of electron-electron correlation in double ionization”. *Physical Review Letters* 112.19 (2014), p. 193002.
- [145] H. J. Wörner and P. B. Corkum. “Imaging and controlling multielectron dynamics by laser-induced tunnel ionization”. *Journal of Physics B: Atomic, Molecular and Optical Physics* 44.4 (2011), p. 041001.
- [146] D. Comtois, D. Zeidler, H. Pépin, J. Kieffer, D. Villeneuve, and P. Corkum. “Observation of Coulomb focusing in tunnelling ionization of noble gases”. *Journal of Physics B: Atomic, Molecular and Optical Physics* 38.12 (2005), p. 1923.

- [147] X. Hao, W. Li, J. Liu, and J. Chen. “Effect of the electron initial longitudinal velocity on the nonsequential double-ionization process”. *Physical Review A* 83.5 (2011), p. 053422.
- [148] H. Xiao-Lei, L. Wei-Dong, L. Jie, and C. Jing. “The effect of electron initial longitudinal velocity on the non-sequential double ionization process in an elliptically polarized laser field”. *Chinese Physics B* 21.8 (2012), p. 083304.
- [149] A. N. Pfeiffer, C. Cirelli, A. S. Landsman, M. Smolarski, D. Dimitrovski, L. B. Madson, and U. Keller. “Probing the longitudinal momentum spread of the electron wave packet at the tunnel exit”. *Physical Review Letters* 109.8 (2012), p. 083002.
- [150] W. Ming-Yan, W. Yan-Lan, L. Xiao-Jun, L. Wei-Dong, H. Xiao-Lei, and C. Jing. “Effect of Electron Initial Longitudinal Velocity on Low-Energy Structure in Above-Threshold Ionization Spectra”. *Chinese Physics Letters* 30.7 (2013), p. 073202.
- [151] X.-H. Tu, X.-L. Hao, W.-D. Li, S.-L. Hu, and J. Chen. “Nonadiabatic Effect on the Rescattering Trajectories of Electrons in Strong Laser Field Ionization Process”. *Chinese Physics Letters* 33.9 (2016), p. 093201.
- [152] W. Quan, M. Yuan, S. Yu, S. Xu, Y. Chen, Y. Wang, R. Sun, Z. Xiao, C. Gong, L. Hua, et al. “Laser intensity determination using nonadiabatic tunneling ionization of atoms in close-to-circularly polarized laser fields”. *Optics Express* 24.20 (2016), p. 23248.
- [153] J. Cai, Y.-j. Chen, Q.-z. Xia, D.-f. Ye, J. Liu, and L.-b. Fu. “Nonadiabaticity of electron-tunneling-ionization processes in elliptical strong laser fields”. *Physical Review A* 96.3 (2017), p. 033413.
- [154] C. Hofmann, T. Zimmermann, A. Zielinski, and A. S. Landsman. “Non-adiabatic imprints on the electron wave packet in strong field ionization with circular polarization”. *New Journal of Physics* 18.4 (2016), p. 043011.
- [155] N. Teeny, E. Yakaboylu, H. Bauke, and C. H. Keitel. “Ionization time and exit momentum in strong-field tunnel ionization”. *Physical Review Letters* 116.6 (2016), p. 063003.
- [156] N. Camus, E. Yakaboylu, L. Fechner, M. Klaiber, M. Laux, and C. H. Keitel. “Experimental Evidence for Quantum Tunneling Time”. *Physical Review Letters* 119.2 (2016), p. 023201.
- [157] H. Ni, N. Eicke, C. Ruiz, J. Cai, F. Oppermann, N. I. Shvetsov-Shilovski, and L.-W. Pi. “Tunneling criteria and a nonadiabatic term for strong-field ionization”. *Physical Review A* 98.1 (2018), p. 013411.
- [158] M. P. Bircher, E. Liberatore, N. J. Browning, S. Brickel, C. Hofmann, A. Patoz, O. T. Unke, T. Zimmermann, M. Chergui, P. Hamm, et al. “Nonadiabatic effects in electronic and nuclear dynamics”. *Structural Dynamics* 4.6 (2017), p. 061510.
- [159] C. F. de Morisson Faria, X. Liu, A. Sanpera, and M. Lewenstein. “Classical and quantum-mechanical treatments of nonsequential double ionization with few-cycle laser pulses”. *Physical Review A* 70.4 (2004), p. 043406.
- [160] G. Sansone, C. Vozzi, S. Stagira, and M. Nisoli. “Nonadiabatic quantum path analysis of high-order harmonic generation: Role of the carrier-envelope phase on short and long paths”. *Physical Review A* 70.1 (2004), p. 013411.

- [161] L. Arissian, C. Smeenk, F. Turner, C. Trallero, A. Sokolov, D. Villeneuve, A. Staudte, and P. Corkum. “Direct test of laser tunneling with electron momentum imaging”. *Physical Review Letters* 105.13 (2010), p. 133002.
- [162] M. Krüger, M. Schenk, and P. Hommelhoff. “Attosecond control of electrons emitted from a nanoscale metal tip”. *Nature* 475.7354 (2011), p. 78.
- [163] K. Liu, S. Luo, M. Li, Y. Li, Y. Feng, B. Du, Y. Zhou, P. Lu, and I. Barth. “Detecting and Characterizing the Nonadiabaticity of Laser-Induced Quantum Tunneling”. *Physical Review Letters* 122.5 (2019), p. 053202.
- [164] I. Ivanov and A. Kheifets. “Strong-field ionization of He by elliptically polarized light in attoclock configuration”. *Physical Review A* 89.2 (2014), p. 021402.
- [165] I. Ivanov, A. Kheifets, and V. V. Serov. “Attosecond time-delay spectroscopy of the hydrogen molecule”. *Physical Review A* 86.6 (2012), p. 063422.
- [166] I. Ivanov. “Evolution of the transverse photoelectron-momentum distribution for atomic ionization driven by a laser pulse with varying ellipticity”. *Physical Review A* 90.1 (2014), p. 013418.
- [167] M. De Boer and H. Muller. “Observation of large populations in excited states after short-pulse multiphoton ionization”. *Physical Review Letters* 68.18 (1992), p. 2747.
- [168] R. Jones, D. Schumacher, and P. Bucksbaum. “Population trapping in Kr and Xe in intense laser fields”. *Physical Review A* 47.1 (1993), R49.
- [169] B. Walker, B. Sheehy, L. F. DiMauro, P. Agostini, K. J. Schafer, and K. C. Kulander. “Precision measurement of strong field double ionization of helium”. *Physical Review Letters* 73.9 (1994), p. 1227.
- [170] S. Eilzer and U. Eichmann. “Steering neutral atoms in strong laser fields”. *Journal of Physics B: Atomic, Molecular and Optical Physics* 47.20 (2014), p. 204014.
- [171] U. Eichmann, A. Saenz, S. Eilzer, T. Nubbemeyer, and W. Sandner. “Observing rydberg atoms to survive intense laser fields”. *Physical Review Letters* 110.20 (2013), p. 203002.
- [172] E. Wells, I. Ben-Itzhak, and R. Jones. “Ionization of atoms by the spatial gradient of the pondermotive potential in a focused laser beam”. *Physical Review Letters* 93.2 (2004), p. 023001.
- [173] U. Eichmann, T. Nubbemeyer, H. Rottke, and W. Sandner. “Acceleration of neutral atoms in strong short-pulse laser fields”. *Nature* 461.7268 (2009), p. 1261.
- [174] S. Popruzhenko. “Quantum theory of strong-field frustrated tunneling”. *Journal of Physics B: Atomic, Molecular and Optical Physics* 51.1 (2017), p. 014002.
- [175] H. Lv, W. Zuo, L. Zhao, H. Xu, M. Jin, D. Ding, S. Hu, and J. Chen. “Comparative study on atomic and molecular Rydberg-state excitation in strong infrared laser fields”. *Physical Review A* 93.3 (2016), p. 033415.
- [176] E. Volkova, A. Popov, and O. Tikhonova. “Ionization and stabilization of atoms in a high-intensity, low-frequency laser field”. *Journal of Experimental and Theoretical Physics* 113.3 (2011), p. 394.
- [177] Q. Li, X.-M. Tong, T. Morishita, H. Wei, and C. D. Lin. “Fine structures in the intensity dependence of excitation and ionization probabilities of hydrogen atoms in intense 800-nm laser pulses”. *Physical Review A* 89.2 (2014), p. 023421.

- [178] H. Liu, Y. Liu, L. Fu, G. Xin, D. Ye, J. Liu, X. He, Y. Yang, X. Liu, Y. Deng, et al. “Low yield of near-zero-momentum electrons and partial atomic stabilization in strong-field tunneling ionization”. *Physical Review Letters* 109.9 (2012), p. 093001.
- [179] B. Zhang, W. Chen, and Z. Zhao. “Generation of Rydberg states of hydrogen atoms with intense laser pulses: The roles of Coulomb force and initial lateral momentum”. *Physical Review A* 90.2 (2014), p. 023409.
- [180] A. Landsman, A. Pfeiffer, C. Hofmann, M. Smolarski, C. Cirelli, and U. Keller. “Rydberg state creation by tunnel ionization”. *New Journal of Physics* 15.1 (2013), p. 013001.
- [181] L. Ortman, C. Hofmann, and A. Landsman. “Erratum: Dependence of Rydberg-state creation by strong-field ionization on laser intensity [Phys. Rev. A 98, 033415 (2018)]”. *Physical Review A* 99.1 (2019), p. 019901.
- [182] N. Delone and V. P. Krainov. “Energy and angular electron spectra for the tunnel ionization of atoms by strong low-frequency radiation”. *JOSA B* 8.6 (1991), p. 1207.
- [183] I. Dreissigacker and M. Lein. “Quantitative theory for the lateral momentum distribution after strong-field ionization”. *Chemical Physics* 414 (2013), p. 69.
- [184] H. Zimmermann, S. Patchkovskii, M. Ivanov, and U. Eichmann. “Unified time and frequency picture of ultrafast atomic excitation in strong laser fields”. *Physical Review Letters* 118.1 (2017), p. 013003.
- [185] I. Burenkov, A. Popov, O. Tikhonova, and E. Volkova. “New features of interaction of atomic and molecular systems with intense ultrashort laser pulses”. *Laser Physics Letters* 7.6 (2010), p. 409.
- [186] M. V. Fedorov, N. P. Poluektov, A. M. Popov, O. V. Tikhonova, V. Y. Kharin, and E. A. Volkova. “Interference stabilization revisited”. *IEEE Journal of Selected Topics in Quantum Electronics* 18.1 (2012), p. 42.
- [187] Q. Li, X.-M. Tong, T. Morishita, C. Jin, H. Wei, and C. Lin. “Rydberg states in the strong field ionization of hydrogen by 800, 1200 and 1600 nm lasers”. *Journal of Physics B: Atomic, Molecular and Optical Physics* 47.20 (2014), p. 204019.
- [188] H. Zimmermann, S. Meise, A. Khujakulov, A. Magaña, A. Saenz, and U. Eichmann. “Limit on Excitation and Stabilization of Atoms in Intense Optical Laser Fields”. *Physical Review Letters* 120.12 (2018), p. 123202.
- [189] H. Yun, J. H. Mun, S. I. Hwang, S. B. Park, I. A. Ivanov, C. H. Nam, and K. T. Kim. “Coherent extreme-ultraviolet emission generated through frustrated tunnelling ionization”. *Nature Photonics* 12.10 (2018), p. 620.
- [190] L. Diamante. *New Way to Control Meandering Electrons and Generate Extreme-Ultraviolet Emissions*. [https://www.ibs.re.kr/cop/bbs/BBSMSTR\\_000000000738/selectBoardArticle.do?nttId=16234](https://www.ibs.re.kr/cop/bbs/BBSMSTR_000000000738/selectBoardArticle.do?nttId=16234). 2018 (accessed February 8, 2019).
- [191] J. H. Mun, I. A. Ivanov, H. Yun, and K. T. Kim. “Strong-field-approximation model for coherent extreme-ultraviolet emission generated through frustrated tunneling ionization”. *Physical Review A* 98.6 (2018), p. 063429.

- [192] R. D. Glover, D. Chetty, B. A. deHarak, A. J. Palmer, M. A. Dakka, J. L. Holdsworth, I. V. Litvinyuk, A. N. Luiten, P. S. Light, and R. T. Sang. *Frustrated Tunnel Ionization with Few-cycle Pulses*. <http://www.osapublishing.org/abstract.cfm?URI=FiO-2018-JW3A.54>. 2018 (accessed April 1, 2018).
- [193] J. Dubois, S. Berman, C. Chandre, and T. Uzer. “Capturing Photoelectron Motion with Guiding Centers”. *Physical Review Letters* 121.11 (2018), p. 113202.
- [194] J. Dubois, S. Berman, C. Chandre, and T. Uzer. “Guiding-center motion for electrons in strong laser fields”. *Physical Review E* 98.5 (2018), p. 052219.
- [195] J. Dubois, S. Berman, C. Chandre, and T. Uzer. “Inclusion of Coulomb effects in laser-atom interactions”. *arXiv preprint* 1902.01607 (2019).
- [196] B. Piraux, F. Mota-Furtado, P. O’Mahony, A. Galstyan, and Y. V. Popov. “Excitation of Rydberg wave packets in the tunneling regime”. *Physical Review A* 96.4 (2017), p. 043403.
- [197] J. Venzke, R. Reiff, Z. Xue, A. Jaroń-Becker, and A. Becker. “Angular momentum distribution in Rydberg states excited by a strong laser pulse”. *Physical Review A* 98.4 (2018), p. 043434.
- [198] L. Novotny and B. Hecht. *Principles of nano-optics*. Cambridge university press, 2012.
- [199] E. Betzig and J. K. Trautman. “Near-field optics: microscopy, spectroscopy, and surface modification beyond the diffraction limit”. *Science* 257.5067 (1992), p. 189.
- [200] S. Lal, S. Link, and N. J. Halas. “Nano-optics from sensing to waveguiding”. *Nature Photonics* 1.11 (2007), p. 641.
- [201] A. V. Zayats, I. I. Smolyaninov, and A. A. Maradudin. “Nano-optics of surface plasmon polaritons”. *Physics Reports* 408.3-4 (2005), p. 131.
- [202] X. Zhang and Z. Liu. “Superlenses to overcome the diffraction limit”. *Nature Materials* 7.6 (2008), p. 435.
- [203] S. C. Kehr, R. G. McQuaid, L. Ortmann, T. Kämpfe, F. Kuschewski, D. Lang, J. Döring, J. M. Gregg, and L. M. Eng. “A local superlens”. *ACS Photonics* 3.1 (2015), p. 20.
- [204] A. Kabashin, P. Evans, S. Pastkovsky, W. Hendren, G. Wurtz, R. Atkinson, R. Pollard, V. Podolskiy, and A. Zayats. “Plasmonic nanorod metamaterials for biosensing”. *Nature Materials* 8.11 (2009), p. 867.
- [205] V. Fiehler, F. Patrovsky, L. Ortmann, S. Derenko, A. Hille, and L. M. Eng. “Plasmonic nanorod antenna array: Analysis in reflection and transmission”. *The Journal of Physical Chemistry C* 120.22 (2016), p. 12178.
- [206] S. Kawata, M. Ohtsu, and M. Irie. *Nano-optics*. Vol. 84. Springer, 2012.
- [207] P. Bazylewski, S. Ezugwu, and G. Fanchini. “A review of three-dimensional scanning near-field optical microscopy (3D-SNOM) and its applications in nanoscale light management”. *Applied Sciences* 7.10 (2017), p. 973.
- [208] E. Bailo and V. Deckert. “Tip-enhanced Raman scattering”. *Chemical Society Reviews* 37.5 (2008), p. 921.



- [209] R. M. Stöckle, Y. D. Suh, V. Deckert, and R. Zenobi. “Nanoscale chemical analysis by tip-enhanced Raman spectroscopy”. *Chemical Physics Letters* 318.1-3 (2000), p. 131.
- [210] A. Hartschuh, E. J. Sánchez, X. S. Xie, and L. Novotny. “High-resolution near-field Raman microscopy of single-walled carbon nanotubes”. *Physical Review Letters* 90.9 (2003), p. 095503.
- [211] R. C. Reddick, R. Warmack, D. Chilcott, S. Sharp, and T. Ferrell. “Photon scanning tunneling microscopy”. *Review of Scientific Instruments* 61.12 (1990), p. 3669.
- [212] T. Ferrell, S. Sharp, and R. Warmack. “Progress in photon scanning tunneling microscopy (PSTM)”. *Ultramicroscopy* 42 (1992), p. 408.
- [213] H. Schneckenburger. “Total internal reflection fluorescence microscopy: technical innovations and novel applications”. *Current Opinion in Biotechnology* 16.1 (2005), p. 13.
- [214] D. Axelrod. “Total internal reflection fluorescence microscopy in cell biology”. *Traffic* 2.11 (2001), p. 764.
- [215] M. Grundmann. *Nano-optoelectronics: concepts, physics and devices*. Springer Science & Business Media, 2002.
- [216] W. M. Duncan. “Near-field scanning optical microscope for microelectronic materials and devices”. *Journal of Vacuum Science & Technology A: Vacuum, Surfaces, and Films* 14.3 (1996), p. 1914.
- [217] G. S. Shekhawat and V. P. Dravid. “Nanoscale imaging of buried structures via scanning near-field ultrasound holography”. *Science* 310.5745 (2005), p. 89.
- [218] G. Herink, D. Solli, M. Gulde, and C. Ropers. “Field-driven photoemission from nanostructures quenches the quiver motion”. *Nature* 483.7388 (2012), p. 190.
- [219] F. Süßmann, S. L. Stebbings, S. Zherebtsov, S. H. Chew, M. I. Stockman, E. Rühl, U. Kleineberg, T. Fennel, and M. F. Kling. “Attosecond nanophysics”. *Attosecond and XUV Physics: Ultrafast Dynamics and Spectroscopy* (2014), p. 421.
- [220] M. Krüger, M. Schenk, P. Hommelhoff, G. Wachter, C. Lemell, and J. Burgdörfer. “Interaction of ultrashort laser pulses with metal nanotips: a model system for strong-field phenomena”. *New Journal of Physics* 14.8 (2012), p. 085019.
- [221] M. Krüger, S. Thomas, M. Förster, and P. Hommelhoff. “Self-probing of metal nanotips by rescattered electrons reveals the nano-optical near-field”. *Journal of Physics B: Atomic, Molecular and Optical Physics* 47.12 (2014), p. 124022.
- [222] B. Förg, J. Schötz, F. Süßmann, M. Förster, M. Krüger, B. Ahn, W. Okell, K. Wintersperger, S. Zherebtsov, A. Guggenmos, et al. “Attosecond nanoscale near-field sampling”. *Nature Communications* 7 (2016), p. 11717.
- [223] P. Hommelhoff, C. Kealhofer, and M. A. Kasevich. “Ultrafast electron pulses from a tungsten tip triggered by low-power femtosecond laser pulses”. *Physical Review Letters* 97.24 (2006), p. 247402.
- [224] P. Hommelhoff, C. Kealhofer, A. Aghajani-Talesh, Y. R. Sortais, S. M. Foreman, and M. A. Kasevich. “Extreme localization of electrons in space and time”. *Ultramicroscopy* 109.5 (2009), p. 423.



- [225] J. Vogelsang, J. Robin, B. J. Nagy, P. Dombi, D. Rosenkranz, M. Schiek, P. Groß, and C. Lienau. “Ultrafast electron emission from a sharp metal nanotaper driven by adiabatic nanofocusing of surface plasmons”. *Nano Letters* 15.7 (2015), p. 4685.
- [226] M. Krüger, C. Lemell, G. Wachter, J. Burgdörfer, and P. Hommelhoff. “Attosecond physics phenomena at nanometric tips”. *Journal of Physics B: Atomic, Molecular and Optical Physics* 51.17 (2018), p. 172001.
- [227] E. Jones, M. Becker, J. Luiten, and H. Batelaan. “Laser control of electron matter waves”. *Laser & Photonics Reviews* 10.2 (2016), p. 214.
- [228] M. Kozák, J. McNeur, K. J. Leedle, H. Deng, N. Schönenberger, A. Ruehl, I. Hartl, J. Harris, R. Byer, and P. Hommelhoff. “Optical gating and streaking of free electrons with sub-optical cycle precision”. *Nature Communications* 8 (2017), p. 14342.
- [229] E. Quinonez, J. Handali, and B. Barwick. “Femtosecond photoelectron point projection microscope”. *Review of Scientific Instruments* 84.10 (2013), p. 103710.
- [230] A. Bainbridge, C. Barlow Myers, and W. Bryan. “Femtosecond few- to single-electron point-projection microscopy for nanoscale dynamic imaging”. *Structural Dynamics* 3.2 (2016), p. 023612.
- [231] M. Muller, V. Kravtsov, A. Paarmann, M. B. Raschke, and R. Ernstorfer. “Nanofocused plasmon-driven sub-10 fs electron point source”. *ACS Photonics* 3.4 (2016), p. 611.
- [232] S. Kim, J. Jin, Y.-J. Kim, I.-Y. Park, Y. Kim, and S.-W. Kim. “High-harmonic generation by resonant plasmon field enhancement”. *Nature* 453.7196 (2008), p. 757.
- [233] M. Sivis, M. Duwe, B. Abel, and C. Ropers. “Nanostructure-enhanced atomic line emission”. *Nature* 485.7397 (2012), E1.
- [234] S. Kim, J. Jin, Y.-J. Kim, I.-Y. Park, Y. Kim, and S.-W. Kim. “Kim et al. reply”. *Nature* 485.7397 (2012), E1.
- [235] N. Pfullmann, C. Waltermann, M. Noack, S. Rausch, T. Nagy, C. Reinhardt, M. Kovačev, V. Knittel, R. Bratschitsch, D. Akemeier, et al. “Bow-tie nano-antenna assisted generation of extreme ultraviolet radiation”. *New journal of Physics* 15.9 (2013), p. 093027.
- [236] M. Sivis, M. Duwe, B. Abel, and C. Ropers. “Extreme-ultraviolet light generation in plasmonic nanostructures”. *Nature Physics* 9.5 (2013), p. 304.
- [237] A. Blättermann, C.-T. Chiang, and W. Widdra. “Atomic line emission and high-order harmonic generation in argon driven by 4-MHz sub- $\mu$ J laser pulses”. *Physical Review A* 89.4 (2014), p. 043404.
- [238] M. F. Ciappina, J. A. Pérez-Hernández, A. S. Landsman, W. A. Okell, S. Zherebtsov, B. Förg, J. Schötz, L. Seiffert, T. Fennel, T. Shaaran, et al. “Attosecond physics at the nanoscale”. *Reports on Progress in Physics* 80.5 (2017), p. 054401.
- [239] I.-Y. Park, S. Kim, J. Choi, D.-H. Lee, Y.-J. Kim, M. F. Kling, M. I. Stockman, and S.-W. Kim. “Plasmonic generation of ultrashort extreme-ultraviolet light pulses”. *Nature Photonics* 5.11 (2011), p. 677.

- [240] S. L. Stebbings, F. Süßmann, Y. Y. Yang, A. Scrinzi, M. Durach, A. Rusina, M. Stockman, and M. F. Kling. “Generation of isolated attosecond extreme ultraviolet pulses employing nanoplasmonic field enhancement: optimization of coupled ellipsoids”. *New Journal of Physics* 13.7 (2011), p. 073010.
- [241] A. Husakou, S.-J. Im, and J. Herrmann. “Theory of plasmon-enhanced high-order harmonic generation in the vicinity of metal nanostructures in noble gases”. *Physical Review A* 83.4 (2011), p. 043839.
- [242] I. Yavuz, E. Bleda, Z. Altun, and T. Topcu. “Generation of a broadband xuv continuum in high-order-harmonic generation by spatially inhomogeneous fields”. *Physical Review A* 85.1 (2012), p. 013416.
- [243] M. Ciappina, S. S. Aćimović, T. Shaaran, J. Biegert, R. Quidant, and M. Lewenstein. “Enhancement of high harmonic generation by confining electron motion in plasmonic nanostructures”. *Optics Express* 20.24 (2012), p. 26261.
- [244] M. Ciappina, J. Biegert, R. Quidant, and M. Lewenstein. “High-order-harmonic generation from inhomogeneous fields”. *Physical Review A* 85.3 (2012), p. 033828.
- [245] T. Shaaran, M. Ciappina, and M. Lewenstein. “Estimating the plasmonic field enhancement using high-order harmonic generation: the role of the field inhomogeneity: JMO Series: Attosecond and Strong Field Science”. *Journal of Modern Optics* 59.19 (2012), p. 1634.
- [246] T. Shaaran, M. Ciappina, and M. Lewenstein. “Quantum-orbit analysis of high-order-harmonic generation by resonant plasmon field enhancement”. *Physical Review A* 86.2 (2012), p. 023408.
- [247] M. F. Ciappina, T. Shaaran, and M. Lewenstein. “High order harmonic generation in noble gases using plasmonic field enhancement”. *Annalen der Physik* 525.1-2 (2013), p. 97.
- [248] T. Shaaran, M. Ciappina, R. Guichard, J. Pérez-Hernández, L. Roso, M. Arnold, T. Siegel, A. Zaïr, and M. Lewenstein. “High-order-harmonic generation by enhanced plasmonic near-fields in metal nanoparticles”. *Physical Review A* 87.4 (2013), p. 041402.
- [249] J. Pérez-Hernández, M. Ciappina, M. Lewenstein, L. Roso, and A. Zaïr. “Beyond carbon K-edge harmonic emission using a spatial and temporal synthesized laser field”. *Physical Review Letters* 110.5 (2013), p. 053001.
- [250] M. Ciappina, J. Pérez-Hernández, T. Shaaran, M. Lewenstein, M. Krüger, and P. Hommelhoff. “High-order-harmonic generation driven by metal nanotip photoemission: Theory and simulations”. *Physical Review A* 89.1 (2014), p. 013409.
- [251] S. Han, H. Kim, Y. W. Kim, Y.-J. Kim, S. Kim, I.-Y. Park, and S.-W. Kim. “High-harmonic generation by field enhanced femtosecond pulses in metal-sapphire nanostructure”. *Nature Communications* 7 (2016), p. 13105.
- [252] S. Ghimire, G. Ndabashimiye, A. D. DiChiara, E. Sistrunk, M. I. Stockman, P. Agostini, L. F. DiMauro, and D. A. Reis. “Strong-field and attosecond physics in solids”. *Journal of Physics B: Atomic, Molecular and Optical Physics* 47.20 (2014), p. 204030.

- [253] G. Vampa, C. McDonald, G. Orlando, D. Klug, P. Corkum, and T. Brabec. “Theoretical analysis of high-harmonic generation in solids”. *Physical Review Letters* 113.7 (2014), p. 073901.
- [254] O. Schubert, M. Hohenleutner, F. Langer, B. Urbanek, C. Lange, U. Huttner, D. Golde, T. Meier, M. Kira, S. W. Koch, et al. “Sub-cycle control of terahertz high-harmonic generation by dynamical Bloch oscillations”. *Nature Photonics* 8.2 (2014), p. 119.
- [255] T. T. Luu, M. Garg, S. Y. Kruchinin, A. Moulet, M. T. Hassan, and E. Goulielmakis. “Extreme ultraviolet high-harmonic spectroscopy of solids”. *Nature* 521.7553 (2015), p. 498.
- [256] G. Vampa, T. Hammond, N. Thiré, B. Schmidt, F. Légaré, C. McDonald, T. Brabec, and P. Corkum. “Linking high harmonics from gases and solids”. *Nature* 522.7557 (2015), p. 462.
- [257] H. Kim, S. Han, Y. W. Kim, S. Kim, and S.-W. Kim. “Generation of coherent extreme-ultraviolet radiation from bulk sapphire crystal”. *ACS Photonics* 4.7 (2017), p. 1627.
- [258] G. Vampa, B. Ghamsari, S. S. Mousavi, T. Hammond, A. Olivieri, E. Lisicka-Skrek, A. Y. Naumov, D. Villeneuve, A. Staudte, P. Berini, et al. “Plasmon-enhanced high-harmonic generation from silicon”. *Nature Physics* 13.7 (2017), p. 659.
- [259] A. Landsman. “High-harmonic generation: The bright side of downsizing”. *Nature Physics* 13.7 (2017), p. 626.
- [260] I. Yavuz. “Gas population effects in harmonic emission by plasmonic fields”. *Physical Review A* 87.5 (2013), p. 053815.
- [261] S. Zherebtsov, T. Fennel, J. Plenge, E. Antonsson, I. Znakovskaya, A. Wirth, O. Herrwerth, F. Süßmann, C. Peltz, I. Ahmad, et al. “Controlled near-field enhanced electron acceleration from dielectric nanospheres with intense few-cycle laser fields”. *Nature Physics* 7.8 (2011), p. 656.
- [262] M. Ciappina, J. Pérez-Hernández, T. Shaaran, L. Roso, and M. Lewenstein. “Electron-momentum distributions and photoelectron spectra of atoms driven by an intense spatially inhomogeneous field”. *Physical Review A* 87.6 (2013), p. 063833.
- [263] P. Hommelhoff, Y. Sortais, A. Aghajani-Talesh, and M. A. Kasevich. “Field emission tip as a nanometer source of free electron femtosecond pulses”. *Physical Review Letters* 96.7 (2006), p. 077401.
- [264] M. Schenk, M. Krüger, and P. Hommelhoff. “Strong-field above-threshold photoemission from sharp metal tips”. *Physical Review Letters* 105.25 (2010), p. 257601.
- [265] A. Apolonski, P. Dombi, G. G. Paulus, M. Kakehata, R. Holzwarth, T. Udem, C. Lemell, K. Torizuka, J. Burgdörfer, T. W. Hänsch, et al. “Observation of light-phase-sensitive photoemission from a metal”. *Physical Review Letters* 92.7 (2004), p. 073902.
- [266] K. L. Kelly, E. Coronado, L. L. Zhao, and G. C. Schatz. “The optical properties of metal nanoparticles: the influence of size, shape, and dielectric environment”. *The Journal of Physical Chemistry B* 107.3 (2003), p. 668.

- [267] S. Thomas, G. Wachter, C. Lemell, J. Burgdörfer, and P. Hommelhoff. “Large optical field enhancement for nanotips with large opening angles”. *New Journal of Physics* 17.6 (2015), p. 063010.
- [268] A. Goncharenko, H.-C. Chang, and J.-K. Wang. “Electric near-field enhancing properties of a finite-size metal conical nano-tip”. *Ultramicroscopy* 107.2-3 (2007), p. 151.
- [269] W. Nolting. “Elektrodynamik”. *Grundkurs Theoretische Physik 3*. Springer, 2013, p. 51.
- [270] G. Lautz. *Elektromagnetische Felder*. Springer-Verlag, 2013.
- [271] J. D. Jackson. *Classical electrodynamics*. 1999.
- [272] S. A. Maier. *Plasmonics: fundamentals and applications*. Springer Science & Business Media, 2007.
- [273] F. Süßmann and M. F. Kling. “Attosecond measurement of petahertz plasmonic near-fields”. *Plasmonics: Metallic Nanostructures and Their Optical Properties IX*. Vol. 8096. International Society for Optics and Photonics. 2011, p. 80961C.
- [274] G. Wachter. “Simulation of condensed matter dynamics in strong femtosecond laser pulses”. PhD thesis. Technische Universität Wien, 2014.
- [275] G. Wachter, C. Lemell, J. Burgdörfer, M. Schenk, M. Krüger, and P. Hommelhoff. “Electron rescattering at metal nanotips induced by ultrashort laser pulses”. *Physical Review B* 86.3 (2012), p. 035402.
- [276] M. Ciappina, J. Pérez-Hernández, T. Shaaran, J. Biegert, R. Quidant, and M. Lewenstein. “Above-threshold ionization by few-cycle spatially inhomogeneous fields”. *Physical Review A* 86.2 (2012), p. 023413.
- [277] M. F. Ciappina, J. Pérez-Hernández, L. Roso, A. Zaïr, and M. Lewenstein. “High-order harmonic generation driven by plasmonic fields: a new route towards the generation of UV and XUV photons?” *Journal of Physics: Conference Series*. Vol. 601. 1. IOP Publishing. 2015, p. 012001.
- [278] T.-Y. Du, Z. Guan, X.-X. Zhou, and X.-B. Bian. “Enhanced high-order harmonic generation from periodic potentials in inhomogeneous laser fields”. *Physical Review A* 94.2 (2016), p. 023419.
- [279] C. Zagoya, M. Bonner, H. Chomet, E. Slade, and C. F. de Morisson Faria. “Different time scales in plasmonically enhanced high-order-harmonic generation”. *Physical Review A* 93.5 (2016), p. 053419.
- [280] T. Shaaran, R. Nicolas, B. Iwan, M. Kovacev, and H. Merdji. “Nano-plasmonic near field phase matching of attosecond pulses”. *Scientific Reports* 7.1 (2017), p. 6356.
- [281] Y. Xiang, Z. Cui, J. Lu, Y. Xu, H. Feng, X. Wang, and J. Wang. “Isolated sub-30-as pulse generation from few-cycle spatially inhomogeneous laser pulses”. *Journal of Nonlinear Optical Physics & Materials* 26.02 (2017), p. 1750026.
- [282] F. Kelkensberg, A. F. Koenderink, and M. J. J. Vrakking. “Attosecond streaking in a nano-plasmonic field”. *New Journal of Physics* 14.9 (2012), p. 093034.
- [283] E. Skopalová, D. Lei, T. Witting, C. Arrell, F. Frank, Y. Sonnefraud, S. Maier, J. Tisch, and J. Marangos. “Numerical simulation of attosecond nanoplasmonic streaking”. *New Journal of Physics* 13.8 (2011), p. 083003.

- [284] C. Blaga, F. Catoire, P. Colosimo, G. Paulus, H. Muller, P. Agostini, and L. DiMauro. “Strong-field photoionization revisited”. *Nature Physics* 5.5 (2009), p. 335.
- [285] I. Pupeza, D. Sánchez, J. Zhang, N. Lilienfein, M. Seidel, N. Karpowicz, T. Paasch-Colberg, I. Znakovskaya, M. Pescher, W. Schweinberger, et al. “High-power sub-two-cycle mid-infrared pulses at 100 MHz repetition rate”. *Nature Photonics* 9.11 (2015), p. 721.
- [286] J. Dura, N. Camus, A. Thai, A. Britz, M. Hemmer, M. Baudisch, A. Senftleben, C. Schröter, J. Ullrich, R. Moshhammer, et al. “Ionization with low-frequency fields in the tunneling regime”. *Scientific Reports* 3 (2013), p. 2675.
- [287] B. Wolter, M. G. Pullen, M. Baudisch, M. Sclafani, M. Hemmer, A. Senftleben, C. D. Schröter, J. Ullrich, R. Moshhammer, and J. Biegert. “Strong-field physics with mid-IR fields”. *Physical Review X* 5.2 (2015), p. 021034.
- [288] W. Quan, Z. Lin, M. Wu, H. Kang, H. Liu, X. Liu, J. Chen, J. Liu, X. He, S. Chen, et al. “Classical aspects in above-threshold ionization with a midinfrared strong laser field”. *Physical Review Letters* 103.9 (2009), p. 093001.
- [289] C. Wu, Y. Yang, Y. Liu, Q. Gong, M. Wu, X. Liu, X. Hao, W. Li, X. He, and J. Chen. “Characteristic spectrum of very low-energy photoelectron from above-threshold ionization in the tunneling regime”. *Physical Review Letters* 109.4 (2012), p. 043001.
- [290] M. Möller, F. Meyer, A. Sayler, G. Paulus, M. F. Kling, B. Schmidt, W. Becker, and D. Milošević. “Off-axis low-energy structures in above-threshold ionization”. *Physical Review A* 90.2 (2014), p. 023412.
- [291] T.-M. Yan, S. Popruzhenko, M. Vrakking, and D. Bauer. “Low-energy structures in strong field ionization revealed by quantum orbits”. *Physical Review Letters* 105.25 (2010), p. 253002.
- [292] Q. Xia, D. Ye, L. Fu, X. Han, and J. Liu. “Momentum distribution of near-zero-energy photoelectrons in the strong-field tunneling ionization in the long wavelength limit”. *Scientific Reports* 5 (2015), p. 11473.
- [293] A. Kästner, U. Saalman, and J.-M. Rost. “Electron-energy bunching in laser-driven soft recollisions”. *Physical Review Letters* 108.3 (2012), p. 033201.
- [294] K. Zhang, Y. H. Lai, E. Diesen, B. E. Schmidt, C. I. Blaga, J. Xu, T. T. Gorman, F. Légaré, U. Saalman, P. Agostini, et al. “Universal pulse dependence of the low-energy structure in strong-field ionization”. *Physical Review A* 93.2 (2016), p. 021403.
- [295] X. Tong and C. Lin. “Empirical formula for static field ionization rates of atoms and molecules by lasers in the barrier-suppression regime”. *Journal of Physics B: Atomic, Molecular and Optical Physics* 38.15 (2005), p. 2593.
- [296] G. Paulus, W. Nicklich, H. Xu, P. Lambropoulos, and H. Walther. “Plateau in above threshold ionization spectra”. *Physical Review Letters* 72.18 (1994), p. 2851.
- [297] G. Paulus, W. Becker, and H. Walther. “Classical rescattering effects in two-color above-threshold ionization”. *Physical Review A* 52.5 (1995), p. 4043.



- [298] T. F. Gallagher. “Above-threshold ionization in low-frequency limit”. *Physical Review Letters* 61.20 (1988), p. 2304.
- [299] D. B. Milošević, G. G. Paulus, D. Bauer, and W. Becker. “Above-threshold ionization by few-cycle pulses”. *Journal of Physics B: Atomic, Molecular and Optical Physics* 39.14 (2006), R203.
- [300] E. Fill, L. Veisz, A. Apolonski, and F. Krausz. “Sub-fs electron pulses for ultrafast electron diffraction”. *New Journal of Physics* 8.11 (2006), p. 272.
- [301] C. Kealhofer, W. Schneider, D. Ehberger, A. Ryabov, F. Krausz, and P. Baum. “All-optical control and metrology of electron pulses”. *Science* 352.6284 (2016), p. 429.
- [302] É. Mathieu. “Mémoire sur le mouvement vibratoire d’une membrane de forme elliptique.” *Journal de mathématiques pures et appliquées* 13 (1868), p. 137.
- [303] J. C. Gutiérrez-Vega, R. Rodríguez-Dagnino, M. Meneses-Nava, and S. Chávez-Cerda. “Mathieu functions, a visual approach”. *American Journal of Physics* 71.3 (2003), p. 233.
- [304] *Mathematica 11.1.1*. Wolfram Research Inc., 2017.
- [305] M. Protopapas, C. H. Keitel, and P. L. Knight. “Atomic physics with super-high intensity lasers”. *Reports on Progress in Physics* 60.4 (1997), p. 389.
- [306] E. L. Murphy and R. Good. “Thermionic emission, field emission, and the transition region”. *Physical Review* 102.6 (1956), p. 1464.
- [307] D. J. Park, B. Piglosiewicz, S. Schmidt, H. Kollmann, M. Mascheck, and C. Lienau. “Strong field acceleration and steering of ultrafast electron pulses from a sharp metallic nanotip”. *Physical Review Letters* 109.24 (2012), p. 244803.
- [308] H. Ibrahim, C. Lefebvre, A. D. Bandrauk, A. Staudte, and F. Légaré. “ $H_2$ : the benchmark molecule for ultrafast science and technologies”. *Journal of Physics B: Atomic, Molecular and Optical Physics* 51.4 (2018), p. 042002.
- [309] J. Muth-Böhm, A. Becker, and F. Faisal. “Suppressed molecular ionization for a class of diatomics in intense femtosecond laser fields”. *Physical Review Letters* 85.11 (2000), p. 2280.
- [310] X. Zhou, X.-M. Tong, Z. Zhao, and C.-D. Lin. “Alignment dependence of high-order harmonic generation from  $N_2$  and  $O_2$  molecules in intense laser fields”. *Physical Review A* 72.3 (2005), p. 033412.
- [311] R. De Nalda, E. Heesel, M. Lein, N. Hay, R. Velotta, E. Springate, M. Castillejo, and J. Marangos. “Role of orbital symmetry in high-order harmonic generation from aligned molecules”. *Physical Review A* 69.3 (2004), p. 031804.
- [312] M. Lein. “Antibonding molecular orbitals under the influence of elliptically polarized intense light”. *Journal of Physics B: Atomic, Molecular and Optical Physics* 36.10 (2003), p. L155.
- [313] V. I. Usachenko and S.-I. Chu. “Strong-field ionization of laser-irradiated light homonuclear diatomic molecules: A generalized strong-field approximation–linear combination of atomic orbitals model”. *Physical Review A* 71.6 (2005), p. 063410.



- [314] K. Lin, X. Jia, Z. Yu, F. He, J. Ma, H. Li, X. Gong, Q. Song, Q. Ji, W. Zhang, et al. "Comparison study of strong-field ionization of molecules and atoms by bicircular two-color femtosecond laser pulses". *Physical Review Letters* 119.20 (2017), p. 203202.
- [315] G. Gibson, M. Li, C. Guo, and J. Neira. "Strong-field dissociation and ionization of  $H_2^+$  using ultrashort laser pulses". *Physical Review Letters* 79.11 (1997), p. 2022.
- [316] P. Dietrich and P. B. Corkum. "Ionization and dissociation of diatomic molecules in intense infrared laser fields". *The Journal of Chemical Physics* 97.5 (1992), p. 3187.
- [317] K. Codling and L. Frasinski. "Dissociative ionization of small molecules in intense laser fields". *Journal of Physics B: Atomic, Molecular and Optical Physics* 26.5 (1993), p. 783.
- [318] B. Sheehy, B. Walker, and L. F. DiMauro. "Phase control in the two-color photodissociation of  $HD^+$ ". *Physical Review Letters* 74.24 (1995), p. 4799.
- [319] T. Seideman, M. Y. Ivanov, and P. B. Corkum. "Role of electron localization in intense-field molecular ionization". *Physical Review Letters* 75.15 (1995), p. 2819.
- [320] M. Lein. "Attosecond probing of vibrational dynamics with high-harmonic generation". *Physical Review Letters* 94.5 (2005), p. 053004.
- [321] M. Kling, C. Siedschlag, A. J. Verhoef, J. Khan, M. Schultze, T. Uphues, Y. Ni, M. Uiberacker, M. Drescher, F. Krausz, et al. "Control of electron localization in molecular dissociation". *Science* 312.5771 (2006), p. 246.
- [322] L. Frasinski, K. Codling, P. Hatherly, J. Barr, I. Ross, and W. Toner. "Femtosecond dynamics of multielectron dissociative ionization by use of a picosecond laser". *Physical Review Letters* 58.23 (1987), p. 2424.
- [323] K. Codling, L. Frasinski, P. Hatherly, and J. Barr. "On the major mode of multiphoton multiple ionisation". *Journal of Physics B: Atomic and Molecular Physics* 20.16 (1987), p. L525.
- [324] T. S. Luk and C. K. Rhodes. "Multiphoton dissociative ionization of molecular deuterium". *Physical Review A* 38.12 (1988), p. 6180.
- [325] J. Verschuur, L. Noordam, and H. V. L. Van Den Heuvel. "Anomalies in above-threshold ionization observed in  $H_2$  and its excited fragments". *Physical Review A* 40.8 (1989), p. 4383.
- [326] K. Codling, L. J. Frasinski, and P. A. Hatherly. "On the field ionisation of diatomic molecules by intense laser fields". *Journal of Physics B: Atomic, Molecular and Optical Physics* 22.12 (1989), p. L321.
- [327] K. Boyer, T. Luk, J. Solem, and C. Rhodes. "Kinetic energy distributions of ionic fragments produced by subpicosecond multiphoton ionization of  $N_2$ ". *Physical Review A* 39.3 (1989), p. 1186.
- [328] C. Cornaggia, J. Lavancier, D. Normand, J. Morellec, and H. Liu. "Intensity dependence of the multielectron dissociative ionization of  $N_2$  at 305 and 610 nm". *Physical Review A* 42.9 (1990), p. 5464.

- [329] P. H. Bucksbaum, A. Zavriyev, H. G. Muller, and D. W. Schumacher. “Softening of the  $H_2^+$  molecular bond in intense laser fields”. *Physical Review Letters* 64.16 (1990), p. 1883.
- [330] D. Normand, L. Lompre, and C. Cornaggia. “Laser-induced molecular alignment probed by a double-pulse experiment”. *Journal of Physics B: Atomic, Molecular and Optical Physics* 25.20 (1992), p. L497.
- [331] M. Klaiber and J. S. Briggs. “Crossover from tunneling to multiphoton ionization of atoms”. *Physical Review A* 94.5 (2016), p. 053405.
- [332] T. Zimmermann, S. Mishra, B. R. Doran, D. F. Gordon, and A. S. Landsman. “Tunneling time and weak measurement in strong field ionization”. *Physical Review Letters* 116.23 (2016), p. 233603.
- [333] J. Posthumus. “The dynamics of small molecules in intense laser fields”. *Reports on Progress in Physics* 67.5 (2004), p. 623.
- [334] A. D. Bandrauk. *Molecules in laser fields*. CRC Press, 1993.
- [335] M. Haertelt, X.-B. Bian, M. Spanner, A. Staudte, and P. B. Corkum. “Probing molecular dynamics by laser-induced backscattering holography”. *Physical Review Letters* 116.13 (2016), p. 133001.
- [336] Y. Huismans, A. Rouzée, A. Gijsbertsen, J. Jungmann, A. Smolkowska, P. Logman, F. Lepine, C. Cauchy, S. Zamith, T. Marchenko, et al. “Time-resolved holography with photoelectrons”. *Science* 331.6013 (2011), p. 61.
- [337] T. Marchenko, Y. Huismans, K. Schafer, and M. Vrakking. “Criteria for the observation of strong-field photoelectron holography”. *Physical Review A* 84.5 (2011), p. 053427.
- [338] X.-B. Bian and A. D. Bandrauk. “Attosecond time-resolved imaging of molecular structure by photoelectron holography”. *Physical Review Letters* 108.26 (2012), p. 263003.
- [339] M. Meckel, A. Staudte, S. Patchkovskii, D. Villeneuve, P. Corkum, R. Dörner, and M. Spanner. “Signatures of the continuum electron phase in molecular strong-field photoelectron holography”. *Nature Physics* 10.8 (2014), p. 594.
- [340] C. Lin, A.-T. Le, Z. Chen, T. Morishita, and R. Lucchese. “Strong-field rescattering physics – self-imaging of a molecule by its own electrons”. *Journal of Physics B: Atomic, Molecular and Optical Physics* 43.12 (2010), p. 122001.
- [341] J. Xu, C. I. Baga, K. Zhang, Y. H. Lai, C. Lin, T. A. Miller, P. Agostini, and L. F. DiMauro. “Diffraction using laser-driven broadband electron wave packets”. *Nature Communications* 5 (2014), p. 4635.
- [342] M. Lein, J. Marangos, and P. Knight. “Electron diffraction in above-threshold ionization of molecules”. *Physical Review A* 66.5 (2002), p. 051404.
- [343] B. Wolter, M. G. Pullen, A.-T. Le, M. Baudisch, K. Doblhoff-Dier, A. Senfleben, M. Hemmer, C. D. Schröter, J. Ullrich, T. Pfeifer, et al. “Ultrafast electron diffraction imaging of bond breaking in di-ionized acetylene”. *Science* 354.6310 (2016), p. 308.
- [344] M. Peters, T. Nguyen-Dang, C. Cornaggia, S. Saugout, E. Charron, A. Keller, and O. Atabek. “Ultrafast molecular imaging by laser-induced electron diffraction”. *Physical Review A* 83.5 (2011), p. 051403.

- [345] M. Peters, T. Nguyen-Dang, E. Charron, A. Keller, and O. Atabek. "Laser-induced electron diffraction: a tool for molecular orbital imaging". *Physical Review A* 85.5 (2012), p. 053417.
- [346] X.-B. Bian and A. D. Bandrauk. "Orientation-dependent forward-backward photoelectron holography from asymmetric molecules". *Physical Review A* 89.3 (2014), p. 033423.
- [347] M. Li, J. Yuan, X. Sun, J. Yu, Q. Gong, and Y. Liu. "Recollision-induced subcycle interference of molecules in strong laser fields". *Physical Review A* 89.3 (2014), p. 033425.
- [348] M. Li, X. Sun, X. Xie, Y. Shao, Y. Deng, C. Wu, Q. Gong, and Y. Liu. "Revealing backward rescattering photoelectron interference of molecules in strong infrared laser fields". *Scientific Reports* 5 (2015), p. 8519.
- [349] J. Marangos. "Development of high harmonic generation spectroscopy of organic molecules and biomolecules". *Journal of Physics B: Atomic, Molecular and Optical Physics* 49.13 (2016), p. 132001.
- [350] Y. Liang, S. Augst, S. Chin, Y. Beaudoin, and M. Chaker. "High harmonic generation in atomic and diatomic molecular gases using intense picosecond laser pulses—a comparison". *Journal of Physics B: Atomic, Molecular and Optical Physics* 27.20 (1994), p. 5119.
- [351] A. D. Bandrauk, S. Chelkowski, S. Kawai, and H. Lu. "Effect of nuclear motion on molecular high-order harmonics and on generation of attosecond pulses in intense laser pulses". *Physical Review Letters* 101.15 (2008), p. 153901.
- [352] O. Smirnova, Y. Mairesse, S. Patchkovskii, N. Dudovich, D. Villeneuve, P. Corkum, and M. Y. Ivanov. "High harmonic interferometry of multi-electron dynamics in molecules". *Nature* 460.7258 (2009), p. 972.
- [353] Y. He, L. He, P. Lan, B. Wang, L. Li, X. Zhu, W. Cao, and P. Lu. "Molecular rotation movie filmed with high-harmonic generation". *arXiv preprint* 1902.05662 (2019).
- [354] M. Lein, T. Kreibich, E. Gross, and V. Engel. "Strong-field ionization dynamics of a model  $H_2$  molecule". *Physical Review A* 65.3 (2002), p. 033403.
- [355] H. Yu, T. Zuo, and A. D. Bandrauk. "Molecules in intense laser fields: enhanced ionization in a one-dimensional model of  $H_2$ ". *Physical Review A* 54.4 (1996), p. 3290.
- [356] A. D. Bandrauk and H. Lu. "Generalized space translation and new numerical methods for time-dependent Schroedinger equations of molecules in intense laser fields". *Journal of Molecular Structure: THEOCHEM* 547.1-3 (2001), p. 97.
- [357] I. Petersen, J. Henkel, and M. Lein. "Signatures of molecular orbital structure in lateral electron momentum distributions from strong-field ionization". *Physical Review Letters* 114.10 (2015), p. 103004.
- [358] M. Abu-Samha and L. B. Madsen. "Interrogation of orbital structure by elliptically polarized intense femtosecond laser pulses". *Physical Review A* 84.2 (2011), p. 023411.

- [359] C. Martiny, M. Abu-Samha, and L. B. Madsen. "Ionization of oriented targets by intense circularly polarized laser pulses: Imprints of orbital angular nodes in the two-dimensional momentum distribution". *Physical Review A* 81.6 (2010), p. 063418.
- [360] D. Milošević. "Strong-field approximation for ionization of a diatomic molecule by a strong laser field". *Physical Review A* 74.6 (2006), p. 063404.
- [361] N. Suárez, A. Chacón, M. F. Ciappina, B. Wolter, J. Biegert, and M. Lewenstein. "Above-threshold ionization and laser-induced electron diffraction in diatomic molecules". *Physical Review A* 94.4 (2016), p. 043423.
- [362] N. Suárez, A. Chacón, E. Pisanty, L. Ortmann, A. S. Landsman, A. Picón, J. Biegert, M. Lewenstein, and M. F. Ciappina. "Above-threshold ionization in multicenter molecules: The role of the initial state". *Physical Review A* 97.3 (2018), p. 033415.
- [363] C. Chirilă and M. Lein. "Assessing different forms of the strong-field approximation for harmonic generation in molecules". *Journal of Modern Optics* 54.7 (2007), p. 1039.
- [364] X.-M. Tong, Z. Zhao, and C.-D. Lin. "Theory of molecular tunneling ionization". *Physical Review A* 66.3 (2002), p. 033402.
- [365] I. V. Litvinyuk, K. F. Lee, P. W. Dooley, D. M. Rayner, D. M. Villeneuve, and P. B. Corkum. "Alignment-dependent strong field ionization of molecules". *Physical Review Letters* 90.23 (2003), p. 233003.
- [366] E. Benis, J. Xia, X. Tong, M. Faheem, M. Zamkov, B. Shan, P. Richard, and Z. Chang. "Ionization suppression of  $Cl_2$  molecules in intense laser fields". *Physical Review A* 70.2 (2004), p. 025401.
- [367] A. Alnaser, S. Voss, X.-M. Tong, C. Maharjan, P. Ranitovic, B. Ulrich, T. Osipov, B. Shan, Z. Chang, and C. Cocke. "Effects of molecular structure on ion disintegration patterns in ionization of  $O_2$  and  $N_2$  by short laser pulses". *Physical Review Letters* 93.11 (2004), p. 113003.
- [368] L. Holmegaard, J. L. Hansen, L. Kalhøj, S. L. Kragh, H. Stapelfeldt, F. Filsinger, J. Küpper, G. Meijer, D. Dimitrovski, M. Abu-Samha, et al. "Photoelectron angular distributions from strong-field ionization of oriented molecules". *Nature Physics* 6.6 (2010), p. 428.
- [369] M. Abu-Samha and L. B. Madsen. "Photoelectron angular distributions from polar molecules probed by intense femtosecond lasers". *Physical Review A* 82.4 (2010), p. 043413.
- [370] H. Li, D. Ray, S. De, I. Znakovskaya, W. Cao, G. Laurent, Z. Wang, M. F. Kling, A.-T. Le, and C. Cocke. "Orientation dependence of the ionization of CO and NO in an intense femtosecond two-color laser field". *Physical Review A* 84.4 (2011), p. 043429.
- [371] J. Wu, L. P. H. Schmidt, M. Kunitski, M. Meckel, S. Voss, H. Sann, H. Kim, T. Jahnke, A. Czasch, and R. Dörner. "Multiorbital tunneling ionization of the CO molecule". *Physical Review Letters* 108.18 (2012), p. 183001.
- [372] R. Murray, W.-K. Liu, and M. Y. Ivanov. "Partial Fourier-transform approach to tunnel ionization: Atomic systems". *Physical Review A* 81.2 (2010), p. 023413.

- [373] R. Murray, M. Spanner, S. Patchkovskii, and M. Y. Ivanov. “Tunnel ionization of molecules and orbital imaging”. *Physical Review Letters* 106.17 (2011), p. 173001.
- [374] M. Liu and Y. Liu. “Application of the partial-Fourier-transform approach for tunnel ionization of molecules”. *Physical Review A* 93.4 (2016), p. 043426.
- [375] N. I. Shvetsov-Shilovski, M. Lein, and K. Tókési. “Semiclassical two-step model for ionization of the hydrogen molecule by a strong laser field”. *The European Physical Journal D* 73.2 (2019), p. 37.
- [376] A. Talebpour, S. Larochele, and S.-L. Chin. “Suppressed tunnelling ionization of the molecule in an intense Ti: sapphire laser pulse”. *Journal of Physics B: Atomic, Molecular and Optical Physics* 31.2 (1998), p. L49.
- [377] D. Normand and M. Schmidt. “Multiple ionization of atomic and molecular iodine in strong laser fields”. *Physical Review A* 53.4 (1996), R1958.
- [378] N. Takemoto and A. Becker. “Multiple ionization bursts in laser-driven hydrogen molecular ion”. *Physical Review Letters* 105.20 (2010), p. 203004.
- [379] N. Takemoto and A. Becker. “Time-resolved view on charge-resonance-enhanced ionization”. *Physical Review A* 84.2 (2011), p. 023401.
- [380] M. Odenweller, N. Takemoto, A. Vredenburg, K. Cole, K. Pahl, J. Titze, L. P. H. Schmidt, T. Jahnke, R. Dörner, and A. Becker. “Strong Field Electron Emission from Fixed in Space  $H_2^+$  Ions”. *Physical Review Letters* 107.14 (2011), p. 143004.
- [381] M. Odenweller, J. Lower, K. Pahl, M. Schütt, J. Wu, K. Cole, A. Vredenburg, L. P. Schmidt, N. Neumann, J. Titze, et al. “Electron emission from  $H_2^+$  in strong laser fields”. *Physical Review A* 89.1 (2014), p. 013424.
- [382] K. Liu and I. Barth. “Identifying the Tunneling Site in Strong-Field Ionization of  $H_2^+$ ”. *Physical Review Letters* 119.24 (2017), p. 243204.
- [383] C. Zhai, X. Zhu, P. Lan, F. Wang, L. He, W. Shi, Y. Li, M. Li, Q. Zhang, and P. Lu. “Diffractive molecular-orbital tomography”. *Physical Review A* 95.3 (2017), p. 033420.
- [384] T. Zuo and A. D. Bandrauk. “Charge-resonance-enhanced ionization of diatomic molecular ions by intense lasers”. *Physical Review A* 52.4 (1995), R2511.
- [385] L. Frasinski, K. Codling, and P. Hatherly. “Covariance mapping: A correlation method applied to multiphoton multiple ionization”. *Science* 246.4933 (1989), p. 1029.
- [386] M. Thompson, M. Thomas, P. Taday, J. Posthumus, A. Langley, L. Frasinski, and K. Codling. “One and two-colour studies of the dissociative ionization and Coulomb explosion of with intense Ti:sapphire laser pulses”. *Journal of Physics B: Atomic, Molecular and Optical Physics* 30.24 (1997), p. 5755.
- [387] D. Ray, F. He, S. De, W. Cao, H. Mashiko, P. Ranitovic, K. Singh, I. Znakovskaya, U. Thumm, G. Paulus, et al. “Ion-energy dependence of asymmetric dissociation of  $D_2$  by a two-color laser field”. *Physical Review Letters* 103.22 (2009), p. 223201.
- [388] K. Betsch, D. Pinkham, and R. Jones. “Directional emission of multiply charged ions during dissociative ionization in asymmetric two-color laser fields”. *Physical Review Letters* 105.22 (2010), p. 223002.



- [389] L. Xin, H.-C. Qin, W.-Y. Wu, and F. He. “Fraunhofer-like diffracted lateral photoelectron momentum distributions of  $H_2^+$  in charge-resonance-enhanced ionization in strong laser fields”. *Physical Review A* 92.6 (2015), p. 063803.
- [390] H. Xu, F. He, D. Kielpinski, R. Sang, and I. Litvinyuk. “Experimental observation of the elusive double-peak structure in R-dependent strong-field ionization rate of  $H_2^+$ ”. *Scientific Reports* 5 (2015).
- [391] J. Wu, M. Meckel, L. P. H. Schmidt, M. Kunitski, S. Voss, H. Sann, H. Kim, T. Jahnke, A. Czasch, and R. Dörner. “Probing the tunnelling site of electrons in strong field enhanced ionization of molecules”. *Nature Communications* 3 (2012), p. 1113.
- [392] B. Ulrich, A. Vredenburg, A. Malakzadeh, M. Meckel, K. Cole, M. Smolarski, Z. Chang, T. Jahnke, and R. Dörner. “Double-ionization mechanisms of the argon dimer in intense laser fields”. *Physical Review A* 82.1 (2010), p. 013412.
- [393] W. Lai and C. Guo. “Direct detection of enhanced ionization in CO and  $N_2$  in strong fields”. *Physical Review A* 90.3 (2014), p. 031401.
- [394] A. Saenz. “Enhanced ionization of molecular hydrogen in very strong fields”. *Physical Review A* 61.5 (2000), p. 051402.
- [395] M. Brewczyk and L. Frasiniski. “Thomas-Fermi-Dirac model of nitrogen molecules ionized by strong laser fields”. *Journal of Physics B: Atomic, Molecular and Optical Physics* 24.13 (1991), p. L307.
- [396] J. H. Posthumus, L. J. Frasiniski, A. Giles, and K. Codling. “Dissociative ionization of molecules in intense laser fields: a method of predicting ion kinetic energies and appearance intensities”. *Journal of Physics B: Atomic, Molecular and Optical Physics* 28.10 (1995), p. L349.
- [397] M. Meckel. “Laser-Induced Electron Tunneling and Diffraction”. PhD thesis. Johann-Wolfgang-Goethe-Universität Frankfurt, 2011.
- [398] P. Hansch, M. Walker, and L. Van Woerkom. “Spatially dependent multiphoton multiple ionization”. *Physical Review A* 54.4 (1996), R2559.
- [399] R. Kopold, W. Becker, M. Kleber, and G. Paulus. “Channel-closing effects in high-order above-threshold ionization and high-order harmonic generation”. *Journal of Physics B: Atomic, Molecular and Optical Physics* 35.2 (2002), p. 217.
- [400] M. Walker, P. Hansch, and L. D. Van Woerkom. “Intensity-resolved multiphoton ionization: Circumventing spatial averaging”. *Physical Review A* 57.2 (1998), R701.
- [401] S. Augst, D. D. Meyerhofer, D. Strickland, and S.-L. Chin. “Laser ionization of noble gases by Coulomb-barrier suppression”. *JOSA B* 8.4 (1991), p. 858.
- [402] G. Gibson, R. Freeman, T. McIlrath, and H. Muller. “Excitation and ionization dynamics in short-pulse multiphoton ionization”. *Physical Review A* 49.5 (1994), p. 3870.
- [403] M. W. Schmidt, K. K. Baldridge, J. A. Boatz, S. T. Elbert, M. S. Gordon, J. H. Jensen, S. Koseki, N. Matsunaga, K. A. Nguyen, S. Su, et al. “General atomic and molecular electronic structure system”. *Journal of Computational Chemistry* 14.11 (1993), p. 1347.



- [404] K. Ramachandran, G. Deepa, and K. Namboori. *Computational chemistry and molecular modeling: principles and applications*. Springer Science & Business Media, 2008.
- [405] K.-P. Huber. *Molecular spectra and molecular structure: IV. Constants of diatomic molecules*. Springer Science & Business Media, 2013.
- [406] B.-P. Stoicheff. “High resolution raman spectroscopy of gases: III. Raman spectrum of nitrogen”. *Canadian Journal of Physics* 32.10 (1954), p. 630.
- [407] D. Page and J. Powles. “The internuclear distance in  $N_2$ , gas and liquid, by neutron diffraction”. *Molecular Physics* 29.4 (1975), p. 1287.
- [408] X. Song, C. Lin, Z. Sheng, P. Liu, Z. Chen, W. Yang, S. Hu, C. D. Lin, and J. Chen. “Unraveling nonadiabatic ionization and Coulomb potential effect in strong-field photoelectron holography”. *Scientific Reports* 6 (2016), p. 28392.
- [409] G. Shi, J. Xu, H. Zhang, C. Lin, X. Song, J. Chen, and W. Yang. “Coulomb potential effects in strong-field photoelectron holography with a midinfrared laser pulse”. *Journal of Physics: Conference Series*. Vol. 869. 1. IOP Publishing. 2017, p. 012003.
- [410] A. Maxwell and C. F. de Morisson Faria. “Coulomb-free and Coulomb-distorted recolliding quantum orbits in photoelectron holography”. *Journal of Physics B: Atomic, Molecular and Optical Physics* 51.12 (2018), p. 124001.
- [411] J. Daněk. “Coulomb effects in the dipole and nondipole regimes of strong-field ionization”. PhD thesis. Ruprecht-Karls-Universität Heidelberg, 2018.
- [412] S. D. López and D. G. Arbó. “Holographic interferences in photoelectron spectra: different approaches”. *The European Physical Journal D* 73.2 (2019), p. 28.
- [413] M. Schultze, M. Fieß, N. Karpowicz, J. Gagnon, M. Korbman, M. Hofstetter, S. Neppl, A. L. Cavalieri, Y. Komninos, T. Mercouris, et al. “Delay in photoemission”. *science* 328.5986 (2010), p. 1658.
- [414] R. Pazourek, S. Nagele, and J. Burgdörfer. “Attosecond chronoscopy of photoemission”. *Reviews of Modern Physics* 87.3 (2015), p. 765.
- [415] J. Dahlström, A. L’Huillier, and A. Maquet. “Introduction to attosecond delays in photoionization”. *Journal of Physics B: Atomic, Molecular and Optical Physics* 45.18 (2012), p. 183001.
- [416] A. Kheifets and I. Ivanov. “Delay in atomic photoionization”. *Physical Review Letters* 105.23 (2010), p. 233002.
- [417] K. Klünder, J. Dahlström, M. Gisselbrecht, T. Fordell, M. Swoboda, D. Guenot, P. Johnsson, J. Caillat, J. Mauritsson, A. Maquet, et al. “Probing single-photon ionization on the attosecond time scale”. *Physical Review Letters* 106.14 (2011), p. 143002.
- [418] S. Nagele, R. Pazourek, J. Feist, K. Doblhoff-Dier, C. Lemell, K. Tórkési, and J. Burgdörfer. “Time-resolved photoemission by attosecond streaking: extraction of time information”. *Journal of Physics B: Atomic, Molecular and Optical Physics* 44.8 (2011), p. 081001.
- [419] M. Sabbar, S. Heuser, R. Boge, M. Lucchini, T. Carette, E. Lindroth, L. Gallmann, C. Cirelli, and U. Keller. “Resonance effects in photoemission time delays”. *Physical Review Letters* 115.13 (2015), p. 133001.

- [420] M. Huppert, I. Jordan, D. Baykusheva, A. Von Conta, and H. J. Wörner. “Attosecond delays in molecular photoionization”. *Physical Review Letters* 117.9 (2016), p. 093001.
- [421] M. Ossiander, F. Siegrist, V. Shirvanyan, R. Pazourek, A. Sommer, T. Latka, A. Guggenmos, S. Nagele, J. Feist, J. Burgdörfer, et al. “Attosecond correlation dynamics”. *Nature Physics* 13.3 (2017), p. 280.
- [422] T. Zimmermann, L. Ortmann, C. Hofmann, J.-M. Rost, and A. S. Landsman. “Attosecond streaking delays in multi-electron systems”. *arXiv preprint* 1804.09583 (2018).
- [423] J. Vos, L. Cattaneo, S. Patchkovskii, T. Zimmermann, C. Cirelli, M. Lucchini, A. Kheifets, A. S. Landsman, and U. Keller. “Orientation-dependent stereo Wigner time delay and electron localization in a small molecule”. *Science* 360.6395 (2018), p. 1326.
- [424] L. Gallmann, C. Cirelli, and U. Keller. “Attosecond science: recent highlights and future trends”. *Annual Review of Physical Chemistry* 63 (2012), p. 447.
- [425] P. Hockett, E. Frumker, D. M. Villeneuve, and P. B. Corkum. “Time delay in molecular photoionization”. *Journal of Physics B: Atomic, Molecular and Optical Physics* 49.9 (2016), p. 095602.
- [426] A. Chacon, M. Lein, and C. Ruiz. “Asymmetry of Wigner’s time delay in a small molecule”. *Physical Review A* 89.5 (2014), p. 053427.
- [427] S. Nagele, R. Pazourek, J. Feist, and J. Burgdörfer. “Time shifts in photoemission from a fully correlated two-electron model system”. *Physical Review A* 85.3 (2012), p. 033401.
- [428] S. Beaulieu, A. Comby, A. Clergerie, J. Caillat, D. Descamps, N. Dudovich, B. Fabre, R. Géneaux, F. Légaré, S. Petit, et al. “Attosecond-resolved photoionization of chiral molecules”. *Science* 358.6368 (2017), p. 1288.
- [429] D. Baykusheva and H. J. Wörner. “Theory of attosecond delays in molecular photoionization”. *The Journal of Chemical Physics* 146.12 (2017), p. 124306.
- [430] G. Wachter, S. Nagele, S. A. Sato, R. Pazourek, M. Wais, C. Lemell, X.-M. Tong, K. Yabana, and J. Burgdörfer. “Protocol for observing molecular dipole excitations by attosecond self-streaking”. *Physical Review A* 92.6 (2015), p. 061403.
- [431] C. Lemell, B. Solleder, K. Tókési, and J. Burgdörfer. “Simulation of attosecond streaking of electrons emitted from a tungsten surface”. *Physical Review A* 79.6 (2009), p. 062901.





---

# Acknowledgments

I remember that I have started thinking about how to write this acknowledgment a long time ago, long before I started writing this thesis or even started thinking about this thesis' other details. The reason for this strange order of events is certainly that throughout my time as a PhD student I have met so many people to whom I owe gratitude that I was looking forward to expressing my thankfulness. And I know I am, rather generally, bad at expressing my appreciation in direct interaction with people, so I was hoping the acknowledgment part of my PhD thesis could be the place to finally say what probably should have been said a while ago.

First of all, I want to express my thanks to Jan-Michael Rost, my 'Doktorvater', who not only bears a lot of the administrative burdens and runs the Finite Systems Department and this institute in a way that allows us to focus on science, but who ensured that everything went smoothly with my PhD studies and my dissertation and who provided encouragement and helpful advice concerning future career perspectives.

Great thanks is also due to my direct supervisor, Alexandra Landsman, aka Sasha. Thank you for getting me involved in so many different and excellent projects and collaborations that whenever I was asked what things I am currently working on, I usually had to briefly stop and think in order to figure out which ones I should mention. And thank you that, besides providing me with great projects, you gave me a lot of freedom to come up with my own ideas. Concerning these projects that I started off my own bat, I am particularly grateful that your experience and ideas helped me steer my work into directions in which it became of interest to more people than just me. Thank you for explaining many strong field effects to me in a way that was more concise, to the point, and intuitive than I could find it in any book or publication. Thank you for introducing me to the art of paper writing, responding to referee comments, reviewing other people's work, and many other academic skills. Thank you for teaching me a lot of the unwritten rules of academia. Thank you for encouraging without pushing.

A special thank goes to Cornelia Hofmann. You took a lot of your time at the beginning of my PhD studies to introduce me to the world of attoscience, nonadiabatic theories and the intricacies of CTMC simulations. I appreciate that you always made me feel welcome, gave in-depth answers to my many questions, discussed a lot of details with me, and always provided encouragement with your uplifting attitude. I want to particularly thank you for a lot of proofreading that you have done for me, for being

thorough without being nitpicky. Not only have you provided great feedback to major parts of this thesis, but I also enjoyed having you as a coauthor on our common publications.

I am deeply indebted to Tomáš Zimmermann, who put a lot of effort and time into introducing me to the intricacies of his implementation of the Classical Wigner Propagation method. Even though I still have not ventured into the deeper layers of the program, or shall I say program package, you have succeeded in teaching me how to use and work with the upper layers of it. Thank you for your indefatigable patience in answering my numerous questions. A quick search through my email account tells me that you have written about 600 emails to me in the past few years, most of which were triggered by me having questions concerning the CWP method, quantum chemistry, or computational details. In addition, you have answered many more questions personally during your time in Dresden. Thank you for your exceptional commitment from which I have benefited a lot!

Also, I want to thank the people in the project with inhomogeneous fields for the great collaboration: Jose Pérez-Hernández, Marcelo Ciappina, Johannes Schötz, Alexis Chacón, Ghassan Zeraouli, Matthias Kling, Luis Roso, and Maciej Lewenstein. Here, I want to specially thank Jose who performed the TDSE simulations and who, together with Marcelo, patiently walked me through my first arXiv upload and my first paper submission.

Alexis Chacón has not only made my involvement in double-ionization with inhomogeneous fields possible, but he also visited us in Dresden several times. Two of those visits were dedicated to giving me a personal introduction into two different codes for calculating HHG in solids, written by him and Edyta Osika, respectively. Thanks for taking the time to teach me how to work with these codes. And thank you, Alexis and Edyta, for sharing your codes with me.

Speaking of visitors, I also want to offer my sincere gratitude to Igor Ivanov, who visited us in Dresden several times as well. Thanks for getting me involved in the project using the functional derivative to calculate the instantaneous ionization rate. And thanks a lot for providing TDSE results for comparison with my nonadiabatic CTMC simulations shown in chapter 3.

I also owe thanks to Liangwen Pi for the idea of using a perturbative approach to describe the movement of the electron in the inhomogeneous field. As you know, Liangwen, the perturbative approach works much better to describe the velocity than the complicated scheme I had devised before you came along with the perturbative ansatz.

Another direct and important contribution to what is presented in this thesis came from André Staudte. He dug up the experimental data presented in chapter 6 and provided crucial additional information on how to deal with and interpret these data. Thanks a lot for your always kind and really helpful emails! Actually, the data on  $N_2$  was not the only occasion on which you provided help – you also helped us with an important question concerning classical simulations for double-ionization, which I want to thank you for as well.

There are various collaborations and projects with different experimental groups which I am grateful to be part of. Even though these projects are still ‘work in progress’ or have not made it into this thesis for other reasons, I consider them part of my PhD studies and therefore consider this dissertation an apt occasion to extend my thank to those great people: I want to thank Matthias Kling, Benjamin Förg and Shubhadeep Biswas for bearing with our theoretical back and forth with ethyl iodide without com-

plaint. Thanks also go to Jens Biegert and coworkers for giving me the opportunity to contribute to the theory explaining your exciting experimental data. I am also grateful to Marcus Ossiander and Martin Schultz for getting me involved into an interesting streaking experiment and for having waited patiently when our calculations were not finished as fast as expected. Thanks is also due to Seunghwoi Han, Yong Woo Kim, Seungchul Kim and all the other people in the rotating sapphire project. This project has been one of the longest I have been involved in and I want to thank you for your perseverance and for sparing no effort to improve our publication.

Without the help from the IT department of our institute a lot of the calculations presented in this thesis and in other work I did during my time as a PhD student would not have been possible. Anyone in this institute who frequently ran the ‘qtop’ command (or, more recently, ‘slurmtop’) has probably noticed that I was one of those users of the institute’s cluster, and of the cluster in Garching as well, who occupied a lot of the computational resources. Needless to say, various challenges appeared while preparing, running (and sometimes even post-processing) these calculations. The IT department, and especially Hubert Scherrer-Paulus, always provided help in these situations. I asked a lot of questions and you spared no effort to answer them or to solve the underlying problem for me yourself. Thank you!

The IMPRS for ‘Dynamical Processes in Atoms, Molecules and Solids’ and later the IMPRS for ‘Many Particle Systems in Structured Environments’ are what made my PhD studies, and thus this dissertation, possible from a financial point of view.

On a more personal note, I want to thank Cornelia Hofmann, Xiao-Yu Dong and Hamed Koochaki Kelardeh for, one after another, having been great office mates. Thanks that all three of you were really nice to me even though I was mostly quiet and reticent. I also want to thank Koen van Kruining for sharing organizational details of handing in a dissertation at TU Dresden with me.

Last but not least, I want to thank my family for their steadfast support. A big thank you goes to my parents and my sister for being a great family to have grown up in. Thank you for putting many efforts into staying in touch with me despite the long distance between Freiburg and Dresden. Thanks for being a living reminder of the fact that there is a life beyond physics. A special thanks goes to my great husband who, being a physicist himself, kept trying to understand what I was working on and who – sometimes just by listening – helped me disentangle my thoughts. Thank you for encouraging me when I was second-guessing myself and for supporting me in so many different ways.







---

# Versicherung

Die vorliegende Arbeit wurde am Max-Planck-Institut für Physik komplexer Systeme unter wissenschaftlicher Betreuung von Prof. Dr. Jan-Michael Rost und Dr. Alexandra S. Landsman durchgeführt.

Hiermit versichere ich, dass ich die vorliegende Arbeit ohne unzulässige Hilfe Dritter und ohne Benutzung anderer als der angegebenen Hilfsmittel angefertigt habe; die aus fremden Quellen direkt oder indirekt übernommenen Gedanken sind als solche kenntlich gemacht. Die Arbeit wurde bisher weder im Inland noch im Ausland in gleicher oder ähnlicher Form einer anderen Prüfungsbehörde vorgelegt.

Ich erkenne die Promotionsordnung der Fakultät Mathematik und Naturwissenschaften der Technischen Universität Dresden vom 23. Februar 2011 an.

---

Ort, Datum, Unterschrift

Lisa Ortmann